Synthesis, structure, microstructure, and thermoelectric properties of perovskite-type manganate phases

Dissertation
zur Erlangung des Doktorgrades
der mathematisch-naturwissenschaftlichen Fakultät
der Universität Augsburg

vorgelegt von

Laura Bocher

Augsburg, January 2009

Solid State Chemistry and Catalysis,
Empa, CH-8600 Dübendorf

EMPA
Materials Science & Technology

Bocher, Laura:

Synthesis, structure, microstructure, and thermoelectric properties of perovskite-type manganate phases

Erstgutachter:	Prof. Dr. Armin Reller
Zweitgutachter:	Prof. Dr. Anke Weidenkaff
	Prof. Dr. Jochen Mannhart

Tag der mündlichen Prüfung: 18.05.2009

Dedicated to my parents and my brother

Nothing in life is to be feared. It is only to be understood
Marie Skłodowska Curie

Abstract

Polycrystalline perovskite-type manganate phases, i.e. $CaMn_{1-x}Nb_xO_3$ (x = 0.02, 0.05, 0.08, and 0.10) and $LaMn_{1-x}Co_xO_3$ (x = 0.05, 0.10, 0.90, and 0.95) phases were studied regarding their thermoelectric properties for high-temperature applications. Different synthesis methods were successfully applied, i.e. the conventional solid state reaction (SSR) method and the "*chimie douce*" synthesis routes, resulting in highly-crystalline tailor-made perovskite particles with a diversity of particle sizes, morphologies, and microstructures. Perovskite-type manganates were investigated concerning their morphology, crystal structure, microstructure, thermal stability, and low-temperature magnetic properties. Their thermoelectric properties were evaluated within the temperature range of $5\ K < T < 1270\ K$.

Nanostructured perovskite-type phases yield peculiar magnetic, electrical and thermal transport properties compared to the bulk counterpart materials. Thermally-stable mesoporous titanate phases and $CaMn_{1-x}Nb_xO_3$ phases characterized by the presence of twinned domains and Ruddlesden-Popper planar defects at the nanometer scale revealed barely low thermal conductivity values, i.e. $\kappa < 1\ W\ m^{-1}\ K^{-1}$; this being one of the essential prerequisites to achieve high-efficient thermoelectric materials.

The perovskite-type $CaMn_{1-x}Nb_xO_3$ phases (x = 0.02, 0.05, 0.08, and 0.10) were investigated as potential *n*-type thermoelectric oxides. The substitution of Mn^{4+} by Nb^{5+} in the $CaMnO_3$ system induces the creation of Mn^{3+} cations which further influences the structural and the physical properties. Tuning the charge carrier concentration, via Nb substitutions, enables to target the best compromise between large Seebeck coefficients and low electrical resistivities, both material properties being interrelated in a conflicting manner. High power factor values combined with low thermal conductivities yield $ZT > 0.3$ at $T \simeq 1000\ K$, making these phases one of the best perovskite-type structures as polycrystalline *n*-type thermoelectric materials operating in air at high temperatures. Remarkable properties such as a low-temperature magnetic transition, a high-temperature structural transition accompanied with a thermal reduction further influence the thermoelectric properties of the Nb-containing $CaMnO_3$ phases. Besides, the *B*-site substitution in the $LaMn_{1-x}Co_xO_3$ phases (x = 0.05, 0.10, 0.90, and 0.95) modifies its thermoelectric properties depending on the predominance of the transition metal.

Zusammenfassung

Polykristalline perovskitische Manganatphasen, wie beispielweise $CaMn_{1-x}Nb_xO_3$ (x = 0.02, 0.05, 0.08, and 0.10) und $LaMn_{1-x}Co_xO_3$ (x = 0.05, 0.10, 0.90, and 0.95), wurden auf ihre thermoelektrischen Eigenschaften für Hoch-Temperatur-Anwendungen untersucht. Unterschiedliche Synthesemethoden, wie die konvenionelle Festphasenreaktion und die *"chimie douce"*-Synthesen, wurden erfolgreich angewendet und fürhrten zu hochkristallinen, maßgeschneiderten Perovskit-Partikeln mit einer Varianz in der Partikelgrösse, Morphologie und Mikrostruktur. Die perovskitartigen Manganate wurden hinsichtlich ihrer Morphologie, Kristallstruktur, Mikrostruktur, thermischen Stabilität und ihrer magnetischen Eigenschaften im Tieftemperaturbereich untersucht. Ihre thermoelektrischen Eigenschaften wurden in einem Temperaturbereich von $5 \text{ K} < T < 1270 \text{ K}$ gemessen.

Die nanostrukturierten Perovskitphasen unterschieden sich durch ihre eigenartigen magnetischen, elektrischen und thermischen Transporteigenschaften sehr von den Volumephasen. Temperaturstabile, mesoporöse Titanatphasen und $CaMn_{1-x}Nb_xO_3$-Phasen wurden durch das Vorhandensein von Zwillingsdomänen und Ruddlesden-Popper-Ebenendefekten im Nanometerbereich charakterisiert und offenbarten nur sehr geringe, thermische Leitfähigkeiten ($\kappa < 1 \text{ W m}^{-1} \text{ K}^{-1}$), die jedoch essentielle Vorraussetzungen sind, um hoch-effektive thermoelektrische Materialien zu erhalten.

Die $CaMn_{1-x}Nb_xO_3$ Perovskitphasen (x = 0.02, 0.05, 0.08, and 0.10) wurden auf ihr Potential als thermoelektrische n-Typ-Oxide unersucht. Der Austausch der Mn^{4+} durch Nb^{5+} im $CaMnO_3$-System, bewirkt die Bildung von Mn^{3+} Kationen, was Auswirkungen auf die strukturellen und physikalischen Eigenschaften des Materials hat. Durch gezielte Veränderung der Ladungsträgerkonzentration mittels Nb-Austausch, erhält man die besten Kompromisse zwischen grossen Seebeckkoeffizienten und geringem, elektrischen Widerstand. Beide Materialeigenschaften sind in gegensätzlicher Weise miteinander verbunden. Grosse Leistungsfaktorwerte in Kombination mit niedriger thermischer Leitfähigkeit liefern $ZT > 0.3$ bei $T \simeq 1000$ K, was diese Phasen zu einer des besten Perovskitstruktur für polykristalline n-Typ Thermoelektrika für die Hochtemperaturanwendung in Luft macht. Magnetische Übergänge bei niedrigen Temperaturen sowie Strukturübergänge bei hohen Temperaturen in Zusammenhang mit thermischer Reduktion, sind ausserordentliche Merkmale, die weiteren Einfluss auf die thermoelektrischen Eigenschaften der Nb-haltigen $CaMnO_3$-Phasen haben. Ausserdem verändert die B-seitige Substitution in der $LaMn_{1-x}Co_xO_3$-Phase (x = 0.05, 0.10, 0.90, and 0.95) deren thermoelektrischen Eigenschaften in Abhängigkeit von der Vorherrschaft der Übergangsmetalls.

Contents

Chapter 1

Introduction

Alarming pollutant emissions, global warming, and rapidly growing energy demands are becoming a problematic issue for society. Fossil fuels currently supply most of the world's energy needs[1], yielding undesirable long-term environmental consequences and global political tensions. An immediate response from science, technology, economy, and politics is required. Alternative renewable energy sources such as biomass, hydropower, wind, geothermal or solar energy, are needed for counteracting the strong dependence on limited fossil fuel resources. Nowadays research focuses on developing functional materials and innovative technologies [Sorrell-2005] that enable the direct conversion of (i) sunlight to electric power using photovoltaic cells [Grätzel-2001], (ii) chemical energy to electricity by means of fuel cells [Steele-2001], or (iii) heat into electrical energy using thermoelectric generators [Snyder-2008]. Likewise, energy storage technologies require the development of advanced materials presenting e.g. high hydrogen-storage capacity [Schlapbach-2001]. Renewable energy technologies, that aim to produce and store "clean" electricity, are expected to be increasingly important for providing energy worldwide in the near future [Dresselhaus-2001].

Among the sustainable energy-conversion technologies, there has been a resurgence of interest in thermoelectrics, i.e. the technology that directly converts heat into electricity. Heat is emitted from boundless sources mostly in form of solar radiation, geothermal heat or waste heat on a daily base by vehicles and factories. Thermoelectric systems can harness thermal energy for generating electric power; therefore they have the potential to enhance the sustainability of our energy demands. Thermoelectric devices consist of alternate p- and n-type thermoelements electrically connected in series and thermally in parallel. As thermoelectric generators are solid-state devices, i.e. with no liquid fuel, no toxic exhaust release, and no moving parts, they are silent, reliable, and easily scalable for domestic use as well as industrial applications [Rowe-2006].

From the discovery of the thermoelectric effects to their technologic applications, the thermoelectric field met three main periods of intensive research activities. The nineteenth century signals

---

[1] about three quarters of the world's total electric power is generated from fossil fuels [Boyle-2004].

the origin of the thermoelectricity with the understanding of the basic effects at the macroscopic level. In 1821, Thomas J. Seebeck discovered that a circuit made from two dissimilar metals with the junctions maintained at different temperatures would deflect a compass needle. He initially concluded that the observed phenomenon was of magnetic origin [Seebeck-1822]. It has been later understood that the temperature difference applied at both ends of a semiconductor generates an electric potential. This phenomenon is known as the *Seebeck effect*. In 1834, Jean Charles A. Peltier discovered the reverse phenomenon, an electrical current would induce heating or cooling at the junctions of two distinct metals, i.e. the *Peltier effect* [Peltier-1834]. Only about 1910, Edmund Altenkirch described for the first time the basis of the thermoelectric conversion and introduced the so-called *figure of merit* $Z = S^2\sigma/\kappa$, which states that a good thermoelectric material should exhibit a large Seebeck coefficient S, high electrical conductivity σ, and low thermal conductivity κ [Altenkirch-1911]. As these transport properties depend on interrelated material characteristics, finding thermoelectric materials with enhanced ZT values remains a challenging issue.

In 1949, Abraham F. Ioffe[1] further developed the principles of thermoelectric conversion, providing the basis of all the modern thermoelectric theory [Ioffe-1957]. A large number of semiconductor materials were investigated by the late 1950's and early 1960's. It resulted in important progress in the development of thermoelectric materials with high efficiencies, e.g. Bi_2Te_3-, PbTe-, and SiGe-based alloys, which are still considered as the state-of-the-art materials [Rowe-2006]. This period was influenced by intensive efforts to make the technology more applicable. Since 1961 in United States, radioisotope thermoelectric generators (RTGs) successfully powered deep space probes for NASA missions such as Apollo, Pioneer, Viking, Voyager[2], Galileo, Ulysse, and Cassini [RPS-2005]. However, thermoelectric generators remained for a long time a niche technology regarding its ineffectiveness to be cost-effective for mainstream applications.

In the mid 1990's, the thermoelectric field received renewed interests mainly as a consequence of environmental concerns. Several novel thermoelectric materials with complex crystal structures such as the skutterudites have been explored leading to high ZT values [Fleurial-1996]. Theoretical predictions and experimental proof-of-principle studies have demonstrated that the thermoelectric efficiency could be further improved through nanostructural engineering [Dresselhaus-2007]. These recent advances triggered a real breakthrough and opened up new horizons for a widespread use of thermoelectricity.

With respect to the environmental sustainability, the composition of the thermoelectric materials should exclude toxic elements such as antimony and lead. Moreover, most of the promising complex thermoelectric materials operate under limited conditions, i.e. they are not stable at high temperatures under oxidative atmospheres. The idea of using thermoelectric oxide materials

---

[1] Abraham F. Ioffe pioneered the development of thermoelectricity including the first practical generators distributed during the World War II [Rowe-2006].

[2] RTG units on Voyager I and II are still operating after 30 years of utilization [RPS-2005].

has been encouraged by the discovery of the promising thermoelectric properties of the layered cobalt oxide $Na_xCo_2O_4$ by Terasaki et *al.* in 1997 [Terasaki-1997]. The layered cobaltate phases benefit from an unusual combination of a metallic-like behavior and a large Seebeck coefficient resulting in high thermoelectric efficiencies. In the past ten years, a large number of transition metal oxides have been identified as potential p- or n-type thermoelectric materials [Koumoto-2006]. One advantage of oxides is their high chemical and thermal stability in air which allow to enlarge the operating temperature range of the thermoelectric modules. The development of all-oxide thermoelectric modules is cost-efficient. Besides, those modules are composed of materials presenting low-toxicity.

In respect to energy-conversion technologies, this thesis has been motivated by the development of functional oxide-based materials for thermoelectric applications at high temperatures. One key challenge in the development of materials, with high thermoelectric efficiencies, is the lowering of the thermal conductivity without disrupting the electrical conductivity. Nanostructuring thermoelectric materials, i.e. synthesizing materials composed of nanometer-size crystallites or with nanometer-scale microstructures, might answer this issue. This thesis has therefore focused on the study of nanostructured perovskite-type manganate oxide phases, from their synthesis to the evaluation of their thermoelectric properties over a wide temperature range, i.e. $5 \text{ K} < \text{T} < 1270 \text{ K}$. The crystal structure, microstructure, thermal stability and magnetic properties are of main interests for understanding the thermoelectric properties.

This manuscript is organized in seven chapters including this introduction. The second chapter will introduce the general principles of thermoelectricity by describing the thermoelectric effects, the thermal and electrical transport coefficients, and the thermoelectric power generation. The so-called thermoelectric parameters, i.e. the Seebeck coefficient, the electrical and thermal conductivities, will also be defined. Their optimization towards the development of highly-efficient thermoelectric materials based on established strategies and new perspectives will be discussed in this context. Finally, state-of-the-art and novel thermoelectric materials will be presented, with a brief summary on the thermoelectric modules. The perovskite-type phases with promising thermoelectric properties will be reviewed in detail, with an emphasis on the manganate phases - the primary interest of this thesis. The third chapter will present the different experimental techniques used for characterizing the crystal structure, microstructure, chemical composition, thermal stability and for evaluating the magnetic and thermoelectric properties. The fourth chapter is devoted to the synthesis of thermoelectric perovskite-type phases by the conventional solid state reaction method and the *chimie douce* synthesis routes. This chapter will also give an overview of the advantages and drawbacks of the applied synthesis methods with a particular focus on the particle morphology. The thermal decomposition of the precursor synthesized by the *chimie douce* method will be studied and a specific example will be given of the formation of high-temperature stable mesoporous titanate phases. The fifth chapter is dedicated to the study of the $CaMn_{1-x}Nb_xO_3$ perovskite-type phases which yields the design of a new promising n-type thermoelectric material for high-temperature applications in air. The morphology, the cationic/anionic composition, and the B-site oxidation states of the Nb-containing $CaMnO_3$ phases will be first presented. The crystal structure and microstructure are important issues regarding their influence on the thermoelectric properties. Hence, the presence of nano-sized twinned domains and anti-phase boundary rock-salt structures will be evaluated by combining imaging and spectroscopy studies. The substitution of Mn^{4+} by Nb^{5+} on the B-site will be studied with respect to its effect on the thermoelectric properties within the temperature range of $5\ K < T < 1270\ K$. A comprehensive study on the low-temperature magnetic transition, the high-temperature structural transition, and the thermal reduction will be given in order to assess their impact on the thermoelectric activity. The chapter six will report on the $LaMn_{1-x}Co_xO_3$ perovskite-type phases concerning their compositional, structural and microstructural features toward the Co substitution. Their thermoelectric properties will be discussed with respect to the predominance of the transition metal. Finally, summary and general conclusions will be presented in chapter seven.

Chapter 2

Thermoelectrics

Thermoelectric materials enable the direct energy conversion of heat into electricity or vice versa, yielding applications in electrical power generation or refrigeration. This chapter gives first an introduction into thermoelectricity in terms of the thermoelectric effects, the thermal and electrical transport coefficients. The thermoelectric power generation and materials selection criteria are introduced in a second part. Furthermore, conventional and novel thermoelectric materials are reviewed. Finally, thermoelectric modules are briefly presented.

2.1 Thermoelectric effects

2.1.1 Seebeck effect

The principle of thermoelectric power generation from various heat sources is based on the Seebeck effect discovered by T. Y. Seebeck in 1821 [Seebeck-1822]. The formation of an electric potential along a solid subjected to a temperature gradient is known as the *Seebeck effect.* In a thermoelectric material which is exposed to a temperature gradient ΔT, the charge carriers diffuse from the hot to the cold side. This charge carrier flow results in a potential gradient. In a n-type material, the mobile charges are electrons, therefore negative charges will established at the cold side. In analogy, positive charges, i.e. holes, will build up at the cold end in a p-type material. Consequently, the induced voltage V depends on the temperature differences between the hot and cold side and is given by the Equation 2.1:

$$V = \int_{T_c}^{T_h} S(T)\,\mathrm{d}T \tag{2.1}$$

where T_h and T_c are the absolute temperatures at the hot and cold side, respectively, and S is the Seebeck coefficient, also termed thermoelectric power or thermopower. By convention, S is negative for n-type and positive for p-type materials. If S is independent of temperature, the Equation 2.1 can be simplified to:

$$V = S\ (T_H - T_C) = S\ \Delta T \tag{2.2}$$

The thermopower is defined as the difference of the electrochemical potential per unit temperature difference taking place across an electrically isolated solid exposed to a temperature gradient. Macroscopic descriptions based on thermodynamics of irreversible processes enable to derive the equations relating thermopower and transport coefficients in absence of temperature gradient [Callen-1948; Domenicali-1954]. S can be expressed as follows:

$$S = -\frac{k_B}{\mid e \mid}\left\{\frac{Q^*}{KT} - \frac{\mu_c}{KT}\right\} \tag{2.3}$$

where e is the absolute value of the electron charge, k_B is the Boltzmann constant, μ_c is the chemical potential, Q^* is defined as the carried heat per particle, and T is the absolute temperature. Q^* is expressed in terms of transport coefficients as $Q^* = e\ \epsilon/\sigma$, where ϵ corresponds to the energy flux per unit of applied electric field and σ is the electrical conductivity. In general cases, Q^* is rather difficult to be determined since it involves transfer integrals t_i which depend on the velocity and flux of the energy. Calculations can be established involving boundary conditions. The Boltzmann transport theory is not suitable for describing systems with narrow bandwidths, W typically of 0.01 eV $< t_i <$ 0.1 eV, where $t_i = W/z$ and z is the coordination number [Chaikin-1976]. In that case and considering the high temperature limit. i.e. $t_i << k_BT$, Q^* can be neglected and the thermopower becomes proportional to the chemical potential related to the entropy of the system:

$$\frac{\mu_c}{T} = \left(\frac{-\partial\mathscr{S}}{\partial N_p}\right)_{U,\mathtt{V}} \tag{2.4}$$

where $\mathscr{S}$ is the configurational entropy, N_p is the number of particles, and U and $\mathtt{V}$ are the internal energy and the internal volume, respectively. The Equation 2.4 clearly demonstrates that the thermopower can be defined as the entropy per charge carrier in a solid [Chaikin-1976]. At high temperatures, the number of configurations Ω can be used to describe the entropy of the system applying the Boltzmann formula defined by $\mathscr{S} = k_B ln\Omega + cst$. For carriers in nondegenerate states and forbidden double occupancy of single sites, Ω is given by the Equation 2.5:

$$\Omega = \frac{N!}{(N-n)!n!} \tag{2.5}$$

Using the Stirling's formula[1], the thermopower can be expressed as function of the charge carrier concentration by the Heikes formula as defined in Equation 2.6 [Heikes-1961]:

$$S\ (T \to \infty) = -\ \frac{k_B}{\mid e \mid} ln\left(\frac{1-c_e}{c_e}\right) \tag{2.6}$$

with $c_e = n/N$, where n is the number of electrons and N is the number of available sites. The Heikes formula can also be defined regarding the hole concentration, c_h, according to Equation 2.7, where $c_h = 1 - c_e$ and $c_h = p/N$, with p the number of holes:

$$S\ (T \to \infty) = +\ \frac{k_B}{\mid e \mid} ln\left(\frac{1-c_h}{c_h}\right) \tag{2.7}$$

---

[1] $ln(N!) = Nln(N) - N$

The Heikes formula was first established for localized and non magnetic systems and later generalized to magnetic systems. The Heikes formalism allows to interpret the thermopower of transition metal oxides and predicts that the Seebeck coefficient is temperature independent at high temperatures. Figure 2.1 presents the evolution of the thermopower with respect to the charge carrier concentration, defined by the Heikes formula. Low-level substitutions, i.e. low charge carrier concentrations, result in large absolute thermopower values, typical for insulators. As the charge carrier concentration increases, the thermopower tends to zero, as observed for metals.

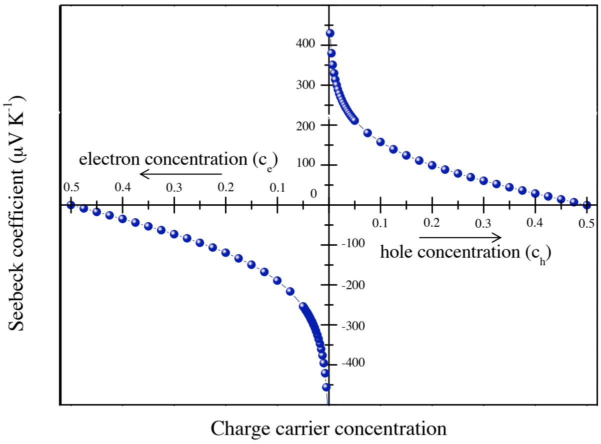

Figure 2.1: Thermopower or Seebeck coefficient as function of the charge carrier concentrations for non magnetic systems.

For magnetic systems, Chaikin and Beni emphasized that if carriers are electrons displaying a spin $\mathtt{S} = 1/2$, the spin degeneracy $\beta_S = 2$ has to be considered [Chaikin-1976]. Systems such as transition metal oxides often present $\mathtt{S} \neq 0$. Therefore, the Heikes formula has to be modified with respect to the Chaikin-Beni assumptions considering that for n electrons, the number of configurations is multiplied by 2^n, according to the Equation 2.8:

$$S\ (T \rightarrow \infty) = -\frac{k_B}{\mid e \mid} ln \left(2\ \frac{1 - c_e}{c_e} \right) \tag{2.8}$$

In analogy, the previous equation can be expressed considering holes as predominant charge carriers:

$$S\ (T \rightarrow \infty) = +\frac{k_B}{\mid e \mid} ln \left(\frac{1}{2}\ \frac{1 - c_h}{c_h} \right) \tag{2.9}$$

Based on the Equations 2.8 and 2.9, a generalization of the Chaikin-Beni formula can be established considering a system of n electrons with a degeneracy factor β_e and a system of p holes with a degeneracy factor β_h, and is given by [Doumerc-1994]:

$$S\ (T \rightarrow \infty) = -\frac{k_B}{\mid e \mid} ln \left(\frac{\beta_e}{\beta_h}\ \frac{1 - c_e}{c_e} \right) = +\frac{k_B}{\mid e \mid} ln \left(\frac{\beta_h}{\beta_e}\ \frac{1 - c_h}{c_h} \right) \tag{2.10}$$

For systems having mixed valence cations $\mathrm{M}^{n+}/\mathrm{M}^{(n+1)+}$, where the spin value of M^{n+} is $\mathtt{S}_n$ and the spin value of $\mathrm{M}^{(n+1)+}$ is $\mathtt{S}_{n+1}$, the Equation 2.10 can be simplified to:

$$S\ (T \to \infty) = -\ \frac{k_B}{\mid e \mid} ln \left(\beta_m\ \frac{1-c_e}{c_e} \right) = +\ \frac{k_B}{\mid e \mid} ln \left(\frac{1}{\beta_m}\ \frac{1-c_h}{c_h} \right) \tag{2.11}$$

where $\beta_m = (2\mathtt{S}_n + 1)/(2\mathtt{S}_{n+1} + 1)$. For systems presenting magnetic ordering, i.e. many transition metal oxides, the spin degeneracy is lifted. Consequently, the β_m value is equal or close to the unity, satisfying the Heikes formula. As later discussed in the Chapter 5, Sections 5.3.1 and 5.4.2.3, the high-temperature Seebeck coefficients of the manganate phases agree with the Heikes formula.

2.1.2 Peltier effect

The process of power generation can be reversed such that an applied current I induces heat transport through a solid. This second thermoelectric phenomenon is known as the *Peltier effect*, revealed by J. C. Peltier in 1834. Depending on the direction of the current flow through the solid, the heat is either absorbed or released to the surrounding. The absorbed/released heat Q is proportional to the applied current and given by the Equation 2.12, where Π is the Peltier coefficient:

$$Q = \Pi\ I \tag{2.12}$$

2.1.3 Thomson effect

The third thermoelectric phenomenon, the *Thomson effect*, describes the generation or absorption of heat by applying a current through a conductor material, which is exposed to a temperature gradient. The rate of heat generation dQ is therefore proportional to both the applied current and the temperature gradient according to the Equation 2.13:

$$\mathrm{d}Q = \beta_{th}\ I\ \mathrm{d}T \tag{2.13}$$

where β_{th} is the Thomson coefficient. W. Thomson (later became Lord Kelvin) demonstrated in 1851 that the Seebeck and Peltier effects are related and established the following Kelvin relationships:

$$\Pi = ST \quad and \quad \frac{dS}{dT} = \frac{\beta_{th}}{T} \tag{2.14}$$

2.2 Thermoelectric power generation and figure of merit

The thermoelectric power generation originates from the direct conversion of heat into electricity. Thermoelectric generators enable this energy conversion based on the Seebeck effect, as shown in Figure 2.2 a). In analogy, the Peltier effect allows the reverse conversion using thermoelectric refrigerators, as represented in Figure 2.2 b).

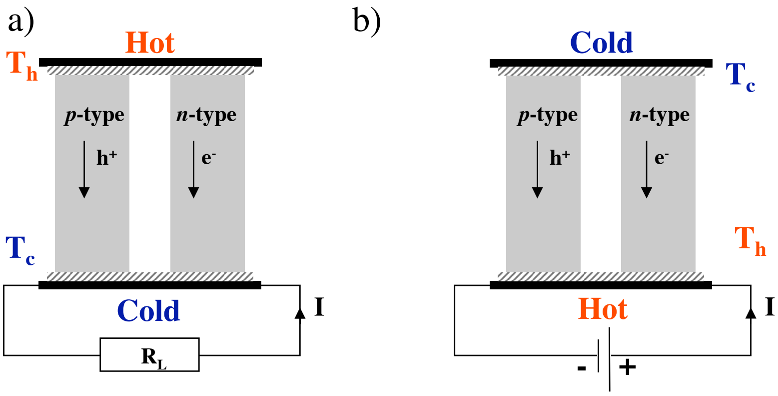

Figure 2.2: a) Thermoelectric generator and b) thermoelectric refrigerator.

2.2.1 Energy conversion efficiency

The efficiency η of the thermoelectric generators is defined as the ratio of electric power P (supplied to the load) to the heat energy Q (provided at the hot junction). Thermoelectric generation can be simplified to the case of a single p- and n-type thermoelement couple. Considering that (i) the Seebeck coefficients, the electrical and thermal conductivities are constant with temperature and (ii) the contact resistance at the cold and hot junctions is negligible, the efficiency η is defined by [Rowe-2006]:

$$\eta = \frac{P}{Q} = \frac{T_h - T_c}{T_H} \cdot \frac{\sqrt{1 + Z\overline{T}} - 1}{\sqrt{1 + Z\overline{T}} + T_c/T_h}, \qquad \text{where} \quad \overline{T} = \frac{T_h + T_c}{2}. \tag{2.15}$$

where T$_h$ and T$_c$ are the absolute temperatures at the hot and cold junctions, respectively. Z is defined as the thermoelectric *figure of merit* of the p- and n-legs and reflects the thermoelectric performance of a material. Since Z varies with temperature, the figure of merit is more meaningful in its dimensionless form ZT. The Equation 2.15 allows to determine the maximal conversion efficiency depending on the operating temperature difference and on the thermoelectric figure of merit, as illustrated in Figure 2.3. Like every heat engine, the thermoelectric generator is limited by the Carnot efficiency, $\eta_c = \Delta T / T_h$, which governs the conversion of available heat. For maximizing η, a large temperature gradient is required. The conversion efficiency is further enhanced by using materials with high figure of merit. One key-advantage of the oxide materials for thermoelectric applications is their thermal and chemical stability at high temperatures. Large temperature gradients, e.g. $\Delta T \simeq 1000\ K$, can be therefore applied on thermoelectric oxide generators.

The best commercialized thermoelectric materials achieve so far $ZT \simeq 1$. It corresponds to a conversion efficiency of 15% when applying a temperature gradient of 900 K with a cold junction temperature of T$_c$ = 300 K. Commercialized thermoelectric modules are currently composed of alloys, e.g. $(Bi,Sb)_2(Te,Se)_3$ alloys, which present limited operating temperatures to 450 K [Rowe-2006]. For comparison with another renewable energy technology, photovoltaic cells provide conversion efficiencies of 6% to 18% depending on the applied technologies[1] [IEA-PVPS-2007]. To achieve equivalent conversion efficiencies, thermoelectric materials should present ZT values between $ZT = 0.3$ with $\Delta\mathrm{T} \simeq 800$ K ($\eta_c = 6\%$) to $ZT = 1.0$ with $\Delta\mathrm{T} \simeq 1200$ K ($\eta_c = 18\%$).

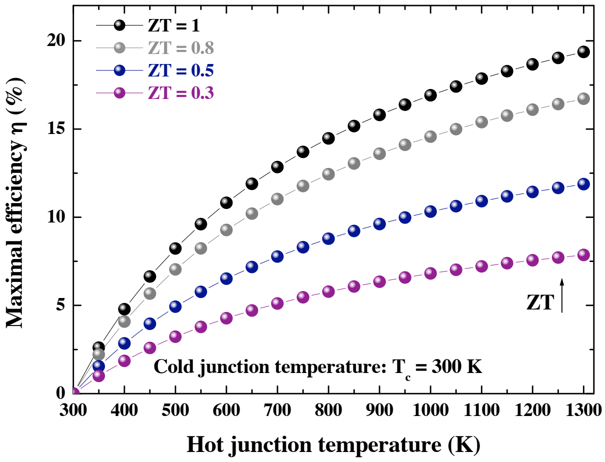

Figure 2.3: Maximal generating efficiency as function of the temperature at the hot junction and the figure of merit Z. (The temperature at the cold junction is considered to be equal to 300 K.)

In practice, assuming that both p- and n-thermoelements have similar thermoelectric properties[2], the concept of thermoelectric figure of merit Z can be applied for a specific material and Z is defined as follows:

$$Z = \frac{S^2}{\rho\kappa} = \frac{S^2\sigma}{\kappa} \tag{2.16}$$

where ρ is the electrical resistivity (inversely equal to the electrical conductivity σ) and κ is the thermal conductivity. The power factor $PF = S^2/\rho$ reflects the electrical transport properties of the material. The thermoelectric figure of merit of a material is determined by measuring the Seebeck coefficient under small temperature gradient of $5 \text{ K} < \Delta T < 10$ K, the electrical resistivity under isothermal conditions, and the thermal conductivity under $\simeq 1$ K temperature gradient[3]. Thus, the Equation 2.16 is valid only for small temperature gradients.

Thermoelectric oxide modules have the advantage to operate under large temperature gradients which would result in a higher conversion efficiency. Further considerations are required to determine the figure of merit under large temperature gradients. Min *et al.* emphasized that the ZT value decreases with increasing the temperature gradient, e.g. for a given temperature, the ZT measured under a $\Delta\mathrm{T} = 88$ K is 28% smaller than the ZT obtained under small

---

[1] nowadays solar cells are based on single crystal or multicrystalline silicon technologies. Besides, amorphous silicon thin films emerge as an alternative technology.

[2] i.e. both thermoelectric materials should have electrical resistivity values in the same order of magnitude, similar thermal conductivity and absolute Seebeck coefficient values.

[3] these measurement characterizations are detailed in the Chapter 3.

temperature difference, i.e. $\Delta\ T\ < 10$ K [Min-2004]. In the case of large ΔT, the determination of ZT using the Equation 2.16 results in an overestimation of its value. The Thomson effect is the main responsible phenomenon for the observed ZT reduction with increasing ΔT. The Thomson coefficient should be considered into the heat balance equation at the hot side for determining more accurately the figure of merit under large temperature gradients. The heat balance equation at the hot side can therefore be formulated as follows:

$$Q_h = S_h T_h I - \frac{1}{2} R I^2 + K\Delta T - \frac{1}{2}\beta_{th}\Delta T I \tag{2.17}$$

where S_h and T_h are the Seebeck coefficient and the temperature at the hot side, respectively. I is the electric current, R is the electrical resistance, with $R = \rho(l/A_{cs})$, K is the thermal resistance with $K_R = \kappa(A_{cs}/l)$, (l/A_{cs}) is the ratio of the length to the cross sectional area, ΔT is the temperature gradient, and β_{th} is the Thomson coefficient. The Equation 2.17 can also be expressed by:

$$Q_h = S_{eff} T_h I - \frac{1}{2} R I^2 + K\Delta T, \qquad \text{with} \quad S_{eff} = \left(S_h - \beta_{th}\frac{\Delta T}{2T_h}\right) T_h I \tag{2.18}$$

where S_{eff} is defined as the effective Seebeck coefficient in which the contribution of the Thomson effect is considered. Thus, a modified figure of merit Z_m can be derived introducing the effective thermopower:

$$Z_m = \frac{S_{eff}^2}{\rho\kappa} = \frac{(S_h - \beta_{th}\Delta T/2T_h)^2}{\rho\kappa} \tag{2.19}$$

If the $(\beta_{th}\Delta T/2T_h)$ term tends to zero for small temperature gradients, the usual formulation of the figure of merit is obtained. The accurate evaluation of thermoelectric modules operating under large temperature gradients requires the determination of the Thomson coefficient. Experimental studies estimate the Thomson coefficient for conventional tellurite thermoelectric materials to β_{th} = 60 - 80 μV K^{-1} [Rowe-1995].

2.2.2 Thermoelectric parameters

The optimization of the figure of merit is a key-point for the development of thermoelectric generators. A thermoelectric material should present a high figure of merit, $Z = S^2/\rho\kappa$, by combining (i) a large Seebeck coefficient S to efficiently convert the temperature gradient into electricity, (ii) a low electrical resistivity ρ to enhance the charge carrier transport and reduce the Joule effect, and (iii) a low thermal conductivity κ to maintain the temperature gradient. The three thermoelectric parameters are functions of the carrier concentration, generally expressed in terms of density of states (DOS) at the Fermi level E$_F$ [Rowe-2006], they are interrelated in a conflicting manner.

2.2.2.1 Seebeck coefficient and electrical resistivity

In semiconductors, i.e. conventional thermoelectric materials, large Seebeck coefficients are achieved for materials having a high density of states at the Fermi level, reflecting the carrier concentration dependence of the thermopower in such materials. The electrical conductivity, derived from the Ohm law, is defined by $\sigma = 1/\rho = ne\mu$, where μ is the carrier mobility. Therefore, the electrical resistivity decreases with increasing the carrier concentration. Hence, the power factor S^2/ρ can be optimized at carrier concentration between 10^{18} to 10^{21} carriers per cm^{-3} for classic thermoelectric materials.

2.2.2.2 Thermal conductivity

In a crystalline solid, heat can be carried by the motion of charge carriers and by the lattice vibrations, described as the electronic contribution κ_{el} and the lattice component $\kappa_{lattice}$ of the total thermal conductivity, respectively [Blakemore-1998]. The total thermal conductivity κ is therefore defined as the sum of the electronic and the lattice components.

The electronic contribution κ_{el} depends on the carrier concentration and is directly related to the electrical conductivity through the Wiedemann-Franz law:

$$\kappa_{el} = L\sigma T \tag{2.20}$$

where L is the Lorenz factor which is equal to the Lorenz number $L_o \approx 2.51 * 10^{-8} W\ \Omega\ K^{-2}$ for metals [Kittel-2004].

Lattice vibrations are observed in all crystalline solids, regardless whether they are metals or insulators. $\kappa_{lattice}$ is independent on the carrier concentration. The lattice thermal conductivity dominates the heat conduction process in insulators, while it remains the minor contribution in metals. The lattice thermal conductivity corresponds to the propagations of phonons in the three space dimensions through the crystal lattice and is defined as:

$$\kappa_{lattice} = \frac{1}{3}\ C_v\ \nu_s\ l_{ph} \tag{2.21}$$

where C_v is the specific heat per unit volume, ν_s the velocity of sound, and l_{ph} the phonon mean free path, which is defined as the average distance a phonon travels before colliding with another particle [Kittel-2004]. The evolution of $\kappa_{lattice}$ with the temperature depends on the dominating interactions occurring in the lattice. At low temperatures, the phonon mean free path is limited by the grain size and the defect concentration. The specific heat presents a temperature dependence proportional to T^3 according to the Debye approximation. This results in a variation of the thermal conductivity with T^3 at $\mathrm{T} << \theta_D$, with θ_D the Debye temperature. At high temperatures, the collisions between phonons dominate, this phenomenon is known as the Umklapp process. At $\mathrm{T} >> \theta_D$, C_v tends to an asymptotic limit which is known as the

Dulong and Petit value [Kittel-2004]. For perovskite-type phases, the specific heat tends to 125 J mol^{-1} K^{-1} in the high-temperature limit, i.e. T > 200 K. Thus, the thermal conductivity is proportional to T^{-1}, assuming that the collision frequency between phonons varies with T.

The generalized carrier concentration dependence of S, ρ, and κ for conventional thermoelectrics is presented in Figure 2.4. Insulating materials present large Seebeck coefficients, low thermal conductivities but high electrical resistivity values due to low charge carrier concentrations. Metals are good electrical conductors but display low thermopower and significantly high thermal conductivities explained by the Wiedemann-Franz law. Consequently, the figure of merit can be optimized at carrier concentration between 10^{17}-10^{20} carriers per cm^{-3}, i.e. corresponding to heavily-doped semiconductors or semi-metals.

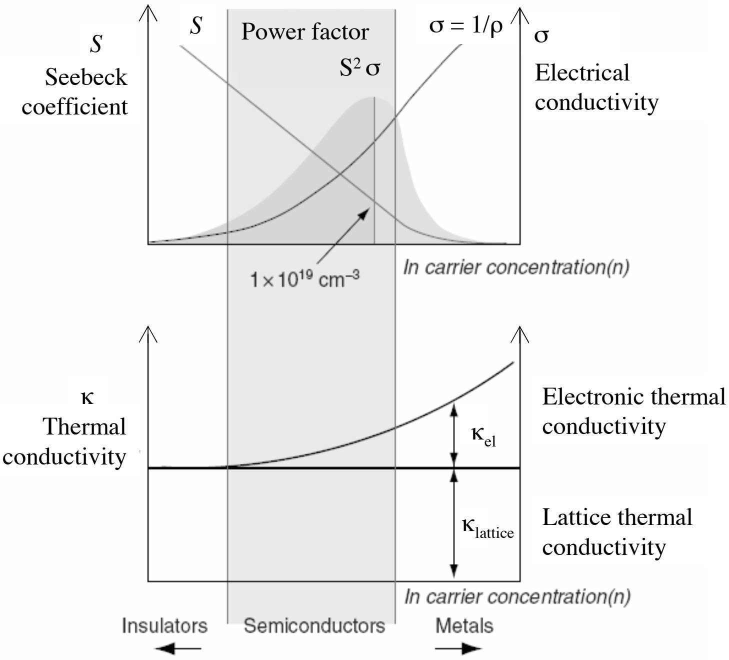

Figure 2.4: Room temperature Seebeck coefficient S, electrical resistivity ρ, and thermal conductivity κ as function of carrier concentration n for conventional thermoelectrics. Figure adapted from [Rowe-2006].

One strategy for improving the figure of merit ZT is to lower the lattice thermal conductivity while keeping the electronic properties undisturbed [Tritt-2004]. By replacing the thermal conductivity κ by the electronic and lattice contributions and applying the Wiedemann-Franz law in the Equation 2.16, the figure of merit can also be expressed by:

$$ZT = \frac{S^2 T\sigma}{LT\sigma + \kappa_{lattice}} = \frac{S^2}{L} * \frac{\kappa_{el}}{\kappa_{el} + \kappa_{lattice}} \tag{2.22}$$

The Equation 2.22 emphasizes that ZT can be enhanced when $\kappa_{lattice}/\kappa_{el} << 1$. Therefore, lowering $\kappa_{lattice}$ is a main challenge for the development of thermoelectric materials with high efficiencies. Different general strategies are currently applied for reducing the lattice thermal conductivity. They are all based on phonon scattering mechanisms that take place in a solid[1] [Nolas-2001]:

- Materials composed of heavy elements, i.e. with high atomic weights such as Bi, Te, Pb, present low phonon energies and decreased sound velocities ν_s.
- Alloying between isomorphous compounds leads to low lattice thermal conductivities in conventional materials since it increases disorder in the lattice.
- Complex crystal structures with many atoms per unit cell such as the perovskite-type structure, allow to reduce C_v. Likewise, phonons are efficiently scattered within the unit cell in cage-like structures, e.g. filled skutterudites or clathrates. Such complex crystal structures contain rattling ions in large interstitial voids which interact resonantly with low-frequency acoustic phonons, leading to a significant reduction of the lattice thermal conductivity.
- Low dimensional systems enable to scatter phonons at interfaces and grain boundaries. Nanostructured materials such as nanoparticles, nanowires or superlattices can shorten the phonon mean free path when the grain size is in the range of l_{ph}, i.e. in the nanometer scale [Dresselhaus-2007]. Multiphase composites mixed at the nanometer scale can be an alternative solution. The nanostructuring approach as effective phonon scattering is detailed in this Chapter, Section 2.3.2.2 and has been applied to enhance the figure of merit in manganate phases, as later discussed in the Chapter 5, Section 5.3.2.

2.2.3 Selection criteria

As previously presented, thermoelectric modules result in enhanced efficiencies by combining a large temperature gradient ΔT and a high figure of merit ZT. Targeting the best p- and n-thermoelectric materials implies to seek for materials with high ZT values and similar thermoelectric properties for both thermoelements at a specific operating temperature.

From a technologic point of view, further criteria have to be considered. In respect to the environmental sustainability, the thermoelectric materials should not contain toxic elements. As thermoelectric modules are low-maintenance, long-term utilizations can be envisaged. Chemical, thermal and mechanical stabilities are essential prerequisites that should be satisfied with respect to the operating conditions (temperatures and atmospheres). Morphologies and microstructures of potential nanostructured materials should be thermally stable to avoid any deterioration of the thermoelectric properties in a long term process. Finally, cost-efficient materials will be a valuable asset for widespread applications. Likewise, easy scale-up synthesis and processing have to be considered for suitable low-cost system integration and packaging.

---

[1] the different phonon scattering processes can arise simultaneously in a material.

2.3 Thermoelectric materials

2.3.1 State-of-the-art materials

To date, most commercial thermoelectric devices are based on $(Bi,Sb)_2(Te,Se)_3$ alloys, which present good ZT values in the low-temperature range, i.e. up to 450 K. PbTe compounds are mainly used in the intermediate temperature range (T $\simeq$ 700 K), and SiGe alloys are applied at high temperatures (T $>$ 1000K). The best thermoelectric performance of these established materials are presented in Figure 2.5. However, these conventional thermoelectric materials present important drawbacks: ZT hardly exceeds unity. Besides, they are composed of scarce and toxic elements, e.g. Sb, Te or Se, and present chemical instability at high temperatures in oxidative atmospheres.

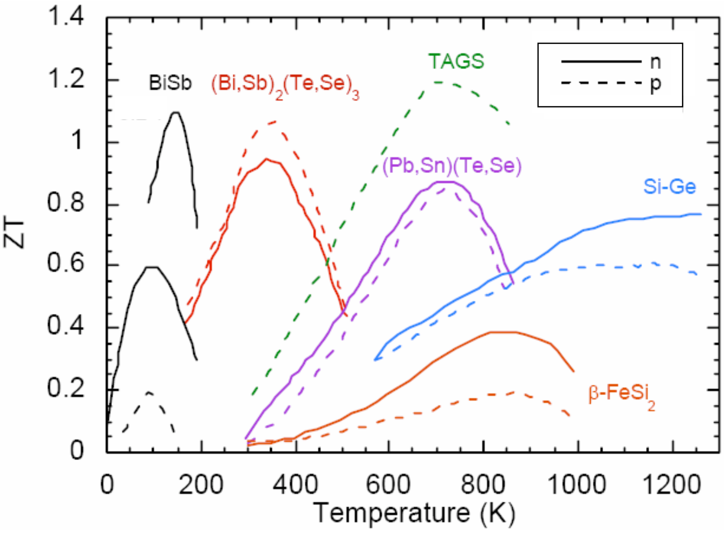

Figure 2.5: Dimensionless figure of merit ZT of some conventional thermoelectric materials. Figure adapted from [Rowe-2006]. (TAGS: $(AgSbTe_2)_{1-x}(GeTe)_x$). All the results were obtained under inert atmosphere.

2.3.2 New perspectives

Since 1995, two research approaches are currently being pursued to improve the figure of merit by reducing the lattice thermal conductivity. On one hand, efforts are focused on the identification of new bulk thermoelectric materials with $ZT > 1$. On the other hand, thermoelectric properties of low dimensional systems with enhanced ZT are of great interests. These both strategies are discussed in the following sections.

2.3.2.1 Phonon-Glass Electron-Crystal concept

The search of improved thermoelectric materials led G. A. Slack to introduce the concept of *"phonon-glass electron-crystal"*, so called PGEC approach. This concept enables an independent control of the electronic and the lattice properties [Rowe-1995]. PGEC materials would possess electronic properties of good crystalline semiconductors combined with "glass-like" thermal conductivities. Slack suggested that minimal thermal conductivity κ_{min} might be obtained if the phonon mean free path is equal to its wavelength. Based on this hypothesis, κ_{min} is estimated to be equal to 0.2 W m^{-1} K^{-1} at $T \rightarrow \infty$. Then, once the low κ material is identified, its electronic properties can be further optimized by suitable substitutions.

The introduction of the PGEC concept to thermoelectrics is the origin of an intensive research over the past decade. As a result, novel families of thermoelectric materials emerged such as skutterudites, clathrates, Zintl phases, semi-Heusler, and layered cobalt oxides.

The filled skutterudites are among the most promising intermetallic materials. Skutterudites include binary compounds of the composition MX_3, where M is a metal atom such as Co, Ir or Rh and X represents a pnicogen atom such as As, P or Sb. Skutterudites crystallize in a body-centered cubic structure belonging to the space group[1] *Im-3* (N°204). The skutterudite structure is based on eight cubes per unit cell, where two of the available cubes remain empty, forming voids. The open nature of the structure is the key-point of these phases with respect to their potential thermoelectric properties. The main drawback of the binary skutterudites remains the large thermal conductivity values, e.g. $CoSb_3$ phases present $\kappa \simeq 10$ W m^{-1} K^{-1} at 300 K with $\kappa_{lattice}$ contributing with 90% to the thermal conductivity [Caillat-1996]. Filled skutterudites with the composition $A_yM_4X_{12}$ result when rare-earth ions A are inserted in the "empty" voids. The presence of guest ions in the voids allows to fine-tune both the electronic and lattice properties by combining suitable substitutions on both the M and the X sites and introducing rattlers atoms, respectively. The reduction of the lattice thermal conductivity upon filling the voids results in a considerable enhancement of the figure of merit. The best performance for bulk skutterudites are reported for the p-type $Ce_yFe_{4-x}Co_xSb_{12}$ with $ZT = 1.4$ at 800 K [Fleurial-1996] and for the n-type $Ba_yCo_{4-x}Ni_xSb_{12}$ with $ZT = 1.2$ at 800 K [Dyck-2002].

An usual problem with these intermetallic materials is their instability in air at high temperatures. In skutterudites, sublimation of Sb occurs above 850 K after long-term utilizations. Encapsulation techniques have to be considered for thermoelectric applications. Recently, antimony Zintl phases of composition $Yb_{14}MnSb_{11}$ revealed thermal stability under air atmopshere without loss of Sb up to 1300 K [Brown-2006]. So far, the highest figure of merit among the Zintl phases is reported for the p-type $Yb_{14}Mn_{0.6}Zn_{0.4}Sb_{11}$ with $ZT = 1.1$ at 1275 K [Brown-2008].

---

[1] space groups are hereafter denoted S.G.

2.3.2.2 Nanostructured materials

The thermal conductivity reduction in nanostructures was first theoretically introduced by Hicks and Dresselhaus in 1993 for quantum-well superlattice structures (2D) [Hicks-1993a] and quantum wires (1D) [Hicks-1993b]. In the last years, this approach was experimentally investigated, resulting in a sudden increase of the figure of merit in nanostructured thermoelectric materials in which ZT exceeds largely the unity at 300 K [Majumdar-2004].

Nanostructuring of state-of-the-art thermoelectric materials reveals considerable enhancement of the figure of merit compared to the bulk materials. The Table 2.1 resumes results obtained on uniform $Bi_2Te_3/Bi_2Te_{2.83}Se_{0.17}$ superlattices of $\simeq$ 6 nm period [Venkatasubramanian-2001] and quantum dot supperlatices of 13 nm period from PbTe/PbSeTe [Harman-2002]. Recently, nanocomposite bulk $Bi_xSb_{2-x}Te_3$ alloys revealed an increase of ZT by 40% compared to the bulk counterpart leading to a figure of merit of $ZT = 1.45$ at 400 K [Poudel-2008]. In this nanocrystalline bulk material, the phonon scattering by grain boundaries and defects causes the thermal conductivity reduction.

	Bi_2Te_3/Sb_2Te_3*		PbTe/PbSeTe**	
	bulk	nanostructured	bulk	nanostructured
S^2/ρ (10^{-4} W m^{-1} K^{-2})	50.9	40	28	32
κ (W m^{-1} K^{-1})	1.45	0.6	2.5	0.6
ZT (T = 300 K)	1.0	2.4	0.3	1.6

Table 2.1: Thermoelectric properties and figure of merit of bulk and nanostructured conventional materials. (Data from * [Venkatasubramanian-2001] and ** [Harman-2002].)

Thus, in nanostructured materials, the thermoelectric properties can be further controlled compared to the bulk counterpart materials since the low dimensionality causes important modifications in the density of electronic states, as illustrated in Figure 2.6 [Dresselhaus-2007]. An enhancement of the density of states at the Fermi level due to the quantum confinement effects results in a thermopower increase without reducing the electrical conductivity. Furthermore, the lattice thermal conductivity can be greatly reduced by the preferential scattering of phonons relative to electrons at the grain boundary interfaces. For instance, the phonon scattering at grain boundaries leads to shorter phonon mean free paths and therefore to lower lattice thermal conductivities. For example, the phonon mean free path of Si is estimated to be 312 nm [Yang-2005]. Modeling calculations on Si demonstrate that phonons traveling less than 10 μm contribute for 80% to the thermal conductivity at 300 K and phonons having $l_{ph} < 100$ nm give rise to 40% of the total thermal conductivity at room temperature [Henry-2008]. In the present study, the approach of decreasing $\kappa_{lattice}$ by means of nanostructured materials is applied to manganate phases in terms of synthesizing nanoparticles and nano-sized twinned domains.

The thermal conductivity is reduced in manganate phases which reveal twinned domains at the nanometer scale, as later discussed in the Chapter 5, Section 5.3.2.

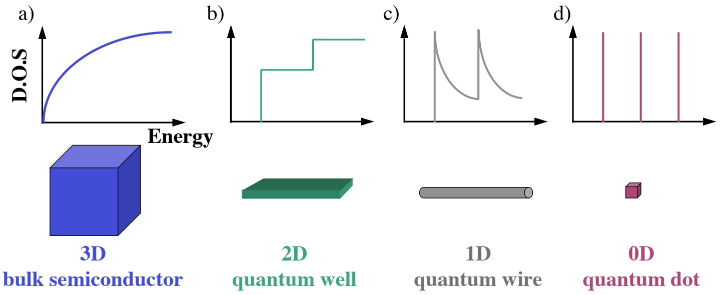

Figure 2.6: Electronic density of state (D.O.S) for a) a bulk 3D crystalline semiconductor, b) a 2D quantum well, c) a 1D quantum wire, and d) a 0D quantum dot. Figure adapted from [Dresselhaus-2007].

In spite of the progress in nanostructuring thermoelectric materials, important questions like "how can the nanostructured systems be integrated into thermoelectric modules without altering their thermoelectric performance?"[1], remain a challenge. The emergence of nanocomposite bulk materials open new horizons for improving the thermoelectric properties of functional materials and developing a new generation of thermoelectric modules.

2.3.3 Transition metal oxides

Oxides are *a priori* considered as bad candidates for thermoelectric applications. The ionic character of the oxide bonds causes a small overlapping of the orbitals which yields small bandwidths. Moreover, localized electrons result from a strong polarization of the interatomic bonding, inducing low carrier mobilities. Despite these predictions, in 1997 Terasaki *et al.* first reported on an unusual large thermopower in metallic Na_xCoO_2 single crystals [Terasaki-1997]. A strong interplay between electron, lattice, orbital and spin degrees of freedom exists in the transition metal oxides defining them as *strongly correlated electron systems*. These interactions yield the emergence of interesting phenomena and properties such as in the high-temperature superconductivity, colossal magnetoresistance or ferroelectricity. Over the past decade, an active research interest, mainly in Japan and in Europe, explored the wide family of oxides allowing the identification of several thermoelectric oxide materials. Oxide thermoelectric materials can be cost-efficient and nontoxic compared to the conventional phases. They can also be chemically and thermally stable at high temperatures in oxidative atmospheres. The Figure 2.7 resumes the best thermoelectric performance of oxide materials over a large temperature range. Most of these promising materials are reviewed in the following sections.

---

[1] Milfred Dresselhaus (Massachusetts Institute of Technology, Boston), at the E-MRS symposium on Unconventional Thermoelectrics, Strasbourg, 27 May 2008.

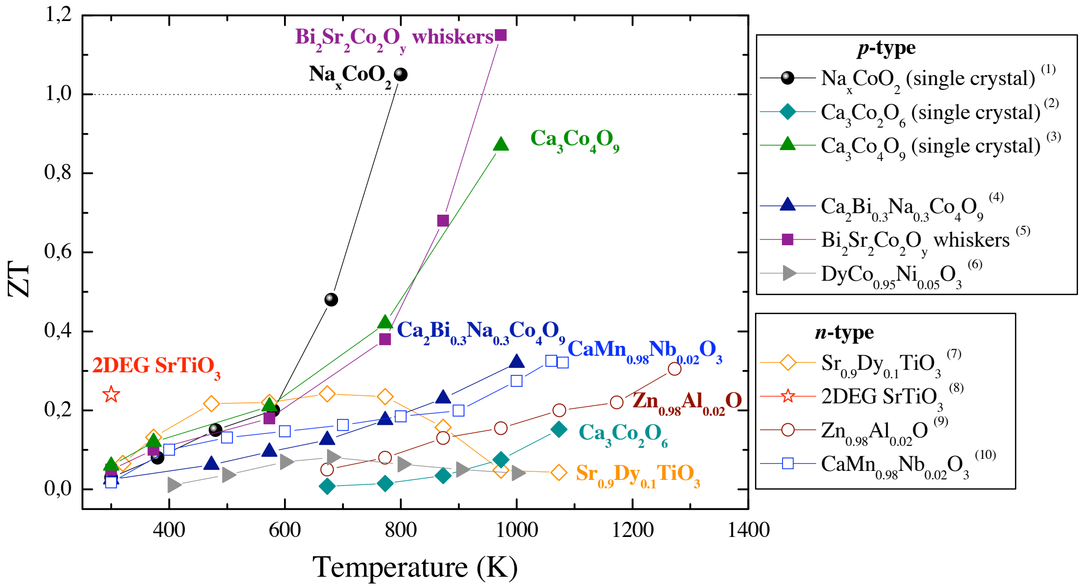

Figure 2.7: Dimensionless figure of merit ZT of oxides. Data from (1) [Fujita-2001], (2) [Mikami-2003], (3) [Shikano-2003], (4) [Xu-2002], (5) [Funahashi-2002], (6) [Robert-2007b], (7) [Muta-2003]*, (8) [Ohta-2007], (9) [Ohtaki-1996], (10) [Bocher-2008b].) *Results obtained under argon atmosphere.

One prime example is the layered cobalt oxides which are nowadays presented as the state-of-the-art p-type thermoelectric oxide materials. Besides, several perovskite-type structures and transparent conducting oxides issue as novel potential thermoelectric phases for high-temperature applications. A particular emphasis is given to n-type manganate phases being of main interest in the present thesis. Structural features of these phases are discussed with respect to the strong interplay existing between their crystal structures and electronic properties.

2.3.3.1 Layered cobalt oxides

a) Crystal Structure

The Na$_x$CoO$_2$ layered structure consists of two subsystems, as depicted in Figure 2.8 a). The first one is composed of successive CdI$_2$-type [CoO$_2$] layers along the c-axis, exhibiting a distorted triangular lattice with edge-sharing CoO$_6$ octahedra. In the second subsystem, intercalated Na ions partially occupy the sites between the [CoO$_2$] layers.

Boulay *et al.* discovered in 1996 the first misfit layered oxide opening new perspectives for functional Co-based oxides [Boulay-1996]. Later, the crystal structure of Ca$_4$Co$_3$O$_9$, shown in Figure 2.8 b), was independently identified by Masset *et al.* [Masset-2000] and Miyazaki *et al.* [Miyazaki-2000] in terms of [Ca$_2$CoO$_3$]$_{0.62}$CoO$_2$. Another remarkable thermoelectric misfit layered cobalt oxide is the Bi$_2$Sr$_2$Co$_2$O$_y$, its crystal structure is illustrated in Figure 2.8 c). The general structure of the misfit layered cobaltates is defined by $[(AO)_n]^{RS}[\mathrm{CoO_2}]_{b1/b2}$ (with A =

Ca, Sr, Ba) and consists of two interpenetrating subsystems corresponding to hexagonal CdI_2-type [CoO_2] layers and a distorted NaCl-type AO rocksalt (RS) layers along the c-axis, where n_{RS} is the integer number of RS layers (n_{RS} = 2, 3, or 4). The two monoclinic subsystems have common β angles, crystallographic a- and c-axes but are incommensurate along the b-axis and therefore referred as a "*misfit*" structure. The misfit parameter is given by the b-axis ratio b_1/b_2 of the two subsystems.

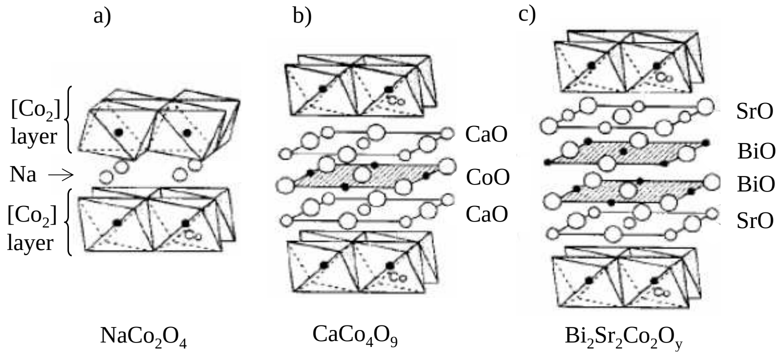

Figure 2.8: Crystal structures of a) the sodium cobaltite Na_xCoO_2, the misfit layered cobalt oxides b) $Ca_3Co_4O_9$, and c) $Bi_2Sr_2Co_2O_y$. Figure adapted from [Koumoto-2006].

b) Thermoelectric properties

Na_xCoO_2 single crystals exhibit large positive thermopower of $S = 100\ \mu V\ K^{-1}$ combined with low electrical resistivity values of $\rho = 200\ \mu\Omega\ cm^1$ at 300 K [Terasaki-1997]. Considering the metallic character of the Na_xCoO_2 phase, the Seebeck coefficient is unusually large, being one order of magnitude higher than the thermopower of classical metals. This result leads to a power factor value of PF = $50*10^{-4}$ W m^{-1} K^{-2} which is comparable to the PF value of conventional thermoelectric materials, e.g. Bi_2Te_3 with PF = $40*10^{-4}$ W m^{-1} K^{-2} at 300 K. In spite of being an oxide, Na_xCoO_2 presents relatively high carrier concentration, in the order of 10^{21}-10^{22} cm^{-3}, which is two orders of magnitude higher than in conventional thermoelectric materials [Terasaki-1997]. Furthermore, Na_xCoO_2 single crystals display relatively low thermal conductivity values of $\kappa = 5$ W m^{-1} K^{-1} resulting in a ZT value which exceeds unity at 800 K. Likewise, polycrystalline Na_xCoO_2 reveals "glass like" thermal conductivities with $\kappa = 2$ W m^{-1} K^{-1} [Takahata-2000]. Besides the interesting thermoelectric properties of the sodium cobalt oxides, the Na_xCo_2-derived phases, i.e. $1.3H_2O*Na_{0.33}CoO_2$, reveal superconductivity properties [Takada-2003].

Among the family of layered cobalt oxides, others phases reveal interesting thermoelectric properties. Polycrystalline misfit layered cobaltates like $Ca_3Co_4O_9$ and $Bi_2Sr_2Co_2O_y$ present the best

---

[1] in the direction parallel to the [CoO_2] layers

p-type thermoelectric figure of merit at high temperatures with $ZT \simeq 0.9$ at 973 K [Shikano-2003][1] and $ZT \simeq 1.1$ at 973 K [Funahashi-2002], respectively. Both phases reveal a metallic-like conduction with large positive Seebeck coefficients of $S \simeq 125$ to 140 μV K^{-1} at 300 K [Masset-2000, Funahashi-2002]. In misfit layered cobaltates, tuning the misfit parameter b_1/b_2 enables to control the Seebeck coefficient value. Kobayashi *et al.* evidenced that increasing the A cation size in the RS layer of the Bi-layered cobalt oxides results in an increase of b_1/b_2. This evolution induces an increase of the Co^{4+} concentration and therefore of S [Kobayashi-2007]. The crystallographic anisotropy of the misfit layered cobaltates yields large differences between the out-of-plane and the in-plane electrical resistivity and thermal conductivity values in single crystals, e.g. for $Bi_{2-x}Pb_xSr_2Co_2O_y$ single crystal: $\rho_c/\rho_{ab} \simeq 10^4$ and $\kappa_c = 30$ W m^{-1} K^{-1} and $\kappa_{ab} = 4$ W m^{-1} K^{-1} [Terasaki-2004]. The texturation of polycrystalline misfit layered cobalt oxides is an important parameter to further enhance their thermoelectric properties [Prével-2007].

The misfit layered cobalt oxides can be regarded as a PGEC system wherein the two sublattices play independent roles in the thermoelectric properties. The [CoO$_2$] planes, common to all layered cobalt oxides, serve as electronic transport layers while the rocksalt layers act as phonon scattering, lowering the lattice thermal conductivity.

c) Origin of the large thermopower in layered cobalt oxides

The origin of such large thermopower and unusual electrical transport properties in the layered cobalt oxides can be explained in terms of the spin and orbital degeneracy on the basis of strongly correlated systems. In an octahedral coordination, as in the [CoO$_2$] layers, the crystal field theory predicts a splitting of the $3d$ central ion level into two degenerate levels: the doubly degenerate upper e$_g$ level and the triply degenerate lower t$_{2g}$ level. The electrons in the $3d$ orbital of the Co^{3+}/Co^{4+} ion can arrange in three spin states, i.e. low spin, intermediate spin, and high spin[2]. Since the generalized Heikes formula given in Equation 2.11 considers solely the spin degeneracy, Koshibae *et al.* suggested a model taking into account the spin and orbital degeneracy. This model considers that the high thermopower of the layered cobaltates depends upon the spin and orbital degeneracy of the Co^{3+} and Co^{4+} states and on the ratio between both of them, i.e. Co^{4+} in the low-spin state is sixfold degenerate, twice from spin and three times from the t$_{2g}$ orbitals [Koshibae-2000]. The following expression is proposed for calculating the thermopower in layered cobalt oxides:

$$S\ (T \rightarrow \infty) = +\,\frac{k_B}{\mid e \mid} ln \left(\frac{g_4}{g_3}\ \frac{x}{1-x} \right) \tag{2.23}$$

where g_3 and g_4 are the numbers of configurations of Co^{3+} and Co^{4+} ions, respectively, and x is the concentration of Co^{4+} ions. The electronic conduction is interpreted as hopping conduction

---

[1] S(T) increases with temperature above 600 K whereas the misfit cobalt oxides should present a S(T) plateau at high temperatures. The atmosphere used during the measurement is not precised in [Shikano-2003].

[2] with the electronic configurations t_{2g}^6 (t_{2g}^5), $t_{2g}^5 e_g^1$ ($t_{2g}^4 e_g^1$) and $t_{2g}^4 e_g^2$ ($t_{2g}^3 e_g^2$), respectively.

of holes in the t_{2g} band of the Co^{3+}-O-Co^{4+} network. The modified Heikes formula, considering the spin and orbital degeneracies, can be applied for determining the thermopower of other oxides.

A second approach has been proposed by Singh for interpreting the unusual thermoelectric properties of the layered cobalt oxides. This concept is based on the influence of the band structure in terms of the t_{2g} degeneracy splitting in the rhombohedral crystalline field [Singh-2000]. The model considers the splitting of the t_{2g} orbitals into e_g' and a_{1g} orbitals with a small energy difference. Theoretical calculations show that both a narrow band a_{1g} and a broad band (a_{1g} + e_g') contribute to the density of states at the Fermi level. Therefore, the narrow and the broad band yield the presence of both localized and itinerant carriers which can explained the metallic-like behavior and the large thermopower, respectively.

Despite some controversies, both models can be considered as an interpretation of the unusual thermoelectric properties of the layered cobalt oxides.

2.3.3.2 Perovskite-type phases

a) Crystal structure

The perovskites have the general formula, ABO_3, where A is typically a rare-earth, alkaline earth, or alkali cations and B represents e.g. a $3d$, $4d$, or $5d$ transition metal. The building block of the perovskite structure is a roughly 3.8 Å^3 cubic unit cell [Galasso-1969]. It can be described in two different ways according to the A cation position, i.e. either at the origin or at the centre of the unit cell. In the first view, shown in Figure 2.9 a), the B transition metal cations are in the centre and the oxygens are at the face centres of the unit cell forming a regular octahedron. The second description, given in Figure 2.9 b), can be regarded as a three-dimensional network of corner-sharing BO_6 octahedra. Eight octahedra form a cube with the A site in its centre, as depicted in Figure 2.9 c). The A cations are twelve-coordinated by oxygen forming a cubo-octahedron and the B cations are surrounded by six oxygens in the octahedral coordination.

The Goldsmith *tolerance factor* t indicates the stability limits of the perovskite structure and is defined as:

$$t = \frac{r_A + r_O}{\sqrt{2}(r_B + r_O)} \tag{2.24}$$

where r_A, r_B and r_O are the ionic radii of the A-, B-site, and oxygen ions, respectively. The ionic radii values of the different ions are available in the literature [Shannon-1976].

For an ideal perovskite structure, the ratio between the radii of the A site cation and the transition metal ion is such that the tolerance factor is equal to one. $SrTiO_3$ is an example of "undistorted" structure (with $Pm\bar{3}m$ S.G., N° 221). Often the perovskite structure distorts

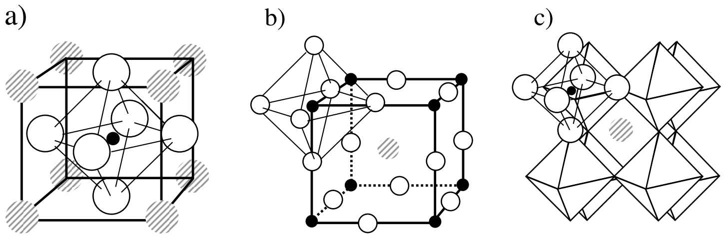

Figure 2.9: Different representations of the cubic perovskite structure where the A cation is a) at the corners and b) at the centre of the cell. c) ABO_3 perovskite structure in a perspective view where the corner-sharing BO_6 octahedra surrounds the A cation. A, B and O ions are represented by hatched, open and small black circles, respectively. The edges of the BO_6 octahedra are indicated by thin lines.

from the ideal cubic structure yielding the orthorhombic or rhombohedral symmetry with t not equal to the unity. As an example, the orthorhombic $CaMnO_3$ phase has a tolerance factor value of 1.0004. Different distortion mechanisms can be involved in the perovskite-type structure: the distortion of the octahedra, the cation displacements within the octahedra, and the rotation or tilting of the octahedra [Mitchell-2002]. The later one is the most common distortion and can be explained as follows: due to the small radius of the A site cation and with respect to its surrounding frame, the BO_6 octahedra tilt and buckle to accommodate the size of the cubo-octahedral void. The octahedra tilting results in (i) changes in the A-O bond length (they are not longer equal), (ii) changes in the A-site coordination, and (iii) to a reduction of the symmetry. There are three possibilities for a rigid BO_6 octahedron to rotate. Glazer identified all the possible sequences of rotations for the perovskite system [Glazer-1972].

The co-operative rotation of BO_6 octahedra around different axes yields the orthorhombic, so-called $GdFeO_3$-type structure. The orthorhombic crystal structure with *Pnma* S.G.[1] (N° 62) is shown in Figure 2.10 a). Orthorhombic manganate phases have space group *Pnma*; this notation is in agreement with crystallographic conventions. This structure is often described with another setting, i.e. the doubled axis is assigned to the c-axis which results to the space group *Pbnm*. Both space groups are equivalent and are related via a simple crystallographic transformation where $a_1 \rightarrow b_2$, $b_1 \rightarrow c_2$, and $c_1 \rightarrow a_2$ [2].

The relationship between orthorhombic and cubic unit cells implies geometrical considerations, as depicted in Figure 2.10 b). In *Pnma* S.G., the cubic unit cell is doubled along the b direction. The ac plane is also doubled, resulting in the following relations: $a_o \simeq c_o \simeq a_c\sqrt{2}$ and $b_o \simeq 2a_c$[3]. Evidently, structural differences emerge with respect to the ideal cubic perovskite structure. While the cubic lattice allows one unique oxygen position, the octahedra tilting arises

---

[1] *Pnma* S.G. is referred to $a^+b^-b^-$ in Glazer's notation.

[2] the subscripts *1* and *2* refer to the *Pnma* and *Pbnm* S.G., respectively.

[3] for convenience, information related to the orthorhombic and cubic crystal structure are labeled with "o" and "c" subscripts, respectively.

two inequivalent oxygen positions in *Pnma* symmetry. The equatorial oxygen[1] is on a general position (x,y,z) while the apical oxygen[2] is located on a fourfold (x, $\frac{1}{4}$, z) position on the mirror plane. Two opposite B-O_2 bonds have the same length while the perpendicular bonds are not equal. The B-O_1 bonds are always of the same length and the buckling (B-O-B) bond angles are fairly less than 180° [Mitchell-2002].

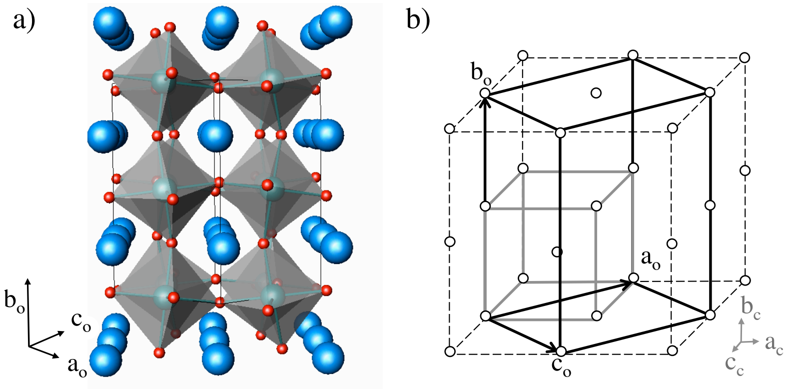

Figure 2.10: Schematic representations of a) an orthorhombic crystal structure with *Pnma* S.G. and b) an orthorhombic unit cell derived from the pseudo-cubic one. Blue spheres correspond to A-sites, green spheres to B-sites, and red spheres to oxygen. The orthorhombic lattice parameters are defined by $a_o/\sqrt{2} \simeq c_o/\sqrt{2} \simeq a_c$ and $b_o/2 = a_c$ in *Pnma* S.G., where a_c is the lattice parameter of the cubic perovskite subcell. The orthorhombic and the cubic cells are indicated with back and grey lines, respectively. The structural model is drawn using the ATOMS software.

The microstructure and the transport properties are strongly influenced by the structural distortions in the orthorhombic structure:

- Despite the rotations and distortions, the orthorhombic structure remains in origin cubic. The orthorhombic lattice parameters deviate slightly from the equivalent cubic ones, i.e. $a_c\sqrt{2} \times 2a_c \times a_c\sqrt{2}$ in the orthorhombic framework [Mitchell-2002]. Therefore, domains with specific orientations of the unit cell can growth coherently on each others yielding a twinning phenomenon. Twinned domains are observed in the orthorhombic $CaMn_{1-x}Nb_xO_3$ and $LaMn_{1-x}Co_xO_3$ phases, as later reported in Chapter 5, Section 5.2.2.1, and Chapter 6, Section 6.1, respectively.
- The deviations of the (B-O-B) bond angle θ from 180° modify the overlap between the O $2p$ and the transition metal $3d$ orbitals which induce changes in the transition metal d bandwidth characterized by the integral hopping W, since $W \propto cos\ \theta$ [Tsuda-2000]. For instance, a larger bending of the B-O bond from 180° implies a smaller overlap of the

---

[1] also termed the in-plane oxygen or O_2.

[2] also named the out-of-plane or O_1.

O 2p and the transition metal 3d orbitals. This results in a narrowing of the d band and therefore influences the electronic properties of perovskites.

Detailed structural investigations of the different synthesized perovskite-type phases will be presented in the following Chapters. The $CaMn_{1-x}Nb_xO_3$ (with x <0.12) (Chapter 5) and $La_{1-x}Ca_xTiO_3$ (x = 0.3, 0.5, and 0.7) (Chapter 4) phases belong to the orthorhombic crystal structure with the *Pnma* S.G. The $LaMn_{1-x}Co_xO_3$ (with x = 0.05, 0.10, 0.90, and 0.95) (Chapter 6) phases crystallize either in the orthorhombic structure with the *Pbnm* S.G. or in the rhombohedral structure with the $R\overline{3}c$ S.G. (N° 167) according to the substitution level. The crystal structure and its evolution upon substitutions and/or temperatures will be discussed with respect to the influence on the microstructure and on the thermoelectric properties.

b) Thermoelectric properties

Perovskite-type oxides present a large variety of physical properties such as high temperature superconductivity, colossal magnetoresistance, ferroelectricity and thermoelectricity [Rao-1998b, Raveau-2007]. Among the perovskite-type phases, cobaltate, titanate, chromate or manganate phases reveal remarkable thermoelectric properties at high temperatures. Since the perovskites possess a flexible crystal structure, their physical-chemical and therefore thermoelectric properties can be tuned in a controlled way by adjusting the cationic compositions and the oxygen content. An overview of the most promising thermoelectric perovskite phases is given with respect to the appropriate substitutions.

Cobaltates: $LaCoO_3$ exhibits a large positive Seebeck coefficient at room temperature with $S = 640\ \mu V\ K^{-1}$ which is characteristic for insulating materials [Maignan-2004]. $LaCoO_3$ crystallizes in the rhombohedral structure ($R\overline{3}c$ S.G.). Substitutions of the trivalent La cation by divalent cations (e.g. Sr^{2+} or Ca^{2+}) generate the formation of holes (Co^{3+}/Co^{4+}). In the opposite, A-site substitutions by tetravalent cations (e.g. Ce^{4+}) induce electrons as charge carriers (Co^{2+}/Co^{3+}) [Hébert-2007]. In analogy, B-site substitutions by divalent (e.g. Ni^{2+}) or tetravalent (Ti^{4+}) cations generate p- or n-type conduction, respectively [Robert-2006]. Thus, the sign of the Seebeck coefficient can be adjusted according to the predominance of the charge carriers, i.e. electrons or holes, as later discussed for the $LaMn_{1-x}Co_xO_3$ phases in the Chapter 6, Section 6.2.1. Low level substitutions allow to achieve semiconducting behavior combined with large Seebeck coefficients, i.e. $|S| > 100\ \mu V\ K^{-1}$ resulting in power factor values of PF = $2.7*10^{-4}$ W m^{-1} K^{-2} at 300 K for the $LaCo_{0.90}Ni_{0.10}O_3$ phase [Robert-2007a]. $LaCoO_3$ undergoes two thermally-activated spin-state transitions inducing interesting magnetic and transport properties strongly related to the different spin configurations of Co^{3+}. First, at T $\simeq$ 100 K the magnetic susceptibility increases due to a spin-state transition from low spin ($t_{2g}^6 e_g^0$) to intermediate spin ($t_{2g}^5 e_g^1$) [Raccah-1967]. A second transition from insulating to metallic behavior occurs at high temperatures, T > 500 K, and is associated to the transition to high spin-state ($t_{2g}^4 e_g^2$) [Yamaguchi-1996]. The effect of the spin-state transition is later presented in the Chapter 6, Section 6.2 regarding the high-temperature thermoelectric properties of the $LaMn_{1-x}Co_xO_3$ phases. Above the intermediate to high spin-state transition, the thermopower converges to a constant value estimated to $S \simeq$ - 37 μV K^{-1} at T $\rightarrow \infty$, independently on the nature and level of substitutions [Hébert-2007]. Thus, the Seebeck coefficient depends mainly on the spins at high temperatures and not longer on the carrier concentrations. For instance, a detailed study on the $Ln Co_{0.95}Ni_{0.05}O_3$ phases (with *Ln*: La, Pr, Nd, Sm, Gd, and Dy) emphasizes the influence of the spin state transition on the thermoelectric properties with respect to various rare-earth ions. The spin state transition temperature varies depending on the *Ln* ion due to structural modifications. An improved figure of merit can be achieved for a specific temperature range by selecting the suitable *Ln* ion [Robert-2007c]. Hence, the highest figure of merit found for $DyCo_{0.95}Ni_{0.05}O_3$ phase is ZT = 0.081 at 660 K [Robert-2007b].

Orthochromates: The orthochromate perovskite-type phases such as $Pr_{1-x}A_xCrO_3$ are recognized as promising *p*-type thermoelectric materials [Pal-2006]. They crystallize in the orthorhombic crystal structure (*Pnma* S.G.). The *A*-site substitutions by divalent cations (e.g. Ca^{2+} or Sr^{2+}) induce the creation of mobile holes (Cr^{3+}/Cr^{4+}) leading to a *p*-type conduction. The $Pr_{0.95}Ca_{0.05}CrO_3$ phase shows large constant Seebeck coefficients over a wide temperature range, i.e. S = 325 μV K^{-1} for 300 K < T < 650 K, combined with electrical resistivity values characteristic of semiconducting materials, i.e ρ = 2 Ω cm at 300 K. The high-temperature thermopower values fit well with the Heikes formula generalized to the spin and orbital degeneracies [Marsh-1996a].

Titanates: Among the perovskite-type structure, $SrTiO_3$ and layered titanate phases reveal fairly good thermoelectric properties as potential *n*-type material. $SrTiO_3$ crystallizes in the ideal cubic structure ($Pm\overline{3}m$ S.G., N° 221) and possesses a peculiar electronic band structure with a band gap energy of 3.2 eV [Okuda-2001]. The conduction band results from the degenerated Ti 3*d* orbitals. A barely metallic conduction is observed in slightly electron-doped phases combined with large Seebeck coefficients, i.e. $|S| >$ 100 μV K^{-1}. The titanate phases are considered as *n*-type degenerate semiconductors. Large thermopower values result from the low Fermi level since the sixfold degeneracy of the Ti $3d$-t_{2g} conduction bands give rise to a large entropy term. Thus, La- or Nb-substituted single crystals show power factor values of PF = 36*10^{-4} W m^{-1} K^{-2} at 300 K, which is comparable to those values reported for conventional thermoelectric materials [Okuda-2001]. The highest figure of merit is obtained for 20% Nb-containing $SrTiO_3$ thin films with ZT = 0.37 at 1000 K [Ohta-2005a]. However, the titanate phases exhibit rather high thermal conductivity values, e.g. $\kappa_{300K} \simeq$ 10 W m^{-1} K^{-1} for La- and Nb-substituted $SrTiO_3$ single crystals [Ohta-2005b]. Ruddlesden-Popper (RP) phases with the composition $Sr_{n+1}Ti_nO_{3n+1}$ (with n is an integer) present equivalent electronic properties and lower thermal conductivities compared to $SrTiO_3$. Polycrystalline Nb-substituted $Sr_3Ti_2O_7$ phases show thermal conductivity values of κ = 3.7 W m^{-1} K^{-1} while the Nb-containing $SrTiO_3$

compounds display $\kappa = 7.3$ W m^{-1} K^{-1} at 300 K [Haeni-2001]. The RP titanate phases are layered perovskite-type structures in which SrO and (SrTiO$_3$)n layers are alternatively stacked in a periodic way. The RP phases can be considered as an example of the PGEC concept, where the SrO layers act as phonon scattering like the rock-salt layers in the misfit cobalt phases while the (SrTiO$_3$)n layers remain good electrical transport properties. Recently, Ohta *et al.* reported on the giant thermoelectric Seebeck of a two-dimensional electron-gas confined within a unit cell layer thickness in SrTiO$_3$ [Ohta-2007]. The figure of merit of the superlattice is estimated to $ZT_{estim.} = 2.4$ and the effective ZT, i.e. including the barrier layer, gives a $ZT_{eff.} = 0.24$ at 300 K. The nanostructuration of oxides in terms of superlattices enlarges the perspectives for developing functional thermoelectric oxide materials. Despite good thermoelectric performances, a main drawback persists in the titanate phases since the Ti^{3+} cation tends to oxidize under oxidative atmospheres at high temperatures leading to Ti^{4+} which is the most stable oxidation state.

c) The perovskite-type manganate phases

Manganates adopting the perovskite structure represent an important family of oxides with various remarkable properties such as ferromagnetism, metallicity and several regions with spin and charge orderings [Rao-1998a]. One of the most eye-catching properties of the manganates is the colossal magnetoresistance (CMR), i.e. the decrease of the electrical resistivity upon applying a magnetic field near the magnetic ordering temperature, so called the Curie temperature T_c [Coey-1999]. Since the discovery of CMR by Chahara *et al.* [Chahara-1993] and von Helmot *et al.* [vonHelmot-1993] in manganate thin films, these materials have been the subject of numerous studies. This phenomenon reflects a strong interplay between the magnetic, the electronic, and the structural properties resulting from the competition of the lattice, charge, spin and orbital degrees of freedom in these systems [Rao-1998a].

Perovskite-type manganate phases with the general composition $R_{1-x}A_x$MnO$_3$ (R is a trivalent rare-earth ion and A is a divalent alkaline earth ion) exhibit rich phase diagrams implying mixed-valence Mn^{4+} and Mn^{3+} cations with $3d^3$ and $3d^4$ electronic configurations, respectively. The Mn $3d$ level in octahedral crystal field splits into the t_{2g} threefold degenerate and the e_g twofold degenerate energy levels. Following the Hund's rule, the $3d$ electrons of the Mn^{4+} cation sit on the t_{2g} orbitals and render unoccupied e$_g$ orbitals, i.e. $t_{2g}^3 e_g^0$. The Mn^{3+} electrons form the high spin state with three electrons in the t_{2g} orbitals and one electron occupying the e$_g$ orbitals, i.e. $t_{2g}^3 e_g^1$, as described in Figure 2.11 b).

The manganate perovskite-type structure undergoes two types of structural distortions. One is the co-operative rotation of MnO$_6$ octahedra. This distortion results to the orthorhombic or GeFeO$_3$-type structure, as previously described in this Chapter, Section 2.3.3.2. The other one is the co-operative Jahn-Teller distortion, namely an alternative elongation of the MnO$_6$ along

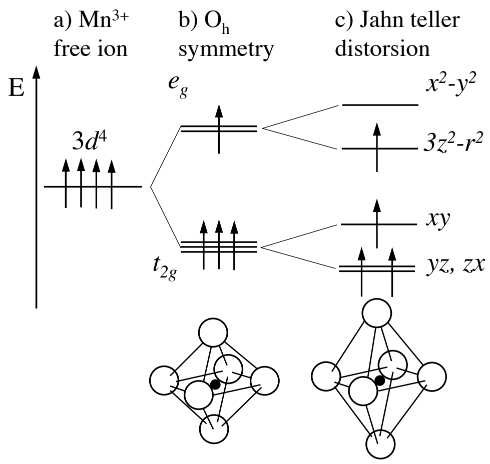

Figure 2.11: Schematic energy levels of a) the Mn^{3+} ion ($3d^4$), crystal field splitting in b) the octahedral environment, and c) according to the Jahn-Teller distortion.

one of the axes in the basal plane of the orthorhombic cell [Mitchell-2002]. The Jahn-Teller distortion exists solely in the trivalent states of the Mn cations since this deformation arises from the degenerate e_g^1 configuration. The Jahn-Teller theorem states that such an electronic configuration is unstable and that the degeneracy has to be lifted by a (local) distortion of the octahedra [Shriver-1999]. When the degeneracy is lifted, one e_g orbital is occupied and the e_g electron is more tightly bound forming a so-called polaron lattice.

$LaMnO_3$ and $CaMnO_3$ are both antiferromagnetic insulators and exhibit large absolute Seebeck coefficients, i.e. $S = 450\ \mu V\ K^{-1}$ for $LaMnO_3$ and $S = -\ 800\ \mu V\ K^{-1}$ for $CaMnO_3$ at 300 K [Autret-2005; Miclau-2007]. Manganate phases having p- or n-type conduction can be accomplished by aliovalent substitutions either on the A- or the B-site in both $RMnO_3$ and $AMnO_3$ insulating systems:

- A-site substitutions: in the $RMnO_3$ system, Mn^{4+} can be introduced in the Mn^{3+} matrix by substituting divalent cations (e.g. Ca^{2+} or Sr^{2+}) for trivalent rare-earth ions which leads to the formation of holes. In the opposite, the substitutions of trivalent for divalent cations in the $AMnO_3$ system induces the creation of electrons, i.e. the insertion of Mn^{3+} species in the Mn^{4+} sublattice.
- B-site substitutions: in the $RMnO_3$ system, the substitution of Mn by a transition metal ion with a valency +2 results in p-type manganate phases. At the reverse, $AMnO_3$ can be substituted by transition metals having valency higher than +4 (e.g. Nb^{5+}, Mo^{6+}) which results in electron-doped manganates.

The Mn^{3+}/Mn^{4+} ratio can also be modified due to cation vacancies and/or oxygen deficiencies in the lattice which influences strongly the transport properties, as it will be later discussed in the Chapter 5, Section 5.4.2.3.

In manganate phases, the electronic and magnetic properties are strongly correlated, e.g. the CMR properties are related to the appearance of ferromagnetism in these phases [Edwards-2002]. Manganates with optimal substitutions, i.e. $R_{0.7}A_{0.3}\mathrm{MnO}_3$, exhibit ferromagnetism and CMR properties [Raveau-1998]. Both phenomena occur usually simultaneously with a metal/insulator transition separating the high-temperature paramagnetic insulating phase from the low-temperature ferromagnetic metallic phase [Tsuda-2000]. The origin of CMR was first explained by Zener's double exchange (DE) mechanism, i.e. the interaction between d metals ions of different oxidation states, mediated by their ligand. In $\mathrm{Mn}^{3+}/\mathrm{Mn}^{4+}$ mixed-valence manganates, it can be described as a simultaneous transfer of (i) an electron from the Mn^{3+} site to the oxygen anion and (ii) an electron from the oxygen anion to the Mn^{4+} site, i.e. $3d^4$ - $3d^3$ $\rightarrow$ $3d^3$ - $3d^4$, as illustrated in Figure 2.12 [Zener-1951]. As the "arriving" and "departing" electrons at the O $2p$ orbital have to present the same spin orientation, the coupling between the Mn^{3+} and the Mn^{4+} ions is ferromagnetic. When applying a magnetic field, the alignment between Mn spins is favored and the resistivity decreases, leading to a negative magneto-resistance. The $\mathrm{CaMn}_{1-x}\mathrm{Nb}_x\mathrm{O}_3$ phases present such negative magneto-resistance effect, as later presented in the Chapter 5, Section 5.4.1.2.

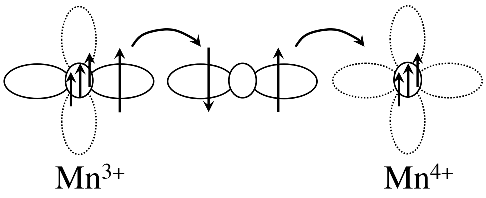

Figure 2.12: Zener's mechanism involves the hopping of an electron from Mn^{3+} to Mn^{4+} ions via the oxygen anion. The Mn ions are represented by a small circle for the t_{2g} orbitals and lobes for the e_g orbitals. The $3d$ electrons are indicated by their spins. The three t_{2g} electrons are assigned as core spins. Empty e_g orbitals are indicated by dotted lines.

However, Millis *et al.* pointed out that DE model can not quantitatively explain the CMR properties [Millis-1995]. The effect of electron-phonon interactions, i.e. polaronic effects, play also an important role. In a solid, the electron-phonon interaction results in the formation of polarons. Weak electron-phonon interactions result in the creation of large polarons. When stronger interactions occur, the electrons push negative ions further away. Thus, the overlap of neighboring orbitals becomes smaller and the electrons finally fall into localized states. This phenomenon is defined as a small polaron [Tsuda-2000]. The small polaron hopping conduction is characterized by $\rho \simeq A\mathrm{T}*(\exp \mathrm{W}_p/k_b\mathrm{T})$ where A is a constant, W_p is the activation energy, and k_B the Boltzmann constant. The activation energy W_p is defined by $W_p = E_H - J$, where E_H is the hopping energy and J is the transfer integral [Maignan-1998a; Hejtmánek-1999]. This conduction model well describes the electrical transport properties of the electron-doped manganate phases at high temperatures, i.e. T > 200 K, as later discussed in the Chapter 5, Section 5.3.1.

While electron-doped manganates such as $Ca_{1-x}Ln_xMnO_3$ (with x $\simeq$ 0.15) [Maignan-1998b; Martin-1999; Martin-2000] or $CaMn_{1-x}M_xO_3$ (with 0.05 $\leq$ x $\leq$ 0.10) are well-known for their interesting CMR properties at low temperatures, i.e. T < 120 K, slightly-substituted manganate phases reveal active thermoelectric properties at high temperatures, i.e T >> 300 K. Potential thermoelectric manganates with low substitutions combine low resistivity and large absolute Seebeck coefficients i.e. $|S| > 100$ μV K^{-1}. However, differences in power factor values exist between the electron- and the hole-doped manganate phases, i.e. the electron-doped $CaMnO_3$ phases exhibit PF values in the order of 1*10^{-4} W m^{-2} K^{-1} while the hole-doped $LaMnO_3$ phases have PF values of one order of magnitudes lower than the electron-doped phases at room temperature [Autret-2005; Maignan-1998a]. Therefore, electron-doped manganates have been extensively studied regarding their thermoelectric properties at elevated temperatures (T >> 300 K). The present study reports on the thermoelectric properties of both electron- and hole-doped manganate phases (Chapters 5 and 6, respectively) with a main emphasis on the *n*-type phases, i.e. $CaMn_{1-x}Nb_xO_3$ phases.

At temperatures above T_c, the electrical transport in the electron-doped manganates is of polaronic conduction-type with a low activation energy reflecting a metallic-like resistivity i.e. $\mathrm{d}\rho/\mathrm{d}T > 0$ [Marsh-1996b, Palstra-1997, Hejtmanek-1999]. In this regime, the Seebeck coefficient behaviour is characteristic of metals i.e. $S(T) \sim T$, despite that these phases exhibit large absolute thermopower values i.e. $|S| > 100$ μV K^{-1}. Ohtaki *et al.* first reported on these promising thermoelectric manganate phases, i.e. the $Ca_{0.9}Bi_{0.1}MnO_3$ phase with a power factor of PF = 2.8*10^{-4} W m^{-1} K^{-2} at 1000 K [Ohtaki-1995]. This phase presents high thermal conductivity values with respect to the minimal $\kappa_{lattice}$ value, i.e $\kappa \simeq 3$ W m^{-1} K^{-1} at 300 K, which results in a figure of merit $ZT = 0.085$ at 1175 K. Further *A*- or *B*-site substituted $CaMnO_3$ have been extensively studied over a wide temperature range (5 K < T < 1300 K) [Maignan-1998a, Hejtmanek-1999, Maignan-2002, Thao-2003, Pi-2003, Zhou-2003, Xu-2004, Flahaut-2006, Hébert-2007, Miclau-2007, Huang-2008]. Among those investigations, the highest figures of merit are reported for $Ca_{0.9}Yb_{0.1}MnO_3$ with $ZT = 0.16$ at 1000 K [Flahaut-2006] and for $Ca_{0.8}Dy_{0.2}MnO_3$ with $ZT = 0.2$ at 1273 K [Thao-2003]. The present thesis reports on the highest ZT value obtained among the electron-doped manganates phases ($ZT > 0.3$ at 1073 K for the $CaMn_{1-x}Nb_xO_3$ phases). These results are discussed in details in the Chapter 5.

2.3.3.3 Transparent conducting oxides (TCO)

The transparent conducting oxides (TCO) such as ZnO, SnO_2 or In_2O_3 belong to the first oxides studied for thermoelectric applications [Ohtaki-1996]. TCO are well-known as widegap oxide semiconductors, e.g. ZnO has a direct transition energy gap of 3.2 to 3.35 eV. They present a broad *s*-*p* band in which the electron mobility is large [Tsuda-2000]. The transport properties in TCO can be described by the classical model of degenerated semiconductors [Ohtaki-1996].

The n-type $Zn_{1-x}Al_xO$ phases[1] present large power factors with values ranging to $10*10^{-4}$ W m^{-1} K^{-2} < PF < $15*10^{-4}$ W m^{-1} K^{-2} in a wide temperature range, i.e. 300 K < T < 1273 K [Ohtaki-1996]. However, TCO materials exhibit fairly high thermal conductivity, e.g. for $Zn_{0.98}Al_{0.02}O$: κ = 40 W m^{-1} K^{-1} at 300 K and κ = 5 W m^{-1} K^{-1} at 1273 K [Tsubota-1997]. Since the thermal conduction in TCO is predominantly dominated by the lattice contribution, nanostructuring of TCO phases can be an interesting approach to reduce the lattice thermal conductivity. Recently, another TCO materials, i.e. Ge-doped In_2O_3, revealed promising n-type thermoelectric properties [Bérardan-2008]. The $In_{2-x}Ge_xO_3$ phases[2] present the highest figure of merit among TCO with $ZT = 0.4$ at 1273 K. These materials are characterized by the presence of a secondary phase in terms of $In_2Ge_2O_7$ inclusions.

2.3.3.4 Summary on thermoelectric oxides

Thermoelectric oxides can be distinguished with respect to their electrical and thermal transport properties:

- the semiconductor-type oxides present large Seebeck coefficients ($S(T) \sim 1/T$) and rather low thermal conductivities. The limited factor is the fairly high electrical resistivities ($d\rho/d\mathrm{T} < 0$). High power factor values can be achieved by adjusting the carrier concentrations according to the Heikes formula. p- and n-type thermoelectric materials can be obtained.
- the metallic-type oxides exhibit large Seebeck coefficients ($S(T) \sim T$) and relatively low electrical resistivities ($d\rho/d\mathrm{T} > 0$), but the thermal conductivities remain too high. The nanostructuration of the materials would be a possible strategy for reducing the thermal conductivity while keeping the electrical transport properties undisturbed. p- and n-type thermoelements can be achieved.
- the misfit layered cobalt oxides remain the model system for thermoelectric oxides since they combine large thermopowers, metallic-like resistivities and low thermal conductivities. This peculiar feature results from a strong interplay between electronic, magnetic and structural properties. However, it exists only good p-type thermoelectric candidates. Besides, problems of texturation occur in the fabrication process of thermoelectric modules.

2.4 Thermoelectric modules

A thermoelectric module is composed of p- and n-type thermoelements which are connected electrically in series and thermally in parallel. The thermoelements are sandwiched between two ceramic plates, which exhibit high thermal conductivity but low electrical conductivity, usually

---

[1] ZnO crystallizes in the hexagonal wurztite structure ($P6_3mc$ S.G., N° 189).

[2] In_2O_3 crystallizes in the body-centred cubic structure ($Ia\overline{3}$ S.G., N° 206).

aluminium oxide plates. The conventional module configuration is shown in Figure 2.13 a). Other architectures can be envisaged to improve the performance of the thermoelectric module. Among them, the multisegmented and the cascade[1] configurations are studied as alternative thermoelectric module designs [Rowe-2006]. Recently, the ”unileg” configuration has been suggested [Marques-2007]. The unileg module consists of a solely *p*- or *n*-type thermoelement. The missing leg is replaced by a conductive wire, e.g. silver strips, which connects the legs from the top to the bottom of the next one, as illustrated in Figure 2.13 b). This unileg architecture has the advantage to rely on one type of material which allows to reduce some of the technological and manufacturing problems, e.g. processing steps and production costs. The risk of thermal short-circuit has to be considered in such module configuration. A thermoelectric unileg oxide module has been already reported using *n*-type manganate phases [Lemonnier-2008].

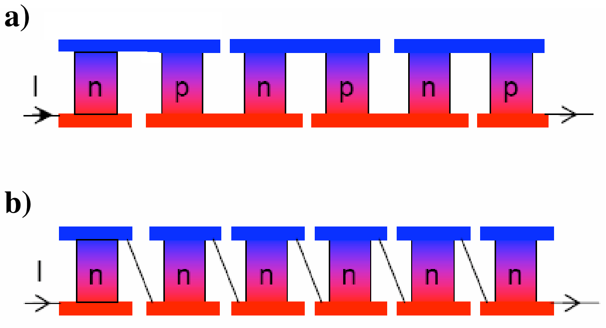

Figure 2.13: Thermoelements electrically connected in series and thermally in parallel for power generation: a) the conventional p/n configuration and b) the ”unileg” design.

The performance of thermoelectric modules can be improved considering different technological criteria such as the thermoelement lengths, the electrical contact resistances, the thermal dilatation between the interface materials etc. The evaluation of thermoelectric modules is based on the power output and the manufacturing factor. A complete homemade thermoelectric oxide module (TOM) composed of *p*-type cobaltate [Robert-2007c] and *n*-type manganate [Bocher-2008b] phases has been already fabricated considering all these parameters [Tomes-2008].

---

[1] functionally graded thermoelectric material (FGTM) are used in the cascade configuration.

Chapter 3

Characterization techniques

The present chapter is dedicated to the different techniques enabling the characterization and the evaluation of the thermoelectric materials[1]. The crystal structures of the perovskite-type phases were determined by X-ray powder diffraction (XRPD), neutron powder diffraction (NPD) and electron diffraction (ED). Non-ambient in situ diffraction experiments were performed in terms of (i) high-temperature XRPD and ED and (ii) low-temperature NPD. The morphological and microstructural features of the synthesised oxides were studied by scanning- and transmission electron microscopy (SEM and TEM, respectively). The cationic compositions were evaluated by energy dispersive X-ray and X-ray photoemission spectroscopies (EDS and XPS, respectively). In addition, electron energy loss spectroscopy (EELS) was performed in a dedicated scanning transmission electron microscope (STEM) to combine imaging and spectroscopy capabilities at the nanoscale. Thermogravimetric analyses (TGA) were performed to study (i) the thermal decomposition/stability and (ii) the anionic composition of the perovskite-type manganate phases. The electrical and thermal transport properties, i.e. the Seebeck coefficient, the electrical conductivity and the thermal conductivity, were measured over a wide temperature range, i.e. 5 K $<$ T $<$ 1240 K. The high-temperature thermal conductivity, i.e. 300 K $<$ T $<$ 1240 K, was indirectly determined via the thermal diffusivity α and the specific heat capacity Cp, respectively measured by the laser flash method (LFA) and differential scanning calorimetry (DSC). The magnetic properties were measured at low temperatures (T $<$ 350 K) by both a physical property measurement system (PPMS) and a superconducting quantum interferences device (SQUID).

3.1 Crystal structure determination

The perovskite-type structure, ABO_3, possesses an attractive crystallographic flexibility which allows the tuning of the physical properties by cationic substitutions and by adjusting the oxygen content. Determining the crystal structure of the thermoelectric perovskite-type phases

---

[1] the different measurements were performed at the Solid State Chemistry and Catalysis laboratory, at Empa, unless precised.

is therefore essential to further evaluate the crystal lattice evolution with different cationic substitution levels, e.g. while increasing the substitution of Mn by Nb in the $CaMnO_3$ phase, or with the temperature, e.g. determination of the thermal expansion. X-ray, neutron, and electron diffractions are complementary characterization methods which allow to determine the crystallographic parameters, i.e. space groups, lattice parameters, atomic positions. Since each diffraction method has its own advantages and drawbacks, as described below, the combination of these diffraction methods allows to get a better insight of the crystal structure and microstructure of the studied phases.

3.1.1 X-ray Powder Diffraction (XRPD)

Polycrystalline perovskite-type phases, i.e. materials containing multiple single crystals (crystallites or grains), are investigated by means of "powder" diffraction methods. Powder X-ray diffraction techniques, developed by Debye and Scherrer, are based on the principle that a monochromatic incident beam irradiates a large number of crystallites randomly oriented. By varying the diffracted angle θ, a larger amount of randomly oriented crystals are diffracted at the appropriate Bragg angles. All the planes of a given interplanar spacing d_{hkl} reflect at the same 2θ angle to the direct beam [Hammond-2006]. The diffracted intensities give rise to uniform cones further detected and recorded as function of 2θ.

Since X-ray sources produce divergent beams, high resolution powder diffractometers employ generally self-focusing geometries such as the Bragg Brentano focusing geometry for enhancing the diffracted intensity of the instrument [Pecharsky-2005]. This can be achieved using highly precise X-rays optics, as described in Figure 3.1 a). First, the divergence of the X-ray source is limited by soller slits producing a source of X-rays which further irradiates the sample. Then, the diffracted beam converges at the receiving slit and passes trough the second soller slit before reaching the detector. Equal distances and angles are required between the X-ray source/sample and the sample/receiving slit for satisfying the focusing conditions. Consequently, a 2θ angle continuously varies from the source to the detector tracking round the diffraction circle. Additionally, an antiscatter slit is located before the receiving slit in order to reduce the background radiation.

A powder diffraction pattern is considered as the fingerprint of a crystalline material providing information on the crystal structure through:

- the reflection position which is related to the size and shape of the unit cell, i.e. determination of the lattice parameters (see $La_{1-x}Ca_xTiO_{3-\delta}$ phases in Chapter 4, $CaMn_{1-x}Nb_xO_3$ phases in Chapter 5, and $LaMn_{1-x}Co_xO_3$ phases in Chapter 6)
- the reflection intensity which reflects the electron density inside the unit cell, i.e. determination of the atomic positions, via the structure factor determination (see Chapter 5)

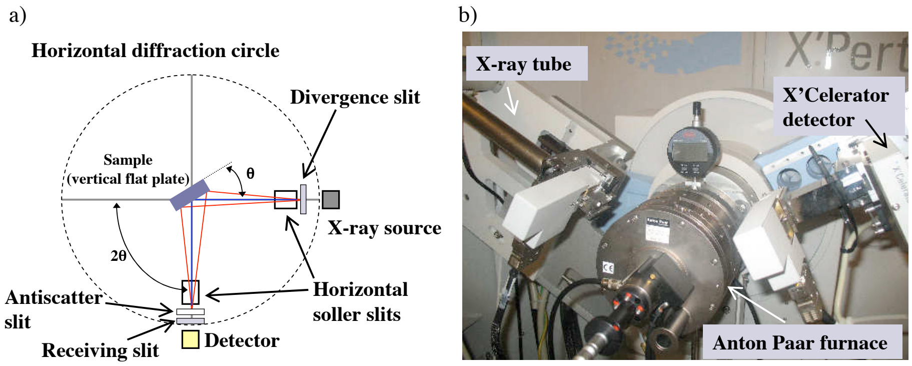

Figure 3.1: a) Principle of the Bragg-Brentano focusing geometry and b) PANalytical X'Pert PRO diffractometer equipped with an Anton Paar furnace.

- the reflection width and shape which give information on deviations from a perfect crystal, i.e. crystallite size and microstrain.

The powder diffraction method is one of the most essential tools in the structural characterization of materials since it allows:

- qualitative analysis: phase identification
- quantitative analysis: phase fraction analysis
- structure refinement using the Rietveld method, as later detailed in this Chapter, Section 3.1.3 (see Chapter 5)
- structure solution applying reciprocal space and real space methods
- peak shape analysis determining the crystallite size distribution and the microstrain analysis.

The completeness of the perovskite phase formation for the $La_{1-x}Ca_xTiO_{3-\delta}$ (x = 0.3, 0.5, and 0.7), $CaMn_{1-x}Nb_xO_3$ (x = 0.02, 0.05 and 0.08), and $LaMn_{1-x}Co_xO_3$ (x = 0.05, 0.10, 0.90, and 0.95) phases were controlled by XRPD technique (see Chapters 4, 5, and 6). The XRPD experiments were performed on a PANalytical X'Pert PRO MPD Θ-Θ diffractometer using a Cu Kα radiation in Bragg-Brentano focusing geometry, and equipped with a linear X'Celerator detector. The crystallographic parameters of the $CaMn_{1-x}Nb_xO_3$ phases were also determined by XRPD technique. For these experiments, the signal-to-noise ratio was minimised using 0.02 rad soller slits enabling a good resolution. The data were collected in an angular range of $20° < 2\theta < 125°$ with a 0.005° step size.

The in situ high-temperature data were collected on a PANalytical X'Pert diffractometer[1] (Figure 3.1 b) using the Bragg-Brentano focusing geometry, equipped with a linear X'Celerator

---

[1] located at the Laboratory of Crystallography, Swiss Federal Institute of Technology Zürich (ETHZ), Switzerland.

detector. The monochromatic Cu Kα radiation was selected by using a Johansson monochromator. An Anton Paar HTK 1200 environmental heating chamber was used for the in situ XRPD studies. The data were collected from 298 K to 1273 K under air atmosphere during isothermal steps at the required temperature. Each scan was recorded in an angular range of $20° < 2\theta < 83°$ with a 0.008° step size with a counting time of 40 s/step. Prior to each measurement, the sample was heated at the desired temperature with a heating rate of 20 K min^{-1} followed by a 5 min isothermal step to perform a fast control scan.

3.1.2 Neutron Powder Diffraction (NPD)

In addition of the XRPD data, NPD measurements were performed on the $\mathrm{CaMn_{1-x}Nb_xO_3}$ phases to accurately determine the atomic positions, especially Mn since the manganese is a good neutron scattering element. Each diffraction method, i.e. X-rays and neutrons, has its own advantages as well as its inherent limitations:

- The major difference between the two diffraction techniques is that neutrons are sensitive to the nucleus, while X-rays reflect the electron density. Neutrons have an intrinsic magnetic moment, thus ordered magnetic structures are determined with NPD data, e.g. the low-temperature magnetic structure of the $\mathrm{CaMn_{0.98}Nb_{0.02}O_3}$ phase was determined (see Chapter 5)
- Neutron beams present high penetration depths ($\simeq$ cm) while the X-rays are highly attenuated by matter (penetration depths $\simeq \mu$m) [RodriguezCarvajal-2001]. Hence, larger fractions of sample are required for neutron experiments.
- Neutron scattering power varies irregularly with the atomic and mass number, whereas X-ray scattering power varies linearly with atomic number. Therefore neutrons are more sensitive to light elements (H, N, O, F, C etc), and allow to distinguish between neighboring elements of the periodic table.

The NPD data were recorded with a high resolution powder diffractometer for thermal neutrons (HRPT)[1] [Fischer-2000]. Polycrystalline samples were placed in cylindrical vanadium cans of 8 mm in diameter. The measurements were performed with a neutron wavelength of $\lambda = 1.494$ Å in a angular range of $4° < 2\theta < 165°$ with a step size of 0.05°. The instrument was operating in a high intensity mode.

3.1.3 Structural refinement: the Rietveld method

The Rietveld method [Rietveld-1967] aimed to refine lattice and structural parameters (coordinates, atomic displacement parameters, occupation factors, and magnetic moments) considering

---

[1] located at the Swiss Spallation Neutron Source (SINQ) in the Paul Scherrer Institute (PSI), Switzerland.

all the reflections from the observed diffraction pattern. Originally dedicated for the analysis of angle-dispersive neutron diffraction [Rietveld-1969], Malmros & Thomas first applied the Rietveld method to X-ray diffraction data [Malmros-1977].

The diffraction pattern can be considered as a succession of intensity values y_i with an increment of i. The Rietveld method consists in fitting a calculated pattern[1] compared to a measured one[2] through the optimization of crystallographic parameters [Young-1993]. The residual value is minimized in the least-squares refinement as shown in Equation 3.1:

$$\chi^2 = \sum_i \omega_i (y_i - y_{ci}(\beta))^2 \tag{3.1}$$

$$\omega_i = 1/\varsigma_i^2 \tag{3.2}$$

where: ς_i is the variance assigned to the intensity value y_i,
y_i is the observed intensity at the ith step,
y_{ci} is the calculated intensity at the ith step,
β is the parameter vector, i.e. the serie of model parameters.

The calculated intensities y_{ci} are determined from the $|F_K|^2$ values of the structural model by summing the calculated contributions from the Bragg reflections plus the background:

$$y_{ci} = S_c \sum_K L_K \; |F_K|^2 \phi_R(2\theta_i - 2\theta_K) P_K A + y_{bi} \tag{3.3}$$

where: S_c is the scale factor,
K represents the Miller indices, *hkl*, for a Bragg reflection,
L_K contains the Lorentz polarisation and multiplicity factors,
ϕ_R is the reflection function,
P_K is the preferred orientation function,
A is the absorption factor,
F_K is the structure factor for the Kth Bragg reflection,
y_{bi} is the background intensity at the ith step.

The Rietveld method requires variable parameters to refine powder diffraction data and therefore to provide the structural information. Background, peak-shift, profile-shape, lattice parameters and anisotropic features have to be refined in addition to scale factors and structural parameters. The "best fit", i.e. minimized residual value, is generally achieved after several refinement cycles. Since different model parameters are usually involved in the Rietveld refinement, the quality and the completion of the analysis are defined following different numerical criteria, commonly called agreement factors or R-factors, and defined as follows:

$$R_p = \frac{\sum_i |y_i - y_{ci}|}{\sum_i y_i} \tag{3.4}$$

$$R_{wp} = \left[\frac{\sum_i |y_i - y_{ci}|^2}{\sum_i \omega_i (y_i)^2} \right]^{1/2} \tag{3.5}$$

---

[1] related to y_{ci}

[2] related to y_i

where R_p and R_{wp} correspond to the residual factors of the pattern and of the weighted pattern, respectively. R_p is, from a mathematical point of view, the most meaningful criterion among the R-factors since the numerator represents the residual value being minimized. R_p and R_{wp} should have values below 0.2 (20%) and 0.25 (25%), respectively.

Crystallographic parameters were obtained from Rietveld refinements of the XRPD and/or NPD data. The reflection shape was modeled by a Thompson-Cox-Hastings pseudo-Voight profile function [Thompson-1987] corrected for asymmetry [vanLaar-1984, Finger-1994] and the background by a 6- or 12-coefficient polynomial function. Rietveld refinements were performed using the FULLPROF program [RodriguezCarvajal-1993].

3.2 Electron Microscopy

The electron microscope allows us to investigate locally the microstructure of materials, to identify new or known phases by electron diffraction (ED), and to give essential information for analytical investigations using e.g. energy X-ray dispersive spectroscopy (EDS) or electron energy loss spectrometry (EELS), both techniques will be detailed in the subsequent sections.

While the resolution of a good light microscope is about 300 nm, modern electron microscopes are capable of imaging details down to the atomic level[1]. De Broglie's equation show that the wavelength of electrons λ is related to their energy E, and neglecting the relativistic effects, it gives approximatively:

$$\lambda \simeq \frac{1.22}{E^{\frac{1}{2}}} \tag{3.6}$$

where λ is given in nanometer and E in electronvolt. Based on de Broglie's ideas of the wave-particle duality, the particle momentum p can be related to its wavelength through Planck's constant, h, according to the Equation 3.7:

$$\lambda = \frac{h}{p} \tag{3.7}$$

In electron microscopes, the momentum to the electrons issues by accelerating it through a potential drop V, giving it a kinetic energy eV, and can be expressed as follows:

$$p = m_o\nu = (2m_oeV)^{\frac{1}{2}} \tag{3.8}$$

where m_o is the electron mass and ν the electron velocity. Thus, the relationship between the electron wavelength and the accelerating voltage of electron microscopes is defined by:

$$\lambda = \frac{h}{(2m_oeV)^{\frac{1}{2}}} \tag{3.9}$$

---

[1] conventional modern electron microscopes allow sub-nanometer scale spatial resolution while the last generation of electron microscopes, i.e. Cs-corrected electron microscopes, yield atomically-resolved images, as it will be detailed in the following section.

Considering a 100 keV electron source, $\lambda \simeq 4$ pm[1] which is much smaller than the diameter of an atom. In practice, limitations due to optical aberrations decrease the spatial resolution of electron microscopes from the sub-nanometer to the atomic scale allowing already to image and characterize details of the investigated material. For illuminating a sample, different sources of electrons can be used. It exists two types of sources to generate the electron beam: thermoionic and field-emission sources. Tungsten filaments or lanthanum hexaboride (LaB_6) crystals belong to the thermoionic sources, and field emitters are made of fine tungsten needles.

When electrons interact with matter, a wide range of secondary signals which arise from the sample, as represented in Figure 3.2 a) [Williams-1996a]. Hence, electrons can either be elastically scattered, i.e. no loss of energy, or inelastically scattered, i.e. loss of a part of their energy. Therefore, the electrons traveling through the specimen will either remain unaffected by the specimen or will be scattered by a variety of processes. Elastically scattered electrons are the major source of contrast in TEM or STEM images and also create the intensity distribution in diffraction patterns. Diffraction is governed mainly by the incidence angle of the electron beam to the atomic planes in the specimen. Thus, this low-angle scattering yields precious information for the characterization of the specimen crystal structure.

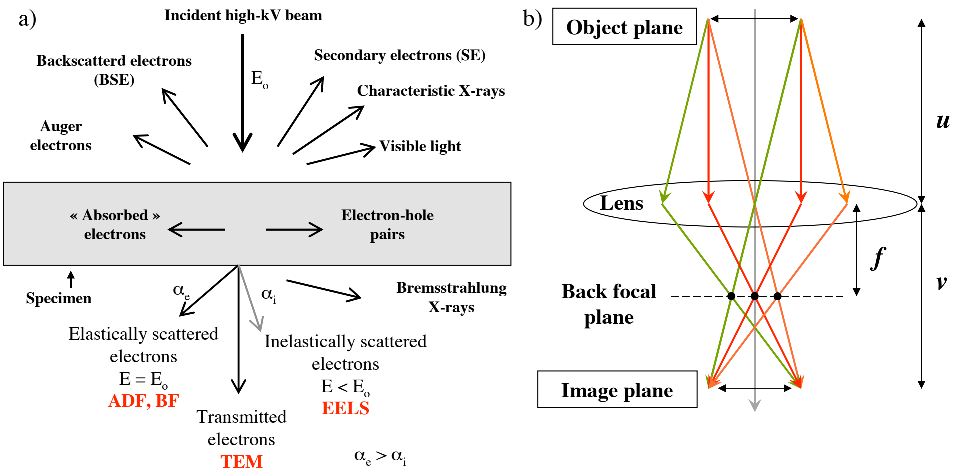

Figure 3.2: a) Signals generated when a high-energy beam of electrons interacts with a sample and b) Complete ray diagram for a finite object, symmetrically positioned around the optic axis. (u, v and f are the object/lens, lens/image, and lens/focal plane distances, respectively.) Figures adapted from [Williams-1996a]

By comparing X-ray and electron diffraction techniques, both methods present advantages and drawbacks:

- The electron beam can be highly focused, generally onto a surface of few μm^2 whereas focusing X-rays remains difficult.

---

[1] assuming perfect electron lenses.

- X-rays present penetration depths in the range of the μm, whereas electrons are strongly attenuated by matter (penetration depths in the nanometer range) [RodriguezCarvajal-2001]. Therefore, ED data have to be collected from a thin sample under high vacuum conditions.
- The electron scattering power strongly drops off as function of 2θ. Hence, the data sets for electrons are often collected over a very limited angular range ($\pm$ 4° in 2θ).
- Diffracted electrons can strongly interact with the lattice (possible damaging of the sample) making it difficult to get reliable intensities, therefore structural refinement is challenging [Williams-1996b]. Whereas, X-ray intensities and peak positions can be determined with a great accuracy.

XRPD technique provides an averaged crystallographic information of the studied phases. ED is an essential tool allowing the analysis of local structures within the crystal[1], beyond the capability of X-ray or neutron techniques. Thus, XRPD, NPD, and ED techniques are used as complementary methods.

3.2.1 Transmission Electron Microscopy (TEM): diffraction and imaging modes

One of the main advantage of using TEM is the possibility to form, in parallel modes, (i) static-beam images and (ii) diffraction patterns in a common instrument. From an optical point of view (Figure 3.2 b), the basic setting of an electron microscope can be interpreted as follows [Williams-1996a]: the rays, emerging from the object plane, are collected by the lens, and further concentrated to the image plane. In addition, all parallel rays are focused in the back focal plane to form the diffraction pattern. When the electrons are considered as particles, the objective lens collects the electrons arising from the surface of the sample, scatter them to generate a diffraction pattern at the back focal plane, and recombines them to form an image at the image plane. In practice:

- the diffraction pattern is formed when the back focal plane becomes the object plane of the intermediate lens by specific adjustment. Thus, the diffracted beam is directly projected onto the viewing screen as shown in Figure 3.3 a).
- by readjusting the intermediate lens, the object plane acts as the image plane of the objective lens, and the image is formed onto the viewing screen as represented in Figure 3.3 b).

A fundamental aspect of imaging in a TEM is to first record the diffraction pattern [Williams-1996b]. The appropriate orientation and area of a sample can be adjusted by viewing the diffraction pattern, and then the imaging can be performed at the required magnification. A second important point is the contrast of the TEM image, which can be adjusted by selecting either the direct or scattered electrons in the selected-area diffraction (SAD) aperture, i.e.

---

[1] the electron beam has a size of approximately 30 nm.

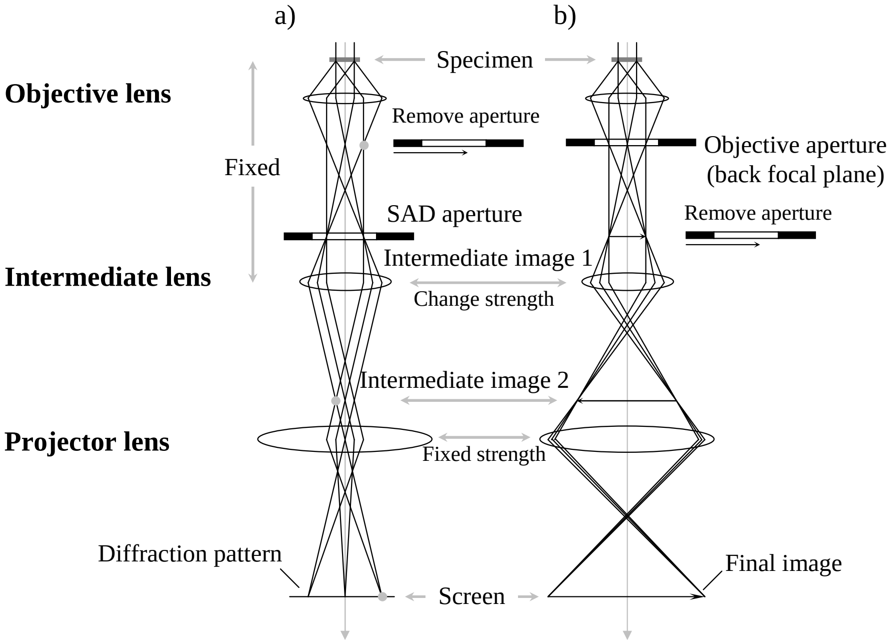

Figure 3.3: Schematic representations of a TEM operating in a) diffraction or b) imaging modes. Figures adapted from [Williams-1996a].

generating bright field (BF) or dark field (DF) images, respectively [Williams-1996c]. Mass-thickness contrast, arising from incoherent (Rutherford) elastically scattered electrons, is an additional aspect to consider. Indeed, the cross section for Rutherford scatter depends on the atomic number Z, namely termed Z-contrast, and on the mass thickness of the sample. The Z-contrast analysis provides chemical information since the contrast reflects the atomic number of the chemical elements, i.e. $I_{contrast} \propto Z^{4/3}$. In practice, dark contrast appears (i) if many atoms are scattered, i.e. thick areas darker than thin areas, and (ii) if heavy atoms are scattered, i.e. areas having heavy atoms darker than those with light atoms.

High resolution transmission electron microscopy (HRTEM) images reveal local structures of crystals through the atomic potential projection. Typical resolutions of conventional TEM working at 300 keV[1] are in the range of 2-3 Angstroms. Lattice fringes and atomic columns of perovskite-type phases can therefore be clearly imaged since the lattice parameter for the cubic perovskite structure is $\simeq 3.9$ $\AA$. HRTEM originates from multibeam imaging, i.e several beams are allowed to pass through the objective aperture. However, the resolutions of HRTEM images are limited by the performance of the spherical and chromatic aberration of the electromagnetic lenses. In a electron microscope, several kind of lenses are used for improving the resolution limit of the instrument. While glass lenses are used in optical microscopes, the electron-counterpart microscope employs electromagnetic lenses for collecting or focusing the electron beam. Figure 3.4 a) illustrates the ideal case where a perfect lense focuses at point

---

[1] without aberration correctors.

source to a single image point. In practice, the electromagnetic lenses are required to correct the spherical aberration, the chromatic aberration, and the astigmatism [Williams-1996c].

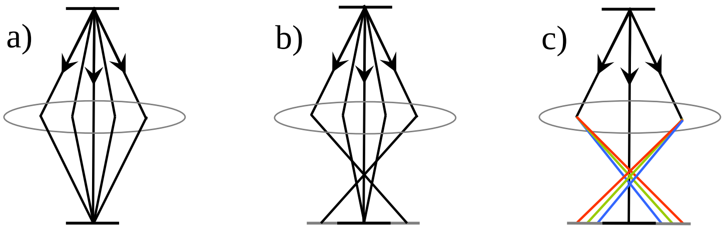

Figure 3.4: Illustrations of the main aberrations in electron microscopy, a) ideal case, b) spherical aberration, and c) chromatic aberration (the different energies are indicated by different colors).

- Spherical aberration, i.e. Cs, causes rays at higher angles to be overfocused, as represented in Figure 3.4 b). The spherical aberration is the most important defect in the objective lens since it limits the magnification detail as required. This last decade has seen strong efforts for designing new optics in electron microscopes, so called aberration-corrected electron microscopes. Hence, major technological developments were introduced to reduce the effect of the spherical aberrations yielding Cs-corrected electron microscopes enabling to reach the atomic-scale resolution.
- Chromatic aberration, i.e. Cc, gives rise to rays at different energies to be focused differently, as described in Figure 3.4 c). In ideal case, electrons are monochromatic. In practice, the chromatic aberration occurs when electrons, with a wide range of energies, are focused in different planes. For TEM images, the thinner the sample is, the minimum the chromatic aberration is.
- Astigmatism is caused due to a nonuniform applied magnetic field, thus the electron beam is represented as a distorted circle at the image plane. The astigmatism can be easily corrected using stigmators, which use a compensating field to avoid the inhomogeneities caused by astigmatism. The condenser and the objective lenses, i.e. the illumination and imaging system, respectively, require the use of stigmators.

In 1936, Scherzer showed that the main aberrations of round lenses, i.e. Cs and Cc, will always be positive [Scherzer-1936], and therefore proposed to introduce the suitable combinations of lenses with a non-cylindrical symmetry yielding a negative component in Cs [Scherzer-1947]. Aberration-correctors in TEM or STEM instruments are nowadays based on the Scherzer's ideas using different lenses design, as mentioned in the following section.

The local crystallinity and microstructure of the studied perovskite-type phases were studied by ED and HRTEM, respectively (see Chapters 4, 5, and 6). The TEM studies were performed using a Philips CM30 electron microscope equipped with a double tilt sample holder (± 30°).

The high-temperature TEM studies were performed on a JEOL JEM 3010 electron microscope equipped with a Gatan model 652 double tilt heating sample holder (± 30°) (see Chapter 5). Both microscopes operated at 300 kV using a LaB_6 crystal as electron source. TEM samples were prepared by the dispersion of ground powders in ethanol and their subsequent deposition on a holey carbon film supported by (i) a Cu ring for the room-temperature experiments and (ii) a Mo ring for the high-temperature studies.

3.2.2 Aberration Corrected Scanning Transmission Electron Microscopy and Electron Energy Loss Spectroscopy (Cs-STEM/EELS)

The principle of imaging in scanning transmission electron microscopy (STEM) differs from that one employed in a conventional TEM. In STEM instruments, a focussed beam is scanned over the sample. The transmitted electrons are detected pixel by pixel using one of the three detectors, as presented in Figure 3.5 a) [Williams-1996d]:

- the BF-detector is placed in the center in order to record the undiffracted electrons
- the DF-detector is a ring-shaped detector adjacent to the BF-detector. It records electrons scattered under a relatively low angle ($> 2^o$).
- the high-angle annular DF-detector (HAADF) is a ring-shaped detector positioned at some lateral distance from the DF-detector. It allows to collect electrons scattered under a high angle (3-8^o).

The image formation can take several seconds to be achieved. This process is based on the scanned-probe microscope, commonly used in scanning electron microscopes. BF- and DF-STEM images provide comparable information than BF and DF TEM. Also, performing HAADF in STEM results in a strong dependence on atomic number or Z-contrast imaging, i.e. a chemical contrast imaging.

The aberration corrections of an image implies different problems when using a STEM or a TEM. In the first case, only the spot of the focused beam should be corrected while in a TEM the image correction has to be apply on a large field of view. Hence, solutions for aberration-correctors in a STEM were first introduced, and are nowadays developed by NION Co. The NION's corrector comprises sixteen quadrupoles and three quadrupoles-octupoles correcting up to the fifth order aberrations [Krivanek-1999]. A different design of aberration corrector for TEM was suggested by Rose based on the combination of hexapoles technology and known nowadays as the CEOS corrector [Haider-2000].

EELS corresponds to the analysis of the energy distribution of inelastically scattered electrons. It can be performed within a conventional TEM in diffraction mode, or with a dedicated STEM. The unfiltered image passes through a magnetic prism spectrometer, which is a highly sensitive device, typically 1 eV resolving energy power while the incident electron beam possesses an

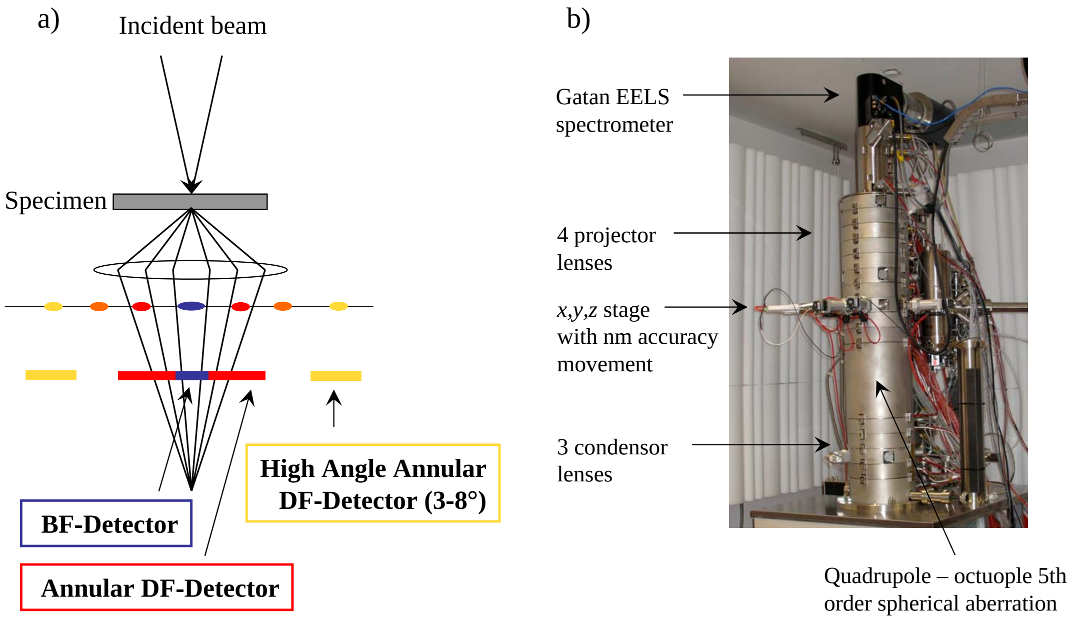

Figure 3.5: a) Schematic principle of STEM with emphasis on the capabilities of the three available detectors (BF-, DF- and HAADF-detectors), and b) SuperSTEM2, one of the UltraSTEM-100 Nion Co, at the Daresbury SuperSTEM Laboratory, UK.

energy up to 300 kV. EELS directly studies the primary processes for exciting the electrons of a solid, each of which results in a fast electron losing a characteristic amount of energy.

Two kinds of interactions electron-matter can be considered, i.e. inner-shell and outer-shell, and are correlated to two types of electronic transitions in the solid and to two energy ranges in the EELS spectrum (low-loss and core-loss regions), as presented in Figure 3.6. The inner-shell electrons (whose ground-state energy lies typically hundreds or thousands of eV below the Fermi level) can make an upwards transition to the unoccupied states, which are above the Fermi level, if they receive an amount of energy greater than their binding energy. As the total energy is conserved, the fast electron (incident electron) loses an amount of energy equal to that communicated by the inner-shell electron and it is scattered at an angle of approximately 1 mrad for a primary energy 100 keV and an energy loss of 100 eV. These transitions are reflected in the EELS spectrum by the formation of core edges, which rise at the corresponding binding energy. Typically the involved binding energies are larger than 50 eV. Single excitations involving outer-shell electrons can also occur. Then the fast electron is scattered through an angle 10 times smaller. Many electrons can also be involved in this kind of transition and a collective excitation of the valence electrons, i.e. plasmon, takes place. The associated energy loss lie in the range of 0 - 50 eV, this low loss energy region also involves the electrons, which have not interacted with the sample (or whose energy-loss is to small to be detected), i.e. the zero-loss peak.

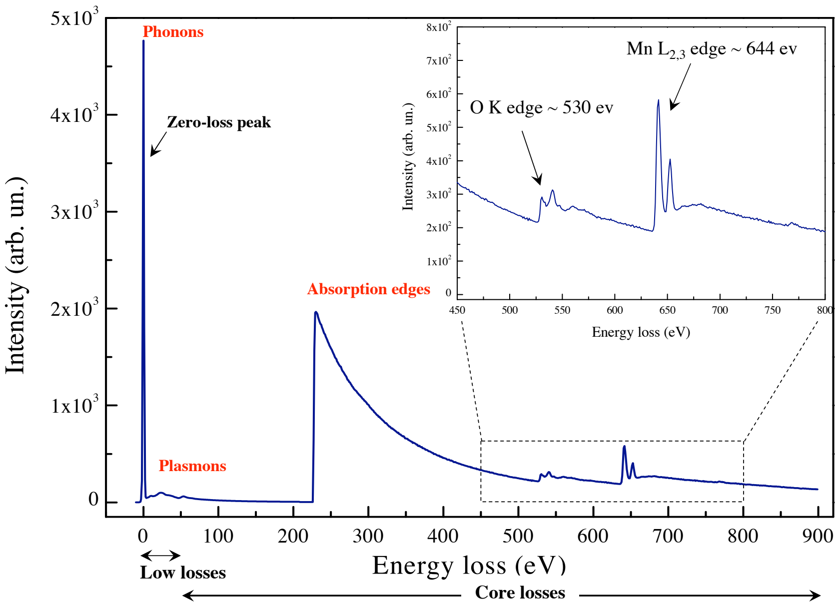

Figure 3.6: An EELS spectrum of MnO_2. The zero-loss peak is an order of magnitude more intense than the low-loss region. Figure from EELS Atlas, Digital Micrograph, Gatan. [DM-Gatan]

The information contained in an EELS spectrum is manifold and can be extracted after more or less refined spectrum analysis. From the low-loss region, the electronic density of the material, the sample thickness and optical information from the analyzed material can be determined. The core-loss region corresponds to the binding energy of the core electrons, i.e. 285 eV for C and 399 eV for N, thus the identification of the elements present in the sample can be performed. These core-loss edges are superimposed upon a monotically decreasing background, which is due to the excitation of core levels of lower binding energy. Moreover, information about the local electronic structure can also be extracted from the spectrum. The characteristic edges arise from the excitation of the inner-shell electrons. The basic edges shapes are determined by atomic physics and are therefore independent of the environment or bonding of the atom. Superimposed on the basic shape, one sees oscillations, often called fine structures, which are strongly dependent on bonding, coordination, or nearest neighbor distances. Two areas are defined in the fine structure, strong oscillations up to 20 - 30 eV above threshold called Electron Loss Near Edge Structure (ELNES) and weaker oscillations beyond about 30 eV, called the extented fine structure (EXFELS). The near edge structure provides information about the bonding configuration in the system.

Hence a dedicated analytical STEM is a powerfool tool for combining imaging and spectroscopy capabilities [Bleloch-2004]. HAADF images can be acquired and in parallel elemental and chemical analyses using EELS can be performed at the same spatial resolution. Besides, the spectrum-imaging approach, i.e. spatially-resolved EELS [Jeanguillaume-1989] consists in acquiring a series of spectra while the probe is scanned over the sample following a well digitally controlled

1D or 2D pattern. This technique provides an accurate correlation between spectroscopic information and a specific (sub)-nanometer area of the sample defined by the probe size.

Experimental investigations on the polycrystalline $CaMn_{0.92}Nb_{0.08}O_3$ phase were performed on the SuperSTEM2[1], i.e. an aberration-corrected instrument. SuperSTEM2, shown in Figure 3.5 c), is a Nion UltraSTEM 100, operating at 100 kV using a cold field-emission emitter. The UltraSTEM corrects up to fifth order spherical aberrations using a series of quadrupoles and octupoles, producing a focused probe which achieves a sub-Angstrom resolution with a ± 30° tilting angle allowing a large flexibility in the specimen orientation. The imaging modes on UltraSTEM allow to simultaneously acquire both the bright field and the high angle annular dark field images. Further, the combination of the Gatan Enfina spectrometer with the high probe current enables fast spatially-resolved elemental and electronic structure analysis of specimens using electron energy loss spectroscopy. The spatial resolution of EELS core loss signal is about $2\mathring{A}$ with a energy resolution of 0.3 eV.

The sample preparation was identical to that one for TEM studies. Since the nano-diffraction mode requires a different alignment than in the STEM mode, the selection of a correctly oriented crystallite remains rather difficult using only the STEM mode. The idea was to preselect the appropriate crystallites with the aid of ED patterns acquired in a conventional TEM. Prior to the experiments at SuperSTEM2, the samples were investigated on the conventional TEM at Empa, to localize the selected crystallites, i.e. by determining the coordinates on the carbon film and the tilting orientations.

For each probe position, EEL spectra are acquired over an energy-loss spectral domain incorporating all edges of interest, within typical recording times from ten to hundreds milliseconds for each core-loss spectrum. The large data sets are analyzed a posteriori using the Gatan Digital Micrograph software. Details of the fine structure evolution for the most important signals O-K, Ca-$L_{2,3}$, and Mn-$L_{2,3}$ are extracted for specific analyses.

3.3 Morphological and compositional studies

3.3.1 Scanning Electron Microscopy (SEM)

In scanning electron microscopy, a finely focused electron beam probe moves over the sample point by point leading to a raster pattern. As previously mentioned in this Chapter, Section 3.2.1, the interaction of electrons with matter produces several signals such as secondary electrons (SE), back-scattered electrons (BSE), and characteristic X-rays. 3-D topography images[2] result from SE and present a resolution between 1 to 10 nm [Reimer-1998]. SE involve low energy (> 50 eV) allowing a facile deflection of the beam. Hence, surfaces and volumes can be imaged by

---

[1] located at the Daresbury SuperSTEM Laboratory, UK.

[2] due to the shadowing effects.

SEM. BSE images give information on the composition (Z-contrast) of the sample. Conductive materials or samples having a coated conductive layer (e.g. carbon, gold) on the surface are required to be imaged in SEM.

The morphology of synthesised particles and cross-sectional view of fractured sintered pellets were investigated using either a conventional and a high resolution SEM, i.e. a LEO JSM-6300F and a Hitachi FEG - SEM S4700, respectively.

3.3.2 Electron Dispersive X-ray Spectroscopy (EDS)

Qualitative and quantitative chemical analyses can be performed using the EDS technique. An energy window of characteristic X-rays can be selected for specific elements resulting to an elemental mapping of the sample [Williams-1996d]. The EDS detectors can be coupled with all kinds of electron microscopes. EDS spectra are displayed in X-ray counts versus X-ray energy.

The cationic composition of randomly selected particles was analyzed by EDS coupled either to the SEM or to the TEM instruments. Results of independent EDS determinations were averaged.

3.3.3 X-ray Photoemission Spectroscopy (XPS)

X-ray photoemission spectroscopy (XPS), also known as electron spectroscopy for chemical analysis (ESCA), is a surface-sensitive technique. When highly monochromatic X-rays irradiate the surface of a sample, an incident photon of energy E_{photon} is absorbed and simultaneously a photoelectron in an atomic energy level of a binding energy $E_{binding}$ is emitted. The kinetic energy of the photoelectrons, measured by XPS, is expressed as follows: $E_{kinetic} = E_{photon} - E_{binding} - \phi$, where ϕ is the work function of the spectrometer [Kittel-2004]. Since the kinetic energies of the photoelectrons are in the range of $0 - 1500$ eV, the paths of the electrons are short, and the photoelectrons have to originate at the surface to be measured. Elemental compositions of the sample surface ($\simeq$ 1 to 10 nm) or chemical/electronic states of the elements present at the surface can be determined by XPS.

The manganese and niobium oxidation states in the $\mathrm{CaMn}_{1-x}\mathrm{Nb}_x\mathrm{O}_3$ (x $<$ 0.10) phases were investigated by XPS. The XPS measurements were performed on a PHI Quantum 2000 spectrometer using monochromatic Al Kα x-rays (1486.6 eV). The hemispherical energy analyzer was operated at a constant pass energy of 58.7 eV and a resolution of 0.25 eV. Prior to the measurements, the sintered samples were sputtered for 120 sec causing a decrease in thickness of approximately 10 to 20 nm. The sample charge was neutralized with electron flood and ion guns. XPS spectra were recorded at room temperature at a photoelectron take off angle of 45° with respect to the surface plane. The background was subtracted using the Shirley method and all spectra were referenced to the O *1s* line at 530 eV [Moulder-1995].

3.4 Thermal analysis techniques

Thermal analyses are essential for determining the thermal properties of the studied materials. Thermally-activated reactions such as thermal decomposition evolving gas release, or thermal transport properties such as specific heat capacity were investigated by different thermal analysis techniques described below.

3.4.1 Thermogravimetric, Evolved-Gas and Differential Thermal Analysis (TGA, EGA and DTA)

The thermogravimetric analysis (TGA) technique is mainly used for the studies of thermal stability, decomposition, and reactivity of the compounds. TGA enables to measure the weight change caused by a solid-gas reaction, as function of temperature or time [Czichos-2006]. Dynamic or isothermal (static) experiments can be performed under inert or reactive atmospheres at different heating/cooling rates. Further information can be obtained by studying the evolved gases during the thermal decompositions of the compounds. Evolved-gas analysis (EGA) can be achieved using a dedicated Mass Spectrometer (MS) coupled to the TGA instrument [Czichos-2006].

TGA is a quantitative and dynamic technique that can be affected by different factors. Temperature gradients, convection currents within the furnace tube and others aspects which contribute to the so called *buoyancy effect*[1]. A correction or baseline curve has to be determined prior to the experiment to compensate the buoyancy effect, and to avoid any possible uncertainties arising from the experimental conditions. The effects of sample size and surface-to-volume ratio can affect the thermal decomposition measurements, while solid-state phase changes may not be altered by the sample geometry. Hence, packing the powders becomes an important parameter in decomposition reactions. Large variations in measurements can be obtained on powders and bulk samples for an identical compound.

In differential thermal analysis (DTA), the temperature difference that occurs between a sample and an inert reference material exposed to identical experimental conditions, is measured as function of temperature or time [Czichos-2006]. This temperature difference indicates qualitatively a heat exchange. Endothermal or exothermal reactions, i.e. the absorption or the release of heat, respectively, can be detected relative to the reference. DTA is also used for the study of phase changes or thermal properties which do not lead to a variation of enthalpy.

The combination of TGA, EGA and DTA techniques gives several information related to a thermal event, e.g. the combustion of organic matter in air is an exothermic reaction induced by consumption of O_2 resulting in a release of CO_2 and a weight loss.

---

[1] a sample heated in any gas atmosphere will present apparent changes in weight with temperature due to weight variation of the surrounded gas. Hence, the sample weight will increase upon heating.

Thermal analyses were performed using a Netzsch STA 409 CD thermobalance, recorded simultaneously TGA and DTA signals, and additionally coupled to a Netzsch QMS 403 C Aëlos mass spectrometer. The design of the STA 409 CD instrument is based on a vertically-arranged thermobalance with top-loaded samples. The equilibration of the thermobalance is achieved by electromagnetic compensation, i.e. an electromagnetic coil stabilizes each arm of the balance. The microbalance has a resolution of 5 μg. The sample holder consists of a type *S* thermocouple[1] for each crucible, i.e. the sample and the reference (usually an empty crucible), which is surrounded by aluminium oxide shielding plates to ensure the heat distribution. The samples are placed in small crucibles ($>$ 5 mm in diameter) designed with an indentation on the base allowing a perfect fit over the thermocouple. The crucibles (platinum or aluminium oxide) used for the different investigations were chosen depending on the temperature and the nature of the experiment. The quadrupole MS is equipped with a capillary coupling system, in which the gas is preheated to 573 K avoiding any condensation. The evolved gas arises into a separate detection system leading to a better flexibility of the equipments. The studied manganate and titanate phases were investigated by TGA, EGA and DTA techniques according to the following experiments:

- The thermal decomposition of citrate precursors predecomposed at 423 K ($\simeq$ 100-150 mg) were performed under synthetic air atmosphere (20% vol H_2/He) with a gas flow rate of 50 mL min^{-1} at a heating rate of 2 K min^{-1} up to 1473 K.
- The thermal stability of both powders and bulk samples ($\simeq$ 30-50 mg) were controlled upon two successive heating/cooling cycles under synthetic air atmosphere (20% vol H_2/He) with a gas flow rate of 50 mL min^{-1}. During each thermal cycle, the sample was (i) heated up to 1253 K at a heating rate of 10 K min^{-1}, (ii) maintained at the desired temperature for an one-hour isothermal step, and finally (iii) cooled down to 500 K at a cooling rate of 10 K min^{-1}.
- The oxygen content of the $CaMn_{1-x}Nb_xO_{3\pm\delta}$ and the $LaMn_{1-x}Co_xO_{3\pm\delta}$ phases was determined by thermogravimetric reduction experiments. As an example, the orthorhombic $CaMnO_3$ phase can be topotactically reduced at high temperatures leading to the formation of $CaMnO_2$, defined by the Equation 3.10 [Poeppelmeier-1982a]. The polycrystalline compounds were heated up to 1173 K at a rate of 10 K min^{-1} under reducing atmosphere (20% vol H_2/He). The oxygen content of the starting compound was determined from the recorded weight loss. The phase purity of the final product was systematically confirmed by XRPD.

$$CaMnO_3(s) + H_2(g) \rightarrow CaMnO_2(s) + \frac{1}{2}O_2(g) \tag{3.10}$$

---

[1] a type *S* thermocouple is composed of Pt10%/Pt-Rh.

3.4.2 Differential Scanning Calorimetry (DSC)

The differential scanning calorimetry (DSC) technique measures the energy required to remain a nearly zero temperature difference between a sample and an inert reference material exposed to identical experimental conditions [Höhne-2003]. In analogy, the DTA technique is also based on a temperature difference.

In a heat-flux DSC equipped with disc-type measuring system, the sample and the reference (usually an empty pan) are connected by a heat flow path, i.e. a disc-plate controlled by thermal resistances. Any variation of energy between the sample and the reference is detected by measuring a temperature difference. The resulting heat flow rate ϕ is directly deduced from the intensity of the heat exchange [Höhne-2003]. In practice, when the system is at thermal equilibrium, equal heat quantity[1] flows through the conduction path into the sample and the reference. Upon heating, the steady-state equilibrium is disturbed inducing a differential temperature signal ΔT. This temperature difference is directly proportional to the difference between the heat flow rates of the sample ϕ_s and the reference ϕ_r, according to the Equation 3.11, where T_s and T_r are the temperatures of the sample and the reference, respectively:

$$\phi_s - \phi_r \sim -\Delta T \quad and \quad \Delta T = T_s - T_r \tag{3.11}$$

The determination of specific heat capacities C_p by DSC experiments is explained in detail in this Chapter, Section 3.5.3. The heat-flux DSC instrument with disc-type measuring system, a Netzsch DSC 404 C Pegasus, was used in the temperature range of 300 K < T < 1350 K under inert or reactive atmospheres. The C_p high-accuracy sample holder was equipped with type S thermocouples embedded onto the disc. To ensure that both crucibles are subjected to identical temperature regimes, it is important to obtain small temperature differences. Therefore, a high resolution sample holder is required to achieve accurate and reproducible measurements.

3.5 Thermal transport measurements at high temperatures (300 K <T 1273 K)

3.5.1 Thermal conductivity

The thermoelectric properties of a material are evaluated from the measurement of the Seebeck coefficient S, the electrical resistivity ρ, and the thermal conductivity κ. Reliable and accurate determinations of the thermoelectric properties is a crucial point. Error measurements on S, ρ, and κ can lead to 10% error on the Figure of Merit ZT[2] [Rowe-2006]. Among the three thermoelectric parameters, the accurate determination of the thermal conductivity is one of the most difficult measurement to perform on a bulk material. Furthermore, good thermoelectric materials present low thermal conductivity values, typically $\kappa < 3$ W m^{-1} K^{-1}, inducing additional potential errors and corrections to be considered [Tritt-2004].

---

[1] assuming ideal conditions, i.e. the sample and reference should be symmetrically positioned.

[2] the thermoelectric figure of merit ZT is defined as $ZT = S^2\sigma T/\kappa$.

Several techniques exist for the determination of the thermal conductivity such as the steady-state technique[1], the 3ω method, and the thermal diffusivity measurement [Tritt-2004]. The classical steady-state method can be applied to directly determine the thermal conductivity of bulk materials. However, this measurement method suffers from heat losses at high temperatures (T > 200 K) mainly due to radiation effects which displays a temperature dependence proportional to T^3. The 3ω technique is more appropriate for specific sample geometry such as thin films. Finally, the thermal conductivity of bulk materials can be determined by the laser-flash thermal diffusivity method: the thermal conductivity κ is related to the thermal diffusivity α, the specific heat capacity C_p, and the relative bulk density d by the following Equation 3.12:

$$\kappa = d\ \alpha\ C_p \tag{3.12}$$

Hence, the thermal conductivity, the thermal diffusivity and the specific heat capacity characterize the ability of a material to conduct, to transfer, and to store/release the heat, respectively [Czichos-2006]. The thermal diffusivity measurement is based on the "flash method", and the specific heat capacity can be determined by differential scanning calorimetry. Both techniques are described in the subsequent sections. Separately, the density can be measured using the Archimedes principle[2].

3.5.2 Thermal diffusivity

The "flash method", pioneered by Parker *et al.* [Parker-1961], is nowadays acknowledged as the most popular method to determine the thermal diffusivity of solid materials above room temperature.

The principle of the flash method is illustrated in Figure 3.7 a) [Rowe-2006]. The sample can be considered as a thick layer, e.g. disc-shaped sample. A light source, e.g. laser or electron beam, irradiates one side of the sample by a short heating pulse (< 1ms). The temperature on the backside is recorded by a detector, e.g. photodiode, infrared camera or thermocouple. The heating pulse causes a temperature rise on the backside of the sample due to heat propagations. At first, the temperature increases due to the heating pulse, and then decreases asymptotically until room temperature. Thus, the time to reach half of the maximal temperature, so called "half time" i.e. $t_{1/2}$, allows to determine the thermal diffusivity defined by following the Equation 3.13, where th is the sample thickness [Parker-1961]:

$$\alpha = \frac{1.37\ th^2}{\pi^2\ t_{1/2}}. \tag{3.13}$$

The equation 3.13 is valid assuming isotropic and adiabatic[3] conditions. Various algorithms can

---

[1] the measured sample has to be maintained at thermal equilibrium.

[2] the mass is measured in air (m_1) and within a liquid of known density d_0 (m_2). By consideration of the buoyancy effect, the density of the sample is given by $d = \frac{m_1}{m_1 - m_2}\ d_0$.

[3] no heat loss.

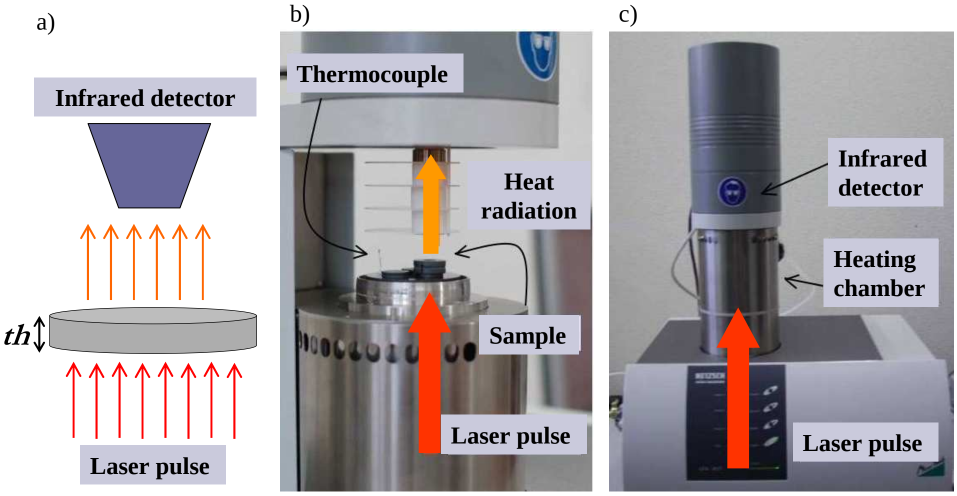

Figure 3.7: a) Schematic representation of the flash method principle, b) and c) magnification and large view of the Netzsch LFA 457 Microflash thermal diffusivity instrument, respectively.

be applied to model more accurately the heat losses and the finite pulse duration [Cape-1963]. The flash method is a rapid measurement technique since the acquisition is performed before reaching the thermal equilibrium of the sample.

The reproducibility of the measurements require a specific sample preparation. In ideal cases, the sample is considered as a black body, i.e.:

- the sample surface absorbs perfectly the light of the heating pulse.
- the sample should presents a high emissivity ($\varepsilon \simeq 1$) for accurate detections of temperature changes after the heating pulse.

In practice, the sample should be optically nontransparent and dark colored. A thin graphite coating layer can be deposited on both sides of the sample to fulfill these conditions. The sample size is another important criterium to achieve accurate measurements. On one hand, the sample thickness th should be sufficiently thin allowing the heating pulse to reach the backside of the sample without heat losses. On the other hand, thick samples are required since the half time has to be longer than (i) the heating pulse and (ii) the detection time ($\simeq$ 0.5 ms). Therefore, appropriate thicknesses range between 0.5 to 5 mm depending on the sample diameter and the specific thermal properties of the studied sample.

The thermal diffusivity of the perovskite-type phases was measured using a Netzsch LFA (Laser Flash Apparatus) 457 Microflash system (Figure 3.7b and c). The LFA 457 Microflash instrument uses a solid-state laser (λ = 1064 nm) and an InSb infrared detector. The thermal diffusivity of a disc-shaped sample ($\simeq$ 1 mm thickness $\times$ 10 mm diameter) was determined in different atmospheres (air or argon, with a gas flow rate of 50 mL min^{-1}) between 300 K and 1273 K at a heating rate of 5 K min^{-1}. Measurements were performed every 50 K and repeated

5 times at each temperature. The thermal diffusivity measurements were evaluated by using the Netzsch Proteus LFA analysis software, including modeling correction methods.

3.5.3 Specific heat capacity

The specific heat capacity or simply specific heat C_p is an intrinsic property of the material. It determines the required energy to increase the temperature of a solid from an initial temperature T_o to $(T_o{+}dT)$ at a defined temperature. For thermodynamic systems, the specific heat is defined by the Equation 3.14, where Q is the heat energy and $\mathscr{S}$ is the entropy:

$$C_p = \left(\frac{dQ}{dT}\right)_P = T\left(\frac{d\mathscr{S}}{dT}\right)_P \tag{3.14}$$

Specific heat can be determined at constant pressure ${C_p}^1$ or at constant volume C_v. In analogy, C_v is given by the Equation 3.15:

$$C_v = \left(\frac{dQ}{dT}\right)_V = T\left(\frac{d\mathscr{S}}{dT}\right)_V \tag{3.15}$$

The internal energy variation of a solid is defined by the Equation 3.16:

$$dU = Td\mathscr{S} - pdV \tag{3.16}$$

Since the enthalpy is defined as follows $H = U + PV$, its variation corresponds to the Equations 3.17 and 3.18:

$$dH = dU + pdV + vdP \tag{3.17}$$

$$dH = Td\mathscr{S} + vdP \tag{3.18}$$

Thus, the specific heat capacity at constant pressure is given by the Equation 3.19 [Kittel-2004], and corresponds to the enthalpy rising by one degree for a solid with a defined unit mass:

$$C_p = \left(\frac{\partial H}{\partial T}\right)_P \tag{3.19}$$

This principle can be applied to the heat-flux DSC measurements considering the Equation 3.20:

$$\Delta\phi = \phi_s - \phi_r = C_s\left(\frac{dT_s}{dt}\right) - C_r\left(\frac{dT_r}{dt}\right) = (C_s - C_r)\text{ß} \tag{3.20}$$

where C_s and C_r are the specific heat of the sample and the reference, respectively. The heating rate is defined by ß $= (dT/dt)$. Assuming C_r is known, C_s can be easily determined from the measurement of the heat flow rate difference $\Delta\phi$. In practice, a three step procedure is applied to determine the specific heat by the ratio method [Höhne-2003].

1. The calibration or baseline curve is measured with both crucibles empty upon dynamic heating. It allows to determine the calibration heat flow rate $\phi_o(T)$.

---

[1] the subscript p denotes the term "at constant pressure". In practice, the C_p measurement involved crucibles, lightly closed, and constituted of a pan and a top cap over the sample.

2. A standard sample (usually sapphire), with a known specific heat C_r, and a defined mass m_r, is measured under identical experimental conditions as for the calibration. Thus, $\phi_s(T)$ can be determined and the following relationship is valid: $C_r \cdot m_r \cdot ß = K_\phi(T) \cdot (\phi_r - \phi_o)$. K_ϕ(T) is a temperature dependent calibration factor.
3. Finally, the sample with an unknown specific heat C_s and a defined mass m_s, is measured under identical experimental conditions as previously. It can be stated by analogy: $C_s \cdot m_s \cdot ß = K_\phi(T) \cdot (\phi_s - \phi_o)$

The specific heat capacity at a defined temperature can be calculated using the ratio method according to the Equation 3.21:

$$C_s = \left(\frac{\phi_s - \phi_o}{\phi_r - \phi_o}\right) \cdot \left(\frac{m_r}{m_s}\right) C_r \tag{3.21}$$

The specific heat capacities of the sintered perovskite-type phases were determined using a Netzsch DSC 404 C Pegasus. The samples were heated from room temperature to 1350 K at a heating rate of 20 K min^{-1} under synthetic air atmosphere (20% vol O_2/He) or argon atmosphere with a gas flow rate of 50 mL min^{-1}.

3.6 Electrical transport and thermopower measurements at high temperatures (340 K < T < 1240 K)

The electrical resistivity and the Seebeck coefficient of the perovskite-type manganate phases were determined over a wide temperature range, under different atmospheres, and upon heating/cooling cycles. The measurements were performed on bar-shaped samples ($\simeq 1.5 \times 1 \times 5$ mm^3) using a RZ2001i unit (Figures 3.8 a and b) from Ozawa Science (Japan). Electrical resistivity and thermopower values were measured every 20 K in a temperature range of 340 K < T < 1240 K while heating and then cooling. This gives a measurement time of approximatively 25 hours. At each measurement step, the electrical resistivity was first measured 5 times and then the thermopower was determined for 5 different temperature gradients. The linear fits of the ρ and S measurements should present a correlation factor of r > 0.999 to ensure reliable data.

3.6.1 Electrical resistivity

The electrical resistivity ρ is typically measured by the four-probe method in which the current is supplied through the wires and the voltage is measured using another set of wires, as shown in Figure 3.8 c). This method allows to eliminate the contributions of the wires and the contacts in the sample voltage measurement. The electrical resistivity is determined knowing the dimensions of the bar-shaped sample and the distance between the voltage wire contacts l, using the Equation 3.22:

$$\rho = \frac{V}{I}\frac{A_{cs}}{l} \tag{3.22}$$

where A_{cs} is the cross-sectional area of the bar-shaped sample. The accurate determinations of the sample dimensions are very important.

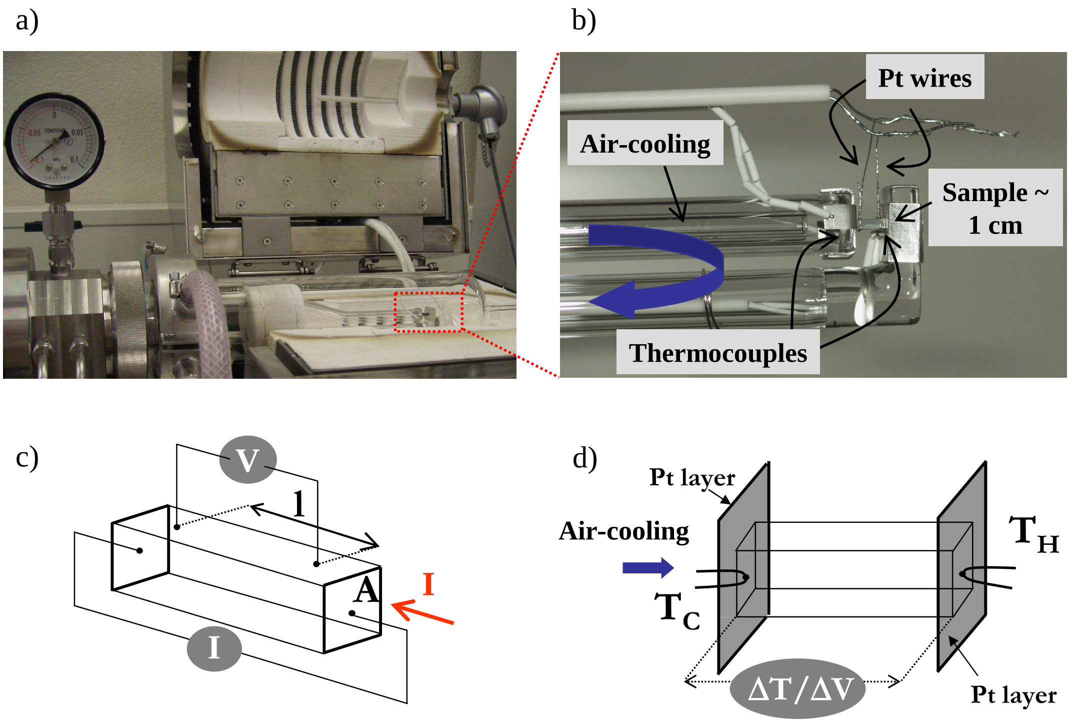

Figure 3.8: a) RZ2001i unit for the Seebeck and electrical resistivity measurement in the temperature range of 340 K < T < 1240 K under different atmospheres, b) highlight on the sample holder, c) and d) schematic representations of the electrical resistivity and Seebeck coefficient measurements, respectively.

In the RZ2001i unit, the electrical resistivity values were measured by the DC four-probe technique. Two platinum contacts placed at the ends of the bar-shaped sample inject the current and two platinum wires looped around the pellet measure the potential difference. The platinum wires have to be closely attached around the sample for achieving low resistance contacts.

3.6.2 Seebeck coefficient or thermopower

The Seebeck coefficient or thermopower S is an intrinsic property of the material. The thermopower can be determined by the ratio measurement of the sample voltage ΔV to the temperature difference ΔT, following the Equation 3.23, where T_H and T_C are the temperatures and V_H and V_C are the voltages measured on the hot and cold side of the sample, respectively:

$$S_{measured} = \frac{\Delta V}{\Delta T} = \frac{V_H - V_C}{T_H - T_C} \tag{3.23}$$

The simplest and more accurate technique for measuring thermopower is the steady-state method which consists on fixing the sample temperature and varying a small temperature gradient across the sample. The sample voltage is recorded as function of the temperature gradient resulting in a linear slope of value S. This technique is relatively slow, particularly for measurement over a wide temperature range but remains the best method for determining S [Rowe-2006].

Among the three thermoelectric parameters to measure, the Seebeck coefficient determination is conceptually the easiest one. However, special cautions have to be considered. The accurate measurements of the thermopower rely on the precise determination of the temperature T_H and T_C at the position of the voltage probes, V_H and V_C. Experimentally, the thermopower of a studied material S_{sample} can not be determined directly from the measurement since $S_{sample} = S_{measured} - S_{wires}$. The wires contributions S_{wires} have to be subtracted from each data point and at each temperature.

In the RZ2001i unit, the Seebeck coefficient was measured using the steady-state method. The measurement cell was placed into a high-temperature furnace allowing to achieve a fixed sample temperature (Figure 3.8 a). The temperature gradient (3 K $<$ ΔT $<$ 10 K) was then applied with an air cooling system on one end. ΔT was measured by two type R thermocouples[1] attached to the platinum layer contacts from which the potential difference ΔV was recorded (Figures 3.8 b and d). The resulted linear slope gave the measured thermopower value. The contributions of the wires, here the Pt thermocouples, were subtracted to obtain the Seebeck coefficient value of the material. The thermopower measurements at T $<$ 340 K were not possible since the air cooling system at room temperature does not provide a sufficient temperature gradient for performing the measurement.

3.7 Electrical transport and magnetic properties measurements at low temperatures (5 K < T < 350 K)

Thermopower and electrical resistivity values of the $CaMn_{1-x}Nb_xO_3$ phases were measured at low temperatures using two different devices (see Chapter 5):

- Electrical resistivity measurements were performed on a standard resistivity option puck (sample holder), from Quantum Design. S was measured using a home-made apparatus. This set up, designed by Dr. Hetjmanek[2] [Hejtmánek-1999], was mounted on a resistivity puck, and used at the CRISMAT laboratory[3] (Figures 3.9 a and b).
- The low-temperature measurements of S and ρ were also performed using the commercial thermal transport option (TTO) puck from Quantum Design (Figure 3.9 c). Since the

---

[1] a type R thermocouple is composed of Pt / Pt + 13 % Rh.

[2] Institute of Physics of *ASCR*, Prague, Czech Republic.

[3] UMR6508 CNRS et ENSICAEN, Caen, France.

$CaMn_{1-x}Nb_xO_3$ phases present interesting magnetic properties at low temperatures, electrical resistivity and thermopower were measured under applied magnetic field ($0 < H < 7$ T).

The measurements were performed, in both cases, on bar-shaped samples ($\simeq 1.5 \times 1 \times 5$ mm^3) in a temperature range of 5 K $< T <$ 350 K, using a physical properties measurement system (PPMS) from Quantum Design. An isothermal radiation shield was placed onto the home-made and TTO pucks to avoid radiative heat losses. The home-made apparatus, TTO and resistivity pucks were placed into a cryostat, and the measurement were performed under secondary vacuum (10^{-5} - 10^{-6} mbar) for the home-made/TTO devices and under primary vacuum (10^{-4} mbar) for the resistivity measurement.

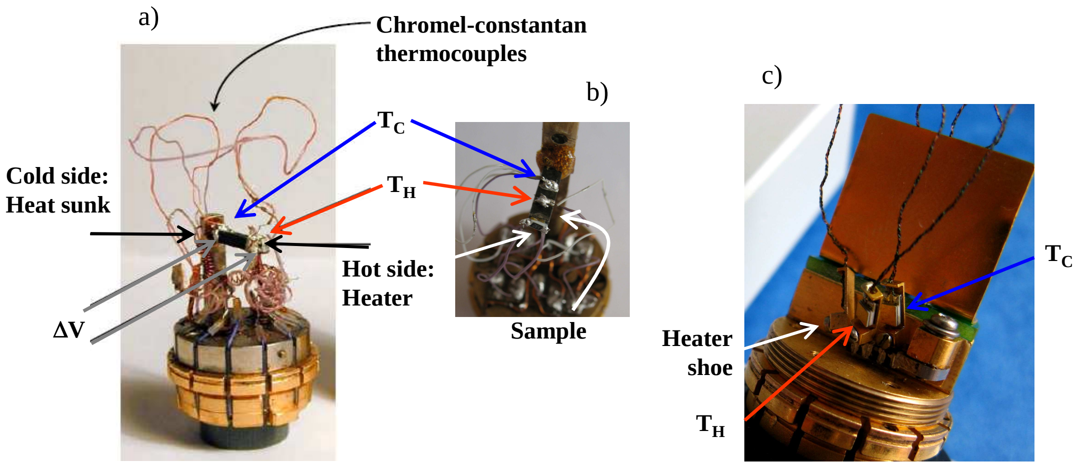

Figure 3.9: a) and b) Front view and top view of the low-temperature measurement device, respectively, designed by Dr. Hejtmanek, and c) commercial TTO option from Quantum Design.

3.7.1 Electrical resistivity

The electrical resistivity measurement was based on the four-probe method, previously detailed in this Chapter, Section 3.6.1. Copper wires and silver paste contacts were used for connecting the sample to the resistivity puck. The measurements were performed in AC mode, in which the DC current is injected into the sample and a potential drop is recorded. The resolution of the PPMS is in the order of 4 $\mu\Omega$ cm for a maximal current of 5 mA. Maximal resistivity values of 4 MΩ can be measured with a precision of 1% which is a suitable limit for thermoelectric materials.

3.7.2 Seebeck coefficient

In both devices, home-made and commercial one, the steady-state method was applied for determining the Seebeck coefficient, as previously detailed in this Chapter, Section 3.6.2, using in both cases a small heater to achieve the temperature gradient. This technique can appear relatively slow since the stabilization of T and ΔT has to be reached. However, the measurement time can be reduced by modeling the temperature gradient by the 2τ method which was applied in the PPMS device.

In the home-made device, the thermocouples were contacted onto the sample using indium contacts deposited by ultrasounds. The sample was fixed to the heat sunk on one end side (cold side), and to a small resistance with $R = 3.3$ kΩ on the other end side (hot side) (Figure 3.9 b). On both sides, GE varnish glue was used to ensure the thermal anchoring. The temperature gradient was generated by Joule effect, where the dissipative energy W_J is equal to $W_J = RI^2$. The applied temperature gradient $\Delta T = 0.0015T + 1K$ was relatively low and depended on the temperature measurement [Hejtmánek-1999]. Two type E thermocouples[1] were used for determining the temperatures at the hot and the cold sides, T_H and T_C, respectively. The contributions from the chromel-constantan thermocouples were subtracted from the total value, for obtaining the thermopower values of the material.

In the commercial device, the electrical contacts were made of copper wires looped around the sample, and improved with silver paste contacts onto the sample. The wires were screwed into the small Cernox (thermometers). The heater shoe was connected to the sample via a copper wire.

3.7.3 Magnetic susceptibility

The paramagnetic susceptibility χ obeys the Curie-Weiss law [Blakemore-1998]:

$$\chi = \frac{C}{T + \theta_W} \tag{3.24}$$

where C is the Curie constant, and θ_W is the Weiss temperature. The effective magnetic moment μ_{eff} can be calculated by $\mu_{eff} = \sqrt{3k_BC/N_A}$, where N_A is the Avagadro's number and k_B is the Boltzmann constant. The effective magnetic moment is given in μ_B the Bohr's magneton.

The magnetic susceptibility of the $CaMn_{1-x}Nb_xO_3$ phases was measured with a vibrating sample magnetometer (VSM) in PPMS device or with a superconducting quantum interference device (SQUID) magnetometer[2] (see Chapter 5). Magnetic susceptibilities were measured during zero-field cooled (zfc)[3] measurement upon heating, then a magnetic field was applied in the paramagnetic temperature region (e.g. at T ≃ 300 K) to perform a field cooled (fc)[4] measurement upon heating.

---

[1] a type E thermocouple corresponds to a chromel (Ni + 10% Cr) - constantan (Ni + 45% Cu) thermocouple.

[2] at the CRISMAT laboratory, Caen, France.

[3] a zfc measurement is performed without applying a magnetic field.

[4] a fc measurement is performed applying a magnetic field.

- The PPMS magnet provides the magnetic field, in the case of the VSM measurement. The VSM detection coil is inserted into the PPMS sample chamber. The sample oscillates near a detection pickup coil, and a induced voltage is synchronously detected. The sample is attached at the end of a sample rod and driven sinusoidally. The resolution of the magnetometer is less than 10^{-6} emu at a data rate of 1 Hz. The applied magnetic field can vary from -7 T to 7 T with a temperature rang of $5 \text{ K} < \text{T} < 400 \text{ K}$.
- In a SQUID magnetometer, superconductive coils generate a continuous uniform magnetic field, and the sample moved inside/outside of the superconductive coils thanks to a linear motor. Superconductive coils are coupled to a highly sensitive SQUID detection allowing a maximal resolution of 10^{-8} emu. The applied magnetic field can vary from -5 T to 5 T with a temperature rang of $1.9 \text{ K} < \text{T} < 320 \text{ K}$.

Chapter 4

Synthesis of thermoelectric perovskite-type phases

Perovskite-type phases are synthesised by applying divers methods to investigate the influence of the morphology and the microstructure on their thermoelectric properties. This chapter gives an overview on the different applied synthesis routes, i.e. the conventional solid state reaction (SSR) method and the *"chimie douce"* synthesis routes, with a special emphasis on the resulting particle morphologies. The thermal decomposition of the *chimie douce* precursors and the perovskite phase formation are studied in detail. The versatility of the *chimie douce* synthesis method is illustrated by an example of the formation of thermally stable and highly crystalline mesoporous titanate phases. The thermal transport properties of these mesoporous titanate phases are reported within the range of 300 K $<$ T $<$ 1000 K. Thermal conductivities of the SSR-derived polycrystalline and single crystal perovskite-type titanate phases are further reported for comparison.

4.1 Solid state reaction (SSR) method

The solid state reaction method corresponds to the conventional ceramic route for the synthesis of oxide materials. It involves the thermal reaction of intimately mixed oxide or carbonate powders (with grain sizes of several μm) at relatively elevated temperatures, e.g. the $CaMn_{1-x}Nb_xO_3$ phases are synthesized at T = 1673 K when applying the SSR method. The solid-solid reaction initially takes place at point contacts between the grains, i.e. the phase boundary reaction, and later by diffusion of the ions through the product phase. As the solid state reaction progresses, the thickness of the product layer increases according to the parabolic law [Schmalzried-1995]. The SSR method is characterized by long diffusion paths, i.e. in the order of few μm, and slow kinetics, e.g. in the $LaMnO_3$ phase, the thickness of the product layer increases of $\simeq$ $1.2*10^{-4}$ mm^2 $hour^{-1}$ at 1673 K [Palcut-2006]. Starting reactants should be finely grounded in order to enhance their surface areas and therefore the reaction rates. Intermediate regrindings are usually required to accelerate the reaction, to homogenize the product phase, and to complete the reaction. The sintering of pressed powders slightly improves the diffusion process due to a better interconnection between grains at high temperatures but it also favors the grain growth due to the coarsening phenomenon[1]. The SSR method results in polyhedral grains of few micrometers size with a nonuniform grain size distribution. Thermoelectric perovskite-type phases generally involve low-level cationic substitutions, which makes the reproducibility of the synthesis method an important prerequisite. Homogeneous cationic compositions with low-level substitutions are rather difficult to control by applying the SSR method since it depends on the diffusion rate of each ion in the product phase. In the $LaMnO_{3\pm\delta}$ phase, the diffusion of Mn^{3+} cations dominates over the La^{3+} diffusion with a diffusion coefficient of Mn^{3+} in the $LaMnO_{3\pm\delta}$ phase in the range of $3.6{*}10^{-5}$ mm^2 $hour^{-1}$ at 1673 K [Palcut-2006]. The solid state reaction method presents certain limitations for the synthesis of thermoelectric oxide phases regarding the homogeneity of the cationic composition and the control of particle morphology. Despite these drawbacks and its time-consuming synthesis conditions, most of the thermoelectric oxides are still prepared by the SSR method. In the present study, manganate phases are synthesized by the SSR method to compare the effects of different morphologies and microstructures, issued from others alternative synthesis methods, on the thermal conductivity and in general on the thermoelectric properties.

Polycrystalline perovskite-type phases of $CaMn_{1-x}Nb_xO_3$ (with $x < 0.10$) were obtained by thoroughly mixing stoichiometric amounts of $CaCO_3$ (Alfa Aesar; > 99.5%), MnO_2 (Specpure) and Nb_2O_5 (Specpure) in ethanol; the starting reactants have grain sizes < 10 μm. The mixtures were pressed into pellets to increase the contact area between grains and sintered in air at 1673 K for 6 h including several intermediate grindings resulting to single phase polycrystalline oxide powders.

4.2 *Chimie douce* synthesis route

Alternatively, *chimie douce* approaches, discovered in France by Livage *et al.*, can be applied for the synthesis of a wide variety of oxide materials [Livage-1988]. This synthesis route is based on the thermal decomposition of amorphous polymeric precursors which contain a homogeneous intermix of cations, forming an organic-inorganic network at the molecular level [Kupricka-2002, Weidenkaff-2004]. Polyhydroxylated ligands such as the α-hydroxyacids, e.g. citric acid, glycolic, tartaric or malic acids, are typically used to complex all the cations in aqueous solution. Polydentate ligands can create chelates, i.e. complexes in which the ligands form a ring enclosing the metal cation [Shriver-1999]. Citric acid (CA) as bidentate ligand creates six-membered rings where the oxygen atoms bridge two coordination sites of the metal cation *M*, as illustrated in Figure 4.1. In the present thesis, the metal-citrate complexes derived from a modified Pechini process [Pechini-1967] are thermally decomposed either by stepwise calcinations (SC) or by a

---

[1] the coarsening effect occurs when larger grains growth at the expense of smaller ones.

ultrasonic spray combustion (USC) process. Both methods result in the degradation of the organic matter yielding the formation of the desired crystalline phase. The stepwise calcination process, referred hereafter as the SC synthesis method, has already proven to be a successful technique for synthesizing perovskite-type cobaltate [Weidenkaff-2004, Robert-2007a], titanate [Bocher-2007], ferrate, nickelate [Kupricka-2002] and manganate [Bocher-2008a] phases. The USC process is presented in this Chapter, Section 4.3

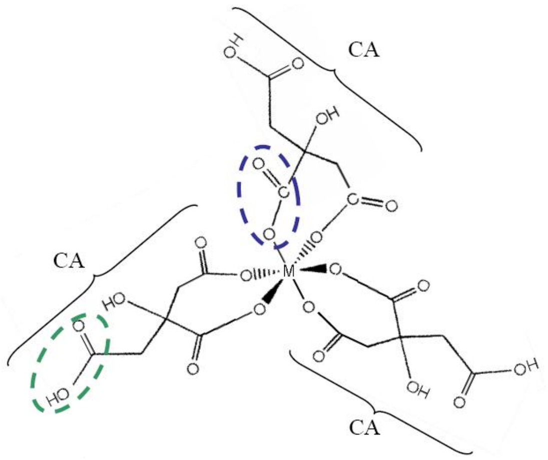

Figure 4.1: One possible representation of the metal-citrate precursor. Characteristic functional groups, i.e. carboxylic acid function (green) and carboxylate function (blue) are indicated by dotted lines.

The *chimie douce* synthesis route presents several advantages compared to the solid state reaction method. The homogeneous molecular intermix of all the reactants in aqueous solution enables a precise control of the stoichiometry compared to the SSR method. The SC method results in high purity oxide phases presenting a homogeneous distribution of substituted elements in the cationic sublattice. This aspect remains an important issue since the presence of any segregation at the grain boundary or secondary phase can influence the thermoelectric properties of oxide phases. Moreover, while heating the citrate precursor at T $\simeq$ 423 K, the gel undergoes a volume expansion of $\simeq$ 1000% forming a porous voluminous structure, a so called xerogel characterized by a high surface area. A controlled thermal decomposition of the xerogel results in a tuning of the particle size. The perovskite phase formation occurs at relatively low temperatures, i.e. 873 K $<$ T $<$ 1073 K, since nearly no diffusion processes are necessary unlike in the SSR method. The implemented SC route allows to shorten the calcination time and to lower the calcination temperature compared to the SSR method, e.g. the $\mathrm{CaMn_{1-x}Nb_xO_3}$ phases are achieved at T = 1073 K for 2 h when synthesizing by the SC method. This low-temperature solution chemistry-based approach offers the possibility to synthesize tailor-made materials. However, several synthesis parameters such as the precursor properties or the thermal treatments have to be controlled for tuning the desired morphology and microstructure of the particles, as later discussed in this Chapter, Section 4.2.2.

Polycrystalline $CaMn_{1-x}Nb_xO_3$ (with $x < 0.30$) and $LaMn_{1-x}Co_xO_3$ (with $x = 0.05, 0.10, 0.90$, and 0.95) perovskite-type phases were obtained by thermal decomposition of the corresponding polymeric citrate precursors [Bocher-2008b, Bocher-2006]. The precursors are prepared by dissolving the required amounts of $Ca(NO_3)_2 * 4\ H_2O$ (Fluka; $\geq 99\%$), $La(NO_3)_3 * 6\ H_2O$ (Merck; $\geq 97\%$), $Mn(NO_3)_2 * 4H_2O$ (Merck; $> 98.5\%$), or $Co(NO_3)_2 * 6H_2O$ (Merck; $> 97\%$) in deionized water. $NbCl_5$ (Aldrich; $> 99.5\%$) was added to the solution after prior dissolution in hydrochloric acid. Citric acid ($C_6H_8O_7$, Riedel-de Häen; $> 99.5\%$) was used as chelating agent and added in excess with a citric acid/metal cations molar ratio of 2/1 in order to prevent precipitation and $NbCl_5$ hydrolysis. A 0.5 M precursor solution was obtained by homogenization and subsequent polymerization at 353 K for 3 h under continuous stirring. No precipitation was observed indicating the formation of water-soluble polymeric complexes. The obtained xerogel precursor was heated in air with a rate of 20 K h^{-1} to a final temperature of 573 K and maintained at this temperature for another 3 h. After an intermediate grinding, the ash-like powder was calcined at 1073 K for 6 h leading to polycrystalline SC-derived manganate phases.

Polycrystalline $La_{1-x}Ca_xTiO_{3\pm\delta}$ (with $x = 0.30$, 0.50, and 0.70) perovskite-type phases were prepared by a modified *chimie douce* synthesis method [Bocher-2007]. The production of water-soluble titanium precursors is fairly difficult due to the facile hydrolysation of titanium salts. Complex polymerization processes involving peroxy groups are used since the peroxy ions ${O_2}^{2-}$ are known to be strong chelating ligands with respect to the metal ions [Schwarzenbach-1970]. Ti metal powder (Alfa Aesar; $\geq 99.99\%$) was dissolved in hydrogen peroxide aqueous solution (30 wt% in water) and ammonia hydroxide aqueous solution (25 wt% in water) to form a metastable titanium-peroxo-complex according to Equation 4.1 [Camargo-2000]:

$$Ti + 3H_2O_2 + OH^- \leftrightarrow Ti[(OH)_3O_2]^- + 3H_2O \tag{4.1}$$

After continuous stirring for 5h, the transparent solution presented a pH = 11. The yellow-orange color of the resulting solution is attributed to the formation of peroxy species. Citric acid is added to the solution to create a stable citrato-peroxo-titanate-precursor as described in Equation 4.2. The pH of the citrate precursor was adjusted to a pH range of $4 < pH < 5$.

$$Ti[(OH)_3O_2]^- + 2H^+ + C_6H_5O_7^- \leftrightarrow [Ti(C_6H_5O_7)O_2]^{2-} + 3H_2O \tag{4.2}$$

Then, the required amounts of $La(NO_3)_3 * 6\ H_2O$ (Merck; $\geq 97\%$) and $Ca(NO_3)_2 * 4\ H_2O$ (Fluka; $\geq 99\%$) were added to the citrato-peroxo-titanate-precursor solution. In addition, an excess of citric acid was added to complex all the cations present in solution. Different citric acid/metal cations ratio (CA/M = 3/1 or 10/1) were used in order to assess the influence of different polymerization levels on the perovskite phase formation, as later discussed in this Chapter, Section 4.2.2. This precursor solution was thermally decomposed in air with a rate of 20 K h^{-1} to a final temperature of 573 K for 3 h. After an intermediate grinding, the ash-like powder was calcined at 973 K for 1 h leading to polycrystalline SC-derived phases.

4.2.1 Particle morphologies

Fine perovskite-type manganate particles issued from the thermal decomposition of the corresponding citrate precursor are shown in Figures 4.2. Scanning electron microscopy (SEM) images reveal an uniform particle size distribution with primary particle sizes ranging from 100 − 120 nm to 250 − 500 nm in diameter, this depending on the phase composition[1]. The SC-made $CaMn_{0.95}Nb_{0.05}O_3$ particles form aggregates (chemically-sinter bonded) of primary particles while the SC-derived $LaMn_{0.05}Co_{0.95}O_3$ particles correspond to agglomerates (physically bonded) of aggregates mixed with primary particles. Despite the different clusters of primary particles, all the SC-made particles form a 3D porous network. This feature arises from the thermal decomposition of the citrate precursor and the subsequent crystallization process. The citrate precursor is a homogeneous intermix of cations in a polymeric matrix. The ignition of the citrate precursor causes a gradual decomposition of the organic matter yielding gas releases. This destruction of the organic matrix results in the formation of a xerogel, i.e. a 3D amorphous porous structure. With additional thermal treatments, the crystallization process takes place leading to the formation of independent primary crystallites. Each crystalline nucleus tends to growth until a neighbored crystallite limits its expansion leading to such 3D crystalline porous structures.

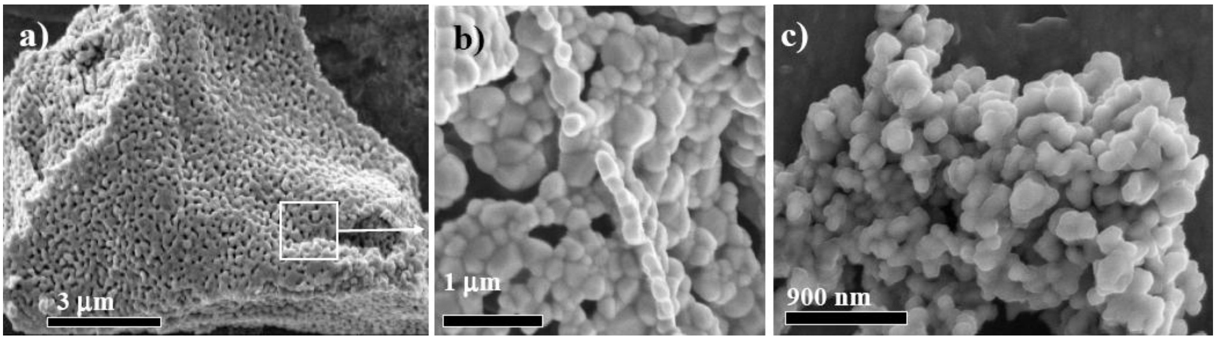

Figure 4.2: SEM images of powders synthesised by the SC method: a), b) $CaMn_{0.95}Nb_{0.05}O_3$, and c) $LaMn_{0.05}Co_{0.95}O_3$ perovskite particles (calcined at 1073 K for 6 h in air).

The size of the SC-primary crystallites is an important issue with respect to the final size, morphology, and microstructure of the sintered crystallites. The nature of *A* and *B*-site cations can also influence the morphology and the size of the resulting crystallites. A complete understanding of the synthesis process allows a tuning of the particle morphology and size, as explained in the next section.

---

[1] the manganate phases were all prepared with identical thermal treatments, i.e. calcination at 1073 K for 6 h in air.

4.2.2 Thermal decomposition of the citrate precursor

The thermal decomposition of the citrato-peroxo-titanate-precursor is investigated by combining in-situ thermogravimetric analyses and infrared spectroscopy studies [Bocher-2007]. The thermochemical reactions involved in the thermal decomposition of the citrate precursor can influence on the resulting particle morphology. A comprehensive study of the thermal decomposition process is required to further tailor the desired particle size and morphology.

The functional group coordinations of the organic ligands were studied at different temperatures. The IR spectrum of the (La,Ca)Ti-citrate precursor at T = 423 K, shown in Figure 4.3, emphasizes the presence of different functional groups originated from the organic network and those coordinated to the transition metal ion. The predominant bands at $\nu = 1700$ cm^{-1}, 1405 cm^{-1} and 1295 cm^{-1} can be assigned to the carboxylic acid functions of the free citric acid [Lin-Vien-1991]. The broad band around $\nu = 3200$ cm^{-1} can be attributed to the bonded hydroxide stretches [Lin-Vien-1991]. Absorption bands of the carboxylate ions at $\nu = 1560$ cm^{-1} and 1410 cm^{-1} [Hennings-1978] are also evidenced. The formation of metal-citrate complexes is confirmed by the presence of the C-O stretch, observed at $\nu = 1560$ cm^{-1}, which corresponds to the α-hydroxy group of the citric acid coordinated to the metal ion [Nelis-2005].

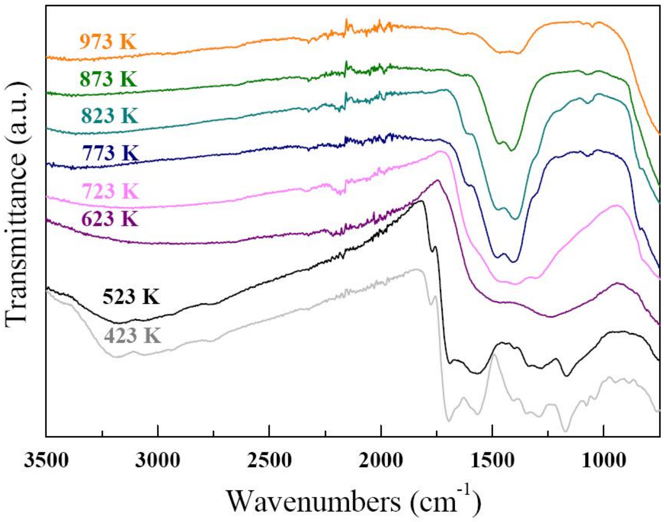

Figure 4.3: IR spectra of (La,Ca)-Ti citrate precursors calcined at different temperatures in air.

The thermal decomposition of the (La,Ca)Ti-citrate xerogel (predried at T = 423 K) is presented in Figures 4.4. First, at 423 K < T < 523 K (step 1), a partial decomposition of the organic network corresponding to a weight loss of 18.6 wt% occurs simultaneously with releases of H_2O (m/z 18), CO (m/z 28), O_2 (m/z 32), CO_2 (m/z 44) and citric acid fragments $C_2H_2O_2^+$ (m/z 58), as presented in Figures 4.4 c) and d). The loss of CO_2 is attributed to the cracking of the carboxylic acid function groups coming from the citric acid ligands, as depicted in Figure 4.1.

The IR spectrum at T = 523 K evidences the disappearance of different organic species, i.e. the carboxylic acid function, the bonded hydroxide, the carboxylate ions and the metal-citrate complex coordination, which confirms the decomposition of the citrate xerogel. Similar investigations under inert atmosphere (not shown) reveal releases of citric acid fragments, CO_2 and H_2O which confirm that the CO_2 emissions originate from the citric acid decomposition and not from a possible combustion reaction.

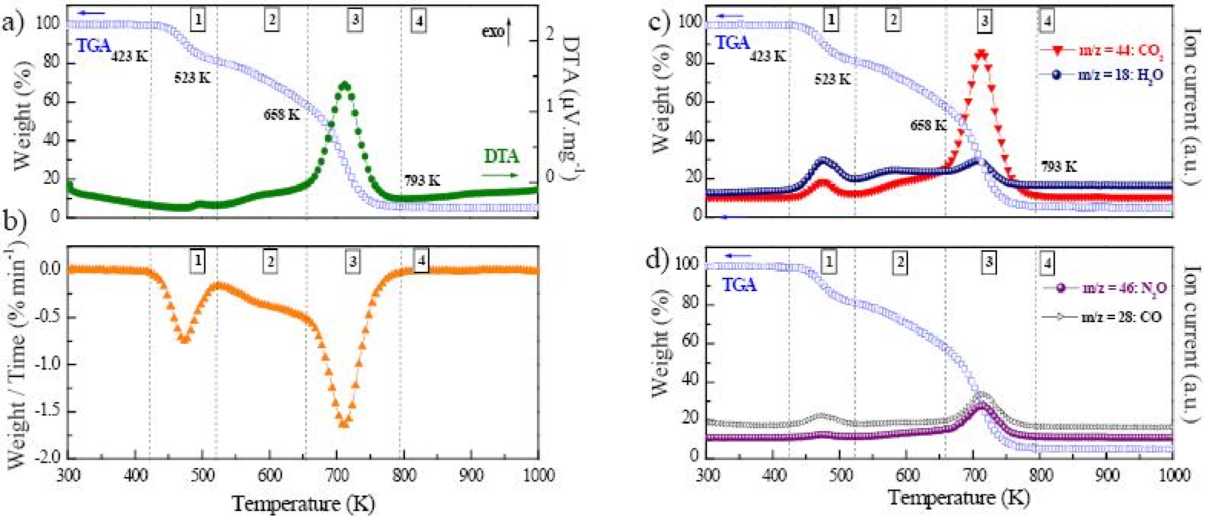

Figure 4.4: Thermal decomposition analyses of the (La,Ca)-Ti citrate precursor (under synthetic air, 2 K.min^{-1}). a) TGA and DTA curves, b) DTG plot, c) and d) TGA and MS signals with m/z 44: CO_2, m/z 18: H_2O in Figure c) and m/z 28: CO, m/z 46: NO_2 (enlarged) in Figure d).

In the second step, at 523 K $<$ T $<$ 658 K, the metal-citrate coordination network is rearranged, as observed in the IR spectra. The absorption bands of the organic fragments completely disappear from T $>$ 623 K. The decomposition of the chelating citrate ligands coordinated to the metal ions is confirmed since the metal-citrate complex band, i.e. $\nu = 1080$ cm^{-1}, disappears at this temperature. This thermal event causes a weight loss of 23.4 wt% characterized by reaction rate of 0.15 to 0.50 wt% min^{-1}, which corresponds to a lower reaction rate compared to the previous one (step 1: reaction rate up to 0.75 wt% min^{-1}), as indicated on the DTG curve in Figure 4.4 b). The second step is marked by the molecular reorganization of the citrate complex precursor where the direct organic sphere coordinated to the metal cations is decomposed.

A strong exothermic event occurs in the third temperature region, at 658 K $<$ T $<$ 793 K, resulting in a weight loss of 52.2 wt%. Releases of H_2O, NO_2, CO and CO_2 are attributed to the decomposition of the residual organic network inducing the exothermal reaction. Since no consumption of oxygen is observed in this temperature range, a possible self-oxidation process could be at the origin of this exothermic combustion reaction. The peroxogroups formed during the dissolution of Ti metal are suitable oxidizing agents in this combustion process. Furthermore, the existence of CO_3^{2-} carbonate ions is identified from T = 773 K with the presence of the characteristic vibrations, i.e. ν = 1460 cm^{-1}, 1060 cm^{-1}, and 860 cm^{-1} [Hennings-1978]. This finding indicates the formation of intermediate carbonates. In presence of CO_2 atmosphere, the cation carbonization appears more favorable than the direct oxidation [Fjellvag-1995]. The intermediate species are certainly formed during a gas-solid reaction between the amorphous xerogel and the released CO_2 which remains present in the surrounding environment. In contrast, under inert atmosphere (not shown), the DTA signal presents a broad endothermic peak and a gradual decomposition of the residual organic matter takes place and is not completed at 1273 K.

Finally, further small weight losses (0.5 wt%) occur at 793 K < T < 1023 K. During this last decomposition stage, no significant CO_2 emission is observed with respect to the mass spectrometer detection limit. The intermediate species, i.e. the carbonate groups, disappear at T = 823 K yielding most probably the formation of the perovskite-type titanate phase. Compounds thermally decomposed at T = 873 K reveal weak reflections assigned to the perovskite phase. Those reflections are largely overlapped by broad peaks arising from the amorphous part, as indicated on the X-ray powder diffraction (XRPD) pattern in Figure 4.5 a). The completeness of the perovskite phase formation is evidenced at T = 973 K. The phase crystallinity improves with thermal treatments and the thermal stability is confirmed by a constant weight up to T = 1273 K.

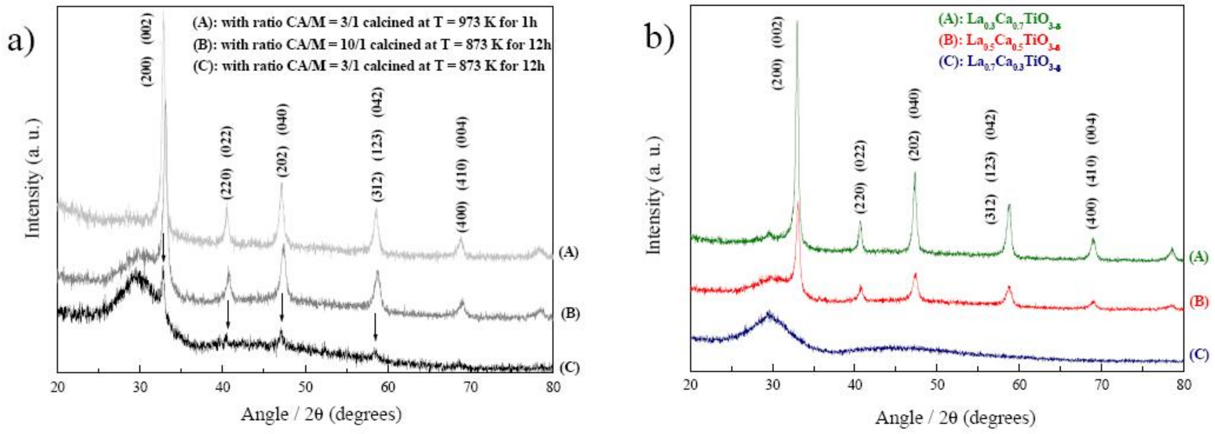

Figure 4.5: XRPD patterns of a) $La_{0.50}Ca_{0.50}TiO_{3\pm\delta}$ prepared with different (CA/M) molar ratio and calcined at different temperatures and times and b) $La_{1-x}Ca_xTiO_{3\pm\delta}$ (for x = 0.30, 0.50, and 0.70), prepared with a (CA/M) molar ratio of (10/1) and calcined in air at T = 823 K for 12 h. The reflections are indexed in the orthorhombic type structure (*Pnma* S.G.).

4.2.3 Thermally stable and highly crystalline mesoporous phases

The polycrystalline $La_{1-x}Ca_xTiO_{3\pm\delta}$ titanate phases, synthesized by the SC-modified method, is characterized by a highly crystalline mesoporous microstructure [Bocher-2007]. The following investigations illustrate how different (i) SC synthesis conditions and (ii) nature/level of substitutions can affect the final microstructure of the perovskite-type phases.

(i) The (La,Ca)Ti-citrate precursor was prepared with different citric acid/metal cations molar ratio (CA/M). The perovskite phase formation occurs at T = 873 K when the CA/M molar ratio is assigned to 10/1, as shown on the XRPD pattern in Figure 4.5 a). At the same calcination temperature, the citrate precursor prepared with a CA/M = 3/1 remains partly amorphous with the appearance of weak perovskite reflections, as indicated by arrows. In this compound, the perovskite phase formation is achieved for higher calcination temperature, i.e. at T = 973 K. Higher exothermic reactions occur when larger amounts of organic matter are thermally decomposed, since it induces an increase of the local temperature in the surrounding environment of the citrate precursor. Therefore, the proportion of citric acid in the starting precursor solution is directly correlated with the resulting crystalline fraction and the temperature of phase formation. Furthermore, the crystallinity is visibly improved during annealing process due to the enhancement of the crystal growth.

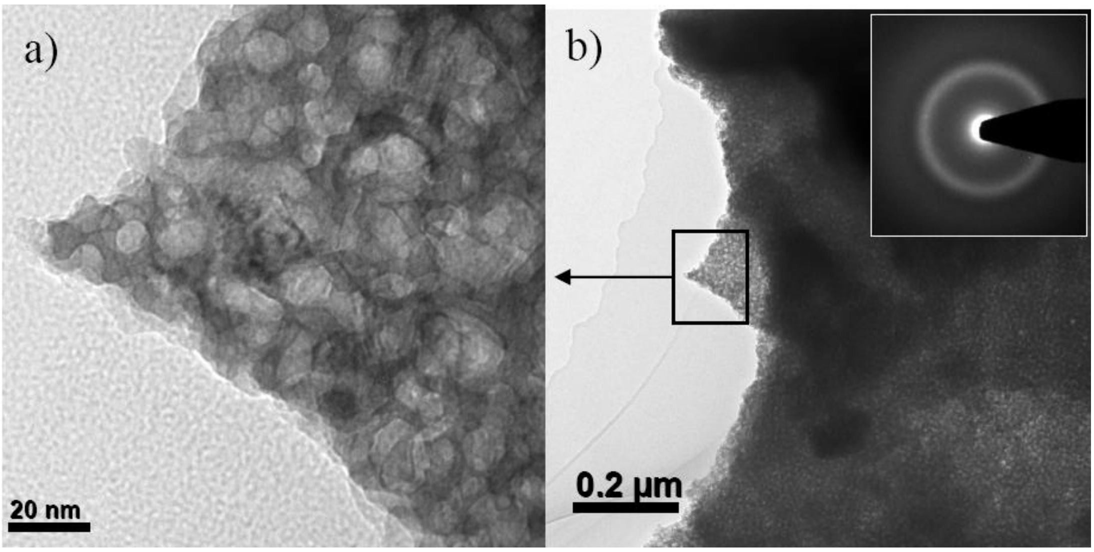

Figure 4.6: a) medium- and b) low-resolution TEM pictures of $La_{0.70}Ca_{0.30}TiO_{3\pm\delta}$ synthesised by the SC method and calcined at T = 823 K in air.

(ii) Various $La_{1-x}Ca_xTiO_{3\pm\delta}$ titanate phases (with x = 0.3; 0.5; and 0.7), calcined at T = 873 K, are investigated concerning their phase formation and the related microstructure. The XRPD patterns of the titanate phases shown in Figure 4.5 b) reveal different crystallization stages depending on the Ca content. The cationic composition is determined by energy dispersive X-ray spectroscopy (EDS) analyses as follows: $La_{0.72\pm0.01}Ca_{0.28\pm0.01}TiO_{3\pm\delta}$ for the La-rich phase, $La_{0.55\pm0.01}Ca_{0.45\pm0.01}TiO_{3\pm\delta}$ for the half-substituted phase, and $La_{0.25\pm0.02}Ca_{0.75\pm0.02}TiO_{3\pm\delta}$ for the Ca-rich phase.

The La-rich phase, i.e. $La_{0.7}Ca_{0.3}TiO_{3\pm\delta}$, is amorphous as indicated by the presence of broad reflections in the XRPD pattern and confirmed from the analysis of the transmission electron microscopy (TEM) data. The measured electron diffraction (ED) pattern, inserted in Figure 4.6 b), displays one single-ring caused by the diffused scattering characteristic of amorphous compounds. The ring is spread around $d_{110} \simeq 0.27$ nm indicating that the studied phase is in the first stage of the perovskite phase formation. The medium-resolution TEM image of the La-rich phase reveals a porous microstructure which is characterized by a tunnel-like shape, as shown in Figure 4.6 a).

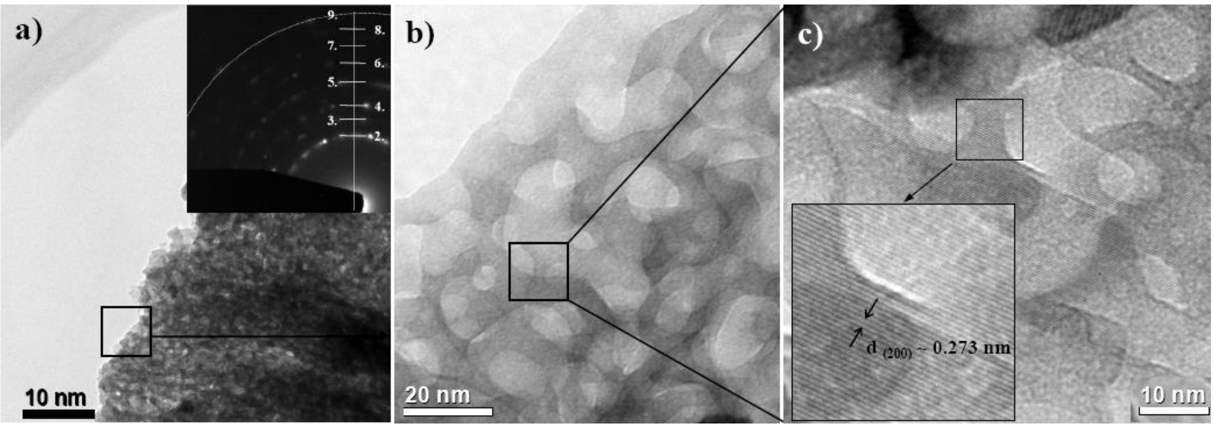

Figure 4.7: a) low-, b) medium-, and c) high-resolution TEM pictures of $La_{0.50}Ca_{0.50}TiO_{3\pm\delta}$ synthesised by the SC method and calcined at T = 823 K in air. The inset in Figure a) presents the experimental ED ring pattern indexed in orthorhombic crystal structure (see Table 4.1).

At identical calcination temperatures, i.e. at T = 823 K, the $La_{0.5}Ca_{0.5}TiO_{3\pm\delta}$ phase presents structural and microstructural differences with respect to the previous one. The experimental ED pattern, shown in Figure 4.7 a), combines spread rings due to diffuse scatterings and multiple-diffracted spots with discontinuous rings arising from the randomly-oriented polycrystalline fraction of the compound. The diffraction pattern can be indexed in the orthorhombic structure (S.G., *Pnma*). The corresponding interplanar distances d_{hkl} determined from the ED pattern are reported in Table 4.1. The XRPD pattern of the corresponding phase exhibits characteristic reflections of the perovskite phase. A broad reflection peak still remains resulting from the amorphous fraction. The $La_{0.5}Ca_{0.5}TiO_{3\pm\delta}$ phase combines amorphous regions characterized by round-shaped channels and open hexagonal channels delimited by crystalline walls which correspond to the {110} planes. A mesoporous microstructure composes the crystalline regions of the $La_{0.5}Ca_{0.5}TiO_{3\pm\delta}$ phase, as illustrated in Figures 4.7 b) and c).

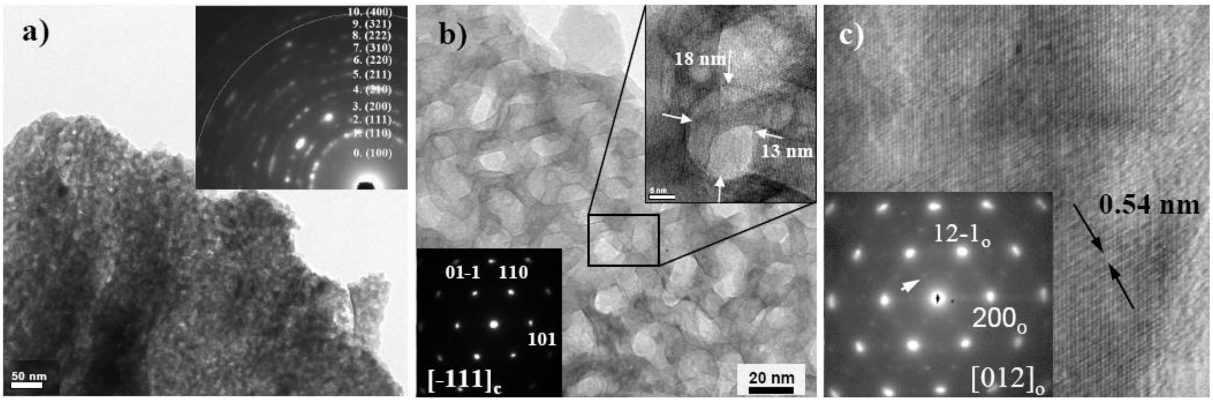

Figure 4.8: a) low-, b) medium-, and c) high-resolution TEM pictures of $La_{0.30}Ca_{0.70}TiO_{3\pm\delta}$ synthesised by the SC method and calcined at $T = 823$ K in air. The inset in Figure a) presents the ED ring pattern of the selected area which is indexed in the orthorhombic crystal structure (see Table 4.1). The ED patterns inserted in Figures b) and c) are indexed either in b) the pseudocubic or in c) the orthorhombic crystal structure.

The Ca-rich phase, i.e. $La_{0.7}Ca_{0.3}TiO_{3\pm\delta}$ exhibits high crystallinity after similar thermal treatments at T = 873 K, as evidenced from the XRPD pattern and the TEM data. The ED pattern in Figure 4.8 a) presents defined rings which originate from the diffracted spots. No diffuse scattering is observed in the Ca-rich phase. The ring pattern can be indexed in the orthorhombic structure (S.G., *Pnma*) and the experimental d_{hkl} are reported in Table 4.1. The *hkl* Miller indices can be assigned either in the pseudocubic or in the orthorhombic crystal structure. The Figure 4.8 b) gives a general overview of the mesoporous microstructure which is characterized by the presence of well-defined hexagonal channels of $\simeq$ 20 nm in diameter. The high-resolution TEM (HRTEM) image in Figure 4.8 c) confirms the highly crystalline nature of the Ca-rich phase. The diffraction patterns inserted in Figures 4.8 b) and c) are indexed in the pseudocubic or orthorhombic symmetry[1], respectively. The orthorhombic symmetry is confirmed by the extra spots observed on the ED pattern, as indicated by the arrow. The HRTEM images presented in Figures 4.9 a) and b) highlight few hexagonal channels delimited by highly-crystalline $\{110\}_c$ planes. The fast Fourier transform (FFT) of the corresponding HRTEM image (Figure 4.9 a) consists of two overlapped diffraction patterns arising from different crystallites oriented along the [-111] zone axis and rotated of a few degrees from each other. The HRTEM image with a larger magnification, i.e. Figure 4.9 b), emphasizes the boundary of hexagonal mesopores oriented in the $[-111]_c$ zone axis. The mesoporous nature of the crystallized materials is confirmed by nitrogen physisorption. The Ca-rich phase exhibits a type-IV nitrogen sorption isotherm

---

[1] for convenience, information related to the orthorhombic and cubic structure are hereafter labelled with "o" and "c" subscripts, respectively.

(not shown) with a specific surface area of 49 m^2 g^{-1}. The estimated pore size based on the Barrett-Joyner-Halenda (BJH) method [Barrett-1951] confirms the mesoporosity observed by electron microscopy.

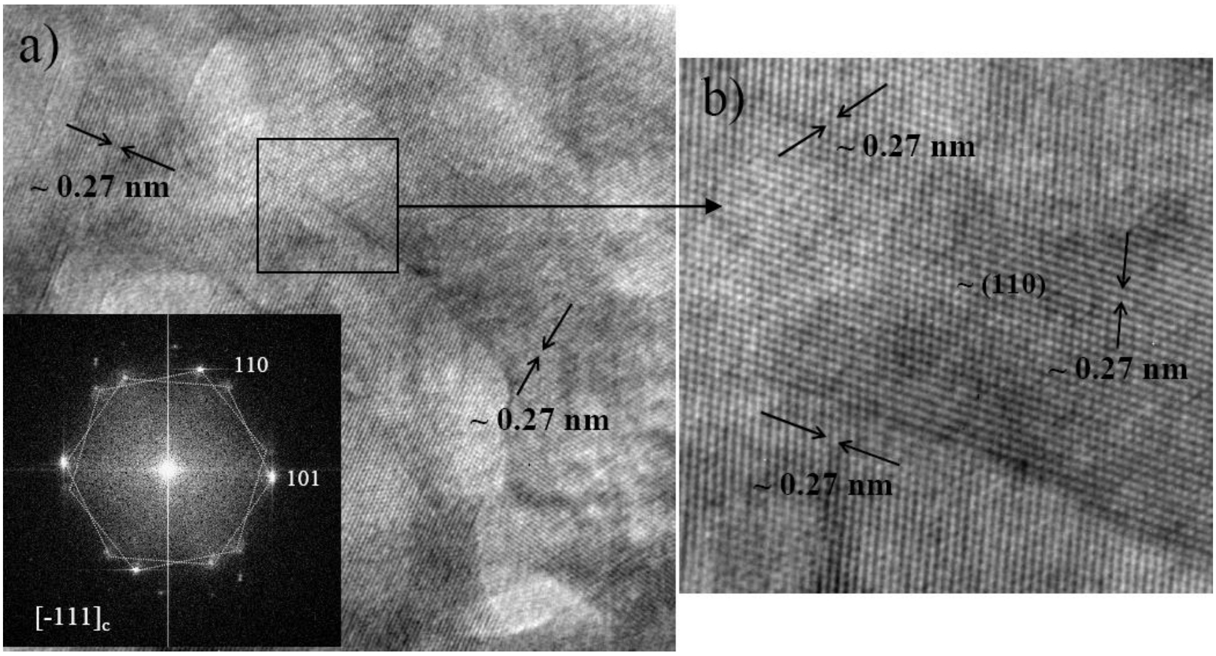

Figure 4.9: a) and b) HRTEM images of $La_{0.30}Ca_{0.70}TiO_{3\pm\delta}$ synthesised by the SC method and calcined at T = 823 K in air. The inset in Figure a) shows the fast Fourier transform (FFT) exhibiting diffraction patterns of overlapped grains oriented on the [-111]$_c$ zone axis.

This study evidences the impact of the precursor composition on the crystallization process. For similar thermal treatments, the perovskite-type titanate phases reveal different crystal growth stages depending on the Ca content, i.e. the substitution of La by Ca favors the formation of a mesoporous microstructure at relatively low temperatures. Templating techniques are already known to form mesoporous structures. The use of soft structure-directing organic assemblies usually yields residual amorphization and structural collapses at high temperature (T $\simeq$ 650 K) [Yang-1998, Yang-1999]. Hard-templating chemistries employ inorganic precursors more suitable for high-temperature applications but it requires time-consuming synthesis conditions [Li-2004]. The present synthesis method results to thermally stable and highly crystalline mesoporous microstructures in a "*one-pot*" synthesis process [Bocher-2007]. Furthermore, the well-defined mesoporosity is favored by the crystallization process at high temperatures. The mesopores remain intact at temperatures as high as 1073 K since no evidence of collapsing effect has been observed by imaging techniques. As a result, the highly crystalline mesostructure reveals higher specific surface areas (SSA) than the amorphous La-rich phase, e.g. for $La_{0.3}Ca_{0.7}TiO_{3\pm\delta}$: SSA = 49 m^2 g^{-1} and for $La_{0.7}Ca_{0.3}TiO_{3\pm\delta}$: SSA = 21 m^2 g^{-1}, respectively. However, the amorphous phases also result in highly crystalline mesoporosity with additional thermal treatments

No.	$hkl_{pseudocubic}$	$hkl_{orthorhombic}$	d_{hkl} (nm) $La_{0.50}Ca_{0.50}TiO_{3\pm\delta}$	d_{hkl} (nm) $La_{0.30}Ca_{0.70}TiO_{3\pm\delta}$
0	100	020, 101	-	0.390
1	110	200, 1221, 002	0.27	0.273
2	111	220, 022	0.22	0.220
3	200	040, 202	0.19	0.191
4	210	222, 311	0.17	0.170
5	211	321, 240, 042	0.15	0.154
6	220	400, 242,004	0.14	0.136
7	310	402, 161, 323, 204, 430, 412	0.12	0.119
8	222	440, 044, 432, 234	0.11	0.110
9	321	442, 244, 361, 163	-	0.101
10	400	080, 404	-	0.095

Table 4.1: Interplanar distances d_{hkl} determined from experimental ED patterns of $La_{0.50}Ca_{0.50}TiO_{3\pm\delta}$ (Figure 4.7) and $La_{0.30}Ca_{0.70}TiO_{3\pm\delta}$ (Figure 4.8). To establish the correspondence, simulation of the diffraction was made by JEMS software [Stadelmann-1987] (with orthorhombic structure, *Pnma*, a = 0.546 nm, b = 0.7709 nm, c = 0.544 nm).

at higher temperatures.

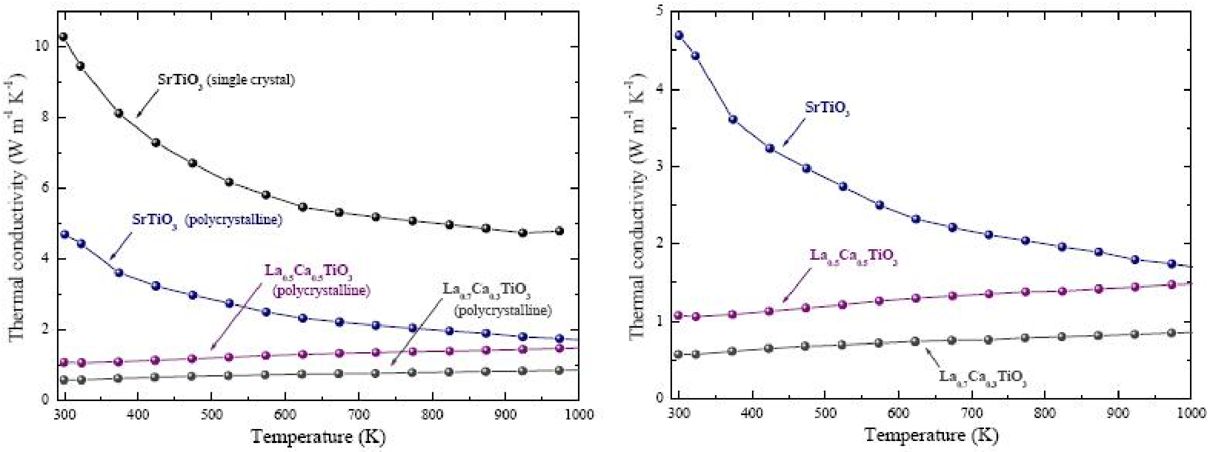

Figure 4.10: a) and b) Thermal conductivity temperature dependence of mesoporous $La_{1-x}Ca_xTiO_{3\pm\delta}$ (x = 0.3 and 0.5), polycrystalline $SrTiO_3$ synthesized by the SSR method and single crystal $SrTiO_3$.

The $La_{1-x}Ca_xTiO_{3\pm\delta}$ phases, characterized by a mesoporous microstructure at the nanometer scale, are evaluated regarding their thermal transport properties. The thermal conductivities of the polycrystalline SSR-derived $SrTiO_3$ compound and the single crystal $SrTiO_3$ are reported for comparison. All the studied phases are insulators, which enables to directly determine the impact of the microstructure on the lattice thermal conductivity. The single crystal reveals the highest thermal conductivity values in the whole temperature range, i.e. 300 K $<$ T $<$ 1000 K, compared to the polycrystalline titanate phases, e.g. at 300 K: κ = 10.3 W m^{-1} K^{-1} for the SrTiO$_3$ single crystal and κ = 4.7 W m^{-1} K^{-1} for the SrTiO$_3$ polycrystalline compound, as shown in Figure 4.10 a). In polycrystalline phases, phonons are scattered at the grain boundaries resulting in a lowering of the thermal conduction while the absence of grain boundaries in single crystals favors the traveling of phonons through the crystal lattice. Among the polycrystalline titanate phases, different thermal conductivity values are observed, especially in the low-temperature range, i.e. T $<$ 600 K, as presented in the Figure 4.10 b). The SSR-derived SrTiO$_3$ compound presents an usual temperature dependence, i.e. dκ/dT $<$ 0, while the thermal conductivity of the mesoporous La$_{1-x}$Ca$_x$TiO$_{3\pm\delta}$ phases (x = 0.3 and 0.5) is characterized by a nearly temperature independent behavior. Lower thermal conductivity values are achieved with the mesoporous titanate phases compared to the SSR-derived compound, e.g. at 425 K: κ = 3.2 W m^{-1} K^{-1} for the SSR-derived SrTiO$_3$ compound and κ = 0.65 W m^{-1} K^{-1} for the mesoporous La$_{0.7}$Ca$_{0.3}$TiO$_{3\pm\delta}$ phase. The microstructure of the La$_{1-x}$Ca$_x$TiO$_{3\pm\delta}$ phases is characterized by nano-sized hexagonal crystalline channels. In the mesoporous titanate phases, phonons might be efficiently scattered at the channel interfaces on the nanometer scale and at the grain boundaries on the micrometer scale yielding a significant lowering of the thermal conduction compared to the SSR-derived titanate phase.

4.3 Ultrasonic spray combustion (USC) process

Spray combustion involves the use of precursor solutions dissolved in solvents and aerosolized into a droplet stream which is further transported into a tubular reactor or a flame[1] [Gurav-1993]. A large diversity of materials have been synthesized applying this continuous synthesis process achieving single- or multicomponent metals or metal oxides [Kodas-1999]. Generally, the solvent evaporation is accompanied by the precursor precipitation. Chemically *in-situ* driving reactions, i.e. combustion processes, yield the desired phase by means of nanostructured materials. The complete precursor evaporation leads to solid nanoparticles while the incomplete evaporation process results in a surface precipitation followed by a combustion process. At the end, a rapid or gentle drying occurs resulting in shell-like or hollow particles, respectively [Strobel-2007]. Indeed, the precursor composition and its enthalpy of reaction control the evaporation process and therefore the particle morphology [Jain-1997, Okuyama-2003]. A high enthalpy-content organic solution ignites and sustains the spray combustion process since the organic matter acts as fuel while for low enthalpy-content solution, i.e. aqueous, higher external energy source is required. Besides, short residence times and high applied temperatures are important issues for synthesizing nanoparticles by spray combustion process.

---

[1] in that case, the process is referred as flame spray processes.

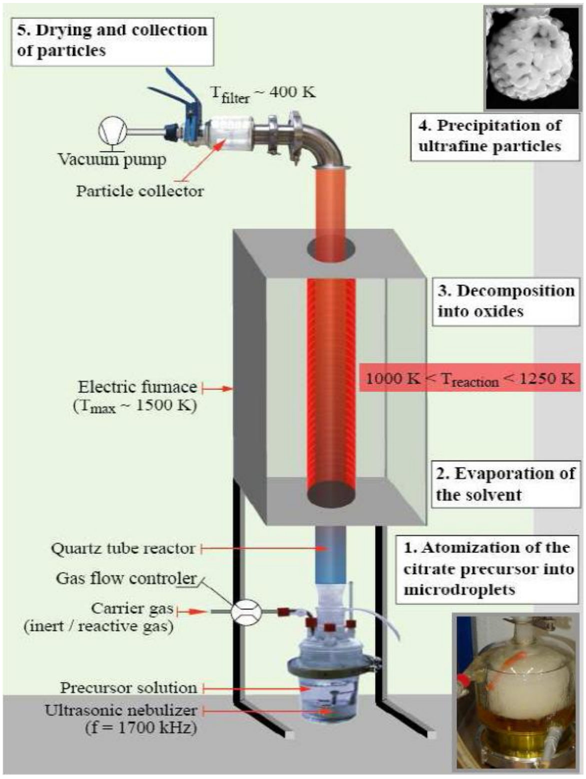

Figure 4.11: Scheme of the ultrasonic spray combustion set-up.

The spray combustion technique presents the advantage to be a continuous synthesis process enabling the up-scale production of nanoparticle materials. The *chimie douce* chemistry-based precursor is thermally decomposed using an ultrasonic spray combustion process. The citrate precursor is first decomposed into ultrasonically generated microdroplets and further carried into a high-temperature reactor leading to perovskite-type nanoparticles collected with the aid of filters, as schematically described in Figure 4.11. Characteristics of USC-made particles rely on the synthesis temperature history, on the precursor properties, i.e. the composition and the concentration, and on the gas flow rates. All these experimental parameters have to be adjusted for tailoring the USC-made particle morphology while optimizing the production rate.

Perovskite-type manganate $CaMn_{1-x}Nb_xO_3$ and titanate $La_{1-x}Ca_xTiO_{3\pm\delta}$ (with $x \leq 0.10$) nanoparticles were synthesised with a home-made USC apparatus [Bocher-2007, Bocher-2008a]. Spraying was accomplished by solution atomization through piezoelectric nebulizers which operate at ultrasonic frequencies (f_u = 1.7 MHz) generating homogeneous droplets of 2-4 μm size with a limited atomization rate of 2 cm^3 min^{-1}. The average size of primary particles $d_{particle}$ can be roughly determined by the Equation 4.3 [Rajan-2001]:

$$d_{particle} = 0.34 \left(\frac{8\pi\gamma}{f_u^2 d_s} \right)^{1/3} \tag{4.3}$$

where f_u is the ultrasonic frequency, γ is the surface tension, and d_s is the density of the precursor solution. Preliminary set of experiments were performed for tuning the different experimental parameters influencing the USC process, as mentioned above, and leading to an optimal experimental procedure. A 0.1 M citrate precursor solution was nebulized and the generated microdroplets were carried by a gas flow rate of 5 L min^{-1} through a quartz tube placed into a high temperature furnace heated at 1023 K $<$ T$_{furnace}$ $<$ 1273 K. Ultrafine perovskite particles were collected onto a glass fibre filter which was heated at 423 K with an average production rate of 200 mg h^{-1}.

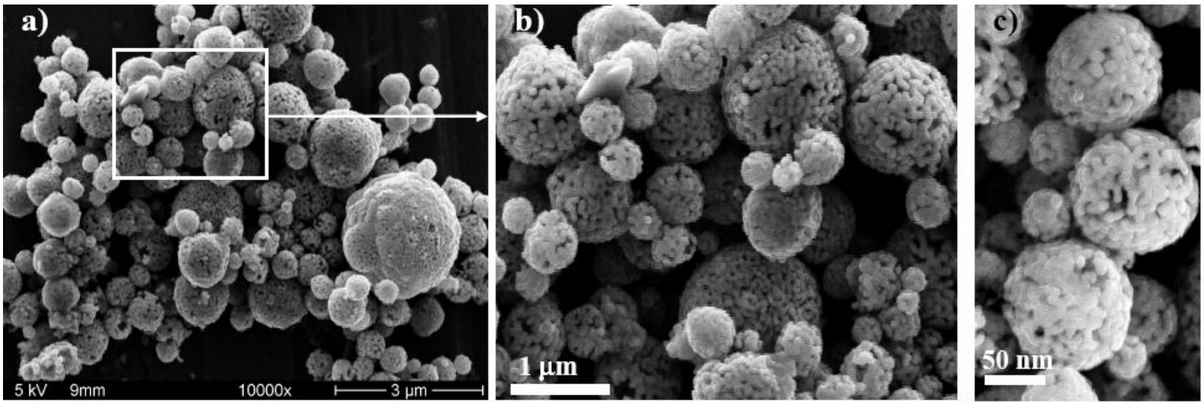

Figure 4.12: a), b) and c) SEM pictures of microspheres consisted of ultrafine $CaMn_{0.95}Nb_{0.05}O_3$ perovskite particles prepared by the USC process.

Figures 4.12 a) and 4.13 a) present manganate and titanate phases, synthesised by the USC process, consisting of individual spheres ranging from 100 nm to 5 μm in diameter. The different magnified SEM images, displayed in Figures 4.12, reveal that these typical USC-microspheres are made of primary spherical nanoparticles of 10 nm to 50 nm in diameter. The low-resolution TEM image in Figure 4.13 a) exhibits a clear contrast between the inner and the outer part of the USC-microspheres. In case of dense spheres, transmitted electrons should be highly scattered showing dark inner regions in bright-field TEM images. However, a brighter area is observed in the centre of the sphere suggesting that USC-microspheres exhibit hollow structures. The experimental ED pattern, inserted in Figure 4.13 a), consists of defined rings arising from multiple-diffracted spots of randomly-oriented crystallites. This finding confirms the highly crystalline nature of the USC perovskite nanoparticles. Larger magnifications of USC-microspheres, presented in Figures 4.13 b) and c), reveal rectangle-like shape crystallites of 15 to 30 nm length displaying lattice fringes of $d_{100} \simeq 3.9$ Å, characteristic of the perovskite cubic lattice.

Since the USC process utilizes a home-apparatus, the morphology of the resulting particles can present divergences with previous works reported on similar spray combustion systems [Gurav-1993]. In the present case, the USC process applied to the decomposition of the *chimie douce* precursors results to an incomplete precursor evaporation inducing a rapid surface precipitation of the precursor which further decomposes into highly crystalline nanoparticle forming hollow microspheres. Hence, the USC-nanostructured materials typically yield large specific area up to 60 m^2 g^{-1}.

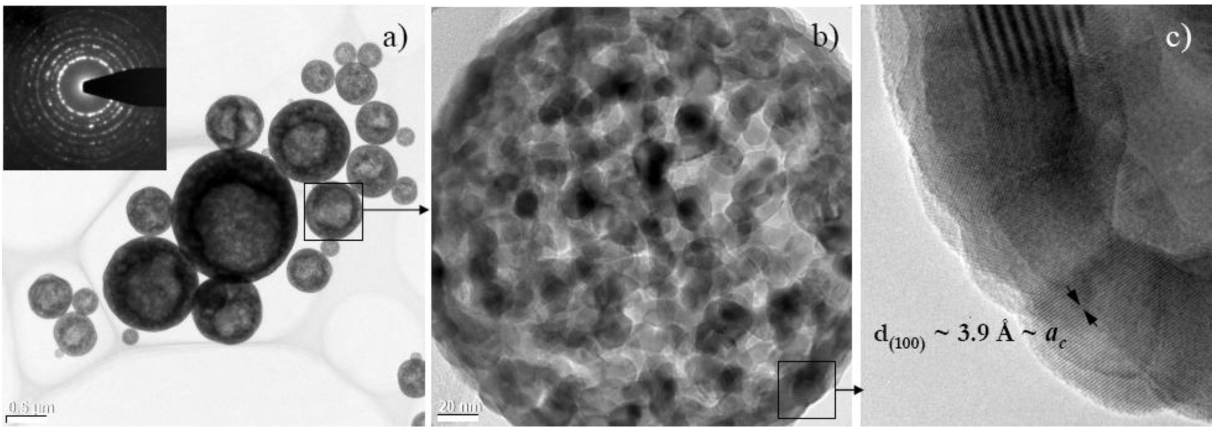

Figure 4.13: a) low-, b) medium-, and c) high-resolution TEM pictures of hollow spheres consisted of ultrafine $La_{0.10}Ca_{0.10}TiO_3$ perovskite particles prepared by the USC process.

4.4 Conclusions

The different applied syntheses yield single phase polycrystalline perovskite-type oxides with a wide diversity of morphologies and microstructures such as the SSR-derived phases leading micrometer-sized polyhedral grains, the SC-series revealing submicrometer primary particles, or the USC-nanostructured materials. The tuning of experimental parameters such as the precursor properties or the thermal treatment conditions, is an essential issue for synthesizing highly crystalline tailor-made perovskite-type oxide materials with the desired morphology and microstructure. Nanoscale perovskite-type oxides are of main interest for exploring the influence of their morphology and microstructure on their thermoelectric properties. In the following chapters (Chapter 5 and Chapter 6), perovskite-type manganate phases involving specific morphologies, e.g. USC-made nanocrystallites and characteristic microstructures, e.g. nano-sized twinned domains, are investigated with respect to their thermoelectric activity.

Chapter 5

Perovskite-type $CaMn_{1-x}Nb_xO_3$

The search of new promising high-temperature thermoelectric oxide materials, i.e with high ZT^1 values, relies on optimizing the three interdependent thermoelectric parameters: S, ρ, and κ. This challenge implies to enhance the power factor PF^2 by tuning the charge carrier concentration and to lower the lattice thermal conductivity via nanostructuring.

The present chapter reports on the Nb-containing $CaMnO_3$ phases and their thermoelectric properties investigated over a large temperature range, i.e. 5 K $<$ T $<$ 1240 K. $CaMnO_3$ is an antiferromagnetic insulator which presents a large negative Seebeck coefficient, i.e. $S = -$ 800 μV K^{-1} at 300 K [Miclau-2007]. Low level aliovalent substitutions at the A- or B-site of the $CaMnO_3$ phase induce the creation of Mn^{3+} cations in the Mn^{4+} matrix which results in good thermoelectric properties, as previously detailed in the Chapter 2, Section 2.3.3.2 [Maignan-1998a; Hejtmánek-1999].

Polycrystalline perovskite-type $CaMn_{1-x}Nb_xO_{3\pm\delta}$ (x = 0.02, 0.05, 0.08, and 0.10) phases synthesized by the solid state reaction (SSR) method and the *"chimie douce"* (SC) synthesis route are studied concerning their morphologies, crystal structures and microstructures (see Sections 5.1 and 5.2). Differences in electrical and thermal transport properties are revealed depending on the applied synthesis method. This result allows the design of the up-to-now best n-type thermoelectric polycrystalline perovskite-type oxides operating in air at high temperatures, i.e. T $\simeq$ 1000 K [Bocher-2008b] (see Section 5.3). The low-temperature magnetic transition is of interest since it is directly related to the thermoelectric properties at T $<$ 200 K (see Section 5.4.1). Unusual magnetic and electrical transport properties are reported below the magnetic transition temperature for nanocrystalline manganates synthesized by the ultrasonic spray combustion (USC) process [Bocher-2008a]. At T $>$ 1100 K, the Nb-substituted $CaMnO_3$ phases undergo a structural transition and a thermal reduction. A comprehensive study examines the impact of both phenomena on the electrical and thermal transport properties in the high-temperature range. [Bocher-2009] (Section 5.4.2).

---

[1] ZT is the thermoelectric figure of merit with $Z = S^2/\rho\kappa$

[2] the power factor is defined by $PF = S^2/\rho$

5.1 Morphology, composition, and *B*-site cation oxidation states

The morphology of $CaMn_{1-x}Nb_xO_3$ sintered pellets issued from the SSR and the SC synthesis routes is characterized by SEM. These observations allow to further study the influence of the morphology on the electrical and thermal transport properties of the SSR- and the SC-derived phases. This aspect is later discussed in this Chapter, Section 5.3. Figures 5.1 and 5.2 display cross sectional views of SSR- and SC-sintered pellets, respectively. Typical grains of 3 to 10 μm in diameter are observed for the SSR phases while the grain size of SC-derived phases is in the submicrometer range, i.e. $\simeq$ 500 to 900 nm in diameter. The SSR-sintered grains are highly compacted with few channels of 2 to 3 μm diameter randomly distributed between the sintered grains, as emphasized in the Figure 5.1 b). This morphology of the SSR-sintered phases results from the sintering process of 6 h at 1673 K. The submicrometer-sized grains are rather interconnected as chains of sintered particles which lead to high surface areas, as highlighted in Figure 5.2 b). This specific morphology results from the crystallization process of the 3D porous citrate xerogel network creating a sponge-like structure, as previously remarked in the Chapter 4, Section 4.2.1. The SC compounds reveal specific surface areas (SSA) in the range of 1.0 - 1.5 m^2 g^{-1}, while the SSR phases have a SSA of approximately 0.5 m^2 g^{-1}.

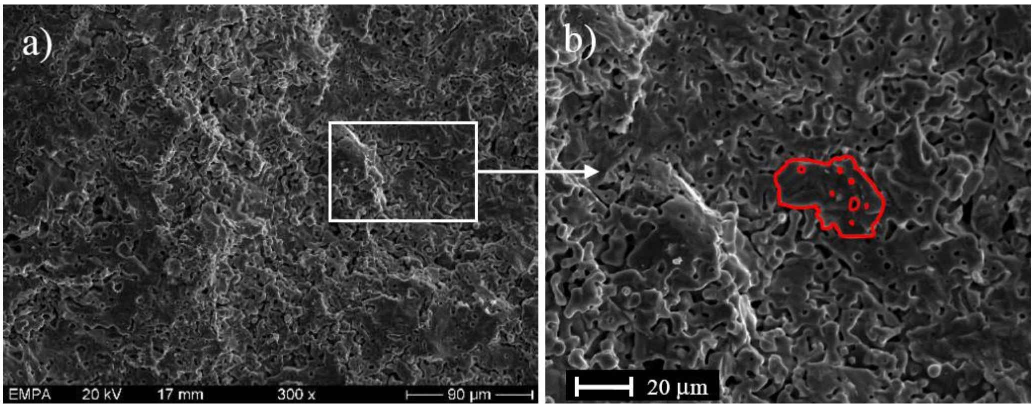

Figure 5.1: a) and b) SEM pictures of $CaMn_{0.95}Nb_{0.05}O_3$ cross section sintered pellets synthesised by the SSR method.

The *B*-site cationic compositions are determined by EDS coupled to the SEM. The oxygen content is measured by thermogravimetric reduction method. The results for all the synthesized phases are presented in Table 5.1. The cationic composition of the compounds are in good agreement with the intended compositions, except for the SSR phase with 8% Nb substitution where the EDS results suggest a lower Nb content than expected. It should be remarked that the error range of the EDS evaluations is higher for Nb (with contents x < 0.10) compared to the main elements, i.e. manganese. As earlier mentioned in the Chapter 4, Section 4.2, the *chimie douce* methods allow a fast and homogeneous distribution of Nb in the cationic matrix since all cations

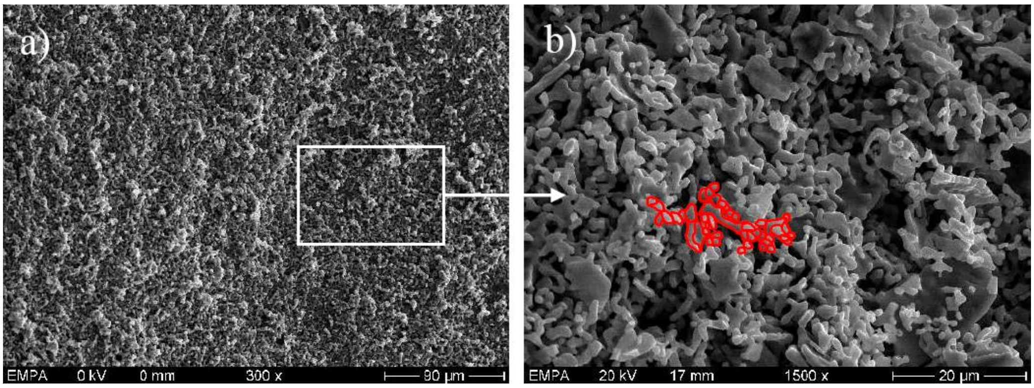

Figure 5.2: a) and b) SEM pictures of $CaMn_{0.95}Nb_{0.05}O_3$ cross section sintered pellets synthesised by the SC method.

are homogeneously mixed in aqueous solution. On the contrary, the interdiffusion of the cations in a solid matrix is necessary to homogenize the phases when applying the conventional ceramic method. Thermogravimetric reduction experiments present a slight oxygen excess for all phases yielding values of $\delta \leq 0.9$. The magnitude of δ is fairly small, these manganates can be therefore considered as near-stoichiometric perovskites. Since no additional oxygen can be inserted in interstitial sites in perovskite phases, the "excess" of oxygen corresponds rather to cation vacancies [Töpfer-1997]. This is confirmed by the presence of CaO rock salt layers which are observed in the $CaMn_{1-x}Nb_xO_3$ phases by STEM studies, as later discussed in this Chapter, Section 5.2.2.2.

Synthesis method	Niobium substitution	Cationic composition Mn	Cationic composition Nb	Oxygen content
SC	0.02	0.98 ± 0.01	0.013 ± 0.075	3.07 ± 0.05
	0.05	0.95 ± 0.01	0.047 ± 0.030	3.06 ± 0.07
	0.08	0.92 ± 0.01	0.079 ± 0.015	3.04 ± 0.05
SSR	0.02	0.98 ± 0.02	0.015 ± 0.070	3.03 ± 0.06
	0.05	0.95 ± 0.02	0.049 ± 0.040	3.08 ± 0.06
	0.08	0.93 ± 0.02	0.069 ± 0.020	3.09 ± 0.05

Table 5.1: *B*-site cationic composition and oxygen content for the $CaMn_{1-x}Nb_xO_{3+\delta}$ series (x = 0.02, 0.05 and 0.08).

The Mn and Nb oxidation states in the SC-derived $CaMn_{1-x}Nb_xO_3$ phases (x = 0, 0.02, 0.05 and 0.08) are analyzed by XPS over a surface area of 10 mm^2. The Nb $3d$ spectra presents an increase of the peak intensities with increasing x, as illustrated in Figure 5.3 a). The binding energies are all assigned to the $3d_{5/2}$ peak at 207.2 eV corresponding to the Nb^{5+} state [Moulder-1995]. Figure 5.3 b) displays the energy shift relative to the Mn $2p_{3/2}$ peak. The $CaMnO_3$ phase presents a maximum at 641.75 eV, which is consistent with the binding energy of the Mn^{4+}

oxidation state [Zampieri-2002]. While increasing the Nb substitution level, a chemical shift toward lower binding energies is observed, e.g. for x = 0.02: Mn 2p $_{3/2}$ = 641.52 eV and for x = 0.08: Mn 2p $_{3/2}$ = 641.45 eV. The XPS analysis confirms the formation of Mn^{3+} in the Mn^{4+} sublattice when substituting Mn by Nb.

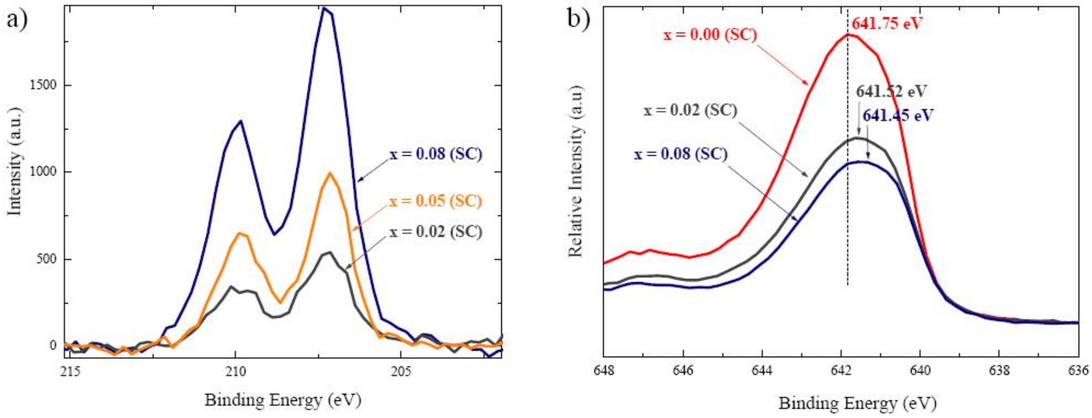

Figure 5.3: XPS spectra of a) Nb $3d_{5/2}$ and b) Mn $2p_{3/2}$ peaks of the $CaMn_{1-x}Nb_xO_3$ (x = 0, 0.02, 0.05 and 0.08) phases synthesized by the SC method.

5.2 Structural and microstructural characterizations at room temperature

Polycrystalline perovskite-type $CaMn_{1-x}Nb_xO_3$ (x = 0.02, 0.05, 0.08) phases are studied concerning their crystal structures and microstructures by combining diffraction, imaging, and spectroscopy techniques. The evolution of the crystal structure with increasing the Nb substitution is evaluated by means of x-ray and neutron powder diffraction (XRPD and NPD). Complex microstructures are characterized by the presence of 90° twinned domains and rock-salt planar defects observed by transmission electron microscopy (TEM) as well as by aberration-corrected scanning transmission electron microscopy (STEM). Furthermore, the combination of dedicated STEM and electron energy loss spectroscopy (EELS) capabilities enables atomic-column analyses at the domain boundaries, which is of main importance to better understand the related thermoelectric properties. This study reports for the first time to our knowledge on the structural, chemical, and electronic features of Ruddlesden-Popper rock-salt layers in potential thermoelectric manganate phases.

5.2.1 Crystal structure determination

The XRPD and NPD data confirm the single phase nature of the synthesised compounds, i.e. the SSR- and the SC-derived phases, as shown in Figures 5.4 a) and b). The reflexions can be indexed in the orthorhombic structure, *Pnma* S.G. with the lattice parameters $a_c\sqrt{2} \times 2a_c \times a_c\sqrt{2}$

($a_c{}^1 \sim 3.74$ Å refers to the lattice parameter of the ideal cubic perovskite structure), corresponding to the $a^+b^-b^-$ type tilting in the Glazer notation. A small amount of $CaMn_2O_4$ (> 2.3%) is occasionally detected as secondary phase in some batches, irrespective of the applied synthesis method. The marokite-type phase $CaMn_2O_4$ crystallizes in the orthorhombic structure (*Pbcm* S.G., N° 57, with $a \approx 3.15$ Å, $b \approx 9.99$ Å, and $c \approx 9.68$ Å [White-2008]).

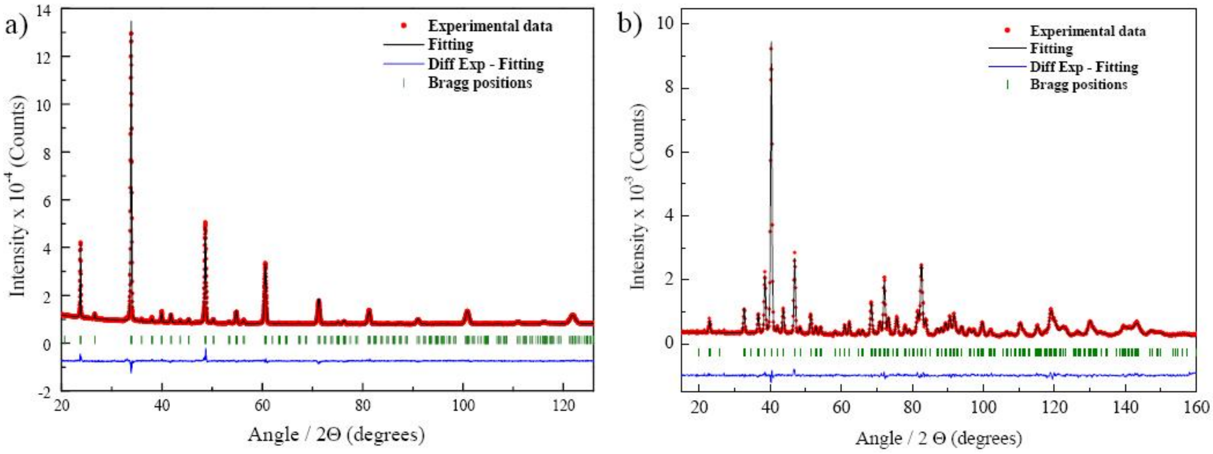

Figure 5.4: Examples of Rietveld refinements from a) the XRPD data of $CaMn_{0.98}Nb_{0.02}O_3$ and b) the NPD data of $CaMn_{0.92}Nb_{0.08}O_3$ recorded at 298 K. (Microstrain parameters were not considered in the present Rietveld refinements.)

Structural refinements were performed using the FULLPROF program [RodriguezCarvajal-1993]. The refined structural parameters, atomic positions and agreement factors from the ND data are summarized in Table 5.2. Figure 5.5 a) shows the evolution of the lattice parameters and the cell volume with increasing the Nb substitution. The following relation is observed: $c < b/\sqrt{2} < a$, indicating an O-type orthorhombic deformation for the $CaMn_{1-x}Nb_xO_3$ phases (with $x \leq 0.08$). The *B*-site Nb substitution causes an increase of the lattice parameters as previously reported [Thao-2003]. This feature is more pronounced in the *a*-*c* basal plane. As a consequence, the orthorhombicity factor a/c gradually increases and the cell volume presents a progressive expansion with increasing the Nb substitution level. Since the substitution of Mn by Nb implies mixed valence phases according to $CaMn^{4+}_{1-2x}Mn^{3+}_xNb^{5+}_xO_3$, the increase of the lattice parameters can be explained by the larger ionic radii of both cations Nb^{5+} and Mn^{3+} in the Mn^{4+} matrix (ionic radii of Mn^{4+}, Mn^{3+} and Nb^{5+} are 0.530 Å, 0.645 Å and 0.740 Å, respectively [Shannon-1976]).

The introduction of Nb at the *B*-site of the $CaMnO_3$ phase influences also the orthorhombic distortion. The changes of Mn-$O_{ap/eq}$ distances, the average bond lengths <Mn-O_{eq}> and <Mn-O_{oct}>, and the distortions angles, i.e. Mn-O_{ap}-Mn and Mn-O_{eq}-Mn, with the Nb extent

---

[1] for convenience, information related to the cubic and orthorhombic crystal structures are labeled with "c" and "o" subscripts, respectively.

Composition		$CaMn_{0.98}Nb_{0.02}O_3$	$CaMn_{0.95}Nb_{0.05}O_3$	$CaMn_{0.92}Nb_{0.08}O_3$
S. G.		*Pnma*	*Pnma*	*Pnma*
a (Å)		5.2902 (1)	5.3031 (2)	5.3194 (2)
b (Å)		7.4693 (1)	7.4842 (2)	7.5041 (3)
c (Å)		5.2762 (1)	5.2866 (2)	5.2975 (2)
V ($Å^3$)		208.48	209.82	211.46
a/c		1.0026	1.0031	1.0041
Ca	x	0.0327 (5)	0.0324 (6)	0.0319 (6)
	y	0.25	0.25	0.25
	z	- 0.0064 (8)	- 0.0073 (10)	- 0.0070 (11)
	Biso ($Å^2$)	0.84 (4)	0.88 (4)	1.03 (4)
	occupancy	0.5	0.5	0.5
Mn / Nb	x	0	0	0
	y	0	0	0
	z	0.5	0.5	0.5
	Biso ($Å^2$)	0.44 (4)	0.57 (4)	0.73(6)
	occupancy	0.490 / 0.010	0.475 / 0.025	0.46 / 0.04
O_{ap}	x	0.4896 (5)	0.4891 (5)	0.4880 (6)
	y	0.25	0.25	0.25
	z	0.0679 (7)	0.0678(6)	0.0660 (7)
	Biso ($Å^2$)	0.66 (7)	0.73(3)	0.96 (4)
	occupancy	0.5	0.5	0.5
O_{eq}	x	0.2866 (4)	0.2873 (3)	0.2880 (4)
	y	0.0337 (2)	0.0333 (3)	0.0342 (3)
	z	0.7129 (4)	0.7127 (3)	0.7132 (4)
	Biso ($Å^2$)	0.70 (4)	0.73 (2)	0.94 (2)
	occupancy	1	1	1
R_{wp}		9.01	9.02	10
R_p		8.44	9.21	9.65
χ^2		1.47	1.78	1.37

Table 5.2: Refined structural parameters, orthorhombicity factor a/c, atomic positions of the $CaMn_{1-x}Nb_xO_3$ series (x = 0.02, 0.05 and 0.08) from NPD data obtained at 298 K. Atoms are located at the following Wyckoff position: Ca: (4c), Mn / Nb: (4b), O_{ap}: (4c) and O_{eq}: (8d).

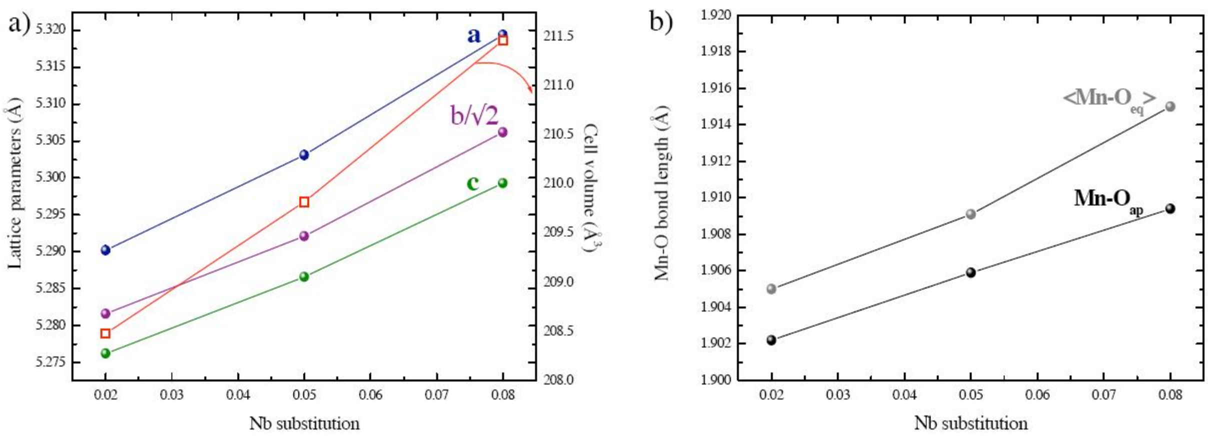

Figure 5.5: a) Lattice parameters, cell volume, b) average <Mn-O_{eq}>, and Mn-O_{ap} bond lengths of the $CaMn_{1-x}Nb_xO_3$ series ($x \leq 0.10$) as function of the Nb substitution, derived from NPD data.

reflect the variations of the orthorhombic distortion. These crystallographic parameters are reported in Table 5.6 along with the Goldsmith tolerance factor. The octahedral distortion is confirmed since the (Mn-O-Mn) buckling bond angles remain fairly smaller than 180°. The (Mn-O-Mn) angles present barely equivalent values for $x \leq 0.05$ and slightly deviated values for $x = 0.08$. The variation of the MnO_6 octahedra distortion is further confirmed by a simultaneous decrease of the tolerance factor and of the octahedral distortion parameter values D with the Nb content. All these findings indicate the enhancement of the octahedral distortion with increasing the Nb concentration in the $CaMn_{1-x}Nb_xO_3$ series. This effect becomes more pronounced with $x > 0.05$. The corresponding data previously reported for the $CaMnO_3$ phase agree with the general tendency that decreasing the Nb substitution level favors the octahedral distortion [Poeppelmeier-1982b, MeloJorge-2005]. Furthermore, a continuous expansion of the Mn-O bond lengths is observed with increasing the Nb content, as illustrated in Figure 5.5 b), resulting in an increase of the MnO_6 octahedra size. This trend is underlined along the a-c basal plane since the <Mn-O_{eq}> bond lengths increase more rapidly than the apical ones, i.e. Mn-O_{ap}, with increasing the Nb content. This finding results from the elongation of the MnO_6 octahedra along the equatorial plane [MeloJorge-2005] due to Jahn Teller distortion. For instance, the Nb substitution in the Mn sublattice generates Jahn-Teller Mn^{3+} cations in the Mn^{4+} matrix.

Hence, the evolution of the crystal structure depends on the Nb content which yields further changes in the electronic band structure and in the microstructure. The deviations of the (Mn-O-Mn) bond angle θ from 180° and therefore the orthorhombic distortion variation modify the Mn d bandwidth characterized by the integral hopping W, since $W \propto cos\ \theta$ [Tsuda-2000]. A larger deviation of the Mn-O-Mn angle from 180° implies a smaller overlap of the O $2p$ and the Mn $3d$ orbitals. This results in a narrowing of the d band and therefore influences on the electronic properties of the perovskites, as later reported in this Chapter, Section 5.3.1. In addition, the microstructure of the orthorhombic phases is significantly affected by both, the lattice variations and the structural distortions, as further discussed in this Chapter, Section 5.2.2.1.

Composition	$CaMnO_3$[§]	$CaMn_{0.98}Nb_{0.02}O_3$	$CaMn_{0.95}Nb_{0.05}O_3$	$CaMn_{0.92}Nb_{0.08}O_3$
t*	1.0004	1.0005	0.99549	0.99052
Mn-O_{ap} x 2 (Å)	1.899 (1)	1.9022 (7)	1.9059 (6)	1.9094 (7)
Mn-O_{eq1} x 2 (Å)	1.9070 (2)	1.9040 (2)	1.9099 (16)	1.9210 (2)
Mn-O_{eq2} x 2 (Å)	1.896 (2)	1.9060 (2)	1.9082 (16)	1.9090 (2)
$\langle$ Mn-O_{eq} $\rangle$ (Å)	1.9020	1.9050	1.9091	1.9150
$\langle$ Mn-$O_{(oct)}$ $\rangle$ (Å)	1.9010	1.9004	1.9008	1.9131
D**	0.9980	0.9985	0.9983	0.9970
Mn-O_{ap}-Mn (°)	154.04	158.03 (3)	158.04 (3)	158.54 (3)
Mn-O_{eq}-Mn (°)	157.44	157.41 (9)	157.38 (7)	157.09 (9)

Table 5.3: Tolerance t factor, bond distances, D values and distortion angles of the $CaMn_{1-x}Nb_xO_3$ series (x = 0.02, 0.05 and 0.08) from NPD data. * The Goldsmith tolerance factor: t for the perovskite structure ABO_3 is defined by $t \approx (r_A + r_O)/\sqrt{2}(r_B + r_O)$. ** D = Mn-O_{apical}/<Mn-$O_{equatorial}$>. § Data of the $CaMnO_3$ phase from [MeloJorge-2005].

5.2.2 Microstructure analysis

The XRPD and NPD investigations of the $CaMn_{1-x}Nb_xO_3$ phases yield a general overview of the crystal structure and its evolution with respect to the Nb substitution. TEM studies allow to give in addition a better insight of the local microstructure. Several SC-derived crystallites of typically 200 - 300 nm in length are investigated by means of high-resolution TEM (HRTEM) images and experimental electron diffraction (ED) patterns.

A first example is given in Figure 5.6 a), where the HRTEM image of $CaMn_{0.98}Nb_{0.02}O_3$ phase reveals lattice fringes with characteristic interplanar distances of $d(110)_o \sim 3.72$Å, i.e. the lattice parameter of the cubic perovskite structure. In Figure 5.6 b), the corresponding ED pattern fits well with the orthorhombic extinctions, as concluded from the Rietveld refinements. The analysis of the HRTEM and ED data confirms the long-range ordered and crystalline nature of the studied material.

5.2.2.1 Twins in orthorhombic phases

Twins are commonly observed in distorted perovskite structures [Wang-2006]. In the present study, the orthorhombic $CaMn_{1-x}Nb_xO_3$ phases exhibit complex microstructures with the coexistence of twinned domains. Figure 5.7 a) illustrates the presence of nano-sized twinned domains ranging from 2 to 10 nm in length which are observed in the $CaMn_{0.98}Nb_{0.02}O_3$ phase. The experimental ED pattern, shown in Figure 5.7 b), can be considered as the superposition of two orthorhombic zone axes: $[101]_o$ and $[-101]_o$, rotated at 90° from each other. The ED pattern

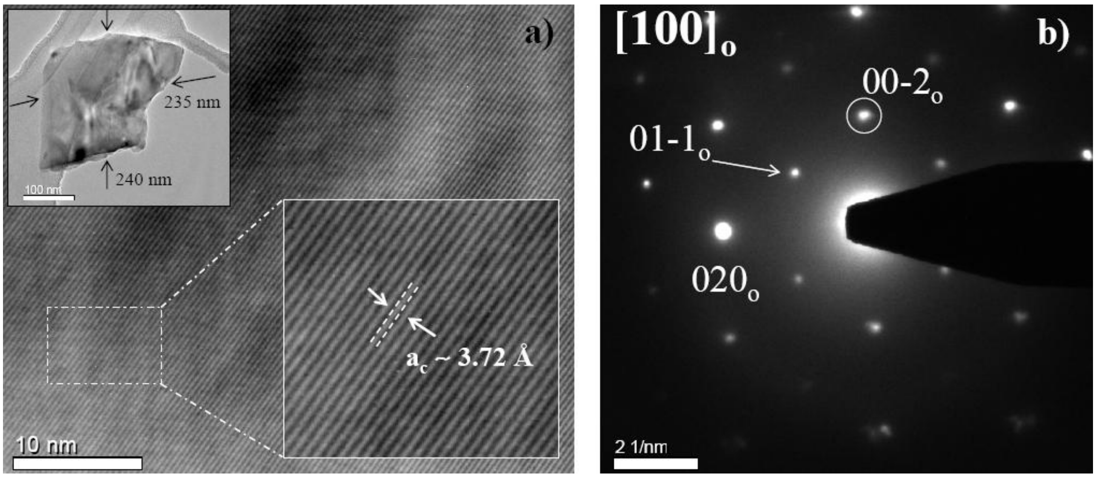

Figure 5.6: a) HRTEM and b) ED of the $CaMn_{0.98}Nb_{0.02}O_3$ phase (synthesized by the SC method) in the $[100]_o$ zone axis. The inset in Figure a) presents a low resolution TEM image of the studied crystallite.

can be indexed with a nearly cubic $2a_c \times 2a_c \times 2a_c$ lattice but does not obey cubic symmetry relations. Forbidden reflections in orthorhombic, i.e. $(0kl)$ with $k+l = 2n+1$, have emerged as indicated by blue and green rings. ED patterns of each domain area are calculated by Digital Micrograph 3.8.2 Gatan software in fast Fourier transform (FFT) mode. The FFTs of the A_1 and B_1 domains are given in the inset of Figure 5.7 a). The FFT of B_1 domain is almost identical to the one of A_1 domain, except that the $(0k0)$ row of reflections has rotated clockwise about the normal to (101) by 90° (on the ED pattern, the blue rings become the green ones). The presence of an additional set of (forbidden) diffraction spots facilitates the identification of the twin orientations, as illustrated in Figure 5.7 c). This finding indicates that moving from A_1 to B_1 across the domain boundary is similar as rotating the orthorhombic unit cell by 90° respect to $[010]_o$, defined by $[010]_{90^\circ}$. This phenomenon is commonly described as rotation twins across $\{101\}_o$ [Wang-2006].

A second example of 90° twinned domains is observed in the $CaMn_{0.95}Nb_{0.05}O_3$ phase, as illustrated in Figures 5.8. The size of the twins varies from 50 to 100 nm in length, which is one order of magnitude larger than those observed in the precedent case. However, no relationship between the size of twins and the Nb substitution extent can be evidenced. Calculated FFTs of each domain, i.e. A_2, B_2 and C_2, are given in the inset of Figure 5.8 a). The FFTs from A_2 and B_2 regions correspond to domains oriented along two perpendicular $\widehat{b}$ axis orientations, i.e. $[\text{-}101]_o$ and $[0\text{-}10]_o$. The FFT in the region C_2 indicates the superposition of the twinned domains A_2 and B_2. The magnified image in Figure 5.8 b) highlights the orientation of twinned domains, where the $\widehat{b}$ axis is either oriented in the plane, i.e. area A_2, or out of the plane, i.e. area B_2. Moreover, no defect or dislocation is observed at the twin boundary, indicating a perfect matching of the twinned domains during their formation process.

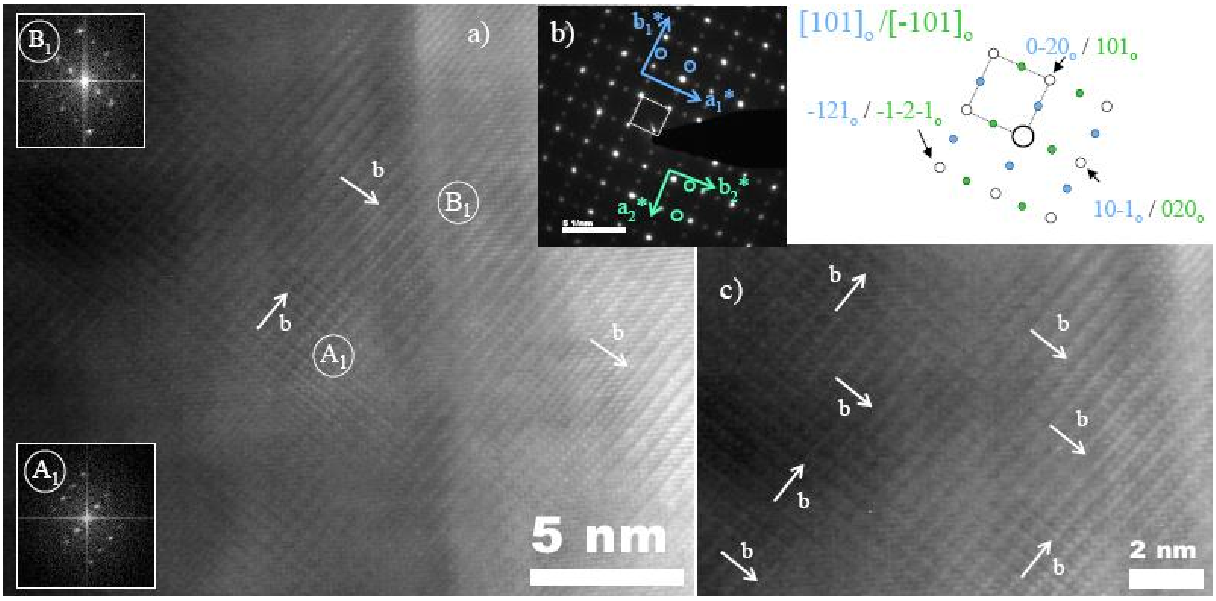

Figure 5.7: a) HRTEM, b) ED pattern of the $CaMn_{0.98}Nb_{0.02}O_3$ phase (synthesized by the SC method), and c) magnified view of the nano-sized twinned domains where the $\widehat{b}$ axis is oriented along the two perpendicular directions in the plane. The inset figures in Figure a) present the fast Fourier transform (FFT) of the domains A_1 and B_1. A schematic interpretation of the experimental ED pattern is reported on top right.

Twinning phenomena can arise upon structural transitions, crystal growth or plastic deformation. For instance, structural transitions involving a change in space group symmetry generate twinned domains or anti-phase boundaries [Nord-1994]. For example, orthorhombic perovskite-type phases, e.g. $CaTiO_3$ (*Pbnm* S.G.), undergo transitions to the cubic phase (*Pm-3m* S.G.) upon heating. The presence of 90° rotation twins about $[001]_o$ and reflections twins on $\{110\}_o$ and $\{112\}_o$ characterised the $CaTiO_3$ phase at room temperature [Wang-1993]. In the studied phases, the $[010]_{90^\circ}$-type rotation corresponds to twins induced by the loss of fourfold rotation axes upon phase transition [Wang-2006]. The $CaMn_{1-x}Nb_xO_3$ phases present a structural transition from cubic to orthorhombic symmetry upon cooling. This issue is later discussed in this Chapter, Section 5.4.2. As a result, twinned domains can coherently growth on each other, yielding a specific microstructure as already observed. The formation of twins is explained by the combination of two structural factors. The distorted orthorhombic crystal structure presents lattice parameters which deviate slightly from the cubic ones i.e. $a_c\sqrt{2} \times 2a_c \times a_c\sqrt{2}$ in the orthorhombic framework [Mitchell-2002], as reported in Table 5.2. This aspect favors the formation of twins. However, the coexistence of twinned domains is directly correlated to the magnitude of the octahedra tilt angle φ around $[111]_c$ for which an upper limit φ_{lim} exists where twins are not observed [Vegas-1986]. In LnCoO$_3$ perovskite-type phases, the $DyCo_{0.95}Ni_{0.05}O_3$ phase does not reveal twins and presents a $\varphi = 18.78^o$ while the $PrCo_{0.95}Ni_{0.05}O_3$ compound exhibits a twinned microstructure with a $\varphi = 10.14^o$ [Aguirre-2007]. Likewise, in rare-earth orthoferrites LnFeO$_3$, the proportion of twinned domains is related to the octahedra rotation angle resulting to an upper limit of $\varphi_{lim} = 17.2^o$ [Marezio-1970]. The octahedra tilt angle φ can be determined from the structural parameters following the O'Keefe expressions [OKeefe-1977]. For the O$_{(equatorial)}$ located at the Wyckoff position (8d), the atomic position y is defined by: $y = -(\tan\varphi)/\sqrt{48}$, resulting in φ values comprised between $12.99^o \leq \varphi \leq 13.33^o$ for the CaMn$_{1-x}$Nb$_x$O$_3$ phases with $0.02 \leq$ x ≤ 0.08. This finding corroborates the presence of twinned domains shown in Figures 5.7 and 5.8. The combination of close lattice parameters, i.e. $a_o \simeq c_o$ and a low octahedra tilt angle φ is a prerequisite for the formation of twins in orthorhombic crystal structures [Aguirre-2003].

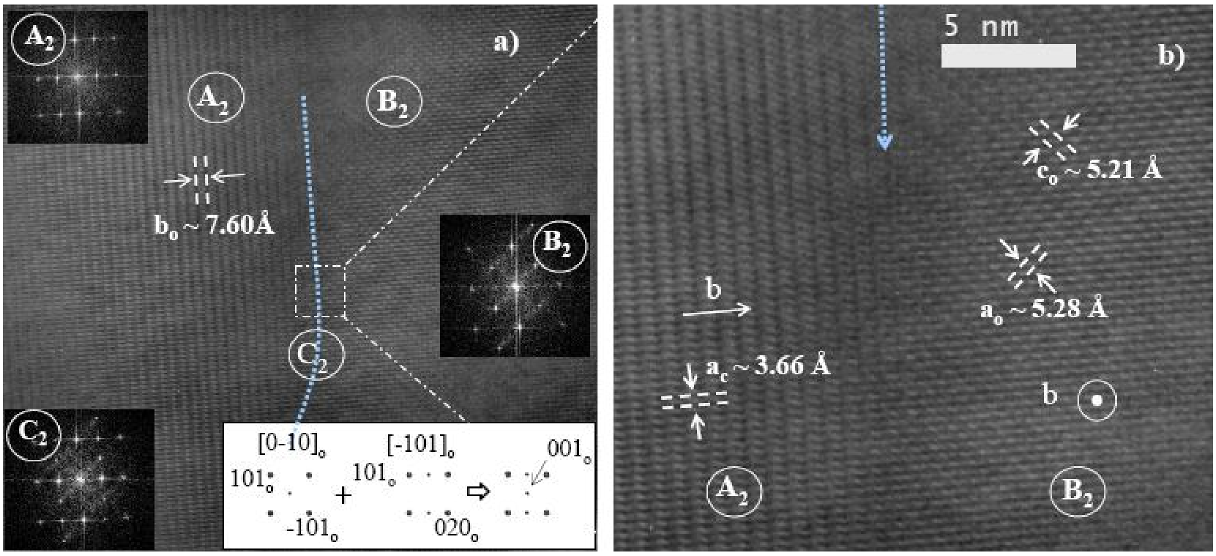

Figure 5.8: a) HRTEM image of 90° twinned domains in CaMn$_{0.95}$Nb$_{0.05}$O$_3$ (synthesized by the SC method) in the [101]$_o$ zone axis and b) Detail of the border area between the two domains A$_2$ and B$_2$. Dotted arrows indicate the domain boundary. The inset figures present the FFTs of the twinned domain A$_2$ and B$_2$ and the superposition of both in region C$_2$. A schematic interpretation of the experimental ED pattern is given in Figure a).

The presence of rotation twins in the CaMn$_{1-x}$Nb$_x$O$_3$ phases triggers off the question whether Nb segregations could exist at the domain boundary. This issue is of main importance considering the potential influence of segregations on the thermoelectric properties of the studied materials. The microstructure of the twin boundary is studied by high-resolution STEM technique in an aberration-corrected instrument, i.e. the NION 100 SuperSTEM. One main advantage of a dedicated STEM is that a variety of detectors can be applied simultaneously, as earlier described in the Chapter 3, Section 3.2.2. For instance, it is possible to record simultaneously both low- and high-angle scattered electrons, as well as those on axis, which can be used to form a bright field (BF) image. The main advantage of STEM compared to conventional electron microscopes is its high compositional sensitivity giving rise to Z-contrast images. Such image is formed by collecting the electrons scattered out to high angles on a high-angle annular dark field (HAADF) detector. Since high Z atoms scatter to higher angles more strongly than lighter atoms, the intensity of a Z-contrast image varies approximately as Z^2 [Williams-1996d]. Recent developments resulted in a new generation of analytical STEMs with aberration corrections yielding a sub-Angstrom spatial resolution [Bleloch-2004].

In the present study, investigations on the polycrystalline $CaMn_{0.92}Nb_{0.08}O_3$ phase were performed on the aberration-corrected NION 100 SuperSTEM. As an example, the Figure 5.9 a) presents a HAADF image of the perovskite lattice along the $[101]_o$ direction. The HAADF image reveals an atomic-resolved resolution allowing the distinction of atomic columns with contrast differences. For the studied phases, B-site columns (Mn, Nb) are observed as bright spots, A-site column (Ca) as relatively dark spots corresponding to weaker intensities compared to the B-site atoms, and oxygen columns are not visible. The structural model of the orthorhombic manganates is presented in Figure 5.9 b) as correspondence.

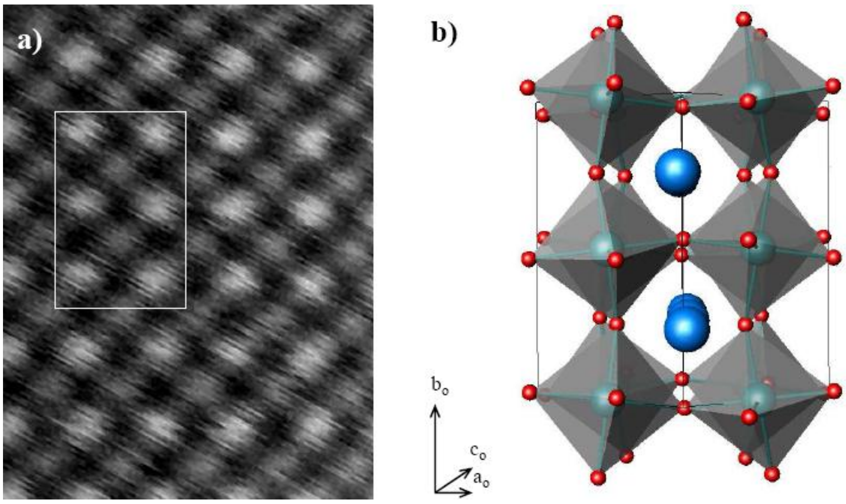

Figure 5.9: a) Example of a high-resolution HAADF image recorded along the $[101]_o$ direction in the $CaMn_{0.92}Nb_{0.08}O_3$ phase. The white rectangle area represents the atomic sequences shown in Figure b). b) Structural model of orthorhombic manganate, $CaMn_{0.92}Nb_{0.08}O_3$. Blue spheres correspond to A-sites (Ca), green spheres to B-sites (Mn, Nb), and red spheres to oxygen. The structural model is designed by ATOMS software.

The rotation twin boundaries are analyzed by STEM technique recording simultaneously BF and HAADF images, as presented in Figures 5.10. The high-resolution BF image, in Figure 5.10 a), illustrates the coexistence of 90° twinned domains, i.e. the A_3 and B_3 regions. The high-spatial resolution achieved in the BF image emphasizes a defined twin boundary which is characterized by a stair-like profile, as indicated by a blue dotted arrow. Calculated FFTs of each domains are given in Figures 5.10 c) and d). The FFTs of the A_3 and B_3 areas can be indexed along the $[-101]_o$ and $[101]_o$ zone axes, that means the $\widehat{b}$ axes are both oriented in the plane but at 90°

from each other. The corresponding HAADF image is presented in Figure 5.10 b) and reveals an homogeneous contrast distribution. Figures 5.10 e) and f) exhibit magnified views of the BF and HAADF images along the twinned domain boundary, respectively. The uniform nature of atomic sequences is confirmed by the Z-contrast image over the studied area. No evidence of Nb segregation by means of contrast changes is observed at the vicinity of the domain boundary. Therefore, the perovskite sequence remains intact at the domain boundary vicinity despite the microstructural intergrowth induced by the twinning phenomenon.

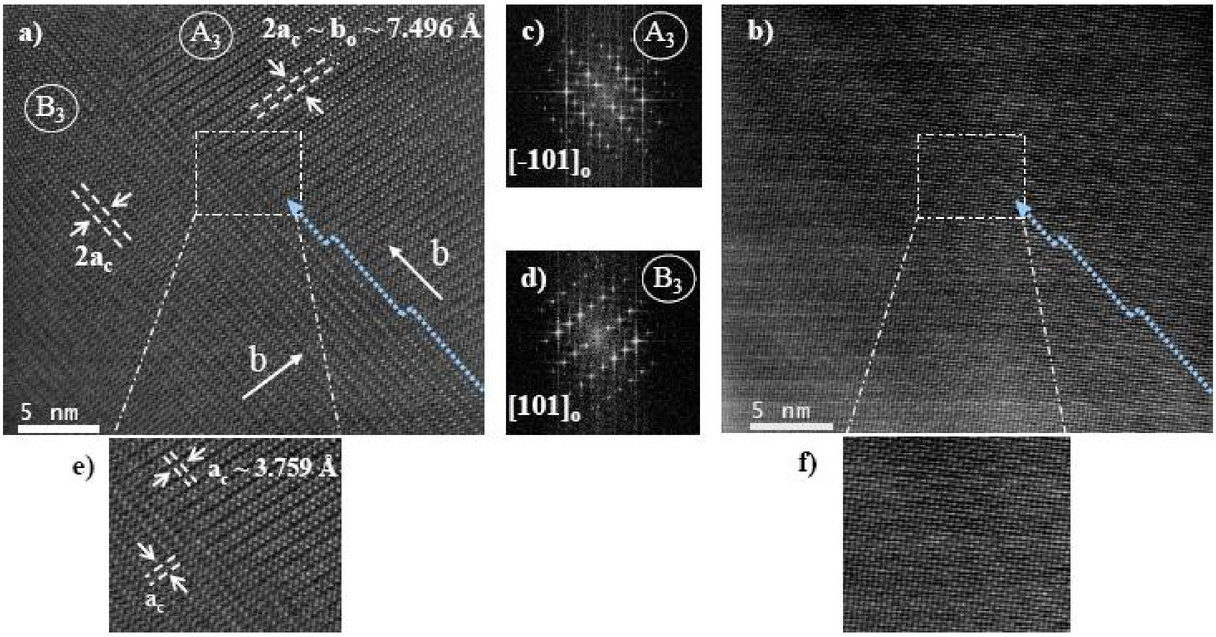

Figure 5.10: a) HRSTEM BF and b) HAADF or Z-contrast images of the $CaMn_{0.92}Nb_{0.08}O_3$ phase (synthesized by the SC method) with the presence of 90° twinned domains, i.e. A_3 and B_3 regions. Dotted blue arrows indicate the domain boundaries forming a stair-like geometry. c) and d) FFTs of the domains B_3 and A_3, respectively. e) and f) Magnified views along the twinned domain boundary of the bright field and the Z-contrast images, respectively.

5.2.2.2 Anti-phase boundary rock-salt layers

A second microstructural feature is observed in the SC-derived $CaMn_{1-x}Nb_xO_3$ phases. The Figure 5.11 a) presents a complex microstructure with the presence of several domain boundaries, assigned as A_4-B_4, B_4-D_4, and A_4-C_4, and evidenced by dotted or dashed arrows. The A_4-B_4 domain boundary is highlighted in Figure 5.11 b) and the corresponding FFTs are given in the inset Figure 5.11 a). The presence of 90° twinned domains is confirmed between the A_4 and the B_4 areas since the $\widehat{b}$ axis is either oriented out of the plane (A_4) or in the plane (B_4). Between the B_4-D_4 regions, the characteristic features of twinned domains are not observed, as presented in Figure 5.11 c). In both domains, the $\widehat{b}$ axis is oriented in the same direction and the lattice fringes present similar values ($b \sim 7.4$ Å). Contrast differences which should emerge between twinned domains, are not observed between both regions. However, the B_4-D_4 defect boundary appears clearly with unusual interdistance equivalent to twice the b-axis length. This domain boundary between the B_4-D_4 regions might be due to a single planar fault involving anti-phase boundaries that can be regarded as a Ruddlesden-Popper intergrowth [Mather-2008]. Ruddlesdsen-Popper series are well-known as layered perovskite-type structure $A_{n+1}B_nO_{3n+1}$ with n the number of AO layers [Mitchell-2002]. Thus, layer perovskite-type manganate phases such as CaO[$(CaMn_{1-x}Nb_xO_3)_n$] could be a planar defect structure localized between the B_4-D_4 regions. This assumption indicates that the main phase is slightly Ca-rich phase. The counterpart Mn-rich phase therefore might be the secondary phase, i.e. $CaMn_2O_4$, revealed in small quantity by Rietveld refinements. The A_4-C_4 domain boundary results certainly from similar planar faults.

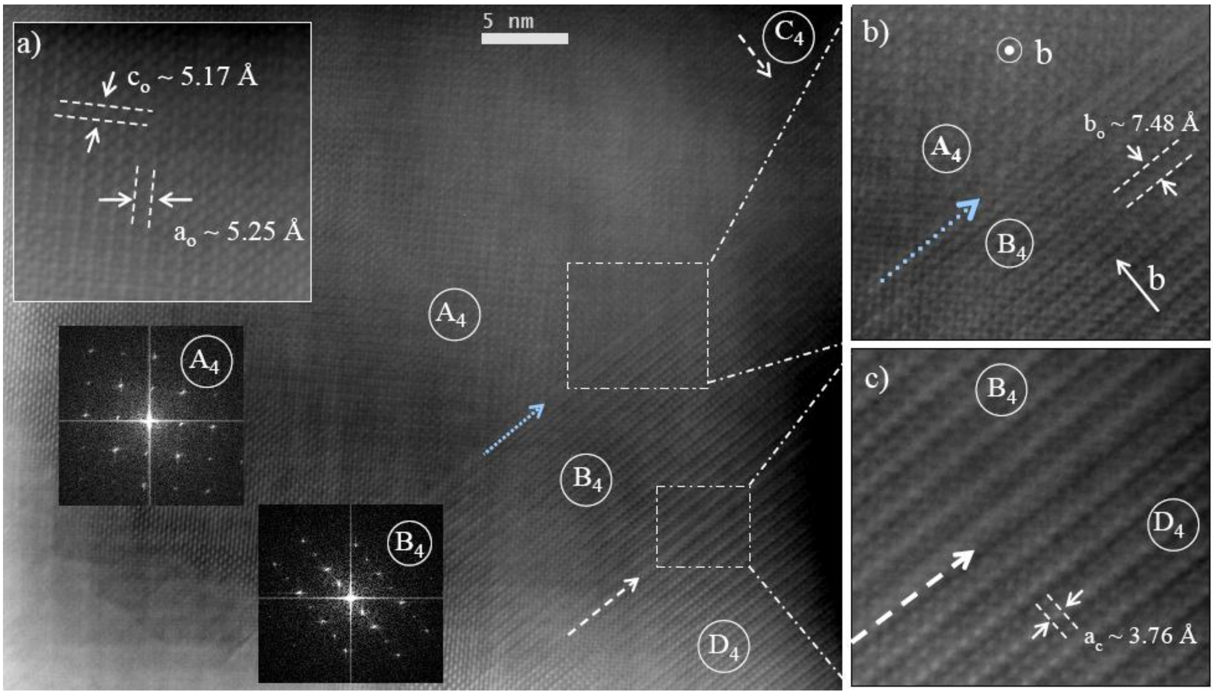

Figure 5.11: a), b) and c) HRTEM images of the $CaMn_{0.98}Nb_{0.02}O_3$ phase (synthesized by the SC method) along a twinned domain boundary. Highlight of a) the A_4 domain, b) and c) the boundary separating the domains A_4 and B_4 and the domains B_4 and D_4, respectively. The inset figures present the FFTs of the domains A_4 and B_4. Dotted arrows indicate the twinned domain boundaries and dashed arrows point out the planar faults.

In analogy to the rotation twins, the planar faults are studied by means of high-resolution STEM technique. Besides, elemental and chemical analysis, i.e. valence state and atomic coordination, can be investigated at the same spatial resolution by EELS analyses.

Figures 5.12 reveal a complex microstructure by combining (i) the presence of 90° twinned

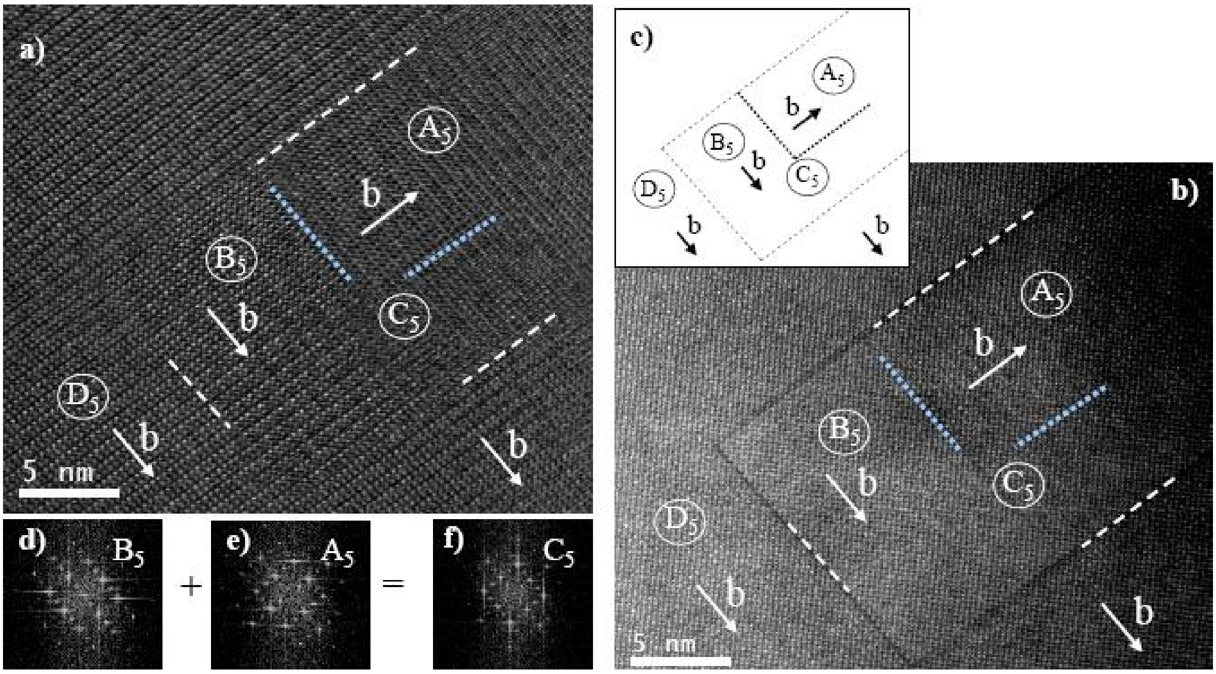

Figure 5.12: a) HRSTEM BF and b) HAADF images of the $CaMn_{0.92}Nb_{0.08}O_3$ phase (synthesized by the SC method) of a complex microstructural area comprising twinned domains (A_5 and B_5 regions) and planar faults. c) Schematic representation of the studied area where twinned domain boundaries are marked by dotted lines and planar faults by dashed lines. d), e) and f) FFTs of the B_5, A_5, and C_5 regions, respectively.

domains, i.e. A_5 and B_5 regions, which is observed in the BF image (Figure 5.12 a), and (ii) the existence of planar faults delimiting e.g. the B_5 and D_5 regions, which is evidenced in the Z-contrast image (Figure 5.12 b). A general overview of this microstructural feature is given in a schematic representation in Figure 5.12 c). The FFTs of the B_5 and A_5 domains, presented in Figure 5.12 d) and e), confirm the twin orientations in perpendicular directions. The FFT recorded in the C_5 region can be regarded as the superposition of the two previous mentioned FFTs, indicating that the C_5 region is situated at the twin boundary. Imaging simultaneously both the BF and the HAADF images is of main importance in the present case, since it reveals essential complementary information, i.e. (i) structural modifications induced by twinning phenomenon in BF mode and (ii) chemical inhomogeneity along planar faults in HAADF mode.

A high-resolution Z-contrast image along a vertical planar fault is presented in Figure 5.13 a) and magnified in Figure 5.13 b). The summed spectrum of the analyzed area is reported in Figure 5.13 c). The core-loss edges of Ca-$L_{2,3}$, O-K, and Mn-$L_{2,3}$ are observed at 347 eV, 530 eV, and 644 eV, respectively. The core-loss edge of Nb-$M_{2,3}$ at 362 eV could not be evidenced on the EEL spectrum since the extended energy loss region of the Ca-$L_{2,3}$ edge overlapped this energy loss range. A prior signal is recorded at 280 eV and can be assigned to the carbon edge arising from the carbon film. The signals of interest are recorded by positioning the electron beam at the planar fault and scanning across it. After background substraction, the intensities of the edges are further integrated and normalized. Figure 5.13 d) shows the profile of the Ca (blue line) and Mn (green line) atoms along the $[100]_c$ zone axis, starting along a Mn-based column as indicated by the white arrow, and crossing the planar fault over a 1 nm length, i.e. in the red rectangle area. First, the brightest contrast in the HAADF image reveals the highest Mn-counts in the EELS profile, confirming the initial position on a Mn-based column. When approaching the planar fault, the Mn concentration starts to decrease until reaching a minimum at the right side of the planar fault. Meanwhile, the Ca concentration increases gradually while crossing the planar fault. Above the planar fault, the Mn signal increases again without attaining the initial concentration while the Ca profile reveals a slightly higher concentration compared to the initial position. The planar fault is characterized by a lower contrast level than that one observed between the Mn columns in the homogeneous perovskite lattice, as previously shown in Figure 5.9 a). This finding coincides with the absence of an expected Mn atom and the fact that the separation between two Ca atoms is fairly narrow. All these observations yield the conclusion that the Mn atomic plane, i.e. the B-site plane, is substituted by a Ca atomic plane, i.e. the A-type atoms. The AO additional plane is then laterally shifted by 1/2 {100} in the cubic lattice, forming an anti-phase boundary. Structurally, this change corresponds to the substitution of an AO atomic plane in the $\{100\}_c$ perovskite sequence by half AO rock-salt unit cell. Thus, the atomic plane stacking sequence across the planar fault consists of MnO-CaO-MnO-CaO-CaO-MnO-CaO... When repeated, this new sequence forms the Ruddlesden-Popper phases

[Ruddlesden-1958]. Hence, the rock salt layers can be imaged in Z-contrast mode since a global reduction of the brightness arises from the presence of the CaO rock-salt layers. For instance, the contrast emerging from the extra Ca atomic planes is not further improved in the HAADF image since the Ca has lower atomic number than Mn. As a result, such dark lines are observed in Z-contrast images like in Figure 5.12 b). Slight oxygen excesses have been previously determined by TGA experiments in the $CaMn_{1-x}Nb_xO_{3+\delta}$ phases, i.e. $\delta \leq 0.09$, which confirmed the presence of CaO rock salt layers in the studied phase. This type of anti-phase boundary Ca-rich rock-salt layers has been earlier reported in the $La_{0.6}Ca_{0.4}CoO_3$ thin film [Bangert-2006].

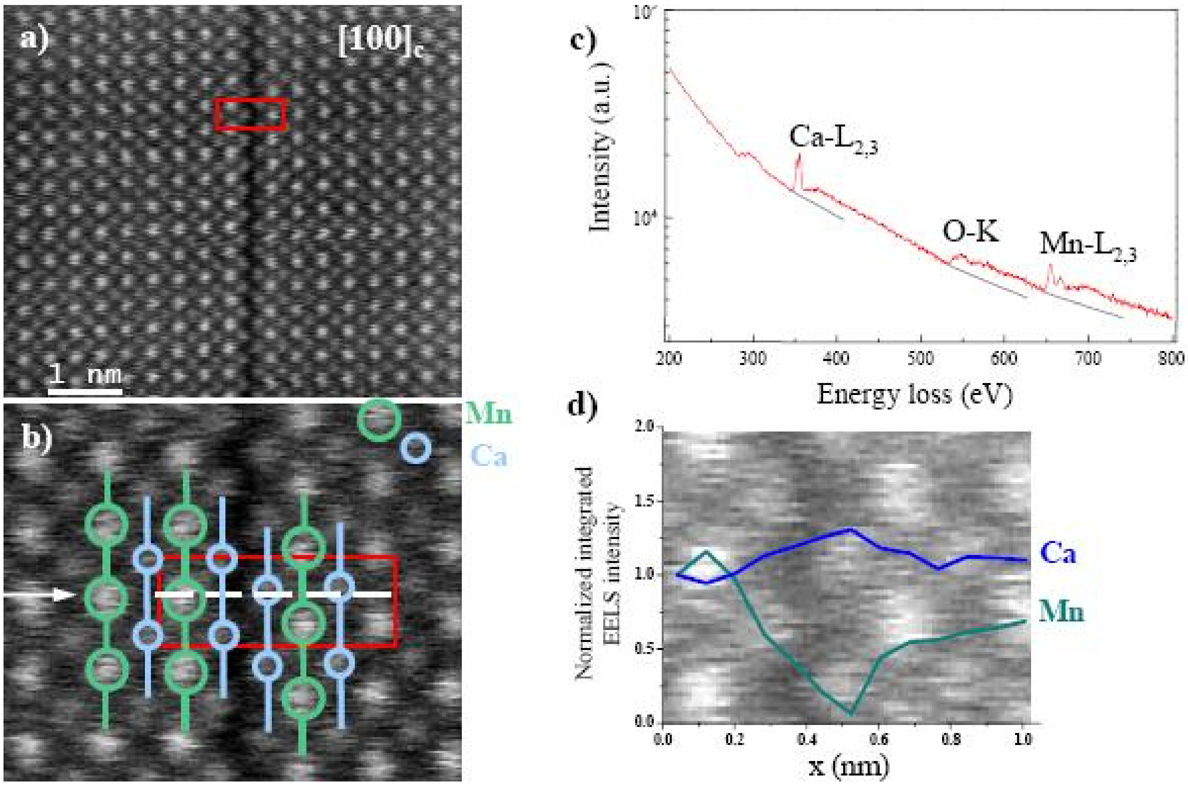

Figure 5.13: High-resolution Z-contrast images of the $CaMn_{0.92}Nb_{0.08}O_3$ phase (synthesized by the SC method) along a vertical planar fault: a) general and b) magnified view. c) EEL spectrum acquired from the red rectangular area. d) Normalized integrated EELS intensity when scanning the electron beam across the planar fault, i.e. along the $[100]_c$ zone axis, and following the direction indicated by the white dashed line (Figure b). In Figure b): the atomic plane stacking sequence across the planar fault corresponds to MnO (green) -CaO (blue) MnO-CaO-CaO-MnO-CaO. In Figure c): the core-loss intensities of the Ca-$L_{2,3}$ and the Mn-$L_{2,3}$ edges are analyzed for determining their respective core-loss elemental profiles (Figure d). In Figure d): the image in the background is just intended to guide the eye with the scale.

EELS is a powerful tool for analyzing in a great detail the structure and electronic properties of transition metal oxides at the atomic scale [Varela-2005]. It can probe the occupancy of the outer d-states of the transition metals M with atomic resolution. The white lines at the onsets of the L_3 and L_2, i.e. absorption edges, of transition metals are a characteristic signature of electronic transitions from the $2p_{1/2}$ and $2p_{3/2}$ M core states to unoccupied d-like states near the Fermi level [Kurata-1993]. For instance in manganate phases, the ratio of the intensity of the L_3 peak to the L_2 peak, i.e. the $L_{2,3}$ ratio, increases as the formal Mn oxidation numbers decreases. In the case of Mn atoms with +3 and +4 formal oxidation states, the $L_{2,3}$ ratio value is equal to $L_{2,3} = 2.7$ for Mn^{3+} and $L_{2,3} = 2.1$ for Mn^{4+} [Kurata-1993].

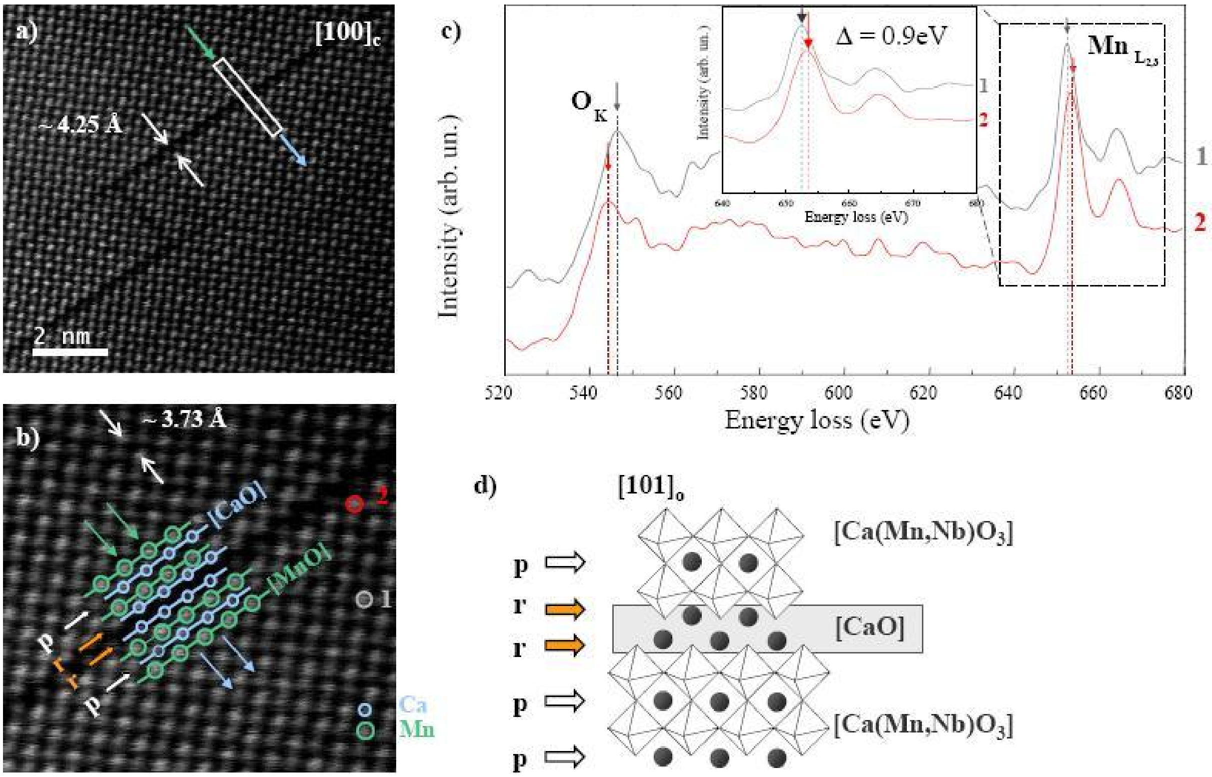

Figure 5.14: High-resolution Z-contrast images of the $CaMn_{0.92}Nb_{0.08}O_3$ phase (synthesized by the SC method) over a planar fault: a) general and b) magnified view. c) EELS spectra extracted from individual Mn columns located on (2) and out off (1) the fault, as indicated in Figure b). The oxygen-K edge and the Mn-$L_{2,3}$ edge are presented. d) Structural model of the anti-phase boundary where one-single CaO rock-salt planar layer is inserted into $Ca(Mn,Nb)O_3$ perovskite layers. The MnO_6 octahedra are shown as polyhedra and the Ca^{2+} ions as spheres. There are two different crystallographic A-sites, i.e. the perovskite block (white arrows labelled "p") and the rock-salt layer (orange arrow labelled "r").

Since the Nb substitution in the $CaMnO_3$ phase induces the creation of Mn^{3+} species in the Mn^{4+} matrix in the perovskite lattice, the evolution of the Mn valence state at the vicinity of the anti-phase boundary is of main interest. Hence, the O-K edge and Mn-$L_{2,3}$ are recorded by pinpointing the electron beam on a single-Mn atomic column situated either in the perovskite lattice (named Mn-type I) or nearby the rock-salt layer (called Mn-type II), as indicated in Figure 5.14 b). Probing the electronic nature of the atoms, atomic column by atomic column should be, however, carefully considered since the detected EEL signal represents electrons which have also interacted through the thin specimen, i.e. through several monolayers of atoms, along the atomic columns. The EEL spectra for the two different Mn-types are given in Figure 5.14 c). The Mn-$L_{2,3}$ signal analysis allows only a qualitative comparison of the Mn electronic properties in the $CaMn_{1-x}Nb_xO_3$ and in the $CaO[(CaMn_{1-x}Nb_xO_3)_n]$ phases. The Mn-L_3 signal undergoes essentially one change since its maximum peak shifts by 0.9 eV towards higher energy losses when going from the Mn-type I to the Mn-type II. This result indicates qualitatively that Mn atoms nearby the rock-salt layers possess higher Mn^{4+} concentration than those located in the perovskite lattice [Maurice-2006]. Furthermore, both Mn-types yield different $L_{2,3}$ ratio values, i.e. $L_{2,3} = 2.04$ for Mn-type I and $L_{2,3} = 2.00$ for Mn-type II. These values are fairly close to the $L_{2,3}$ ratio for Mn^{4+} cations but a little lower than expected [Varela-2005]. The comparison of these experimental $L_{2,3}$ ratio values confirms that the Mn atoms in the perovskite lattice (Mn-type I) present higher Mn^{3+}/Mn^{4+} concentration, i.e. larger electron-doping, than the Mn atoms situated close to the rock-salt layers (Mn-type II). The evolution of the Mn valence state has been previously investigated for studying charge ordering in manganate phases with large cationic substitutions [Varela-2005]. Moreover, the small chemical shift of the O-K edge towards the lower energy losses passing from Mn-type I to Mn-type II corroborates this interpretation [Kurata-1993]. The formation of the anti-phase boundary into the $CaMn_{0.92}Nb_{0.08}O_3$ perovskite lattice yields modifications at the nanoscale of the crystal structure, the microstructure, and the related electronic properties. This can further influence the electrical and thermal transport properties at the macroscopic level.

5.3 Thermoelectric properties

Polycrystalline perovskite-type $CaMn_{1-x}Nb_xO_{3\pm\delta}$ (x = 0.02, 0.05, 0.08) phases are further evaluated concerning their potential thermoelectric properties. Seebeck coefficient, electrical and thermal conductivities are determined over a broad temperature range under air atmosphere. The electrical resistivity $\rho(\mathrm{T})$ and the thermopower $S(\mathrm{T})$ curves of the $CaMn_{1-x}Nb_xO_{3\pm\delta}$ phases reveal changes gradually with the temperature, as illustrated in Figure 5.15 with the $CaMn_{0.95}Nb_{0.05}O_3$ phase reported as an example. For instance, $\rho(\mathrm{T})$ varies progressively from a thermally activated to a temperature independent conduction regime. The $CaMn_{1-x}Nb_xO_3$ phases present a transition at $\mathrm{T} \simeq 115$ K from a semiconducting-like behavior with $d\rho/d\mathrm{T} < 0$ and $S(T) \sim 1/T$ to a metallic-type conduction with $d\rho/d\mathrm{T} > 0$ and $S(T) \sim T$. At higher temperatures, i.e. $\mathrm{T} > 1100$ K, the evolution of the $S(\mathrm{T})$ and $\rho(\mathrm{T})$ is modified revealing a breakdown of the conduction regime.

Three different temperature ranges are observed with respect to their thermoelectric properties. In the present section, the electron-doped manganate phases are first studied concerning the middle temperature region, i.e. $300\ \mathrm{K} < \mathrm{T} < 1100\ \mathrm{K}$. Since oxide materials are evaluated concerning their high-temperature thermoelectric applications, this temperature range is of main

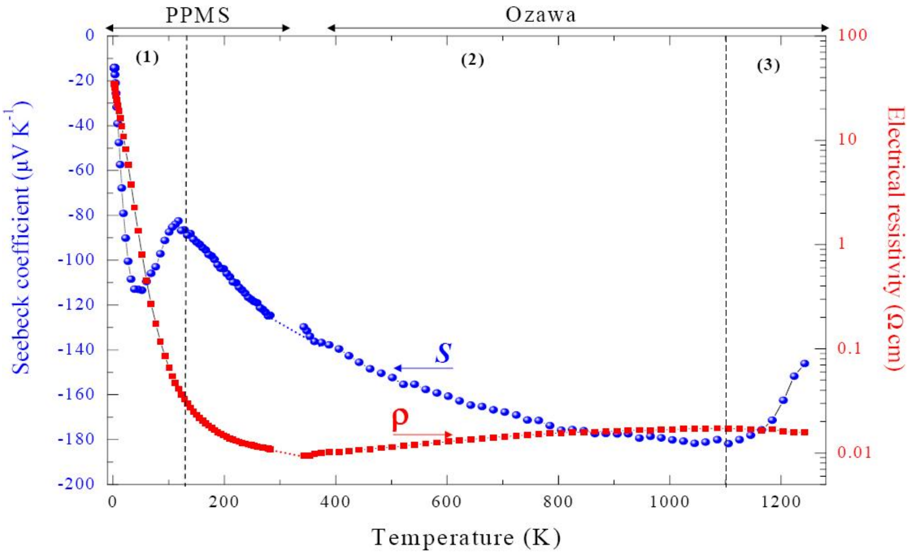

Figure 5.15: Seebeck coefficient and electrical resistivity versus T for the $CaMn_{0.95}Nb_{0.05}O_3$ phase.

interest. The extreme temperature regions of (1) T < 300K and (3) T > 1100 K, are investigated in the next section. A particular attention is given on the influence of (1) the low-temperature magnetic transition and of (3) the structural transition and the thermal reduction occurring at high temperatures.

5.3.1 Electrical resistivity and thermopower

Figure 5.16 a) displays the electrical resistivity within the temperature range of 320 K < T < 1070 K, i.e. in the metallic-like conduction regime, for all the phases synthesized either by the SSR or the SC methods. Both series of compounds present electrical resistivity values as low as are characteristic for metals, e.g. for the SC phase: for x = 0.05: ρ_{400K} = 12.1 mΩ cm. The introduction of a pentavalent cation such as Nb^{5+} generates Mn^{3+} ($e_g{}^1$ $t_{2g}{}^3$) cations in the Mn^{4+} ($e_g{}^0$ $t_{2g}{}^3$) matrix according to $CaMn^{4+}_{1-2x}Mn^{3+}_xNb^{5+}_xO_3$. Electrons in the e_g orbitals act as charge carriers in the Mn^{4+}-O-Mn^{3+} ions framework, as already introduced in the Chapter 2, Section 2.3.3.2. Thus, the ρ(T) tend to lower values with increasing the charge carrier concentration as a consequence of the Nb substitution, e.g. for the SSR phases from ρ_{500K} = 26 mΩ cm for x = 0.02 to ρ_{500K} = 11.3 mΩ cm for x = 0.08, as reported in Table 5.4.

In the studied temperature range, the transport of carriers in manganate phases can be well described by the small polaron hopping model [Maignan-1998a, Hejtmánek-1999], i.e. strong electron-phonon interaction, as earlier detailed in the Chapter 2, Section 2.3.3.2. Based on this conduction model, the experimental data can be fitted within the temperature range of 320 K < T < 800 K using: $\rho = AT * (\exp W_p/k_BT)$, where A is a constant, W_p is the activation energy[1] relative to the hopping conduction, and k_B is the Boltzmann constant, as

---

[1] W_p is defined by $W_p = E_H - J$, where E_H is the hopping energy and J is the transfer integral [Maignan-

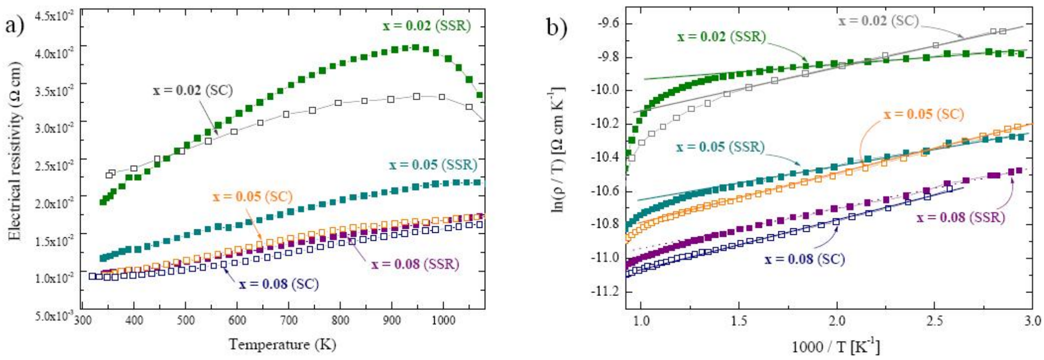

Figure 5.16: a) Temperature dependence of the electrical resistivity and b) small polaron model fitting of the $CaMn_{1-x}Nb_xO_3$ (x = 0.02, 0.05 and 0.08) series synthesized by the SSR (closed symbols) and the SC methods (open symbols). The solid lines represent the fitting curves of the experimental data.

presented in Figure 5.16 b). The corresponding fitting parameters are reported in Table 5.4. The metallic-like behavior of all the studied phases is confirmed by the activation energy values which vary from 11 meV to 25 meV for both series of compounds. Despite that the electrical resistivity values decrease with increasing the Nb substitution, an increase of the activation energies is observed toward higher Nb contents, and this irrespective of the applied synthesis method, e.g. for the SSR compounds: W_p = 11.4 meV for x = 0.02 to W_p = 21.6 meV for x = 0.08. This feature indicates that the formation of small polarons by hopping conduction is enhanced with increasing the Mn^{3+} concentration, as earlier outlined for others electron-doped manganate phases [Maignan-1998a; Hejtmánek-1999; Hébert-2001]. For instance, the transport properties of the $CaMn_{1-x}Nb_xO_3$ phases within the studied temperature range can be understood considering that the polaronic narrow band is progressively filled with e_g electrons while substituting Mn^{4+} by Nb^{5+} cations.

For an equivalent Nb substitution, the SC- and SSR-derived phases present similar electrical resistivity values, e.g. for x = 0.02 at 800 K: ρ = 37.7 Ω cm for the SSR compound and ρ = 32.4 Ω cm for the SC compound, despite that the SC series reveal lower relative densities compared to the SSR ones. This finding emphasizes that the SC-derived phases present a better intrinsic electrical conduction than the SSR series. The different sizes and morphologies of crystallites resulting from the different applied synthesis methods can be considered for explaining this peculiarity. The SC-derived phases reveal a 6 to 10 times smaller grain size than the SSR compounds and specific surface areas at least twice as high as the SSR series. Therefore, the SC series yield larger contact surface between the sintered crystallites than in the SSR compounds. The SC-derived phases are characterized by a particular morphology with good interconnections between the crystallites which promotes the transport of charge carriers.

1998a; Hejtmánek-1999].

Niobium substitution	Mn valency*	Synthesis method	Relative density	ρ (Ω cm) at 800 K	A (Ω cm)	W_p (meV)
0.02	3.98	SSR	86.01%	37.7	4.10*10^{-5}	11.4
		SC	80.77%	32.4	3.07*10^{-5}	22.8
0.05	3.94	SSR	82.74%	19.5	1.52*10^{-5}	17.5
		SC	67.79%	15.6	1.50*10^{-5}	25.7
0.08	3.91	SSR	78.12%	14.8	1.35*10^{-5}	21.6
		SC	72.25%	13.7	1.81*10^{-5}	24.8

Table 5.4: Fitting parameters of the electrical resistivity data depending on the Nb substitution content and on the synthesis method for the $CaMn_{1-x}Nb_xO_3$ series. (* Mn valency $\nu_{(Mn)}$ determined according to $CaMn^{4+}_{1-2x}Mn^{3+}_{x}Nb^{5+}_{x}O_3$ with $\nu_{(Mn)} = (4-5x)/(1-x)$)

The Seebeck coefficient temperature dependences of all the $CaMn_{1-x}Nb_xO_3$ phases are presented in Figure 5.17 a) within the temperature range from 320 K to 1070 K. S(T) reveal large negative thermopower values, i.e. $|S| > 100$ μV K^{-1} indicating that electrons are the predominant charge carriers. Identical thermopower values and S(T) behavior are reported for the compounds with equivalent Nb content irrespective of the applied synthesis method. As S depends only on the nature and the concentration of the charge carriers, manganate phases with identical Mn^{3+}/Mn^{4+} ratio yield equal thermopower values. This confirms that the different microstructures characterizing the SSR- and SC-derived phases do not influence either the charge carrier concentration or the electronic band structure.

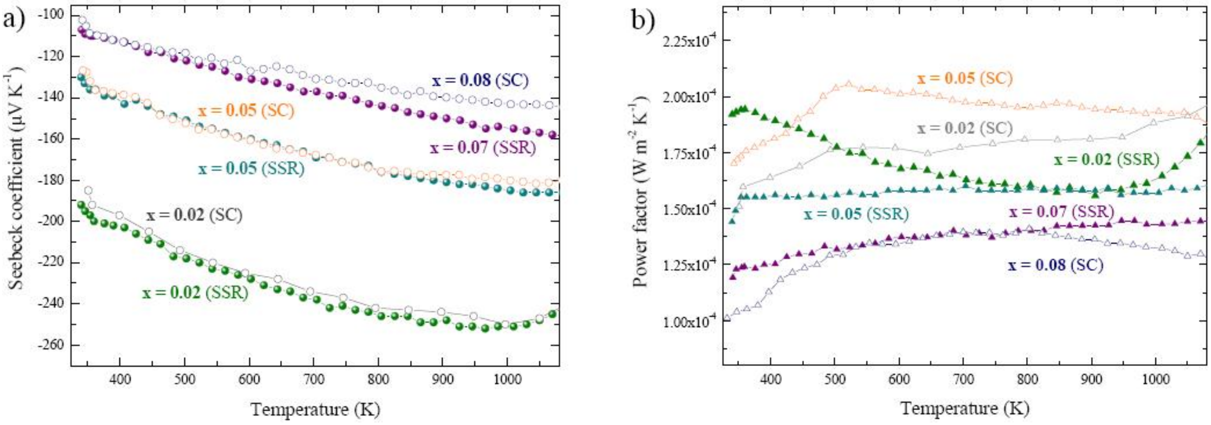

Figure 5.17: Temperature dependences of a) the Seebeck coefficients and b) the power factors $PF = S^2/\rho$ for the $CaMn_{1-x}Nb_xO_3$ (x = 0.02, 0.05 and 0.08) series synthesized by the SSR (closed symbols) and the SC methods (open symbols).

The sole exception is the SSR compound with 8% Nb which reveals a slightly higher absolute thermopower value at T > 500 K compared to the corresponding SC-derived phase. The analysis of the cationic composition indicates a small Nb deficiency in the SSR phase (x = 0.069 ± 0.020)[1] in comparison to the expected composition, which suggests a higher Mn^{4+} concentration associated with a larger $|S|$ value. The charge carrier concentration can be estimated from the experimental thermopower values by applying the Heikes formula, valid in the high-temperature limit, $S = -\frac{k_B}{|e|}\ln\left(\frac{1-c_e}{c_e}\right)$, with c_e is the electron concentration [Heikes-1961]. Hence, the 7% SSR compound presents a $S_{1050K} = -157\ \mu V\ K^{-1}$ corresponding to $c_e = 13.8\%$ while the 8% SC derived phase reveals a $S_{1045\ K} = -143\ \mu V\ K^{-1}$, i.e. $c_e = 15.9\%$. This observation is in agreement with the reported Nb deficient content.

The increase of the Nb content in the Mn sublattice results in a decrease of the absolute Seebeck coefficients from $S_{900K} = -\ 248\ \mu V\ K^{-1}$ for x = 0.02 to $S_{900K} = -150\ \mu V\ K^{-1}$ for x = 0.08, according to the Heikes formula valid at high temperatures. This trend is explained by an increase of the charge carrier concentration inducing a decrease of the electrical resistivity. The largest Seebeck coefficients are therefore reported for both the SSR- and SC-derived 2% Nb substituted $CaMnO_3$ phases, i.e. $S_{1000K} = -251\ \mu V\ K^{-1}$. As a general tendency, the Seebeck coefficient exhibits a linear temperature dependence in the studied temperature region, i.e. $|S(T)| \sim T$. The metallic-like electrical resistivity and linear S(T) behavior of the $CaMn_{1-x}Nb_xO_3$ series allows to apply the modified expression of the single band metal model for the thermopower, as already reported for other electron doped manganate phases [Maignan-1998a; Hejtmánek-1999; Pi-2003; Miclau-2005] and defined by the Equation 5.1:

$$S_{theo} = \frac{-\pi^2 k_B^2}{3e} T \left(\frac{N(E)}{n} + cst\right)_{E=E_f} \tag{5.1}$$

where *N(E)* is the density of states and n is the carrier density. Based on the Equation 5.1, it can be understood that the slope of S(T) results from the charge carrier concentration n at the Fermi level E_f, i.e. the steeper the S(T) slope is, the lower is n. Theoretical Seebeck coefficients can be determined for a defined Nb concentration, e.g. for x = 0.05: the theoretical thermopower values is $S_{theo} = -130\ \mu V\ K^{-1}$, which is in good agreement with experimental values of the $CaMn_{0.95}Nb_{0.05}O_3$ phase: $S_{exp} = -128\ \mu V\ K^{-1}$ at 340 K.

Hence, the SC-derived phases reveal lower resistivity values due to a better interconnection between the crystallites and yield equal thermopower values for equal Nb concentrations. As a result, the SC series present higher power factor PF values than the SSR-derived phases at equivalent Nb content, as shown in Figure 5.17 b). The largest power factor is achieved for the $CaMn_{0.95}Nb_{0.05}O_3$ SC-derived phase ranging from $PF_{450K} = 1.92*10^{-4}\ W\ m^{-2}\ K^{-1}$ to $PF_{1050K} = 2.02*10^{-4}\ W\ m^{-2}\ K^{-1}$.

---

[1] the compound previously referred as 8% Nb SSR phase is hereafter properly termed 7% Nb SSR phase.

5.3.2 Thermal conductivity and figure of merit

The total and lattice thermal conductivities of all the SSR and SC series are presented within the temperature range of 340 K $<$ T $<$ 1070 K in Figure 5.18 a). The thermal conductivity is defined as the sum of the lattice and the electronic components, i.e. $\kappa = \kappa_{lattice} + \kappa_{el}$, as previously introduced in Chapter 2, Section 2.2.2.2. The electronic component κ_{el} can be determined by applying the Wiedemann-Franz law [Kittel-2004]. The calculated κ_{el}, the experimental thermal diffusivity α and conductivity κ_{total} values determined at 800 K are summarized in Table 5.5. The lattice component $\kappa_{lattice}$ is the predominant contribution to the heat conduction in the manganate phases since κ_{el} does not exceed 20% of the total thermal conductivity, which is a common characteristic in oxide materials. The electronic thermal conductivity depends on both the temperature and the charge carrier concentration. Thus, an increase of the Nb concentration in the $CaMnO_3$ system induces an increase of κ_{el}, e.g. for the SSR phases at 800 K: from κ_e = 4.20% for x = 0.02 to κ_e = 8.03% for x = 0.08.

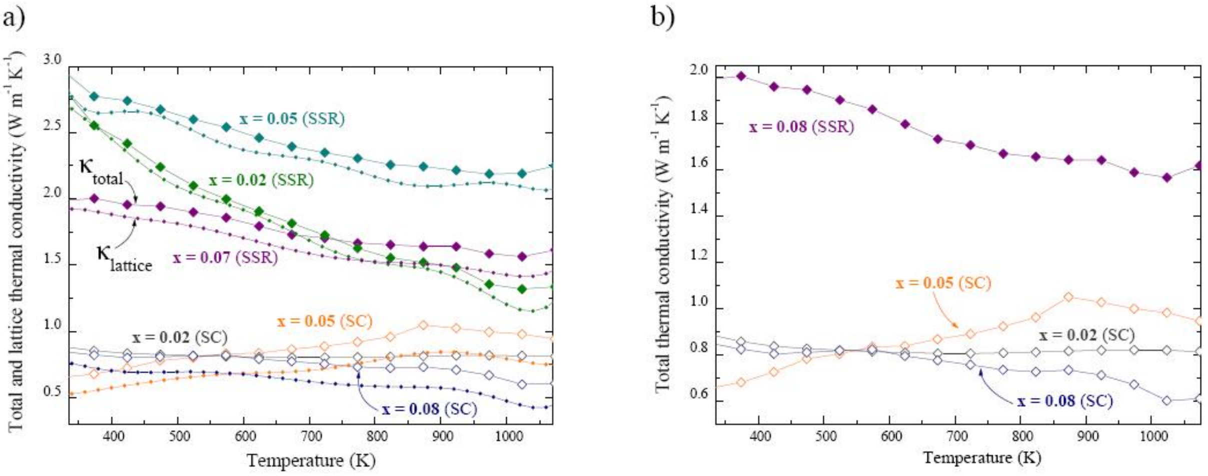

Figure 5.18: a) Total thermal conductivity κ_{total} and lattice contribution $\kappa_{lattice}$ versus T of the $CaMn_{1-x}Nb_xO_3$ (x = 0.02, 0.05 and 0.08) phases synthesised by both the SSR (closed symbols) and the SC (open symbols) methods and b) highlight in the low thermal conductivity range.

As a general tendency, the SC-derived phases yield lower thermal conductivity values, i.e. $\kappa_{total} < 1$ W m^{-1} K^{-1}, compared to the SSR series, i.e. 1.5 W m^{-1} K^{-1} $< \kappa_{total} <$ 3.0 W m^{-1} K^{-1} corresponding to typical values for oxide materials [Ohtaki-1995; Clarke-2003]. The total heat conductivity of the SSR-derived phases reveal a common temperature dependence, i.e. a progressive decrease of κ_{total} with increasing the temperature. This behavior does not apply for the SC series and might be related to their low thermal conductivity values, i.e. $\kappa_{total} < 1$ W m^{-1} K^{-1}. Figure 5.18 b) underlines the gap observed between the thermal conductivities of the SSR and the SC manganate phases. The total thermal conductivity values κ_{total} of both the SSR and the SC series can not be directly compared since they present significant differences in relative densities, i.e. 78 - 86% and 67 - 80%, respectively. Therefore, κ values should rather be related to a 100% dense material according to the Maxwell relation [Schliting-2001; Winter-2007]:

$$\frac{\kappa_{measured}}{\kappa_{dense}} = \left(1 - \frac{3}{2}\phi_V\right) \tag{5.2}$$

where ϕ_V accounts for the volume porosity, assuming spherical pores. This evaluation has to be considered as first approximation since the SC-derived phases are characterized by pores with heterogeneous shapes, as earlier presented in this Chapter, Section 5.1. Calculation results are reported in Table 5.5 and reveal higher κ_{dense} values for the SSR series compared to the SC ones. Furthermore, the SC-derived phases yield lower thermal diffusivity values compared to the SSR compounds, e.g. $\alpha_{SSR} \simeq 0.60$ mm^2 sec^{-1} and $\alpha_{SC} \simeq 0.32$ mm^2 sec^{-1} at 800 K, whereas the thermal diffusivity does not depend on the relative density since it first reflects how quickly a material can change its temperature. Both findings confirm that the low κ values characteristic of the SC phases do not result from different relative densities.

Niobium substitution	Synthesis method	κ_{total} (W m^{-1} K^{-1})	κ_e (%)	κ_{dense} (W m^{-1} K^{-1})	α (mm^2 sec^{-1})
0.02	SSR	1.53	4.20	2.17	0.336
	SC	0.78	7.78	1.06	0.585
0.05	SSR	2.27	4.63	3.05	0.303
	SC	0.91	13.93	1.76	0.688
0.08	SSR	1.66	8.03	2.12	0.341
	SC	0.73	19.57	1.11	0.542

Table 5.5: Total thermal conductivity κ_{total}, electronic contribution κ_{el} relative to κ_{total}, calculated dense thermal conductivity $\kappa_{\ dense}$ and thermal diffusivity α at 800 K for the CaMn$_{1-x}$Nb$_x$O$_3$ series synthesized by both the SSR and the SC methods.

As previously mentioned in the Chapter 2, Section 2.3.2.2, nanostructured materials may yield a reduction of the mean phonon free path and therefore a significant decrease of the lattice thermal conductivity compared to the bulk counterpart. In the present study, the manganate phases are characterized by a specific microstructure comprising 90° twinned domains and rock-salts planar defects. Since the occurrence of twins can be explained based on crystallographic considerations, as mentioned in this Chapter, Section 5.2.2.1, it is obvious to observe twinned domains in both the SSR and the SC-derived phases. However, the SC phases present smaller crystallites, i.e. $\simeq$ 200 nm diameter, than the corresponding SSR series, i.e. in the micrometer range. This divergence yields twinned domains of different dimensions. The existence of nano-sized twins or rock-salt planar defects induce specific internal boundaries at the nanoscale which might scatter more efficiently the phonons in the SC phases than in the SSR compounds.

The efficiency of a thermoelectric material is evaluated regarding its dimensionless figure of merit ZT, which is therefore of main importance for the selection of functional thermoelectric oxides. ZT can be expressed according to: $ZT = (S^2/L) * [1/1 + (\kappa_{lattice}/\kappa_{el})]$[1], as earlier mentioned in the Chapter 2, Section 2.2.2.2. This expression points out how ZT can be maximized by reducing the $(\kappa_{lattice}/\kappa_{el})$ ratio. Figures 5.19 a) and b) present the $(\kappa_{lattice}/\kappa_{el})$ ratio and the corresponding figure of merit ZT of both the SSR and the SC phases within the temperature range of 340 K < T < 1070 K, respectively. The SC-derived phases result in lower $(\kappa_{lattice}/\kappa_{el})$ ratio compared to the SSR ones, despite both series of compounds present similar electrical resistivity values. As a consequence, the SC manganates can be considered as prospective materials to achieve high ZT values in the $CaMn_{1-x}Nb_xO_3$ phases. This is confirmed in Figure 5.19 b) where the SC 2% Nb-containing $CaMnO_3$ phase presents a $ZT = 0.32$ at 1060 K, which is twice as high than the SSR-derived phase with a maximal ZT value of $ZT_{1060\ K} = 0.16$ for the corresponding phase. A previous work reported a ZT value of 0.37 at 1000 K for heterostructures of Nb-doped $SrTiO_3$ epitaxial thin films [Ohta-2005a]. Transparent conducting oxide (TCO) materials reveal as well promising high-temperature thermoelectric properties. The highest ZT values among the TCO materials are reported for the Y substituted In_2O_3-ZnO phases with $ZT_{1073K} = 0.33$ and more recently for the $In_{2-x}Ge_xO_3$ phases with $ZT_{1273K} = 0.4$ [Isobe-2002; Bérardan-2008]. The present result belongs to the best ZT value reported for n-type polycrystalline perovskite-type phases with thermoelectric properties as good as the best TCO materials. The electron doped manganate phases are therefore considered for the development of a thermoelectric oxide module as potential n-type legs associated with p-type $GdCo_{0.95}Ni_{0.05}O_3$ phases previously identified in the group [Robert-2007c]. Both SC-derived manganate and cobaltate phases have been already implemented in a thermoelectric module for further evaluations with respect to the output power and the conversion efficiency of the thermoelectric converter [Tomes-2008].

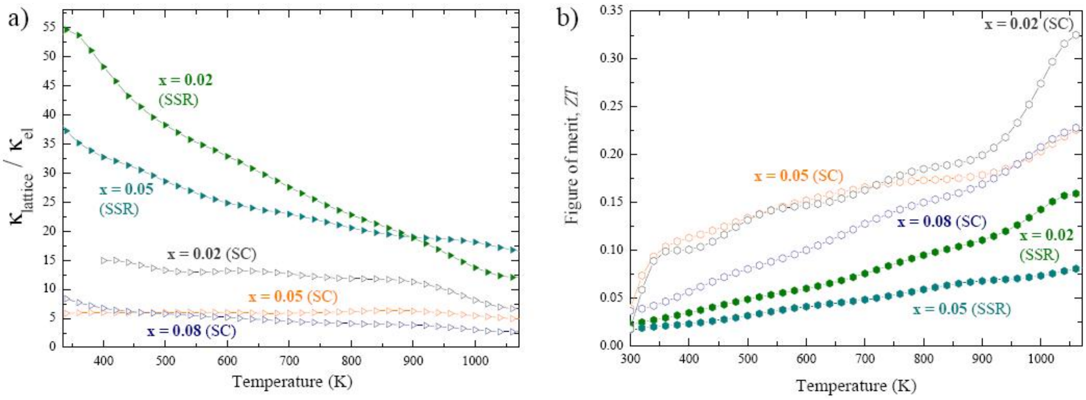

Figure 5.19: Temperature dependences of a) the $\kappa_{lattice}/\kappa_{el}$ ratio and b) the thermoelectric figure of merit ZT for the $CaMn_{1-x}Nb_xO_3$ (x = 0.02, 0.05 and 0.08) series synthesized by both the SSR (closed symbols) and the SC methods (open symbols).

---

[1] where L is the Lorenz factor.

5.4 Phenomena influencing the thermoelectric properties

The $CaMn_{1-x}Nb_xO_3$ phases reveal potential thermoelectric properties at T $\simeq$ 1000 K. These manganate phases present others remarkable properties such as (i) a low-temperature magnetic transition at T $<$ 125 K and (ii) a structural transition accompanied by a thermal reduction at high temperatures, i.e. T $>$ 1100 K. In the present study, both phenomena are investigated regarding their influence on the thermoelectric properties.

5.4.1 Magnetic transition and related physical properties at low temperatures

$CaMnO_3$ undergoes a magnetic transition at T_N[1] $\simeq$ 125 K from paramagnetic (PM) to G-type antiferromagnetic (AFM) states [Goodenough-1955; Wollan-1955]. With aliovalent *A*- or *B*-site substitutions, complex magnetic structures arise below the magnetic ordering temperature T_M[2] involving G-type AFM with small ferromagnetic (FM) fluctuations in confined regions, C-type AFM, and charge-ordered AFM states with increasing the Mn^{3+} concentration [Martin-2001; Maignan-2002]. The Nb^{5+} substitution in the $CaMnO_3$ phase induces mixed valence states, i.e. Mn^{3+} in the Mn^{4+} matrix, and consequently double exchange (DE) phenomena. When applying a magnetic field, the interaction of carriers via t_{2g} spins induce a ferromagnetic coupling due to spin reorientations and a reduction of the electrical resistivity, which results in a negative magneto-resistance effect, as previously described in the Chapter 2, Section 2.3.3.2. At higher temperatures, i.e. above T_M, a polaronic-type conduction dominates the electrical transport properties of the electron-doped $CaMnO_3$ phases leading to a metallic-like behavior, as discussed in the previous section.

In the present work, $CaMn_{1-x}Nb_xO_3$ series synthesized by both the SSR and the SC methods are studied concerning their crystal structure, magnetic, electrical resistivity and thermopower below T_M. The $CaMn_{0.98}Nb_{0.02}O_3$ phase is further investigated with respect to its magneto-transport properties. Finally, the $CaMn_{1-x}Nb_xO_3$ nanocrystallites synthesized by the USC method reveal unusual magnetic and electrical transport properties below the magnetic transition. This peculiar behavior of the USC nanocrystallites is discussed with respect to their specific morphology and size.

5.4.1.1 Structural characterization

The crystal and magnetic structures of the SC-derived $CaMn_{0.98}Nb_{0.02}O_3$ phase are determined from Rietveld refinement analyses of the NPD data recorded at 1 K, 105 K, and 140 K. The structural and magnetic parameters of the $CaMn_{0.98}Nb_{0.02}O_3$ phase are summarized in Table 5.6 for the different investigated temperatures. The orthorhombic crystal structure *Pnma* S.G. is

---

[1] T_N corresponds to the Néel temperature.

[2] T_M is defined as the magnetic ordering temperature no matter which ordered magnetic phase is predominant, i.e. antiferromagnetism or ferromagnetism.

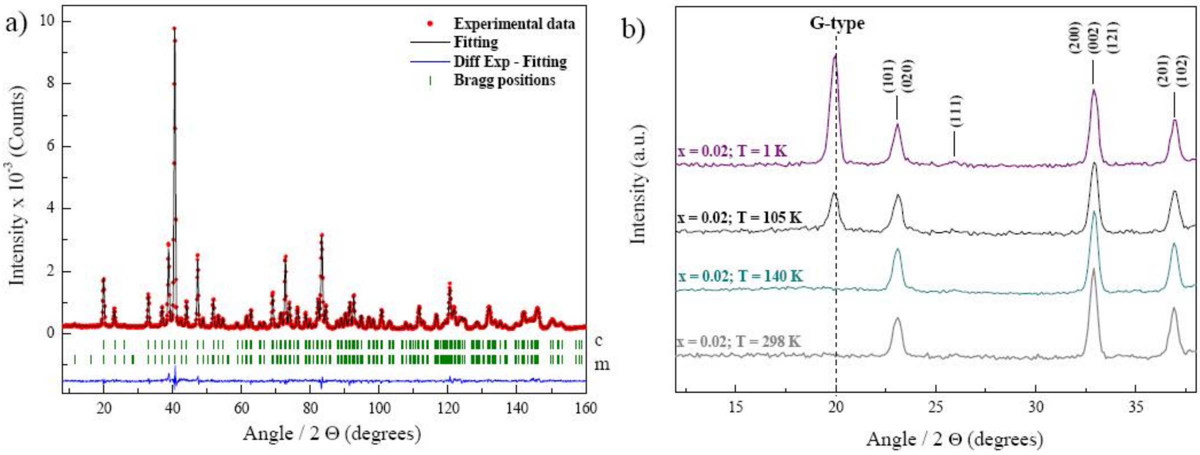

Figure 5.20: a) Example of a Rietveld refinement for the CaMn$_{0.98}$Nb$_{0.02}$O$_3$ phase from the low-temperature NPD data recorded at 1 K and b) low-angles NPD patterns from 1 K to 298 K.

preserved at low temperatures since no structural transition is observed upon cooling within the temperature range of 1 K $<$ T $<$ 298 K. Figure 5.20 a) presents the NPD pattern recorded at 1 K where additional magnetic reflexions can be indexed in the orthorhombic structure *P-1* S.G. (N° 2), indicating that the crystal and magnetic structures are described in the same unit cells. A G-type AFM structure characterizes the 2% Nb-containing CaMnO$_3$ at 1 K and 105 K. In the magnetic phase denoted G-type by Wollan and Koehler [Wollan-1955], each Mn ion is surrounded by six Mn neighbors whose spins are antiparallel to the given ion. The ordered magnetic structure is not further observed at T $>$ 140 K, as emphasized in Figure 5.20 b) in the low angular range, i.e. $12° < 2\theta < 38°$. The refined antiferromagnetic moments m(G) are predominantly oriented along the shortest orthorhombic *Pnma* axis, i.e. [001]. The total magnetic moment is refined to 3.08 μ_B at 1 K, which is in good agreement with the theoretical value of $\sim$ 3.1 μ_B per Mn, as expected for fully aligned spins. The fraction of G-type AFM decreases with increasing the temperature yielding a total magnetic moment of 1.44 μ_B at 105 K, which arises exclusively along the [001] axis.

5.4.1.2 Magnetic and electrical transport properties

The magnetic properties of the SC-derived CaMn$_{1-x}$Nb$_x$O$_3$ series are summarized in Figure 5.21. Upon cooling, the magnetization first slightly increases as the temperature decreases corresponding to the high-temperature paramagnetic region. Below the ordering magnetic temperature T$_M$, the magnetization spontaneously rises until reaching a maximum value at T $\simeq$ 75 K. In this low-temperature region, i.e. T $<$ T$_M$, the zero field cooled (zfc) and field cooled (fc) curves present divergences suggesting a complex magnetic structure of the studied phases. The disordered paramagnetic regime, i.e. T $>$ T$_M$, can be linearly fitted by applying the Curie Weiss law

Temperature		1 K	105 K	140 K
S. G.		*Pnma*	*Pnma*	*Pnma*
a (Å)		5.2828 (1)	5.2830 (1)	5.2844 (1)
b (Å)		7.4453 (1)	7.4498 (2)	7.4526 (1)
c (Å)		5.2620 (1)	5.2635 (1)	5.2649 (1)
V (Å^3)		206.96	207.16	207.35
Ca	x	0.0367 (5)	0.0361 (5)	0.0358 (4)
	y	0.25	0.25	0.25
	z	- 0.0073 (8)	- 0.0069 (8)	- 0.0069 (7)
	Biso (Å^2)	0.65 (4)	0.73 (4)	0.77 (3)
	occupancy	0.5	0.5	0.5
Mn / Nb	x	0	0	0
	y	0	0	0
	z	0.5	0.5	0.5
	Biso (Å^2)	0.63 (4)	0.64 (4)	0.66 (3)
	occupancy	0.49/0.01	0.49/0.01	0.49/0.01
O_{ap}	x	0.4905 (4)	0.4899 (5)	0.4905 (4)
	y	0.25	0.25	0.25
	z	0.0677 (6)	0.0669(6)	0.0681 (5)
	Biso (Å^2)	0.74 (3)	0.74(3)	0.78 (2)
	occupancy	0.5	0.5	0.5
O_{eq}	x	0.2874 (4)	0.2872 (3)	0.2874 (2)
	y	0.0338 (3)	0.0339 (3)	0.0334 (2)
	z	0.7116 (3)	0.7118 (3)	0.7115 (3)
	Biso (Å^2)	0.66 (2)	0.68 (2)	0.72 (2)
	occupancy	1	1	1
m(G) μ_B	μ_x	0.40 (4)	0	0
	μ_y	0.38 (14)	0	0
	μ_z	2.30 (2)	1.44 (4)	0
R_{wp}		9.94	11.1	8.38
R_p		10.9	10.4	7.76
χ^2		1.98	1.95	3.38
Magnetic R		4.87	17.2	-

Table 5.6: Refined structural parameters, atomic positions, and magnetic moments of the $CaMn_{0.98}Nb_{0.02}O_3$ phase from NPD data recorded at 1 K, 105 K, and 140 K. Atoms are located at the following Wyckoff position: Ca: (4c), Mn / Nb: (4b), O_{ap}: (4c) and O_{eq}: (8d).

where the susceptibility χ obeys $\chi = C/(T - \theta_W)^1$, as previously introduced in the Chapter 3, Section 3.7.3. The Weiss temperatures θ_W and the corresponding effective magnetic moments μ_{eff} extracted from the experimental data of the $CaMn_{1-x}Nb_xO_3$ phases recorded at $H = 0.3$ T, are reported in Table 5.7. As the Nb concentration increases, the magnetic interactions vary from antiferromagnetic ($\theta_W < 0$, θ_W = -$T_N{}^2$) to ferromagnetic ($\theta_W > 0$, θ_W = $T_C{}^3$) and the effective magnetic moments increase from $\mu_{eff} = 3.56$ μ_B for x = 0.02 to $\mu_{eff} = 3.84$ μ_B for x = 0.08. However, the small magnetization values indicate that the ferromagnetic interactions remain weaker in the Mn^{3+}-O-Mn^{4+} network, e.g. $M_{max} = 8.4*10^{-2}$ μ_B/Mn for x = 0.05 compared to the theoretical moment (~ 3.1 μ_B per Mn). The Nb^{5+} cations present a d^0 electronic configuration which drastically limits the DE phenomena and prevents a long range FM ordering in the Mn sublattice. These results are in agreement with different Nb^{5+}- or Ta^{5+}-substituted $CaMnO_3$ phases which reveal a maximal magnetization of $0.2\mu_B$ for 6% B-site substitution by pentavalent elements [Raveau-2000].

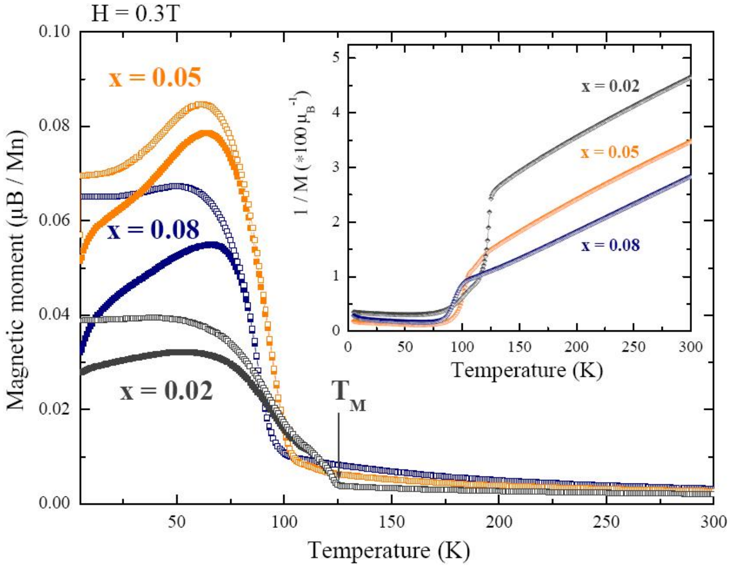

Figure 5.21: Temperature dependences of the zero field cooled (zfc) (open symbols) and field cooled (fc) (closed symbols) magnetizations under 0.3 T applied field for the $CaMn_{1-x}Nb_xO_3$ (x = 0.02, 0.05, and 0.08) phases synthesized by the SC method. The inset figure presents the inverse zfc magnetization where the high-temperature region, i.e. 120 K < T < 300 K, can be linearly fitted with the Curie Weiss law.

All these findings suggest a predominance of the Mn^{4+}-O-Mn^{4+} AFM interactions with low Nb substitution levels, i.e. x < 0.05. With a further increase of the Mn^{3+} concentration, weak FM fluctuations arise in the AFM matrix via the development of itinerant Mn^{3+}-O-Mn^{4+} DE mechanism. For instance, the Nb substitution in the $CaMnO_3$ phase induces an additional

---

[1] θ_W is defined as the Weiss temperature.

[2] T_N corresponds to the Néel temperature.

[3] T_C corresponds to the Curie temperature.

Niobium substitution	$T_M (K)$	θ (K)	μ_{eff} (μ_B)	M_{max} (μ_B/Mn)	ρ (Ω cm) at 5 K	ρ (Ω cm) at 300 K
0.02	125	– 111	3.56	$3.9*10^{-2}$	$9.8*10^{3}$	$3.0 *10^{-2}$
0.05	105	– 21	3.70	$8.4*10^{-2}$	22.5	$1.5 *10^{-2}$
0.08	100	19	3.84	$6.7*10^{-2}$	51.3	$0.9 *10^{-2}$

Table 5.7: Magnetic ordering temperature T_M, fitting parameters of the magnetic properties, i.e. the Weiss temperature θ_W, the experimental effective magnetic moment μ_{eff}, and comparisons of magnetization and electrical resistivity values for the $CaMn_{1-x}Nb_xO_3$ (x = 0.02, 0.05, and 0.08) series. The magnetization values are reported from the zero field cooled data measured under a 0.3 T magnetic field.

electron in the Mn sublattice which is shared in a cube of eight Mn^{4+}, i.e. four spin up and four spin down, in the ideal G-type arrangement. In the "dilute limit", such configurations, i.e. eight Mn^{4+} and one electron, are isolated in the lattice and the electron is dispersed in a random position. With increasing the electron-doping, the extra electrons are not anymore isolated and start to form FM in confined regions. Hence, the low-temperature magnetic state of the $CaMn_{1-x}Nb_xO_3$ phases can be described as FM clusters giving rise to electron itinerancy and persistent ferromagnetism with respect to the DE phenomena. This complex magnetic state characterized by a magnetic phase separation has been previously reported for others electron-doped manganate phases [Martin-1999; Ling-2003].

The temperature dependence of both the electrical resistivity and the Seebeck coefficient for the $CaMn_{1-x}Nb_xO_3$ phases are presented within the range of 5 K < T < 300 K in Figures 5.22 a) and b), respectively. In addition, a comparison of the electrical resistivity values at 5 K and at 300 K is given in Table 5.7 for the studied phases. In the high-temperature paramagnetic state, the electrical transport properties exhibit a linear temperature dependence with $d\rho/d\mathrm{T} > 0$ and $S(T) \sim T$. A systematic decrease of the electrical resistivity and the absolute thermopower values is observed as the Nb content increases in the $CaMnO_3$ matrix, e.g. at 300 K, for x = 0.02: $S_{300K} = -172.7\ \mu$V K^{-1} and x = 0.08: $S_{300\ K} = -69.2\ \mu$V K^{-1}. This evolution corresponds to the introduction of mobile electrons in the e_g band with increasing x, characteristic of a polaronic-type conduction regime, as earlier mentioned in the previous section. Below T $\simeq$ 115 K, all manganate phases reveal a slope change of both $\rho(T)$ and $S(T)$ resulting in a simultaneous increase of the electrical resistivity and the absolute thermopower values. This feature suggests a semiconducting-like behavior at low temperatures. The transition can be attributed to the AFM ordering and the segregation of the non-percolating FM regions which both occur below T_M, as concluded from the magnetic study. Furthermore, the transition temperature T_t defined by the tangent between the low- and the high-temperature regions of the $\rho(T)$ curves, i.e. from the semiconducting to metallic-like regime, increases to higher temperatures with increasing the Nb concentration, e.g. from T_t = 68 K for x = 0.02 to T_t = 123 K for x = 0.08. This trend indicates that the Nb substitution tends to enlarge the low-temperature semiconducting region to higher temperatures. The present results fit well with previous studies reported by Raveau et *al.* on the CaMn$_{1-x}$Nb$_x$O$_3$ series with others Nb substitution levels [Raveau-2000].

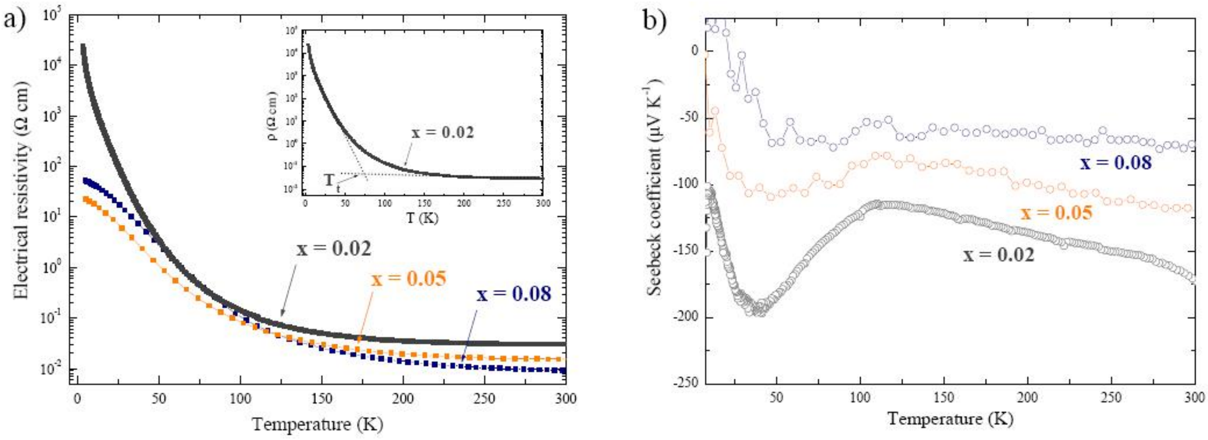

Figure 5.22: a) Electrical resistivity and b) Seebeck coefficient temperature dependences under zero applied field for the CaMn$_{1-x}$Nb$_x$O$_3$ (x = 0.02, 0.05, and 0.08) series synthesized by the SC method. The inset in Figure a) shows the tangents which allow to determine the transition temperature T$_t$.

B-site substitutions with pentavalent or hexavelant d^0 elements such as Nb, Ta, W, and Mo in the CaMnO$_3$ phases have already proven interesting magneto-transport properties [Raveau-2000; Pi-2003]. In the present work, the electrical resistivity and thermopower temperature dependences of the 2% Nb-containing CaMnO$_3$ phase are investigated when applying a magnetic field of $H = 7$ T, as presented in Figures 5.23 a) and b), respectively. A large negative magneto-resistance effect is observed within the range of 5 K < T < 50 K. The evolution of the electrical resistivity ratio expressed as $\rho_{(H=0)}/\rho_{(H)}$ results in a maximum value of 7.75 at 5 K under 7 T applied field, which corresponds to a magneto-resistance MR of 87.02%, with MR defined as follows: $MR = -100\ [(\rho_{(H)}/\rho_{(H=0)}) - 1]$. In analogy, the Seebeck coefficient reflects as well this negative magneto-resistance effect since lower absolute thermopower values are observed when applying a magnetic field, e.g. at 40 K $S_{(0T)} = -194.6\ \mu$V K^{-1} to $S_{(7T)} = -157.8\ \mu$V K^{-1}. When applying a magnetic field, ferromagnetic interactions promote the transport of charge carriers in the Mn^{3+}-O-Mn^{4+} network leading to a simultaneous reduction of the electrical resistivity and of the absolute thermopower values.

Magnetic and electrical transport properties of the USC-derived CaMn$_{1-x}$Nb$_x$O$_3$ nanocrystallites are studied at low temperatures, i.e. at T < 300 K, and further discussed with respect to their characteristic morphology and size. The corresponding properties of the SSR-derived phases are reported for comparison. Nanocrystallites are achieved after sintering of the ultrafine manganate particles synthesized by the USC process, as previously presented in the Chapter 4, Section 4.3.

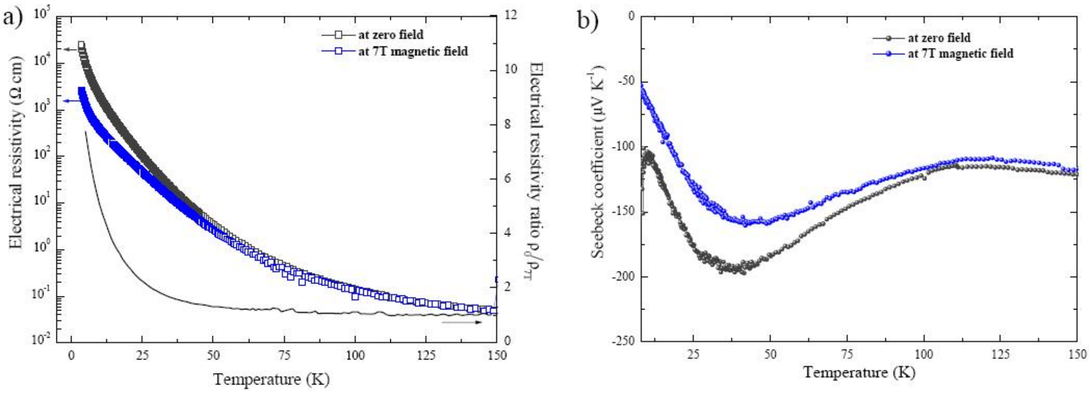

Figure 5.23: a) Electrical resistivity (left axis), electrical resistivity ratio ρ_0/ρ_{7T} (right axis) and b) Seebeck coefficient temperature dependences for the $CaMn_{0.98}Nb_{0.02}O_3$ phase under zero and under 7 T applied field.

The USC nanocrystallites present a defined rhomboid-like shape with crystallite sizes ranging from 20 to 50 nm, as shown in Figures 5.24 a) and b). The HRTEM image in Figure 5.24 b) displays lattice fringes corresponding to $(010)_o$ planes confirming the highly crystalline character of the manganate phases achieved from the USC synthesis. The experimental ED pattern of another USC nanocrystallite in Figure 5.24 c) reveals the presence of 90° twinned domains oriented either (i) in the plane or (ii) out of the plane corresponding to (i) the $[\text{-}101]_o$ or (ii) the $[0\text{-}10]_o$ zone axes. The occurrence of twins in the USC nanocrystallite manganates rely on crystallographic considerations which are satisfied for the perovskite-type orthorhombic $CaMn_{1-x}Nb_xO_3$ phases, as previously discussed in this Chapter, Section 5.2.2.1. The USC nanocrystallites exhibit a well ordered crystalline microstructure with typical textural features of 90° twinned domains. The phase purity and the cationic homogeneity are confirmed by XRPD and by EDS analyses, respectively.

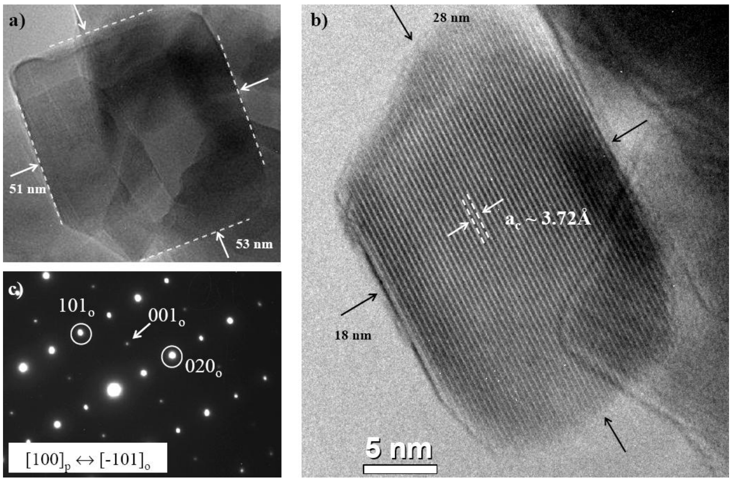

Figure 5.24: a) Low resolution TEM image of a USC nanocrystallite, b) HRTEM image, and c) ED pattern corresponding to the $CaMn_{0.98}Nb_{0.02}O_3$ phase.

The magnetization curves of the $CaMn_{1-x}Nb_xO_3$ series synthesized either by the USC or by the SSR method exhibit different behaviors, as shown in Figure 5.25 a). All the USC phases reveal predominant AFM interactions ($\theta_W < 0$) with low magnetic moments compared to the SSR-derived phases, e.g. at 50 K, for x = 0.05: $M_{(USC)} = 1.2*10^{-2}$ μ_B/Mn and $M_{(SSR)} = 5.9*10^{-2}$ μ_B/Mn. This result indicates a pronounced suppression of the FM fluctuations for the USC nanocrystalline manganate phases. Figure 5.25 b) presents the field dependent magnetization M(H) recorded at 5 K for the USC- and the SSR-derived $CaMn_{0.95}Nb_{0.05}O_3$ phases. For low applied magnetic fields, the M(H) curve of the SSR compound exhibits typical FM-like hysteresis loop yielding a coercive field of $H_c = 0.17$ T and a remanence of $M_R = 5.01*10^{-2}$ μ_B/Mn. The suppression of the FM interactions in the USC-derived phase is confirmed by its hysteresis loop.

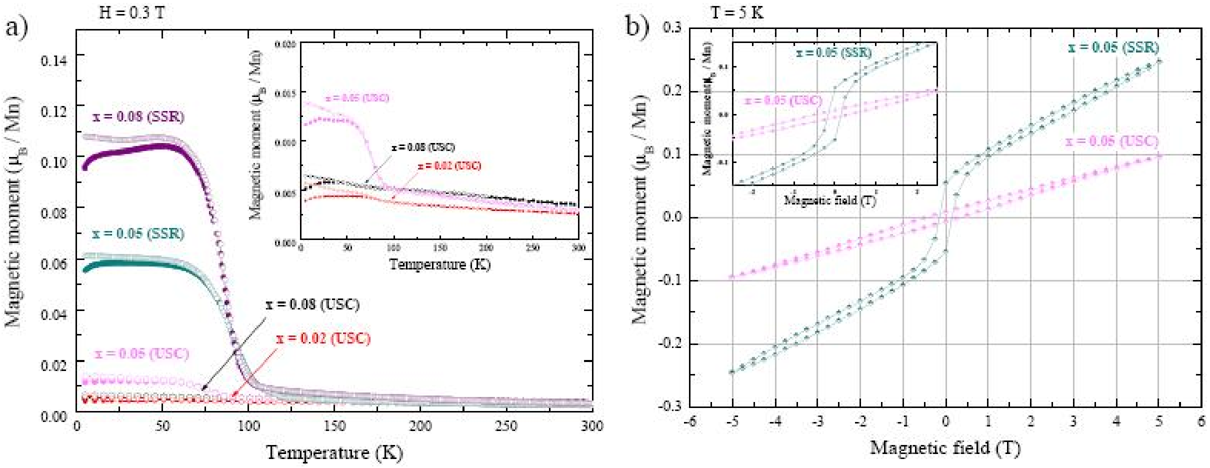

Figure 5.25: a) Temperature dependences of the zero field cooled (open symbols) and field cooled (closed symbols) magnetizations under 0.3 T applied field for the $CaMn_{1-x}Nb_xO_3$ (x = 0.02, 0.05, and 0.08) series synthesized by both the SSR and the USC methods and b) magnetic hysteresis loops recorded at T = 5 K. The insets in Figure a) and b) emphasize the low magnetization range and the hysteresis loops in -3 T $<$ H $<$ 3 T, respectively.

Furthermore, the USC series present higher resistivity values at low temperatures, i.e. T < 100 K, compared to the SSR phases, as illustrated in Figure 5.26 a), e.g. for x = 0.08 at 30 K: $\rho_{(USC)} = 598.2\ \Omega$ cm and $\rho_{(SSR)} = 18.5\ \Omega$ cm, suggesting a weaker ferromagnetic Mn^{3+}-O-Mn^{4+} network for the USC series. The DE mechanism is certainly limited in the USC nanocrystallites which therefore induces a strong suppression of the FM interactions. One possible origin of this unusual magnetic behavior of the USC-derived phases compared to the SSR series could be different Mn oxidation states for identical Nb content due to slight differences in oxygen stoichiometry. This hypothesis is examined by comparing the Seebeck coefficients of both series of compounds, as shown in Figure 5.26 b). The SSR- and USC-derived $CaMn_{0.98}Nb_{0.02}O_3$ phase exhibit similar thermopower values with a linear temperature dependence $S(T) \simeq T$ in the paramagnetic regime, i.e. T > 125 K. This indicates that both type of compounds present the same

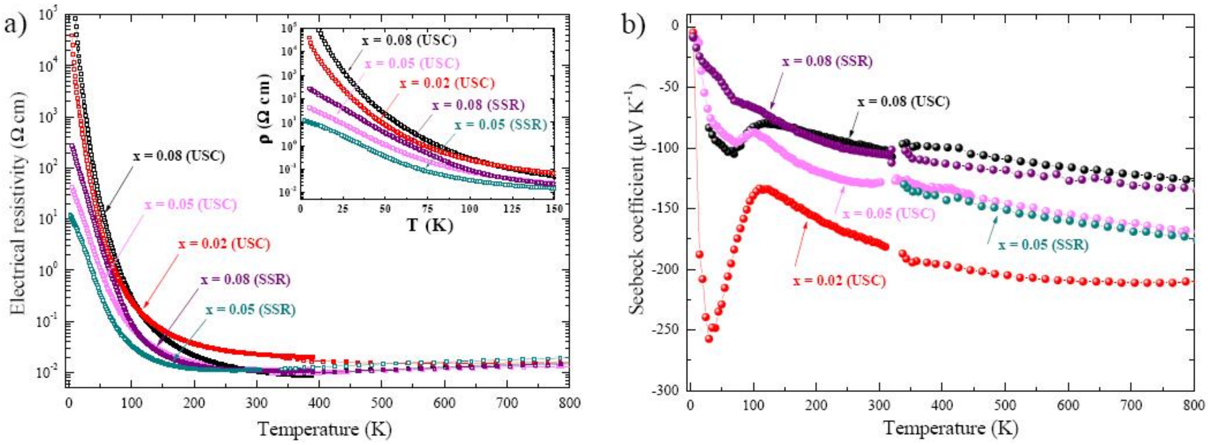

Figure 5.26: a) Electrical resistivity and b) Seebeck coefficient temperature dependences under zero applied field for the $CaMn_{1-x}Nb_xO_3$ (x = 0.02, 0.05, and 0.08) phases synthesized by both the SSR and the USC methods. The inset in Figure a) emphasizes the ρ(T) curves in the low-temperature range, i.e. T < 150 K.

Mn^{3+}/Mn^{4+} concentration ratio, independently of the applied synthesis method. As previously observed, S(T) undergoes a change of slope close to the ordering magnetic temperature, i.e. $S(T) \simeq 1/T$ at T < T_M. However, this sudden increase of $|S|$ leads to higher thermopower values for the USC-derived phases compared to the SSR ones, e.g. at 70 K, for x = 0.08: $S_{(SSR)} = -60.8\ \mu V\ K^{-1}$ and $S_{(USC)} = -104.8\ \mu V\ K^{-1}$, emphasizing different FM strengths between both series of compounds. At a defined temperature, the USC series present higher electrical resistivity and larger absolute thermopower values at T < T_M compared to the SSR compounds. This peculiarity arises from a strong suppression of the FM interactions due to the limitation of the itinerant DE ferromagnetism development. These unusual electrical transport and magnetic properties of the USC-derived phases at low temperatures could be explained by (i) a surface or grain boundary effect or (ii) a size effect of the nanocrystallites limiting the DE mechanism along the Mn^{3+}-O-Mn^{4+} network [Bocher-2008a].

5.4.2 High-temperature crystal structure and thermal stability

Thermoelectric modules are considered as low-maintenance technologies yielding long-term utilizations. The reliability and the durability of the materials are essential prerequisites for thermoelectric applications. For instance, thermoelectric materials should satisfy criteria such as chemical, thermal and mechanical stabilities at specific operating conditions, i.e. temperatures and pressures. The $CaMn_{1-x}Nb_xO_{3\pm\delta}$ phases are investigated concerning their structure, microstructure, and thermal stability as function of the temperature.

At high temperatures (T > 1180 K), $CaMnO_3$ undergoes a structural transition from orthorhombic to cubic structure, i.e. to a higher symmetry [Taguchi-1989]. In manganate phases, high-temperature structural transitions are often related with the formation of oxygen vacancies upon heating [Rørmark-2002, Dabrowski-2003]. Oxygen-deficient $CaMnO_{3-\delta}$ phases have been studied in detail concerning their structures [Poeppelmeier-1982a] and microstructures [Reller-1984], emphasizing the role of the oxygen vacancies in the modification of the crystal structure. Besides, the electrical transport properties of $CaMnO_{3-\delta}$ phases vary with the extent of the oxygen deficiencies as previously reported by Taguchi [Taguchi-1985]. The electrical and thermal transport properties of both A- and B-site substituted $CaMnO_3$ have been studied only up to T $\simeq$ 1000 K [Kobayashi-1991; Ohtaki-1995; Pi-2003; Thao-2003; Xu-2004; Miclau-2005; Flahaut-2006]. The higher temperature range (T > 1100 K) has not been explored so far concerning their thermoelectric properties. The present study focuses on the influence of the high-temperature structural transition, the oxygen vacancy formation, and the effects on the electrical and thermal transport properties in the temperature range of 600 K < T < 1250 K [Bocher-2009]. The investigations regarding the high-temperature range are presented for the $CaMn_{1-x}Nb_xO_{3\pm\delta}$ series synthesized by the SC method since they exhibit the best thermoelectric properties among the investigated phases. However, the Nb-containing $CaMnO_3$ phases synthesized by other techniques, i.e. the SSR and the USC methods, reveal similar trends of their thermoelectric properties in the temperature range of interest.

5.4.2.1 Structural characterization

Figures 5.27 a) and b) present the refined high-temperature XRPD patterns of $CaMn_{0.98}Nb_{0.02}O_3$ at 773 K and 1173 K, respectively. The reflections observed at 773 K can be indexed in the orthorhombic unit cell, *Pnma* S.G., while the XRPD data recorded at 1173 K can be refined using the cubic structural model, $Pm\overline{3}m$ S.G. The orthorhombic structure is generally described as a pseudo-cubic framework of corner-sharing BO_6 octahedra with the A cations in the cuboctahedral coordination. In the studied temperature range, the main phase is either assigned to the orthorhombic or to the cubic structure. A small amount of $CaMn_2O_4$ ($\simeq$ 2.3%) is detected as secondary phase, this irrespective of the investigated temperature.

Figure 5.28 a) depicts the temperature evolution of the $CaMn_{0.98}Nb_{0.02}O_3$ orthorhombic phase. The angular range of $36° < 2\theta < 43°$ is emphasized in Figure 5.28 b) since this region includes superlattice reflections sensitive to the orthorhombic structure and its related tilting system. With increasing temperature, the $(201)_{Pnma}$, $(102)_{Pnma}$ reflections and the $(211)_{Pnma}$,$(112)_{Pnma}$, $(131)_{Pnma}$ triplet decrease in intensity and disappear at 1173 K. The $(220)_{Pnma}$ and $(022)_{Pnma}$ doublet merge to a single $(111)_{Pm-3m}$ reflection at 1173 K. These results indicate that $CaMn_{0.98}Nb_{0.02}O_3$ undergoes a phase transition from orthorhombic to cubic crystal structure at 1073 K < T_s[1] < 1173 K in air. Previous studies on $CaMnO_3$ [Taguchi-1989] reported the existence of successive phase transitions from orthorhombic (*Pnma*) to tetragonal[2] (*I4/mcm*) at 1169 K (o →

---

[1] hereafter, Ts corresponds to the structural transition temperature.

[2] for convenience, information related to the tetragonal crystal structure is labeled with a "t" subscript.

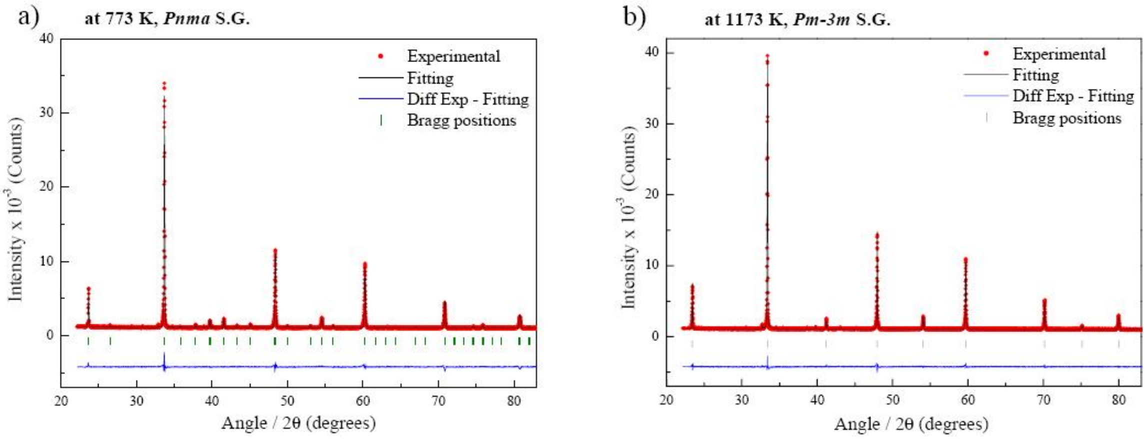

Figure 5.27: Examples of Rietveld refinements from in situ high-temperature XRPD data of $CaMn_{0.98}Nb_{0.02}O_3$ phase recorded at a) 773 K and b) 1173 K under air atmosphere.

t) and further to cubic ($Pm\overline{3}m$) at 1186 K (t → c). In the present case, all orthorhombic superlattice reflections disappear simultaneously at the transition temperature without presence of the intermediate tetragonal phase. The apparent absence of such intermediate transitions for the $CaMn_{0.98}Nb_{0.02}O_3$ phase confirms a limited stability range of the tetragonal phase. Thus, the structural transition temperature determined from the experimental data, i.e. 1073 K $< T_s <$ 1173 K, is consistent with the literature considering the well known transition from orthorhombic to cubic crystal structure upon heating in perovskite-type phases.

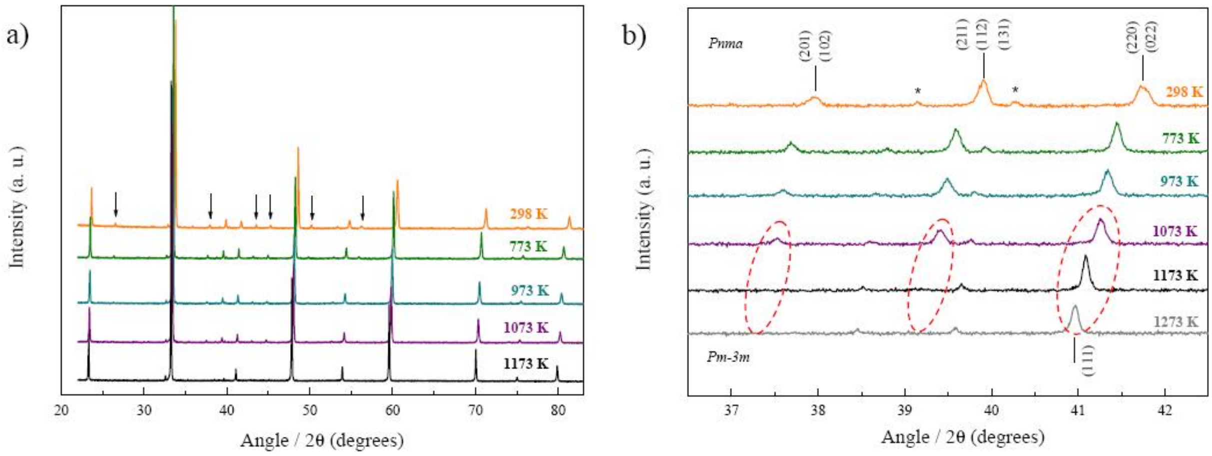

Figure 5.28: a) and b) In situ high-temperature XRPD patterns of $CaMn_{0.98}Nb_{0.02}O_3$ phase from 298 K to 1173 K under air atmosphere. The arrows in Figure a) indicate the reflections disappearing during the phase transition. The angular range of 36° $< 2\theta <$ 43° is enlarged in Figure b) emphasizing the evolution of three main reflections, assigned by red circles, upon heating. The minor reflections indicated by (*) belong to the secondary phase, i.e. $CaMn_2O_4$. The red dotted circles are only intended to emphasize the reflections of main interest.

Temperature		298 K	773 K	973 K	1073 K	1173 K
S. G.		*Pnma*	*Pnma*	*Pnma*	*Pnma*	$Pm\overline{3}m$
a (Å)		5.2884 (1)	5.3125 (1)	5.3288 (2)	5.3426 (1)	3.7901 (1)
b (Å)		7.4639 (1)	7.5239 (1)	7.5463 (1)	7.5595 (1)	
c (Å)		5.2748 (1)	5.3153 (1)	5.3310 (2)	5.3363 (1)	
V* (Å^3)		52.05	53.12	53.73	53.88	54.44
Ca	x	0.0311 (3)	0.0196 (6)	0.0099 (8)	0.0052 (8)	0.5
	y	0.25	0.25	0.25	0.25	0.5
	z	- 0.0082 (9)	- 0.0038 (15)	- 0.0042 (20)	- 0.0023 (2)	0.5
	Biso (Å^2)	0.45 (3)	1.543 (4)	1.783 (4)	1.736 (3)	2.41 (3)
	occupancy	0.5	0.5	0.5	0.5	1
Mn / Nb	x	0	0	0	0	0
	y	0	0	0	0	0
	z	0.5	0.5	0.5	0.5	0
	Biso (Å^2)	0.30 (2)	0.77 (2)	0.60 (3)	0.55 (3)	0.92 (3)
	occupancy	0.49 / 0.01	0.49 / 0.01	0.49 / 0.01	0.49 / 0.01	0.98 / 0.02
O$_{ap}$	x	0.4875 (10)	0.4817 (19)	0.4704 (23)	0.4675 (23)	0.5
	y	0.25	0.25	0.25	0.25	0
	z	0.0765 (19)	0.0686 (25)	0.0279 (27)	0.0175 (30)	0
	Biso (Å^2)	0.37 (2)	2.60 (3)	1.07 (3)	0.931 (3)	0
	occupancy	0.5	0.5	0.5	0.5	3
O$_{eq}$	x	0.2861 (10)	0.2835 (22)	0.2866 (21)	0.2840 (19)	
	y	0.0281 (10)	0.0295 (9)	0.0472 (9)	0.0421 (7)	
	z	0.7084 (10)	0.7155 (22)	0.7205 (23)	0.7181 (17)	
	Biso (Å^2)	0.50*	0.50*	0.439 (18)	0.623 (16)	
	occupancy	1	1	1	1	
R$_{wp}$		4.1	4.04	4.06	3.96	3.9
R$_p$		3.12	3.08	2.98	3.1	2.95
χ^2		1.9	2	1.91	1.82	1.87

Table 5.8: Refined structural parameters and atomic positions of the $CaMn_{0.98}Nb_{0.02}O_3$ phase recorded at different temperatures during in situ high-temperature XRPD measurements. Atoms are located at the following Wyckoff positions: for the *Pnma* S.G.: Ca: (4c), Mn / Nb: (4b), O$_{ap}$: (4c) and O$_{eq}$: (8d); for the $Pm\overline{3}m$ S.G.: Ca: (1a) , Mn/Nb: (1b), O: (3c). (* The cell volumes are calculated based on the cubic cell).

The refined structural parameters, atomic positions and agreement factors from the high-temperature XRPD data are summarized in Table 5.8. The evolution of the lattice parameters and cell volume upon heating are presented in Figure 5.29 a). The thermal expansion causes a near linear increase of the lattice parameters within the studied temperature range. As a consequence, a progressive expansion of the cell volume is observed corresponding to a thermal expansion of 4.4% while heating from 298 K to 1173 K. Table 5.9 presents the Mn-$O_{apical/equatorial}$ distances and the distortion angles at the different temperatures. Figure 5.29 b) reports on the evolution of average bond lengths (Mn-O) and bond angles (Mn-O-Mn) upon heating. A continuous increase of both structural parameters is observed until the structural transition temperature. At higher temperatures, i.e. above T_s, refined bond lengths and angles correspond to values characteristic of the cubic symmetry.

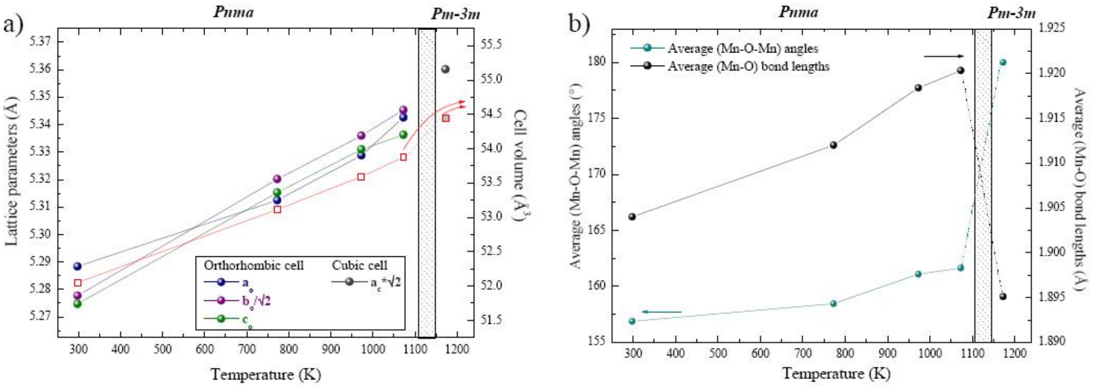

Figure 5.29: Temperature dependences of a) the lattice parameters, cell volumes, b) average (Mn-O-Mn) angles and (Mn-O) bond lengths of the $CaMn_{0.98}Nb_{0.02}O_3$ phase. (The lattice parameters are presented along the orthorhombic frame, where $a_o/\sqrt{2} \simeq c_o/\sqrt{2} \simeq a_c$ and $b_o/2 = a_c$. The cell volumes are calculated based on the cubic cell).

Temperature	298 K	773 K	973 K	1073 K	1173 K
S. G.	*Pnma*	*Pnma*	*Pnma*	*Pnma*	$Pm\overline{3}m$
Mn-O_{ap} x 2 (Å)	1.910 (2)	1.919 (3)	1.899 (2)	1.900 (2)	1.895 (1)
Mn-O_{eq1} x 2 (Å)	1.882 (6)	1.905 (11)	1.957 (11)	1.939 (10)	
Mn-O_{eq2} x 2 (Å)	1.920 (6)	1.912 (11)	1.899 (11)	1.922 (9)	
Mn-O_{ap}-Mn (°)	155.43 (9)	157.19 (13)	166.77 (7)	168.15 (5)	180.00 (1)
Mn-O_{eq}-Mn (°)	158.3 (2)	159.7 (4)	155.6 (4)	155.8 (4)	

Table 5.9: Bond distances and distortion angles of the $CaMn_{0.98}Nb_{0.02}O_3$ phase recorded at different temperatures during in situ high-temperature XRPD measurements.

With respect to the orthorhombic and cubic crystal structures, it should be pointed out that both symmetries involve divergences from each other with respect to the structural parameter, i.e. atomic displacement variations, changes in bond lengths and angles. Figures 5.30 a) and b) (at left) depict the low-temperature distorted orthorhombic and the high-temperature undistorted cubic structural models, respectively. Evidently, structural deviations emerge between the orthorhombic and the cubic symmetries. Schematic representations of the bent and linear (Mn-O-Mn) orbitals is presented in Figures 5.30 a) and b) (at right) corresponding to the orthorhombic and cubic symmetries, respectively. Consequently, the (o → c) structural transition induces certainly changes of the overlap between the O $2p$ and Mn $3d$ orbitals. Such variation of the electronic band structure leads to modifications of the electrical and thermal transport properties.

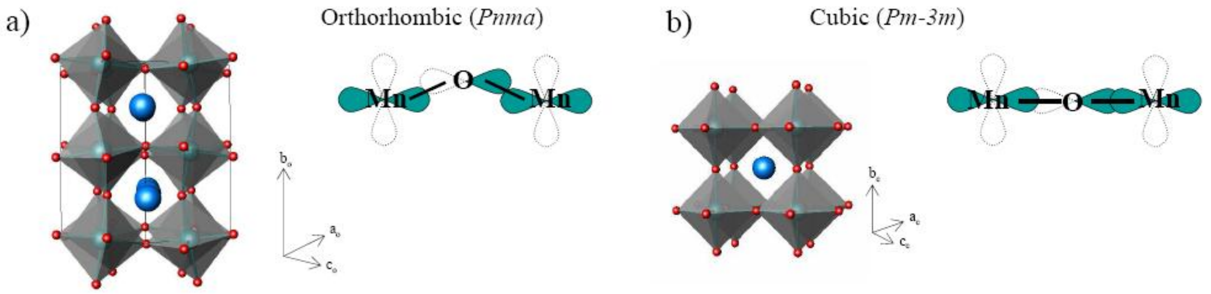

Figure 5.30: Schematic representations of a) the orthorhombic ($Pnma$) and b) the cubic ($Pm\overline{3}m$) crystal structure, respectively. The right draws illustrate the overlap of the O *2p* and the Mn *3d* orbitals, i.e. the a) bent and the b) linear (Mn-O-Mn) orbitals, respectively.

In addition to the high-temperature XRPD measurements, in situ high-temperature ED of the $CaMn_{0.98}Nb_{0.02}O_3$ phase was performed focused on a zone axis which comprises information about the long $\widehat{b}$ axis, characteristic of the orthorhombic structure with $Pnma$ S.G. In Figure 5.31 a), the experimental ED pattern, recorded at room temperature, is indexed in the orthorhombic phase with the $[10\text{-}1]_o$ zone axis. The additional set of diffraction spots, indicated with red rings, confirms the $\widehat{b}$ axis orientation. Examining high-order reflections, e.g. $(-2-4-2)_o$ or $(-1-6-1)_o$ indicated by arrows, spots splitting by $2\Phi \approx 0.295°$ can be distinguished. Spot splitting is caused by a slight discrepancy in the lattice parameters values between the a_o and c_o axes, in the present case. The spot splitting of the two superposed domains can be calculated by the following Equation [Zandbergen-1987]:

$$\Phi = \frac{\pi}{2} \; - \; 2 \; arctg \; (\frac{c_o}{a_o}) \tag{5.3}$$

where a_o and c_o are the lattice parameters of the orthorhombic cell. The high-temperature ED pattern, shown in Figure 5.31 b), can be indexed in the cubic perovskite structure, i.e. with $[001]_c$ zone axis, since no additional set of diffraction spots is observed. The diffraction pattern was carefully recorded on the same region of the particle at room temperature and at T = 770 K. This result confirms the structural transformation from orthorhombic to cubic structure with increasing temperature, as concluded from structural Rietveld refinements. Since the $[010]_o$ 90° rotation twins are a characteristic microstructure of the orthorhombic structure, detwinning phenomenon occurs by reduction of the fourfold rotation axis during the (o → c) structural transition [Wang-2006].

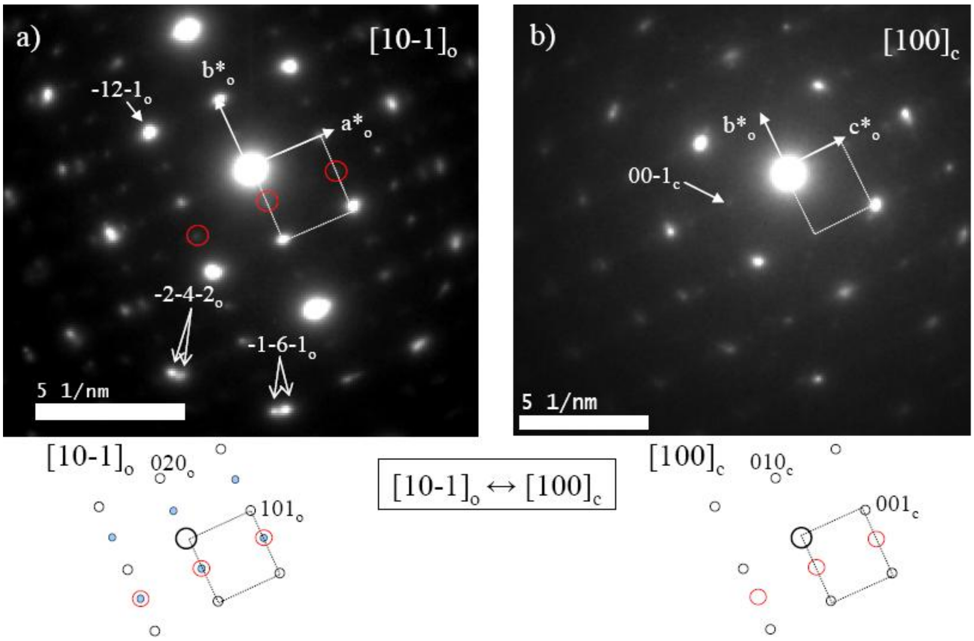

Figure 5.31: In situ high-temperature ED of the CaMn$_{0.98}$Nb$_{0.02}$O$_3$ phase recorded a) at 298 K and b) 770 K. Schematic interpretations of the ED patterns are represented below the figures.

5.4.2.2 Reversible thermal reduction/re-oxidation processes

The thermal stability of the potential thermoelectric manganate phases is evaluated by means of thermogravimetric analyses. Successive in-situ thermal cycles were performed on the CaMn$_{0.98}$Nb$_{0.02}$O$_{2.98}$ phase under synthetic air atmosphere until T = 1253 K. Figure 5.32 a) reveals a weight loss upon heating and a gain of weight upon cooling, recovering the starting sample weight. The loss/gain of weight are related to a reversible oxygen release/uptake, respectively, since the cationic composition remains constant during the thermal experiments.

The subsequent and reproducible thermal reduction and re-oxidation processes occur above T_{HT}[1] = 1090 K in the CaMn$_{0.98}$Nb$_{0.02}$O$_3$ phase. From the thermogravimetric data, the oxygen deficiency δ is determined to be equal to $\delta = 0.047 \pm 0.02$ up to 1253 K. No further oxygen release is observed while sustaining the compound at $T > T_{HT}$ for a one-hour isothermal step. Similar investigations on the CaMn$_{1-x}$Nb$_x$O$_3$ phases present a shift of T_{HT} to higher temperatures with increasing Nb content, i.e. for x = 0.05: $T_{HT} \simeq 1145$ K and for x = 0.08: $T_{HT} \simeq 1180$ K,

---

[1] hereafter, the onset temperature related to the thermal reduction will be termed T_{HT}.

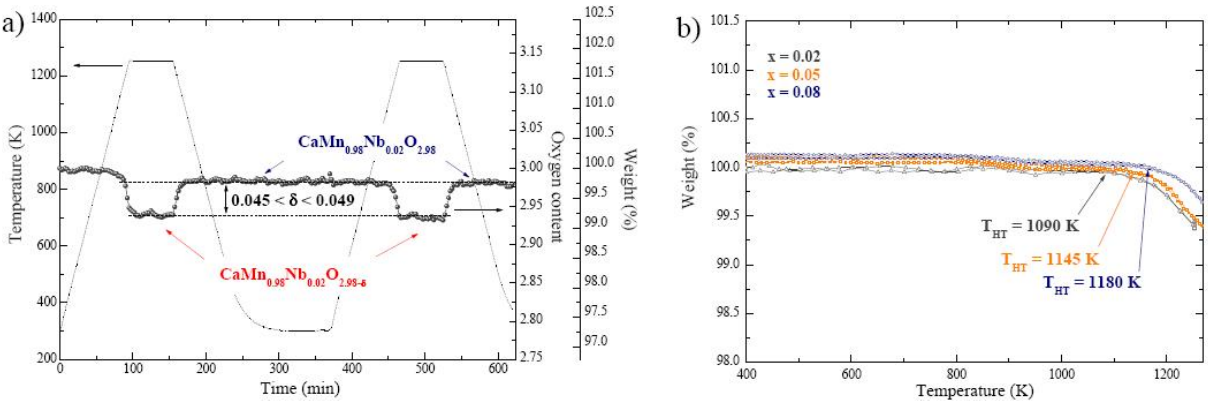

Figure 5.32: In situ thermogravimetric analyses of a) $CaMn_{0.98}Nb_{0.02}O_{2.98}$ and b) $CaMn_{1-x}Nb_xO_3$ (with x = 0.02, 0.05, and 0.08) phases upon heating and cooling cycles under synthetic air atmosphere. Two successive thermal cycles including an one-hour isothermal step at T = 1253 K are presented in Figure a).

as reported in Figure 5.32 b). Previous studies on the $CaMnO_3$ phase reveal a thermal instability above 930 K under air and oxygen atmospheres, reflecting the formation of oxygen vacancies [Dabrowski-2003]. Inserting cations with higher electronegativity, i.e. $\chi_{Mn} = 1.55$ and $\chi_{Nb} = 1.60$, reduces the tendency to form oxygen vacancies. Hence, the thermal stability of the $CaMn_{1-x}Nb_xO_3$ phases can be tuned depending on the Nb substitution levels. Furthermore, the onset of the thermal reduction temperature T_{HT} apparently corresponds to the structural transition temperature T_s. For instance, the XRPD results of the $CaMn_{0.98}Nb_{0.02}O_3$ phase confirm the corresponding thermogravimetric analyses. Dabrowski *et al.* previously argued that the oxygen vacancy formation is directly related to the structural transition from orthorhombic to cubic symmetry in the $Sr_{1-x}Ca_xMnO_3$ phases [Dabrowski-2003]. Based on this hypothesis, a possible mechanism relating the structural transition and the thermal reduction is proposed. On one hand, detwinning phenomena cause structural reconstructions where domain boundaries disappear to accommodate the cubic structure. On the other hand, small amount of oxygen might be released at the twinned domain boundaries. The oxygen vacancy formation and the detwinning of the orthorhombic structure might be interdependent phenomena.

It should be pointed out that the in situ high-temperature TEM investigations were performed under vacuum, therefore a possible thermal reduction could already occur at 500 K < T < 700 K inducing a structural transformation of the phase at lower temperatures than under ambient conditions. The ED pattern recorded at 770 K could be indexed as cubic perovskite structure under vacuum conditions while the structural transition temperature has been defined at 1073 K < T_s < 1173 K from the high-temperature XRPD studies under ambient conditions.

It should be pointed out that the high-temperature study is mainly focused on the $CaMn_{0.98}Nb_{0.02}O_3$ phase which exhibits the lowest thermal reduction temperature among the studied phases since available techniques and equipments could be used only up to 1273 K.

5.4.2.3 Influence on thermoelectric properties

The electrical and thermal transport properties are investigated considering that they could be modified either by (i) the structural transition, by (ii) the thermal reduction/re-oxidation, or simultaneously by (iii) both phenomena. Figure 5.33 presents the temperature dependence of the Seebeck coefficient for the $CaMn_{1-x}Nb_xO_3$ series (for x = 0.02, 0.05, 0.08 and 0.10). Equal thermopower values are obtained upon heating and cooling processes under ambient air atmosphere. This finding indicates that no gradual deterioration of the compounds and their related thermoelectric properties occur after several thermal cycles up to 1273 K. Two different S(T) behaviors can be distinguished in the studied temperature range for all the compositions. The low-temperature region presents a nearly linear temperature dependence of S, characteristic of a polaronic conduction, as previously discussed in this Chapter, Section 5.3.1. A drop of the absolute Seebeck coefficient values is observed above a certain boundary temperature, as indicated by the dotted line on the Figure. The comparison of the thermopower curves for all the studied compositions suggests that an increase of the Nb concentration yields a shift of the S(T) drop to higher temperatures, e.g. from T_{HT} = 1090 K for x = 0.02 to T_{HT} = 1200 K for x = 0.10. In analogy to the thermogravimetric results, this boundary temperature can be assigned to the onset temperature of the thermal reduction process T_{HT}. The sudden change of S(T) slope at $T \simeq T_{HT}$ indicates a modification of the electronic conduction in the high-temperature region.

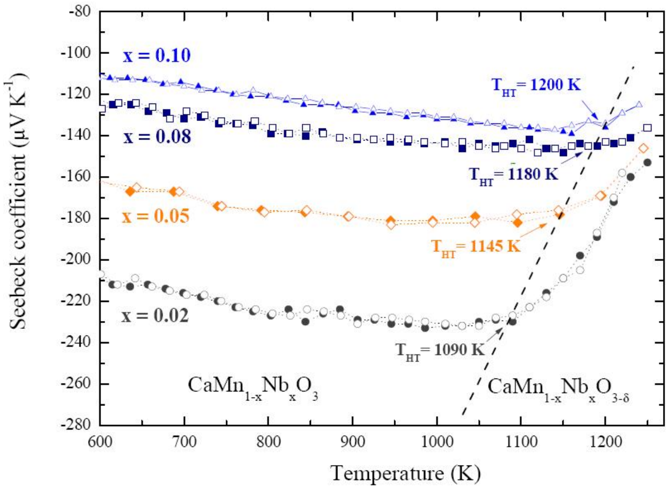

Figure 5.33: Temperature dependence of the Seebeck coefficient for $CaMn_{1-x}Nb_xO_3$ (for x = 0.02, 0.05, 0.08 and 0.10) while heating (closed symbols) and cooling (open symbols) under air atmosphere. The dotted line is just intended to guide the eye with respect to the transition temperature evolution.

The Nb^{5+} insertion in the $CaMnO_3$ insulating phase typically corresponds to an electron doping in the e_g band [Maignan-1998a]. The decrease of $|S|$, above the transition temperature, can be interpreted either as a modification of the band structure due to the structural transition or as an increase of the Mn^{3+} concentration in the Mn^{4+} matrix related to the thermal reduction. On one side, the structural transition from orthorhombic to cubic symmetry leads to a lowering of the overlap between the Mn $3d$ and the O $2p$ orbitals, which therefore influences the transport properties, as previously reported for cobaltate phases [Robert-2007b]. On the other side, the thermal reduction induces oxygen-deficient compounds in which the concentration of Mn^{3+}/Mn^{4+} varies to satisfy the electroneutrality. For systems having mixed valence cations, the Heikes formalism states that the thermopower should tend to $S_{Heikes} = -\frac{k_B}{|e|} \ln \beta_m \frac{1-x}{x}$ in the high temperature limit (where k_B is the Boltzmann constant, x is the charge carrier concentration, and β_m is the degeneracy factor. In the present case, β_m is close to the unity, i.e. $\beta_m = \frac{5}{4}$, satisfying the Heikes formula.) [Doumerc-1994, Heikes-1961], and can be applied at high temperatures for S nearly constant. At high temperatures, the 2% Nb-containing $CaMnO_3$ compound present a $S_{1060K} = -231$ μV K^{-1}, that corresponds to 6% of Mn^{3+} in the manganese sublattice. The thermogravimetric studies previously reveal an oxygen deficiency of $\delta = 0.047 \pm 0.02$ for the high-temperature phase, i.e. $CaMn_{0.98}Nb_{0.02}O_{2.98}$. This reduced compound has a $S_{1273\ K} = -152$ μV K^{-1} corresponding to 14.5% of Mn^{3+} in the Mn^{4+} matrix. With respect to the electroneutrality, the 6% and 14.5% Mn^{3+}-containing phases correspond to $CaMn_{0.98}Nb_{0.02}O_{2.980}$ and $CaMn_{0.98}Nb_{0.02}O_{2.935}$ phases, respectively. The oxygen deficiency determined from the Seebeck coefficient data is equal to $\delta = 0.045$, which fits well with the thermogravimetric results. This finding confirms the influence of the thermal reduction process on the Mn^{3+} concentration and therefore on the thermopower temperature dependence. As a result, upon cooling, the thermal re-oxidation allows to recover the starting Mn^{3+} concentration at room temperature, inducing identical S(T) values after several thermal cycles.

Figure 5.34 a) presents the temperature dependence of the electrical resistivity for the $CaMn_{1-x}Nb_xO_3$ phases with x = 0.02, 0.05, and 0.08. The ρ(T) curve of the 2% Nb-containing $CaMnO_3$ first presents a slope change at T $\simeq$ 800 K leading to nearly constant resistivity values. This could be considered as the onset of the structural transition. At T $>$ 1050 K, a decrease of ρ(T) is clearly observed and fits to the thermopower drop observed at this temperature, as indicated by the dotted line in the Figure. This last finding confirms the variation of the charge carriers concentration in terms of an increase of the Mn^{3+} concentration above T_{HT}. Similar changes of ρ(T) slopes are observed for the 5% Nb- and 8% Nb-containing $CaMnO_3$ phases. Moreover, the electrical resistivity values converge to a metallic resistivity value of 16 mΩ cm for all studied phases, which can be directly correlated to the thermopower evolution in the high-temperature limit. The influence of the oxygen deficiency on the electrical resistivity in $CaMnO_{3-\delta}$ phase has been previously reported by Taguchi [Taguchi-1985]. A shift of the resistivity drop to higher temperatures is observed with increasing the Nb concentrations as a common feature with the thermopower data, and further with the onset temperature of the thermal reduction. The high-temperature thermoelectric properties of the $CaMn_{1-x}Nb_xO_3$ phases are clearly dependent on their Nb content and related thermal stabilities.

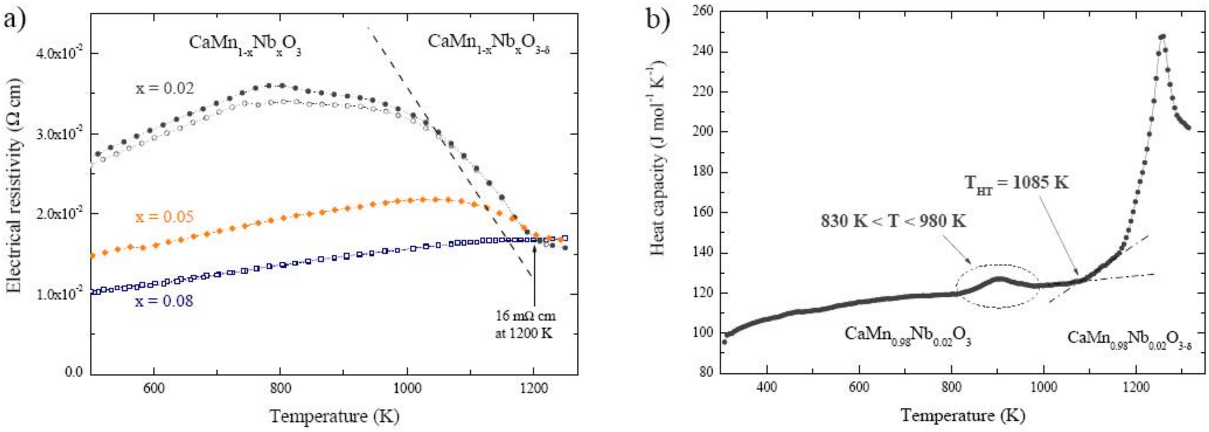

Figure 5.34: a) Temperature dependences of the electrical resistivity for $CaMn_{1-x}Nb_xO_3$ (for x = 0.02, 0.05 and 0.08) while heating (closed symbols) and cooling (open symbols) under air atmosphere and b) the specific heat capacity temperature dependence of $CaMn_{0.98}Nb_{0.02}O_3$. The dotted line is just intended to guide the eye with respect to the transition temperature evolution.

The heat capacity study performed on the 2% Nb-containing $CaMnO_3$ phase is reported in Figure 5.34 b). The manganate phase undergoes two successive endothermic thermal events, at 830 K $< T_1 <$ 980 K and at $T_2 >$ 1085 K, upon heating to 1273 K in ambient air atmosphere. The second peak is energetically more significant than the first one. Previous work on the $CaMnO_{3-\delta}$ phase reported on two endothermic peaks fitting with a weight loss observed by thermogravimetric analysis [Taguchi-1989]. DSC methods allow to monitor enthalpy variations and therefore to observe structural transitions [Aguirre-2008]. However, DSC measurements are also sensitive to thermal reduction events since this process involves changes in the anionic composition. In analogy with the resistivity data, the first peak (T_1) can be assigned to the onset temperature of the structural transition and the second one (T_2) could correspond to the onset temperature of the thermal reduction process. Since different heating rates were used depending on the characterization methods, these assumptions should be carefully considered.

The influence of the oxygen content variation on the thermopower is studied in details by investigating (i) stoichiometric and (ii) oxygen-deficient $CaMn_{0.98}Nb_{0.02}O_{3-\delta}$ phases, i.e. (i) $CaMn_{0.98}Nb_{0.02}O_{2.980}$ and (ii) $CaMn_{0.98}Nb_{0.02}O_{2.965}$, also referred as (i) $\delta = 0.002$ and (ii) $\delta = 0.035$, respectively. The oxygen-deficient manganate phase was obtained by quenching the sample at $T > T_{HT}$, i.e. T = 1273 K. Both samples were investigated during heating/cooling cycles under air to evaluate their oxygen release/uptake capabilities and the direct influence on the thermopower. Figure 5.35 presents S(T) of the oxidized and the reduced compounds. At low temperatures, i.e. at T = 500 K, both phases present different thermopower values. Higher absolute Seebeck coefficient values are obtained for the $CaMn_{0.98}Nb_{0.02}O_{2.980}$ phase compared

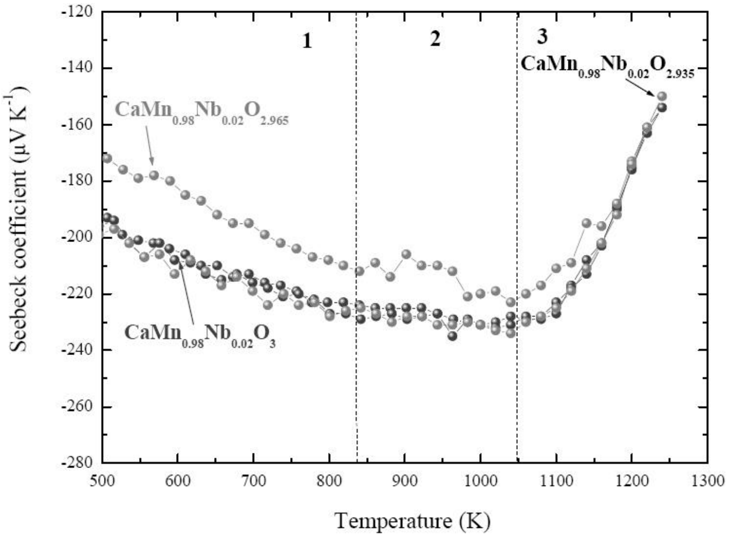

Figure 5.35: Seebeck coefficient temperature dependence of stoichiometric and oxygen deficient $CaMn_{0.98}Nb_{0.02}O_{3-\delta}$ phases upon successive heating and cooling under air atmospheres. Prior to the measurement, the non-stoichiometric compound was prepared by quenching in liquid nitrogen after a 60h isothermal step at T = 1273 K.

to the $CaMn_{0.98}Nb_{0.02}O_{2.965}$ compound, e.g. at T = 500 K: $S_{(\delta\ =\ 0.002)} = -193\ \mu V\ K^{-1}$ and $S_{(\delta\ =\ 0.035)} = -172\ \mu V\ K^{-1}$. The $CaMn_{0.98}Nb_{0.02}O_{2.980}$ phase presents lower $[Mn^{3+}]/[Mn^{4+}]$ ratio than the $CaMn_{0.98}Nb_{0.02}O_{2.965}$ compound involving therefore higher absolute thermopower values according to the Heikes formula. Upon heating (step 1 to 2), the non-stoichiometric $CaMn_{0.98}Nb_{0.02}O_{2.965}$ phase first reveals a linear temperature dependence of S(T) until T $\simeq$ 840 K (zone A). Above this temperature (zones B and C), the characteristic thermopower evolution, i.e. $S(T) \sim T$, is not further observed indicating a variation of the Mn^{3+} concentration and therefore of the oxygen content. From T_{HT} = 1090 K, the non-stoichiometric phase undergoes an additional thermal reduction corresponding to a sudden drop of S(T) to lower absolute thermopower values, i.e. higher Mn^{3+} concentration. Upon cooling (step 2 to 3), the re-oxidation process takes place resulting in identical thermopower values as reported for the stoichiometric phase. This finding indicates that a complete re-oxidation of the non-stoichiometric manganate phases allows to recover the starting $[Mn^{3+}]/[Mn^{4+}]$ ratio of the most stable phase, i.e. the stoichiometric one, leading to the initial thermoelectric properties of the $CaMn_{0.98}Nb_{0.02}O_{2.980}$ phase. The complete re-oxidation of the non-stoichiometric phase is confirmed by a second heating/cooling cycle (step 3 to 5), for which the reoxidized phase exhibits similar thermopower values than the $CaMn_{0.98}Nb_{0.02}O_{2.980}$ phase.

5.5 Conclusions

$CaMn_{1-x}Nb_xO_{3\pm\delta}$ (for x = 0.02, 0.05 and 0.08) perovskite-type phases have been studied concerning their crystal structure, microstructure, thermal stability as well as their magnetic and thermoelectric properties over a broad temperature range, i.e. $5 \text{ K} < \text{T} < 1240 \text{ K}$. The substitution of Mn^{4+} by Nb^{5+} in the CaMnO_3 system induces the creation of Mn^{3+} cations which further influences the structural and the physical properties. Polycrystalline manganates with diverse morphologies and crystallite sizes result from different applied synthesis methods. Complex textural features characterize the $\text{CaMn}_{1-x}\text{Nb}_x\text{O}_3$ phases by means of the presence of 90° twins and intergrowths of Ruddlesden-Popper planar defects involving anti-phase boundaries. Nanosized or nanostructured manganate oxides present particular properties such as the USC-derived phases which strongly suppress the ferromagnetic interactions or the SC series exhibiting thermal conductivities values below $1 \text{ W m}^{-1} \text{ K}^{-1}$. As a result, the SC-derived $\text{CaMn}_{0.98}\text{Nb}_{0.02}\text{O}_3$ phase yields the highest ZT value achieved for n-type polycrystalline perovskites with $ZT_{1060K} = 0.32$. In addition, the high-temperature thermal stability studies remain of main importance with respect to future applications of thermoelectric oxide modules.

Chapter 6

Perovskite-type $LaMn_{1-x}Co_xO_3$

The present chapter is dedicated to $LaMn_{1-x}Co_xO_3$ phases (x = 0.05, 0.10, 0.90, and 0.95) with respect to their morphology, crystal structure and microstructure. The thermoelectric properties of these perovskite-type manganate phases are studied in a wide temperature range, i.e. 300 K < T < 1240 K, as function of the *B*-site composition [Robert-2008].

6.1 Morphology, composition, crystal structure, and microstructure

Polycrystalline perovskite-type $LaMn_{1-x}Co_xO_3$ phases are synthesized by the *"chimie douce"* (SC) synthesis route yielding submicrometer particles, as previously presented in Chapter 4, Section 4.2. The morphology of the sintered pellets is examined by SEM in cross sectional views. Two different types of morphology are observed depending on the predominance of the transition metal in the $LaMn_{1-x}Co_xO_3$ phases (x = 0.05, 0.10, 0.90, and 0.95), as shown in Figures 6.1 a) and b). The Co-rich compounds present compacted polyhedral grains ranging from 1.5 μm to 4 μm in length. The Mn-rich phases reveal individual round-shaped sintered particles mixed with sheet-like shaped grains composed of fine particles having crystallite sizes from 0.5 μm to 1.5 μm in diameter. All sintered pellets exhibit comparable bulk relative densities $\simeq$ 91%.

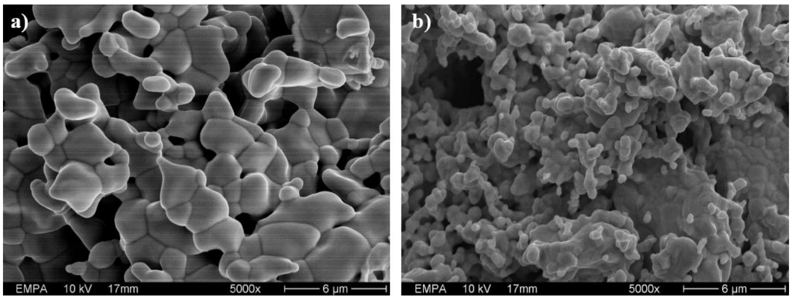

Figure 6.1: Cross sectional SEM images of the a) $LaMn_{0.10}Co_{0.90}O_3$ and b) $LaMn_{0.90}Co_{0.10}O_3$ sintered pellets.

The cationic compositions are analyzed by EDS coupled to the TEM and X-ray fluorescence measurements, both analyses confirm good agreement with nominal compositions[1] and the cationic homogeneity of the synthesized phases. The determination of the oxygen content by thermogravimetric reduction method indicates a slight deficiency of oxygen in the Co-rich compounds, i.e $\delta < 0.06$ for $LaMn_{1-x}Co_xO_{3-\delta}$ (x = 0.90 and 0.95). The Mn-rich phases (x = 0.05 and 0.10) reveal a slight excess of oxygen, i.e $\delta > 0.08$, which rather corresponds to cationic vacancies since the perovskite lattice can not enclosed additional oxygen. This finding has been previously observed in the $LaMnO_3$ phase with aliovalent *A*- or *B*-site substitutions when synthesized under air atmosphere [Autret-2005].

The XRPD data reveal that all compositions are single phase. Two different crystal structures are identified by room-temperature XRPD data regarding the *B*-site composition, as reported in Figures 6.2 a) and b). The Mn-rich $LaMn_{1-x}Co_xO_3$ (x = 0.05 and 0.10) phases crystallize in the orthorhombic structure *Pnma* S.G. with the lattice parameters $a_c\sqrt{2} \times 2a_c \times a_c\sqrt{2}$ (${a_c}^2 \sim 3.9$ Å refers to the lattice parameter of the ideal cubic perovskite structure). The Co-rich compounds (x = 0.90 and 0.95) can be indexed in rhombohedral structure $R\overline{3}c$ S.G. with the lattice parameters close to $a_c\sqrt{2}$ and $\gamma = 60^o$ or in the more common hexagonal setting $a_c\sqrt{2} \times \sim a_c\sqrt{2} \times 2a_c\sqrt{3}$ and $\gamma = 120^o$.

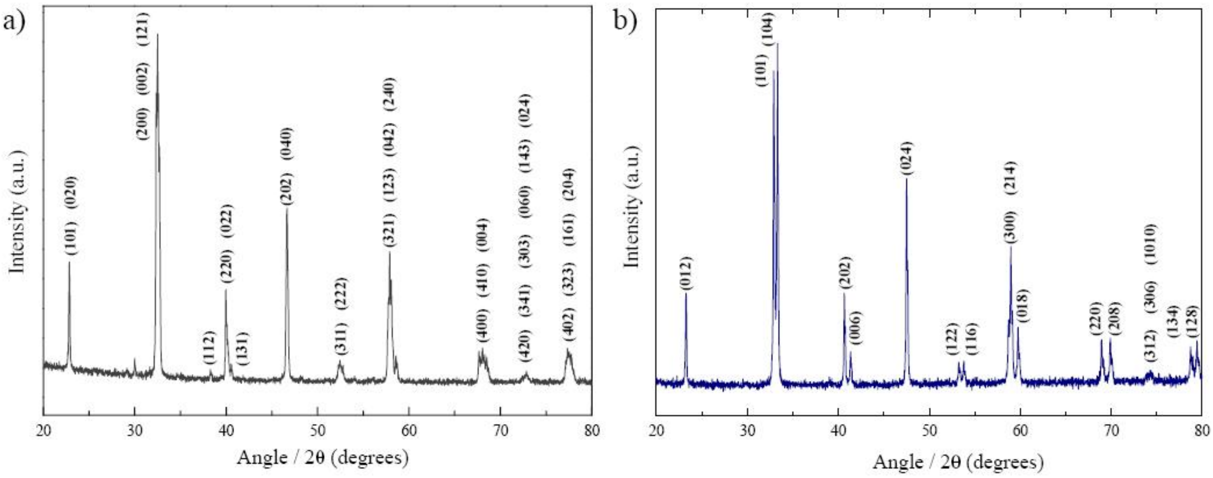

Figure 6.2: Room-temperature XRPD patterns of a) orthorhombic $LaMn_{0.90}Co_{0.10}O_3$ and b) rhombohedral $LaMn_{0.10}Co_{0.90}O_3$ phases.

The microstructural studies of both phases confirm that Mn-rich and Co-rich phases belong to orthorhombic and rhombohedral symmetries, respectively. The $LaMn_{0.10}Co_{0.90}O_3$ phase is

---

[1] with respect to the detection limit of both instruments.

[2] for convenience, information related to the cubic, orthorhombic and rhombohedral crystal structures are labeled with "c", "o", and "r" subscripts, respectively.

characterized by a long-range ordered and crystalline microstructure, as shown in the HRTEM image in Figure 6.3 a). The calculated fast Fourier transform (FFT) of the corresponding HRTEM image can be indexed in rhombohedral crystal structure with lattice parameters of $a_c\sqrt{2} \times a_c\sqrt{2} \times 2a_c\sqrt{3}$, $\gamma = 120°$ (in hexagonal settings). The Mn-rich phases reveal a more complex microstructure with the presence of 90° twinned domains, as earlier observed for the orthorhombic $\mathrm{CaMn_{1-x}Nb_xO_3}$ phases in the Chapter 5, Section 5.2.2.1. The Figure 6.3 b) illustrates this textural feature where nano-sized 90° twins of 100 nm to 150 nm in length are randomly distributed in the plane. The FFT of the corresponding HRTEM image can be indexed in a near cubic $2a_c \times 2a_c \times 2a_c$ lattice. The orthorhombic nature of the Mn-rich phase is confirmed by the presence of an additional set of reflections which are forbidden in the cubic symmetry. The FFT pattern can be regarded as the superposition of two orthorhombic zones axes: $[101]_o$ and $[\text{-}101]_o$, indicating that the twinned domains are oriented at 90° from each other. The orthorhombic $\mathrm{LaMn_{0.90}Co_{0.10}O_3}$ phase yields lattice parameters equal to $a_o = 5.58$ Å, $b_o = 7.79$ Å, and $c_o = 5.53$ Å.

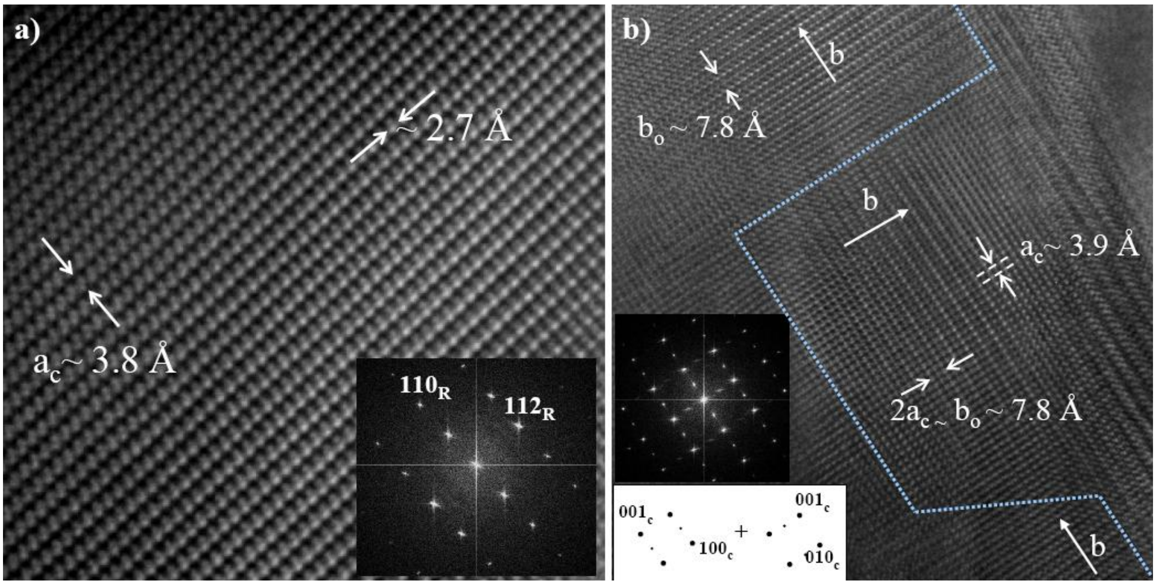

Figure 6.3: HRTEM images of the a) $\mathrm{LaMn_{0.10}Co_{0.90}O_3}$ and b) $\mathrm{LaMn_{0.90}Co_{0.10}O_3}$ phases. The Co-rich phase is indexed in the rhombohedral structure $R\overline{3}c$ S.G. where $a_r \simeq b_r \simeq 5.44$ Å, $c_r = 13.11$ Å, $\gamma = 120°$ (in hexagonal settings). The Mn-rich compound belongs to the orthorhombic structure *Pnma* S.G. where $a_o = 5.58$ Å, $b_o = 7.79$ Å, and $c_o = 5.53$ Å. The Mn-rich phase is characterized by nano-sized 90° twinned domains which are randomly oriented in the plane. Dotted arrows indicate the domain boundary. The inset Figures present the fast Fourier transform (FFT) of the corresponding HRTEM image.

A second example of nano-sized 90° twins is given in Figure 6.4 where the twin boundary is emphasized. The calculated FFTs from the A and B regions indicate the $\widehat{b}$ axis orientation, i.e. either in the plane (region A) or out of the plane (region B) corresponding to $[\text{-}101]_o \leftrightarrow [001]_c$ and $[010]_o \leftrightarrow [010]_c$ zone axes, respectively. A clear structural matching between the twins is observed at the domain boundary without the presence of dislocations. The microstructural studies confirm the highly crystalline and chemically homogeneous nature of the $LaMn_{1-x}Co_xO_3$ phases. No amorphous regions, crystalline impurities or secondary phases are found.

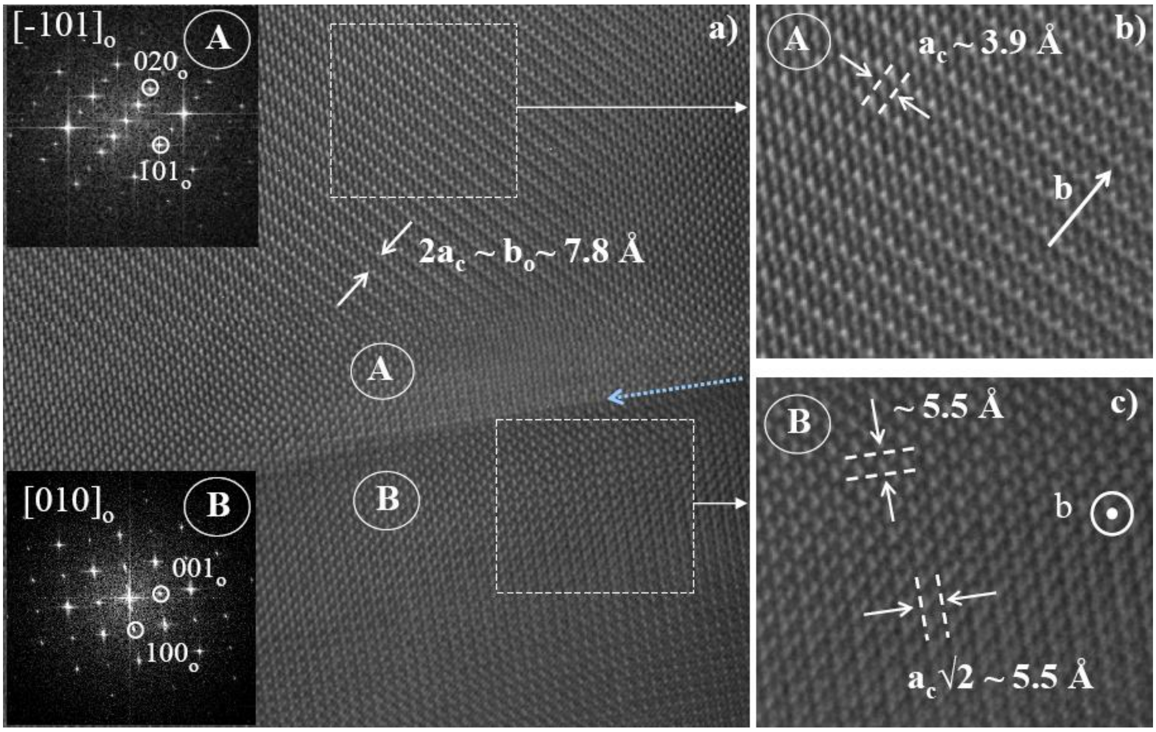

Figure 6.4: HRTEM image of 90° twinned domains in the $LaMn_{0.90}Co_{0.10}O_3$ which is indexed in the orthorhombic structure *Pnma* S.G. where $b_o = 2a_c = 7.8$ Å which are close related to cubic perovskite parameters by $a_c\sqrt{2} \times 2a_c \times a_c\sqrt{2}$. The twins are perpendicularly oriented in the plane (region A) or out of the plane (region B). Dotted arrows indicate the domain boundary.

6.2 Thermoelectric properties

6.2.1 Electrical resistivity and thermopower

Figure 6.5 a) represents the electrical resistivity temperature dependence for the $LaMn_{1-x}Co_xO_3$ phases (x = 0.05, 0.10, 0.90 and 0.95) within the range of 320 K < T < 1240 K. All the studied phases present a semiconducting-like behavior, i.e. $d\rho/d\mathrm{T} < 0$. The Co-rich phases reveal a resistivity drop at T > 520 K which can be associated to the transition from intermediate-spin Co^{3+} ($t_{2g}^5e_g^1$) to high-spin Co^{3+} ($t_{2g}^4e_g^2$) states often observed in the $LaCoO_3$ system [Yamaguchi-1996], as previously discussed in the Chapter 2, Section 2.3.3.2 and already reported for others cobaltate-doped phases [Hébert-2007, Robert-2007c]. Above 800 K, the Co-rich compounds are highly conductive leading to constant and low electrical resistivity values, e.g. at T = 1240K: $\rho = 1.35$ mΩ cm for x = 0.90 and $\rho = 1.21$ mΩ cm for x = 0.95. The Mn-rich phases (x = 0.05 and 0.10) exhibit resistivity values of one order of magnitude higher than the Co-rich counterpart phases, e.g. at T = 1240K: ρ = 10.40 mΩ cm for x = 0.05 and ρ = 12.62 mΩ cm for x = 0.10. The thermally-activated ρ(T) behaviors of all the studied phases follow the Arrhenius law, i.e. $\rho = (\exp E_a/k_BT)$, where E$_a$ is the activation energy and k_B is the Boltzmann constant. The calculated activation energy temperature dependence is reported for the $LaMn_{1-x}Co_xO_3$ phases (x = 0.05, 0.10, 0.90 and 0.95) in Figure 6.5 b). The influence of the spin state transition is clearly evidenced in the Co-rich phases for which maximal E$_a$ values are observed at T $\simeq$ 520K , i.e. E$_a$ = 0.36 eV for x = 0.95 and E$_a$ = 0.28 eV for x = 0.90. The Mn-rich compounds present nearly constant E$_a$ values within the temperature range of 450 K < T < 900 K, e.g. E$_a$ = 0.16 eV for x = 0.10 at T = 520 K. Despite the $LaMn_{1-x}Co_xO_3$ phases (x = 0.90 and 0.95) present semiconducting-like behavior and the $CaMn_{1-x}Nb_xO_3$ have a metallic-like conduction regime, the Mn-rich phases present electrical resistivity values in the same range as the $CaMn_{1-x}Nb_xO_3$ phases, e.g. for 5% charge carrier concentration: $\rho_{1000\ K}$ = 13.6mΩ cm for $LaMn_{0.95}Co_{0.05}O_3$ and $\rho_{1000\ K}$ = 16.8mΩ cm for $CaMn_{0.95}Nb_{0.05}O_3$.

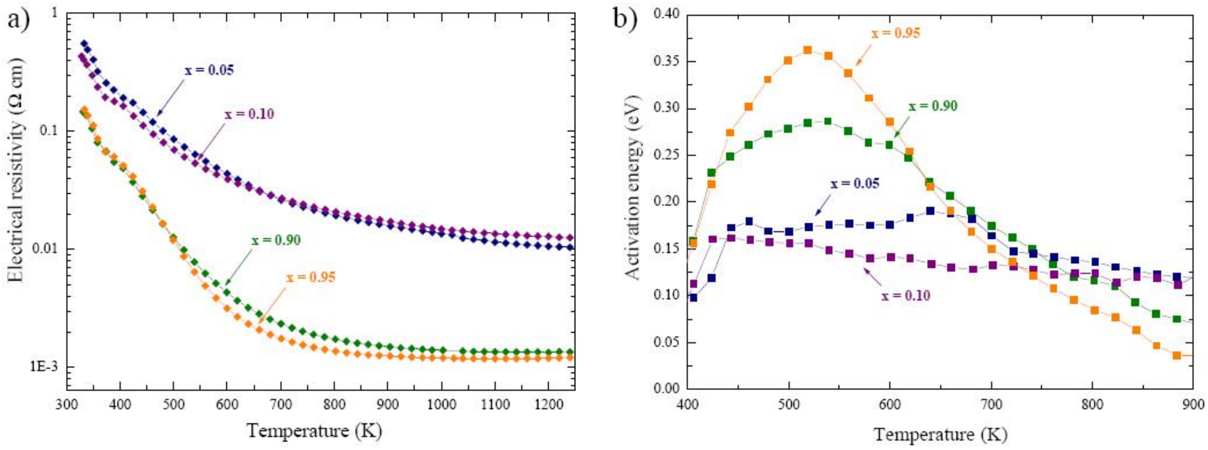

Figure 6.5: Temperature dependences of a) the electrical resistivity and b) the activation energy for the $LaMn_{1-x}Co_xO_3$ phases (x = 0.05, 0.10, 0.90, and 0.95).

The Seebeck coefficient temperature dependence is presented in Figure 6.6 for all the studied phases. The sign and the value of the thermopower depend mainly on the nature and the concentration of the charge carriers. The substitution of Mn^{3+} by Co^{2+} in the $LaMnO_3$ matrix induces the formation of a Mn^{3+}/Mn^{4+} mixed valence system. Therefore, the Mn-rich phases (x = 0.05 and 0.10) exhibit positive Seebeck coefficient representative of predominant hole charge carriers. Upon Co substitution, the thermopower decreases with increasing the Co concentration while its temperature dependence preserves an activated behavior. In contrary, negative thermopower values are observed in $LaCoO_3$-doped phases when a tetravalent cation is substituted at the *A*-site, e.g. Ce, or at the *B*-site position, e.g. Mn [Maignan-2004]. In the Co-rich phases, electron carriers are created by substituting Co^{3+} by Mn^{4+} which subsequently induces the creation of

Co^{2+} cations. Thus, 5% Mn-containing $LaCoO_3$ phase results in a negative seebeck coefficient value of $S = -78.9$ μV K^{-1} at T = 340 K.

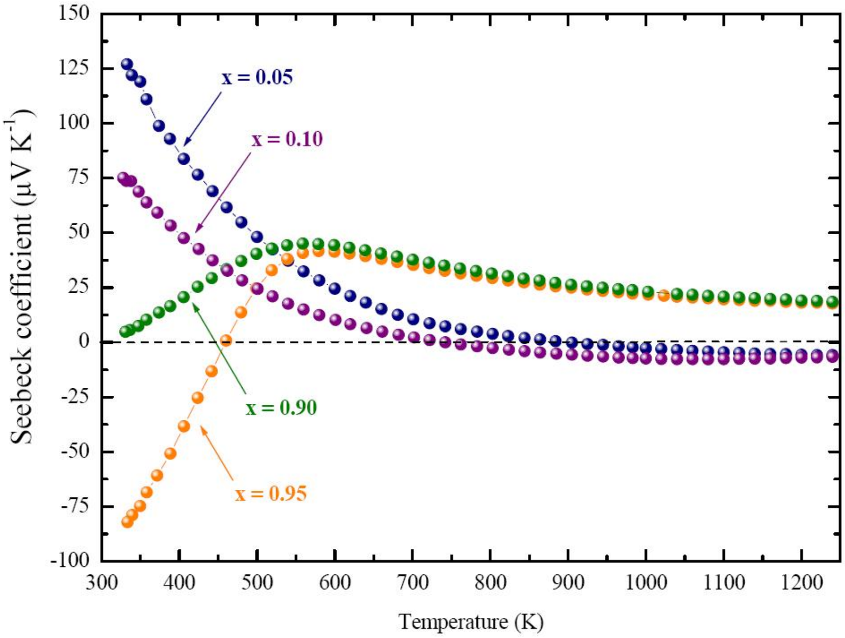

Figure 6.6: Temperature dependence of the Seebeck coefficient for the $LaMn_{1-x}Co_xO_3$ phases (x = 0.05, 0.10, 0.90, and 0.95).

Both Co-rich phases (x = 0.90 and 0.95) present the same thermopower temperature dependence. In the temperature range of 340 K < T < 550 K, the Seebeck coefficient increases with increasing the temperature, i.e. $dS/d\mathrm{T} > 0$. Above T $\simeq$ 550 K, a change to negative slope is observed, i.e. the thermopower decreases with increasing the temperature, as described for the $LaCoO_3$ phase [Heikes-1964]. $LaMnO_3$ perovskite-type phase is characterized by a large Seebeck coefficient at room temperature, i.e. $S = 450$ μV K^{-1} [Autret-2005]. The Mn-rich phases (x = 0.05 and 0.10) exhibit positive Seebeck coefficient values up to T = 700 K. At higher temperatures, S(T) decreases to small negative values becoming temperature-independent at T > 1000 K, e.g. $S_{1240\ K} = -5.35$ μV K^{-1} for x = 0.05 and $S_{1240\ K} = -6.65$ μV K^{-1} for x = 0.10.

6.2.2 Thermal conductivity and figure of merit

The thermal transport properties of the $LaMn_{1-x}Co_xO_3$ phases (x = 0.05, 0.10, 0.90, and 0.95) are summarized in Figures 6.7 a) and b). As a general tendency, an increase of the thermal conductivity is observed for all the studied phases with increasing the temperature. Despite that, κ(T) yields different temperature dependence evolution depending on the predominance of the transition metal. The Mn-rich phases exhibit low thermal conductivity values at room temperature, i.e. $\kappa < 1.5$ W m^{-1} K^{-1}, which correspond to usual thermal conductivity values for $LaMnO_3$-doped phases [Battabyal-2006], and reveal a slight increase of the thermal conductivity at higher temperatures, e.g. $\kappa_{1000\ K} = 2.2$ W m^{-1} K^{-1} for x = 0.10. The Co-rich phases display also low thermal conductivity values, i.e. $\kappa < 2$ W m^{-1} K^{-1} within the temperature range of 300 K < T< 500 K. At higher temperatures, an important increase of κ(T) is observed for the Co-rich phases leading to $\kappa_{1000\ K} = 3.8$ W m^{-1} K^{-1} for x = 0.95. The thermal conductivity can be expressed as the sum of the electronic and lattice contributions, i.e. $\kappa = \kappa_{lattice} + \kappa_{el}$. The electronic component is determined by applying the Wiedemann-Franz law [Kittel-2004], as earlier introduced in Chapter 2, Section 2.2.2.2. Figure 6.7 b) presents the lattice and electronic contributions for the LaMn$_{1-x}$Co$_x$O$_3$ phases (x = 0.10 and 0.90). The electronic component κ_{el} remains almost negligible for the LaMn$_{0.90}$Co$_{0.10}$O$_3$ phase over the investigated temperature range since it contributes 7.7% to the total thermal conductivity at 1020 K. The predominance of the lattice thermal conductivity in the Mn-rich phases are in good agreements with previous results reported for the CaMn$_{1-x}$Nb$_x$O$_3$ phases in the Chapter 5, Section 5.3.2. In the Co-rich phase, i.e. LaMn$_{0.10}$Co$_{0.90}$O$_3$, $\kappa_{lattice}$ represents the main contribution to the thermal conductivity below 500 K. At higher temperatures, the electronic contribution increases with increasing the temperatures contributing 70% to the total thermal conductivity at 1020 K. This feature can be correlated to the resistivity drop observed at T $\simeq$ 520 K resulting from the spin spate transition. The suppression of $\kappa_{lattice}$ above 500 K has been already reported for the LaCo$_{0.95}$Ni$_{0.05}$O$_3$ phase [Robert-2007c] and could be assigned to Jahn-Teller distortions associated to the intermediate-/high-spin state transition [Yan-2004].

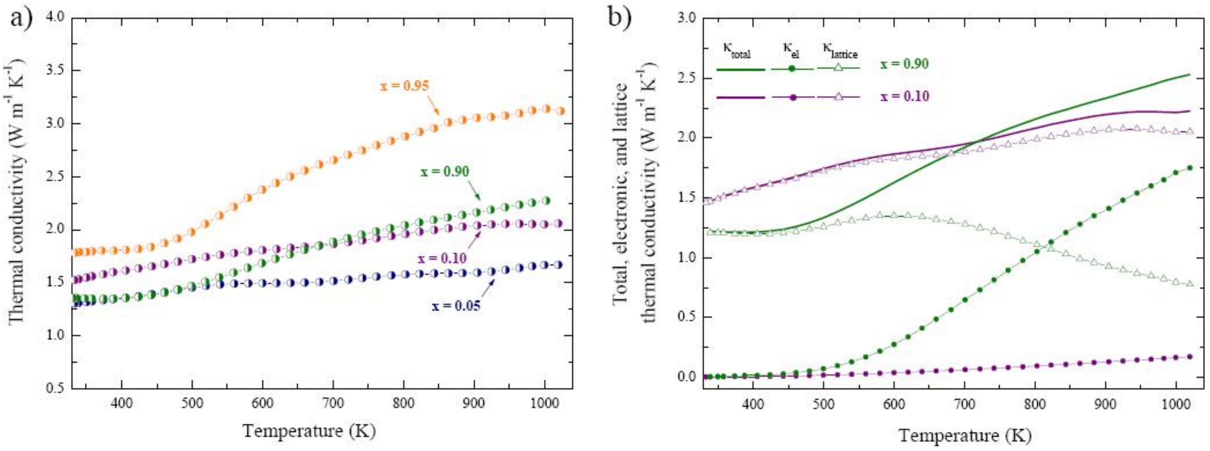

Figure 6.7: a) Total thermal conductivity κ_{total} versus T of the LaMn$_{1-x}$Co$_x$O$_3$ phases (x = 0.05, 0.10, 0.90, and 0.95) and) temperature dependences of the total, electronic κ_{el}, and lattice $\kappa_{lattice}$ thermal conductivities for x = 0.10 and 0.90.

The thermoelectric figure of merit ZT of the Co-rich phases, i.e. LaMn$_{1-x}$Co$_x$O$_3$ phases (x = 0.90 and 0.95), is shown in Figure 6.8. The LaMn$_{0.10}$Co$_{0.90}$O$_3$ phase present the highest ZT value among the investigated LaMn$_{1-x}$Co$_x$O$_3$ phases with a value of $ZT \simeq 0.021$ at 700 K. Since the largest power factor is achieved for the Co-rich phases at 700 K, e.g. PF = 7*10^{-5} W m^{-2} K^{-1}

for x = 0.95, and the thermal conductivity of the Co-rich phases increases significantly above 500 K, higher *ZT* values are limited at higher temperatures.

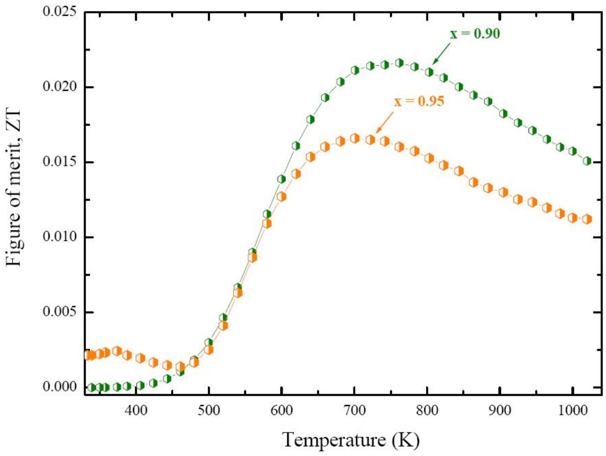

Figure 6.8: Thermoelectric figure of merit *ZT* temperature dependence of the $LaMn_{1-x}Co_xO_3$ phases (x = 0.05, 0.10, 0.90, and 0.95).

6.3 Conclusions

Polycrystalline $LaMn_{1-x}Co_xO_3$ phases (x = 0.05, 0.10, 0.90, and 0.95) crystallize in orthorhombic crystal structure for the Mn-rich phases and in rhombohedral symmetry for the Co-rich counterpart. A typical semiconductor behavior is observed for the $LaMn_{1-x}Co_xO_3$ phases over the investigated temperature region. Depending on the cobalt content, *p*- or *n*-type conduction is achieved at T < 500 K. The Seebeck coefficient temperature dependence of the Co-rich phases reveal a slope change yielding $dS/d\mathrm{T} < 0$ at T $\simeq$ 550 K. The thermal conductivity values of the Mn-rich phases increase slightly with the temperature, the lattice component remaining the main contribution to the total thermal conductivity. The Co-rich phases reveal an important increase of the thermal conductivity above 500 K due to an increase of the electronic contribution in this temperature range. The $LaMn_{0.10}Co_{0.90}O_3$ phase yields a *ZT* value of 0.021 at T = 700 K.

Chapter 7

Summary and conclusions

This thesis aims the development of highly-efficient thermoelectric perovskite-type manganate phases for high-temperature applications through the nanostructuring approach. Different synthesis methods are successfully applied leading to tailor-made perovskite-type oxide particles with various sizes and morphologies. The understanding of the structure-property relationship of the *B*-site substituted manganate phases, i.e. $CaMn_{1-x}Nb_xO_3$ (x = 0.02, 0.05, 0.08, and 0.10) and $LaMn_{1-x}Co_xO_3$ (x = 0.05, 0.10, 0.90, and 0.95), is of particular importance for tuning the electronic properties, i.e. the Seebeck coefficient and the electrical conductivity. Thermoelectric properties of nanostructured materials should depend on the size and the morphology of the textural features. Complex microstructures are therefore studied at the nanoscale to further evaluate their effects on the electrical and thermal transport properties. Perovskite-type manganate phases are investigated with respect to their morphology, crystal structure, microstructure, and thermal stability. Their thermoelectric properties are evaluated within the temperature range of $5 \text{ K} < T < 1270 \text{ K}$.

Different synthesis methods result in highly-crystalline perovskite-type oxides characterized by a diversity of particle sizes, morphologies, and microstructures. The conventional solid state reaction (SSR) method leads to micrometer-sized grains while the "*chimie douce*" synthesis routes produces submicrometer- to nanometer-sized particles, or mesoporous microstructures depending on the thermal decomposition approaches. The versatility of the "*chimie douce*" methods allows a tuning of the experimental synthesis parameters such as the citrate precursor composition or the thermal treatments, those criteria having a direct impact on the particle morphologies and sizes. Furthermore, several examples outline the influence of the morphology and the microstructure on the thermal, electronic, and magnetic properties of the perovskite-type phases. For instance, thermally stable mesoporous titanate phases present lower thermal conductivity values compared to polycrystalline titanate phases synthesized by the conventional SSR method, e.g. at 300 K: $\kappa = 0.57 \text{ W m}^{-1} \text{ K}^{-1}$ for the mesoporous $La_{0.7}Ca_{0.3}TiO_3$ phase and $\kappa = 4.69 \text{ W m}^{-1} \text{ K}^{-1}$ for the SSR-derived $SrTiO_3$ phase. Likewise, $CaMn_{1-x}Nb_xO_3$ phases reveal reduced thermal conductivity values when synthesizing by the "*chimie douce*" (SC) route compared to the SSR-series, e.g. $\kappa < 1$ W m^{-1} K^{-1} for the SC-made phases and $\kappa \simeq 1.5$ - 3 W m^{-1} K^{-1} for the SSR-series. The SC-derived phases are characterized by the presence of nano-sized 90° twinned domains and intergrowths of Ruddlesden-Popper planar defects creating anti-phase boundaries. Such complex microstructures can be regarded as the combination of co-existing nano-sized textural features, which might efficiently scatter the phonons at their interfaces and therefore reduce the lattice thermal conductivity. An alternative decomposition of the "*chimie douce*" precursors by means of ultrasonic spray combustion (USC) process enables the synthesis of $CaMn_{1-x}Nb_xO_3$ nanocrystallites. The USC-nanostructured materials present unusual magnetic and electronic properties at low temperatures, i.e. T < 200 K, which are not observed in the SSR-derived phases. A strong suppression of the ferromagnetic interactions solely takes place in the USC-derived nanocrystallites. This peculiarity could be explained by a surface/grain boundary effect or by a size effect of the nanocrystallites limiting the double exchange ferromagnetism development in the Mn^{3+}-O-Mn^{4+} network.

The $CaMn_{1-x}Nb_xO_3$ phases (x = 0.02, 0.05, 0.08, and 0.10) have been studied as potential *n*-type thermoelectric materials for high-temperature applications, i.e. T >> 300 K. The substitution of Mn^{4+} by Nb^{5+} in the $CaMnO_3$ system induces the creation of Mn^{3+} cations according to $CaMn^{4+}_{1-2x}Mn^{3+}_xNb^{5+}_xO_3$, which further influences the structural and the physical properties.

At room temperature, the $CaMn_{1-x}Nb_xO_3$ phases crystallize in the orthorhombic crystal structure, *Pnma* S.G. with the lattice parameters $a_c\sqrt{2} \times 2a_c \times a_c\sqrt{2}$ (a_c[1] ~ 3.74 Å). The Nb substitution on the *B*-site in the $CaMnO_3$ phase induces a linear increase of the lattice parameters and an enhancement of the octahedral distortions which is accentuated along the Mn-O equatorial planes while increasing the Nb concentration. At low temperatures, i.e. T < 115 K, the Nb-containing manganate phases exhibit a magnetic transition from G-type paramagnetic to ordered antiferro- (AFM) or ferromagnetic (FM) interactions depending on the Nb concentration, i.e. FM fluctuations increase with the Nb content in the AFM matrix. The magnetic structure of the $CaMn_{0.98}Nb_{0.02}O_3$ phase is studied below the ordering magnetic temperature, confirming the predominance of AFM interactions in the Mn sublattice. At high temperatures, i.e. T > 1100 K, the $CaMn_{1-x}Nb_xO_3$ phases undergo a thermal reduction and a structural transition from orthorhombic to cubic symmetry, both phenomena being reversible upon cooling. Increasing the Nb content in the $CaMnO_3$ structure results in a shift of the thermal reduction onset temperature to higher temperatures. Thus, the $CaMn_{1-x}Nb_xO_3$ phases are thermally stable in air up to a high-temperature limit, i.e. T $\simeq$ 1090 K for x = 0.02 to T $\simeq$ 1200 K for x = 0.10. The orthorhombic $CaMn_{1-x}Nb_xO_3$ phases reveal at room temperature complex microstructures. The occurrence of 90° twinned domains is highlighted by high-resolution TEM and electron diffraction studies. The formation of twins in the orthorhombic structures relies

---

[1] a_c refers to the lattice parameter of the ideal cubic perovskite structure

on the combination of close lattice parameters, i.e. $a_o \simeq c_o$ and a low octahedra tilt angle, e.g. $\varphi = 13.3^o$ for x = 0.08. The 90° twins are formed on cooling, upon the structural transition from cubic to orthorhombic, i.e. from higher to lower symmetry, which results in the loss of the fourfold rotation axes. Twinning phenomena induce the emergence of domain boundaries. In the studied $CaMn_{1-x}Nb_xO_3$ phases, twin boundaries are characterized by a perfect structural intergrowth. Z-contrast investigations using an aberrated-correction STEM with sub-Angstrom spatial resolution did not reveal any Nb segregation at the twinned domain boundaries. Furthermore, the combination of imaging and spectroscopy capabilities by means of HAADF and EELS studies enables the identification of intergrowth Ruddlesden-Popper planar defects involving anti-phase boundaries. It consists of a single rock-salt layer where the Ca and Mn columns are shifted by half an unit cell from both sides of the boundary.

The electrical transport properties of the $CaMn_{1-x}Nb_xO_3$ phases vary gradually with the temperature from a thermally activated to a temperature independent conduction regime. A transition from semiconducting-like behavior ($d\rho/d\mathrm{T} < 0$ and $S(T) \sim 1/T$) to metallic-type conduction ($d\rho/d\mathrm{T} > 0$ and $S(T) \sim T$) is observed at T $\simeq$ 115 K for all the studied phases. A breakdown of S(T) and ρ(T) to a more metallic-like behavior is revealed at temperatures higher than 1100 K, reflecting an additional change in the conduction regime. The low-temperature semiconducting regime is attributed to the AFM ordering and the segregation of the non-percolating FM regions, which occurs below the ordering magnetic transition. The transport properties of the manganate phases in the high-temperature paramagnetic state, i.e. 200 K < T < 1100 K, can be described by the small polaron hopping conduction mechanism. The introduction of Nb^{5+} in the $CaMnO_3$ phase generates Mn^{3+} ($e_g{}^1$ $t_{2g}{}^3$) cations in the Mn^{4+} ($e_g{}^0$ $t_{2g}{}^3$) matrix, i.e. mobile electrons in the e_g orbitals act as charge carriers in the Mn^{4+}-O-Mn^{3+} framework. The formation of small polarons is enhanced with increasing the Mn^{3+} concentration since the polaronic narrow band is progressively filled with e_g electrons when substituting Mn^{4+} by Nb^{5+} cations. As a consequence, increasing the charge carrier concentration, i.e. the Nb content, induces a decrease of the electrical resistivity values. In addition, the Nb substitution in the $CaMnO_3$ phase results in a change of overlapping between the oxygen $2p$ and the manganese $3d$ orbitals, i.e. a modification of the Mn d bandwidths, which also influences the electronic properties. According to the Heikes formula, valid in the high-temperature limit, absolute Seebeck coefficients values decrease with increasing the Mn^{3+} concentration. The metallic-like electrical resistivity and the linear S(T) behavior of the $CaMn_{1-x}Nb_xO_{3\pm\delta}$ series allow to apply the modified expression of the single band metal model. Based on this model, theoretical thermopower values can be determined for a defined carrier concentration, e.g. for x = 0.05: $S_{theo} = -130$ μV K^{-1}, and agree with observed thermopower values, e.g. for x = 0.05: $S_{exp} = -128$ μV K^{-1} at 340 K. Since the Seebeck coefficient depends solely on the nature and the concentration of the charge concentration, both the SC- and SSR-derived phases lead to equal thermopower values for equal Nb concentrations. Moreover, the SC-derived phases reveal lower resistivity values due to a better interconnection between the crystallites compared to the SSR-series. The SC-made phases therefore combine low thermal conductivity values, i.e. $\kappa < 1$ W m^{-1} K^{-1}, and enhanced power factors[1] values, i.e. for x = 0.05: PF $\simeq 2*10^{-4}$ W m^{-2} K^{-1} within 450 K < T < 1050 K. As a result, the SC-derived $CaMn_{0.98}Nb_{0.02}O_3$ phase yields the highest ZT value achieved for n-type polycrystalline perovskites with $ZT_{1060\ K} = 0.32$. At higher temperatures, i.e. T > 1100 K, lower absolute Seebeck coefficient and electrical resistivity values are observed in the high-temperature range, indicating an enhancement of the electrical conduction. Such changes in the electrical transport properties are attributed to an increase of the Mn^{3+} concentration in the Mn^{4+} sublattice. The $CaMn_{1-x}Nb_xO_{3\pm\delta}$ phases undergo a reversible thermal reduction/re-oxidation at high temperatures leading to a lowering of the oxygen content, e.g. $\delta = 0.047 \pm 0.02$ for x = 0.02 until 1273 K, and consequently to a modification of the Mn^{3+}/Mn^{4+} concentration ratio. The S(T) and ρ(T) changes occur at higher temperatures with increasing the Nb concentration since the thermal stability of the $CaMn_{1-x}Nb_xO_{3\pm\delta}$ phases increases with the Nb content. The thermoelectric properties of the manganate phases can be tuned with respect to their Nb substitution levels and their temperature of applications. In addition, the manganate phases did not present any degradation of their thermoelectric properties even after several heating/cooling cycles up to 1273 K because of their reversible oxygen release/uptake capabilities.

Polycrystalline $LaMn_{1-x}Co_xO_3$ phases (x = 0.05, 0.10, 0.90, and 0.95) are investigated with respect to their crystal structure, microstructure and thermoelectric properties at high temperatures, i.e. 300 K < T < 1240 K. The Mn-rich phases (x = 0.05 and 0.10) crystallize in the orthorhombic symmetry, *Pnma* S.G. ($a_c\sqrt{2} \times 2a_c \times a_c\sqrt{2}$) while the Co-rich series (x = 0.90 and 0.95) belong to the rhombohedral crystal structure $R\bar{3}c$ S.G. ($a_c\sqrt{2} \times \sim\ a_c\sqrt{2} \times 2a_c\sqrt{3}$ and $\gamma = 120^o$ (in hexagonal settings). The predominance of the transition metal also influences the microstructure of the studied phases. The Mn-rich phases present nano-sized 90° twins, typical in orthorhombic crystal structures, while the rhombohedral Co-rich compounds is characterized by a long-range ordered microstructure. All the studied phases exhibit a typical semiconductor behavior ($d\rho/d$T < 0 and $S(T)\ \sim\ 1/T$) over the investigated temperature region. The substitution of Mn^{3+} by Co^{2+} in the $LaMnO_3$ matrix induces p-type conduction, i.e. predominant hole charge carriers leading to $S > 0$ at T > 500 K. At the reverse, n-type conduction results from the creation of electron carriers by substituting Co^{3+} by Mn^{4+} in the $LaCoO_3$ system. The Seebeck coefficient temperature dependence of the Co-rich phases reveals a slope change, i.e. dS/dT < 0 at T $\simeq$ 550 K, resulting from the Co^{3+} spin state transition. The thermal conductivity values of the Mn-rich phases increase slightly with the temperature, the lattice component remaining the main contribution to the total thermal conductivity. The Co-rich phases reveal an important increase of the thermal conductivity above 500 K due to an increase of the electronic contribution

---

[1] the thermoelectric power factor is defined as $PF = S^2/\rho$.

in this temperature range. The $LaMn_{0.10}Co_{0.90}O_3$ phase yields a ZT value of 0.021 at T = 700 K.

Thermoelectric materials, which can generate electricity from waste heat or renewable energy sources such as solar or geothermal heat, could emerge in the coming years as a partial response in the global energy problem. The design of highly-efficient thermoelectric materials remains a challenge since it involves the combination of conflicting materials properties. Large Seebeck coefficients S, high electrical conductivities σ, and low thermal conductivities κ are required to achieve high ZT values, whilst the electronic and thermal transport properties are inherently interrelated through the tuning of the charge carrier concentration. In this thesis, nanostructured perovskite-type manganates have proven to be promising thermoelectric candidates. The SC-derived $CaMn_{0.98}Nb_{0.02}O_3$ phase yields a ZT value of 0.32 at T = 1060 K, i.e. twice as high compared to the standard SSR phase. Considered as the up-to-now best n-type polycrystalline perovskite-type phases operating in air at high temperatures, this potential material is already implemented in a demonstrator thermoelectric oxide module in combination with p-type cobaltates. Oxide materials are nowadays considered as prospective for high-temperature thermoelectric applications, especially with respect to the environmental concerns and technological limitations, i.e. chemical and thermal stability at high temperatures under air. Designing complex nanostructured oxides could result in thermoelectric materials with higher efficiencies; this making the control and the fine-tuning of the nanostructures the next challenge.

List of publications

- L. Bocher, R. Robert, M. H. Aguirre, L. Schlapbach, and A. Weidenkaff.
  ”Thermoelectric perovskite-type oxides for geothermal and solar energy conversion.”
  Proceedings of the 4th European Conference on Thermoelectrics, **2006**.
- R. Robert, L. Bocher, M. Trottmann, A. Reller, A. Weidenkaff.
  ”Synthesis and high-temperature thermoelectric properties of Ni and Ti substituted $LaCoO_3$.”
  J. Solid State Chem. **2006**, 179, 38933899.
- L. Bocher, M. H. Aguirre, R. Robert, M. Trottmann, D. Logvinovich, P. Hug, and A. Weidenkaff.
  ”*Chimie douce* synthesis and thermochemical characterization of mesoporous perovskite-type titanate phases”
  Thermochim. Acta, **2007**, 457, 11-19.
- R. Robert, L. Bocher, B. Sipos, M. Döbeli, A. Weidenkaff.
  ”Ni-doped cobaltates as potential materials for high-temperature solar thermoelectric converters”
  Prog. Solid State Chem. **2007**, 35, 447-455.
- L. Bocher, R. Robert, M. H. Aguirre, S. Malo, S. Hébert, A. Maignan, and A. Weidenkaff.
  ”Thermoelectric and magnetic properties of perovskite-type manganate phases synthesised by ultrasonic spray combustion (USC).”
  Solid State Sciences, **2008**, 10, 496-501.
- R. Robert, M. H. Aguirre, L. Bocher, M. Trottmann, S. Heiroth, T. Lippert, M. Döbeli, and A. Weidenkaff.
  ”Thermoelectric properties of $LaCo_{1-x}Ni_xO_3$ polycrystalline samples and epitaxial thin films.”
  Solid State Sciences, **2008**, 10, 502-507.
- L. Bocher, M. H. Aguirre, D. Logvinovich, A. Shkabko, R. Robert, M. Trottmann, and A. Weidenkaff.
  ”$CaMn_{1-x}Nb_xO_3$ ($x \leq 0.08$) Perovskite-Type Phases As Promising New High-Temperature *n*-Type Thermoelectric Materials.”
  Inorg. Chem., **2008**, 47, 8077-8085.

- M. H. Aguirre, S. Canulescu, R. Robert, N. Homazava, D. Logvinovich, L. Bocher, Th. Lippert, M. Döbeli, and A. Weidenkaff.
  "Structure, microstructure, and high-temperature transport properties of $La_{1-x}Ca_xMnO_{3-\delta}$ thin films and polycrystalline bulk materials."
  J. Appl. Phys., **2008**, 103, 013703 1-6.
- M. H. Aguirre, D. Logvinovich, L. Bocher, R. Robert, S. Ebbinghaus, and A. Weidenkaff.
  "High-temperature thermoelectric properties of Sr_2RuYO_6 and Sr_2RuErO_6 double perovskites influenced by structure and microstructure."
  Acta Mater., **2008**, 57, 108-115.
- A. Weidenkaff, L. Bocher, R. Robert, M. H. Aguirre, and D. Logvinovich.
  "Thermoelectric Oxides and Oxynitrides with Perovskite-type Structure."
  Mater. Res. Soc. Symp. Proc., **2008**, 1044, 311-317.
- A. Weidenkaff, R. Robert, M. H. Aguirre, L. Bocher, T. Lippert, and S. Canulescu.
  "Development of thermoelectric oxides for renewable energy conversion technologies."
  Renewable Energy, **2008**, 33, 342-347.
- R. Robert, L. Bocher, M. H. Aguirre, and A. Weidenkaff.
  "Thermoelectric properties of *p*- and *n*-type oxides phases prepared by soft chemistry."
  Accepted in *Journal of Applied Energy*, **2008**.
- L. Bocher, M. H. Aguirre, R. Robert, D. Logvinovich, S. Bakardjieva, J. Hetjmanek, and A. Weidenkaff.
  "High-temperature stability, structure and thermoelectric properties of $CaMn_{1-x}Nb_xO_3$ phases."
  Acta Mater., **2009**, 57, 5667-5680.
- D. Logvinovich, L. Bocher, D. Sheptyakov, R. Figi, S.G. Ebbinghaus, R. Aguiar, M. H. Aguirre, A. Reller, and A. Weidenkaff.
  "Microstructure, surface composition, and chemical stability of partly ordered $LaTiO_2N$."
  Solid State Sciences, **2009**, 11, 1513-1519.

References

- A -

[Aguirre-2003] M. H. Aguirre, R. Ruiz-Bustos, and M. A. Alario-Franco, *J. Mater. Chem.*, **2003**, 13, 1156-1160.

[Aguirre-2007] M. H. Aguirre, R. Robert, D. Logvinovich, and A. Weidenkaff, *Inorg. Chem.*, **2007**, 46, 2744-2750.

[Aguirre-2008] M. H. Aguirre, D. Logvinovich, L. Bocher, R. Robert, S. G. Ebbinghaus, and A. Weidenkaff, *Acta Mater.*, **2008**, 57, 108-115.

[Altenkirch-1911] E. Altenkirch, *Physikalische Zeitschrift* **1911**, 12, 920-924.

[Autret-2005] C. Autret, J. Hejtmanek, K. Knizek, M. Marysko, Z. Jirak, M. Dlouha, and S. Vratislav, *J. Phys.: Condens. Matter*, **2005**, 17, 16011616.

- B -

[Bangert-2006] U. Bangert, U. Falke, and A. Weidenkaff, *Mater. Sci. Eng. B*, **2006**, 133, 30-36.

[Barrett-1951] E. P. Barrett, L. G. Joyner, and P. P. Halenda, *J. Mater. Chem. Soc.*, **1951**, 73, 373-380.

[Battabyal-2006] M. Battabyal, and T. K. Dey, *Physica B*, **2006**, 373, 46-53.

[Bérardan-2008] D. Bérardan, E, Guilmeau, A. Maignan, and B. Raveau,*Solid State Commun.*, **2008**, 146, 97-101.

[Blakemore-1998] J. S. Blakemore, *Solid State Physics, Second Ed.*; University Press : Cambridge, **1998**.

[Bleloch-2004] A. Bleloch and A. Lupini,*Mater. Today*, **2004**, 7, 42-48.

[Bocher-2006] L. Bocher, R. Robert, M. H. Aguirre, L. Schlapbach, and A. Weidenkaff, *Proc. 4th European Conference on Thermoelectrics*, **2006**.

[Bocher-2007] L. Bocher, M. H. Aguirre, R. Robert, M. Trottmann, D. Logvinovich, P. Hug, and A. Weidenkaff, *Thermochim. Acta*, **2007**, 457, 11-19.

[Bocher-2008a] L. Bocher, R. Robert, M. H. Aguirre, S. Malo, S. Hébert, A. Maignan, and A. Weidenkaff, *Solid State Sciences*, **2008**, 10, 496-501.

[Bocher-2008b] L. Bocher, M. H. Aguirre, D. Logvinovich, A. Shkabko, R. Robert, M. Trottmann, and A. Weidenkaff, *Inorg. Chem.*, **2008**, 47, 8077-8085.

[Bocher-2009] L. Bocher, M. H. Aguirre, R. Robert, D. Logvinovich, S. Bakardjieva, J. Hejtmanek and A. Weidenkaff, *Acta Mater.*, **2009**, 57, 5667-5680.

[Boulay-1996] P. Boulay, B. Domengès, M. Hervieu, D, Groult, and B. Raveau *Chem. Mater.*, **1996**, 8, 1482-1489.

[Boyle-2004] G. Boyle, *Renewable energy - Power for a sustainable future, 2nd Ed.*; Oxford University Press: Oxford, **2004**.

[Brown-1997] L. M. Brown, *Inst. Phys. Conf. Ser.*, **1997**, 153, 17-22.

[Brown-2006] S. R. Brown, S. M.Kauzlarich, F. Gascoin, and G. J. Snyder, *Chem. Mater.*, **2006**, 18, 1873 -1877.

[Brown-2008] S. R. Brown, E. S. Toberer, T. Ikeda, C. A. Cox, F. Gascoin, S. M. Kauzlarich, and J. G. Snyder, *Chem. Mater.*, **2008**, 20, 3412 - 3419.

- C -

[Caillat-1996] T. Caillat, A. Borshchevsky, and J. P. Fleurial *J. Appl. Phys.*, **1996**, 80, 4442-.

[Callen-1948] H. B. Callen, *Phys. Rev.*, **1948**, 78, 1349-1358.

[Camargo-2000] E. R. Camargo, E. Longo, and E. R. Leite, *J. Sol-Gel Sci. Technol.*, **2000**, 17, 111-121.

[Cape-1963] J. A. Cape, G. W. Lehman, *J. Appl. Phys.*, **1963**, 34, 1909-1913.

[Chahara-1993] K. Chahara, T. Ohno, M. Kasai, and Y. Kozono, *Appl. Phys. Lett.*, **1993**, 63, 1990-1991.

[Chaikin-1976] P. M. Chaikin, and G. Beni, *Phys. Rev. B*, **1976**, 13, 647-651.

[Clarke-2003] D. R. Clarke, *Surf. Coat. Technol.*, **2003**, 67, 163-164.

[Coey-1999] J. M. D. Coey, M. Viret, and S. von Molnar, *Adv. Phys*, **1999**, 48, 167-293.

[Czichos-2006] H. Czichos, T. Saito, L. Smith, *Handbook of Materials Measurement Methods*; Springer-Verlag: Berlin Heidelberg, **2006**.

- D -

[Dabrowski-2003] B. Dabrwoski, O. Chmaissem, J. Mais, S. Kolesnik, J. D. Jorgensen, and S. Short, *J. Solid State Chem.*, **2003**, 170, 154-164.

[DM-Gatan] Digital Micrograph software, V1.70, Gatan.

[Domenicali-1954] C. A. Domenicali, *Rev. Mod. Phys.*, **1954**, 26, 237-275.

[Doumerc-1994] J. P. Doumerc, *J. Solid State Chem.*, **1994**, 110, 419-420.

[Dresselhaus-2001] M. S. Dresselhaus, and I. L. Thomas, *Nature*, **2001**, 414, 332-337.

[Dresselhaus-2007] M. S. Dresselhaus, G. Chen, M. Y. Tang, R. Yang, H. Lee, D. Wang, Z. Ren, J. P. Fleurial, and P. Gogna, *Adv. Mater.*, **2007**, 19, 10431053.

[Dyck-2002] J. S. Dyck, W. Chen, C. Uher, L. Chen, X. Tang, and T. Hirai , *J. Appl. Phys.*, **200**, 91, 3896-3705.

- E -

[Edwards-2002] D. M. Edwards, *Adv. Phys.*, **2002**, 51, 1259-1318.

- F -

[Finger-1994] L. W. Finger, D. E. Cox, and A. P. Jephcoat, *J. Appl. Crystallogr.*, **1994**, 27, 892-900.

[Fischer-2000] P. Fischer, G. Frey, M. Koch, M. Konnecke, V. Pomjakushin, J. Schefer, R. Thut, N. Schlumpf, R. Burge, and U. Greuter, *Physica B: Condensed Matter.*, **2000**, 276-278, 146-147.

[Fjellvag-1995] H. Fjellvag, O. H. Hansteen, B. G. Tilset, A. Olafsen, N. Sakai, and H. Seim, *Thermochim. Acta*, **1995**, 256, 75-89.

[Flahaut-2006] D. Flahaut, T. Mihara, R. Funahashi, N. Nabeshima, K. Lee, H. Ohta, and K. Koumoto, *J. Appl. Phys.*, **2006**, 100, 084911 1-4.

[Fleurial-1996] J. P. Fleurial, A: Borshchvky, T. Caillat, D. T. Morelli, and G. P Meissner *15th Int. Conf. Thermoelectr. Proc.*, **1996**.

[Fujita-2001] K. Fujita, T. Moschida, and K. Nakamura, *Jpn. J. Appl. Phys.*, **2001**, 40, 4644-4647.

[Funahashi-2002] R. Funahashi, and M. Shikano, *Appl. Phys. Lett.*, **2002**, 81, 1459-1461.

- G -

[Galasso-1969] F. S. Galasso, *Structure, Properties and Preparation of Perovskite-type Compounds*; Pergamon Press Ltd.: Oxford, **1969**.

[Glazer-1972] A. M. Glazer, *Acta Crystallogr., Sect. B: Struct. Sci.*, **1972**, 28, 3384-.

[Goodenough-1955] J. B. Goodenough, *Phys. Rev.*, **1955**, 100, 564-573.

[Grätzel-2001] M. Grätzel, *Nature*, **2001**, 414, 338-344.

[Gurav-1993] A. Gurav, T.T. Kodas, T. Pluym, Y. Yong *Aerosol Sci. Technol.* , **1993**, 19, 411-452.

- H -

[Haeni-2001] J. H. Haeni, C. D. Theis, D. G. Schlom, W. Tian, X. Q. Pan, H. Chang, I. Takeuchi, and X.-D. Xiang, *Appl. Phys. Lett.*, **2001**, 78, 3292-3294.

[Haider-2000] M. Haider, S. Uhlemann, and J. Zach, *Ultramicroscopy*, **2000**, 81, 163 - 175.

[Hammond-2006] C. Hammond, *The Basics of Crystallography and Diffraction, Second Ed.*; Oxforf University Oress Inc.: New York, **2006**.

[Harman-2002] T. C. Harman, P. J. Taylor, M. P. Walsh, and B. E. LaForge *Science*, **2002**, 297, 2229-2232.

[Hébert-2001] S. Hébert, C. Martin, A. Maignan, J. Hejtmanek, and B. Raveau, *Proc. 6th European Workshop on Thermoelectrics*, **2001**.

[Hébert-2007] S. Hébert, D. Flahaut, C. Martin, S. Lemonnier, J. Noudem, C. Goupil, A. Maignan, *Prog. Solid State Chem.*, **2007**, 35, 457-467.

[Heikes-1961] R. R.Heikes, and R. W. Ure, *Thermoelectricity: Science and Engineering*; Interscience: New York, **1961**.

[Hejtmánek-1999] J. Hejtmánek, Z. Jirák, M. Marysko, C. Martin, A. Maignan, M. Hervieu, and B. Raveau, *Phys. Rev. B*, **1999**, 60, 14057-14065.

[Hennings-1978] D. Hennings, and W. Mayr, *J. Solid State Chem.*, **1978**, 26, 329-338.

[Henry-2008] A. Henry, and G. Chen, *J. Computional and Theoritical Nanoscience*, **2008**, 5, 141-152.

[Hicks-1993a] L. D. Hicks, and M. S.Dresselhaus, *Phys. Rev. B*, **1993**, 47, 12727-12731.

[Hicks-1993b] L. D. Hicks, and M. S.Dresselhaus, *Phys. Rev. B*, **1993**, 47, 16631-16634.

[Höhne-2003] G. W. H. Höhne, W. F. Hemminger, H. -J. Flammersheim *Differential Scanning Calorimetry, Second Ed.*; Springer-Verlag: Berlin Heidelberg **2003**.

[Huang-2008] X. Y. Huang, Y. Miyazaki, T. Kajitani, *Solid State Commun.*, **2008**, 145, 132-136.

- I -

[IEA-PVPS-2007] S. Nowak, *Report of the International Energy Agency on the Photovoltaic Power Systems*; IEA-PVPS T1-16, **2007**.

[Ioffe-1957] A. F. Ioffe, *Semiconductor Thermoelements and Thermoelectrics Cooling*; Infosearch Ltd: London, **1957**.

[Isobe-2002] S. Isobe, T. Tani, Y. Masuda, W. S. Seo, and K. Koumoto *Jpn. J. Appl. Phys.*, **2002**, 41, 731-732.

- J -

[Jain-1997] S. Jain, D. J. Skamser, and T. T. Kodas *Aerosol Sci. Technol.* , **1997**, 27, 575-590.

[Jeanguillaume-1989] C. Jeanguillaume, and C. Colliex *Ultramicroscopy*, **1989**, 28, 257-252.

- K -

[Kittel-2004] Ch. Kittel, *Introduction to Solid State Physics eighth ed.*; John Wiley Sons, INc: USA, **2004**.

[Kobayashi-1991] T. Kobayashi, H. Takizawa, T. Endo, T. Sato, and M. Shimada *J. Solid State Chem.*, **1991**, 92, 116-129.

[Kobayashi-2007] W. Kobayashi, S. Hébert, H. Muguerra, D. Grebille, D. Pelloquin, and A. Maignan,*26th Int. Conf. Thermoelectr.*, **2007**, 117-120.

[Kodas-1999] T. T. Kodas, and M. J. Hampden-Smith, *Aerosol processing of materials, 1st ed.*; Wiley-WCH: New-York, **1999**.

[Koshibae-2000] W. Koshibae, K. Tsutsui, and S. Maekawa, *Phys. Rev. B*, **2000**, 62, 6869-6872.

[Koumoto-2006] K. Koumoto, I. Terasaki, and R. Funahashi, *MRS Bulletin*, **2006**, 31, 206-210.

[Krivanek-1999] O. Krivanek, N. Delby, and A. R. Lupini *Ultramicroscopy***1999**, 78, 1-11.

[Kupricka-2002] E. Kupricka, A. Reller, and A. Weidenkaff, *Cryst. Eng.*, **2002**, 5, 195-202.

[Kurata-1993] H. Kurata, and C. Colliex *Phys. Rev. B*, **1993**, 48, 2102-2108.

- L -

[Li-2004] W. C. Li, A. H. LU, C. Weidenthaler, and F. Schüth, *Chem. Mater.* **2004**, 16, 5676-5681.

[Ling-2003] C. D. Ling, E. Granado, J. J. Neumeier, J. W. Lynn, and D. N. Argyriou *Phys. Rev. B* **2003**, 68, 134439 1-8.

[Lin-Vien-1991] D. Lin-Vien, N. B. Colthup, W. G. Fateley, and J. G. Grasselli, *The handbook of Infrared and Raman Characteristic Frequencies of Organic Molecules*; Academic Press Inc.: San Diego **1991**.

[Livage-1988] J. Livage, M. Henry, and C. Sanchez, *Prog. Solid State Chem.* **1988**, 18, 259-341.

[Lemonnier-2008] S. Lemonnier, C. Goupil, J. Noudem, and E. Guilmeau, *J. Appl. Phys* **2008**, 104, 014505 1-4.

- M -

[Maignan-1998a] A. Maignan, C. Martin, F. Damay, and B. Raveau, *Phys. Rev. B* **1998**, 58, 2758-2763.

[Maignan-1998b] A. Maignan, C. Martin, F. Damay, and B. Raveau, *Chem. Mater* **1998**, 10, 950-954.

[Maignan-2002] A. Maignan, C. Martin, C. Autret, M, Hervieu, B. Raveaua and J. Hejtmanek, *J. Mat. Chem.* **2002**, 12, 18061811.

[Maignan-2004] A. Maignan, D. Flahaut, and S. Hébert, *Eur. Phys. J. B* **2004**, 39, 145-148.

[Majumdar-2004] A. Majumdar, *Science* **2004**, 303, 777-778.

[Malmros-1977] G. Malmros, and J. O. Thomas, *J. Appl. Crystallogr.* **1977**, 10, 7.

[Marezio-1970] M. Marezio, J. P. Remeika, and P. D. Derneir *Acta Cryst. B* **1970**, 26, 2008-2022.

[Marques-2007] P. Marques, T. Dannoux, and C. Goupil, *Corning Patent* WO2007/065954 **(2007-06-14)**.

[Marsh-1996a] D. B. Marsh, and P. E. Parris, *Phys. Rev. B*, **1996**, 54, 7720-7728.

[Marsh-1996b] D. B. Marsh, and P. E. Parris, *Phys. Rev. B*, **1996**, 54, 16602-16607.

[Martin-1999] C. Martin, A. Maignan, M. Hervieu, B. Raveau, Z. Jirák, A. Kurbakov, V. Trounov, G. André, and F. Bourrée, *J. Magn. Magn. Mater*, **1999**, 205, 184-198.

[Martin-2000] C. Martin, A. Maignan, M. Hervieu and B. Raveau, *Phys. Rev. B*, **2000**, 62, 6442-6449.

[Martin-2001] C. Martin, A. Maignan, M. Hervieu and B. Raveau, *Phys. Rev. B*, **2001**, 63, 100406 1-4.

[Masset-2000] A. C. Masset, C. Michel, A. Maignan, M. Hervieu, O. Toulemonde, F. Studer, B. Raveau, and J. Hejtmanek, *Phys. Rev. B*, **2000**, 62, 166-175.

[Mather-2008] G. C. Mather, F. M. Figueiredo, J. Romero de Paz, S. Garcia-Martin *Inorg. Chem.*, **2008**, 47, 921-929.

[Maurice-2006] J. L. Maurice, D. Imhoff, J. P. Contour, and C. Colliex *Philos. Mag.* **2006**, 86, 2127-2146.

[MeloJorge-2005] M. E. Melo Jorge, M. R. Nunes, R. Silva Maria, and D. Sousa *Chem. Mater.*, **2005**, 17, 2069-2075.

[Miclau-2005] M. Miclau, S. Hébert, R. Retoux, and C. Martin, *J. Solid State Chem.* **2005**, 178, 1104-1111.

[Miclau-2007] M. Miclau, J. Hejtmanek, R. Retoux, K. Knizk, Z. Jirak, R. Frésard, A. Maignan, S. Hébert, M. Hervieu, and C. Martin, *Chem. Mater.* **2007**, 19, 4243-4251.

[Mikami-2003] M. Mikami, R. Funahashi, M. Yoshimura, Y. Mori, and T. Sasaki, *J. Appl. Phys.* **2003**, 94, 5144.

[Millis-1995] A. J. Millis, P. B. Littlewood, B. I. Shraiman, *Phys. Rev. Lett.* **1995**, 74, 6579-6581.

[Min-2004] G. Min, and M. Rowe, *J. Phys. D: Appl. Phys.* **2004**, 37, 13011304.

[Mitchell-2002] R. H. Mitchell, *Perovskites - Modern and Ancient*; Almaz Press Inc.: Thunder Bay, Canada **2002**.

[Miyazaki-2000] Y. Miyazaki, K. Kudo, M. Akoshima, Y. Ono, Y. Koike, and T. Kajitani, *Jpn. J. Appl. Phys.* **2000**, 39, L531-L533.

[Moulder-1995] J. F. Moulder, W. F. Stickle, P. E. Sobol, and K. D. Bomben, *Handbook of X-ray Photoelectron Spectroscopy*; Physical Electronics Inc.: **1995**.

[Muta-2003] H. Muta, K. Kurosaki, and S. Yamanaka, *J. Alloys Compd.* **2003**, 350, 292-295.

- N -

[Nelis-2005] D. Nelis, G. Mondelares, A. Vanhoyland, A. Hardy, K. Van Werde, H. Van den Rul, M. K. Van Bael, J. Mullens, L. C. Van Poucke, and J. D'Haen,, *Thermochim. Acta* **2005**, 426, 39-48.

[Nolas-2001] G. S. Nolas, J. Sharp, and H. J. Goldsmid, *Thermoelectrics; Basic Principles and New Materials Developments*; Springer-Verlag: Berlin Heidelberg, **2001**.

[Nord-1994] G. L. Nord Jr., *Phase Transitions* **1994**, 48, 107-134.

- O -

[Ohta-2005a] S. Ohta, T. Nomura H. Ohta, M. Hirano, H. Hosono, and K. Koumoto *Appl. Phys. Lett.* **2005**, 87, 092108-.

[Ohta-2005b] S. Ohta, T. Nomura H. Ohta, and K. Koumoto *J. Appl. Phys* **2005**, 97, 034106 1-4.

[Ohta-2007] H. Ohta, S. Kim, Y. Mune, T. Mizoguchi, K. Nomura, S. Ohta, T. Nomura, Y. Nakanishi, Y. Ikuhara, M. Hirano, H. Hosono, and K. Koumoto, *Nat. Mater.* **2007**, 6, 129-134.

[Ohtaki-1995] M. Ohtaki, H. Koga, T. Tokunaga, K. Eguchi, and H. Arai, *J. Solid State Chem.* **1995**, 120, 105-111.

[Ohtaki-1996] M. Ohtaki, T. Tsubota, K. Eguchi, and H. Arai, *J. Appl. Phys.* **1996**, 79, 1816-1818.

[OKeefe-1977] M. O'Keefe, and . G. Hyde, *Acta Cryst. B* **1977**, 33, 3802-3813.

[Okuda-2001] T. Okuda, K. Nakanishi, S. Miyasaka, and Y. Tokura, *Phys. Rev. B* **2001**, 63, 113104 1-4.

[Okuyama-2003] K. Okuyama, and I. W. Lenggoro *Chem. Eng. Sci.* **2003**, 58, 537-547.

- P -

[Pal-2006] S. Pal, S. Hbert, C. Yaicle, C. Martin and A. Maignan, *Eur. Phys. J. B* **2006**, 53, 5-9.

[Palcut-2006] M. Palcut, K. Wiik and T. Grande, *J. Phys. Chem. C* **2006**, 2, 813-822.

[Palstra-1997] T. T. M. Palstra, A. P. Ramirez, S-W. Cheong, B. R. Zegarski, P. Schiffer, and J. Zaanen, *Phys. Rev. B* **1997**, 56, 5104-5107.

[Parker-1961] W. J. Parker, R. J. Jenkins, C. P. Butler, and G. L. Abbott, *J. Appl. Phys.* **1961**, 32, 1679-1684.

[Pecharsky-2005] V. K. Pecharsky, and P. Y. Zavalij, *Fundamental of Powder Diffraction and Structural Characterization of Materials*; Springer: New York,**2005**.

[Pechini-1967] M. P. Pechini, *Patent No. 3330697* **1967**, US.

[Peltier-1834] J. C. A. Peltier, *Ann. Chem.* **1834**, LVI, 371-387.

[Pi-2003] L. Pi, C. Martin, A. Maignan, and B. Raveau, *Phys. Rev. B* **2003**, 67, 024430 1-7.

[Poeppelmeier-1982a] K. R. Poeppelmeier, M. E. Leonowicz, and J. M. Longo, *J. Sol. St. Chem.* **1982**, 44, 89-98.

[Poeppelmeier-1982b] K. R. Poeppelmeier, M. E. Leonowicz, J. C. Scanlon, and J. M. Longo, *J. Sol. St. Chem.* **1982**, 45, 71-79.

[Poudel-2008] B. Poudel, Q. Hao, Y. Ma, Y. Lan, A. Minnich, B. Yu, X. Yan, D. Wang, A. Muto, D. Vashaee, X. Chen, J. Liu, M. S. Dresselhaus, G. Chen, and Z. Ren, *Science* **2008**, 320, 634 - 638.

[Prével-2007] M. Prével, O. Perez, and J. G. Noudem, *Solid State Sci.* **2007**, 9, 231-235.

- R -

[Raccah-1967] P. M. Raccah, and J. B. Goodenough, *Phys. Rev.* **1967**, 155, 932-947.

[Rajan-2001] R. Rajan, and A. B. Bandit, *Ultrasonics* **2001**, 39, 235-255.

[Rao-1998a] C. N. R. Rao, and B. Raveau, *Colossal Magnetoresistance*; World Scientific: Singapore, **1998**.

[Rao-1998b] C. N. R. Rao, and B. Raveau, *Transition Metal Oxides: Structure, Properties, and Synthesis of Ceramic Oxides, Second Ed.*; John Wiley & Sons: New York,**1998**.

[Raveau-1998] B. Raveau, A. Maignan, C. Martin, and M. Hervieu *Chem. Mater.* **1998**, 10, 2641-2652.

[Raveau-2000] B. Raveau, Y. M. Zhao, C. Martin, M. Hervieu, A. Maignan, *J. Solid State Chem.* **2000**, 149, 203-207.

[Raveau-2007] Raveau, B. *Prog. Solid State Chem.* **2007**, 35, 171-173.

[Reimer-1998] L. Reimer, *Scanning Electron Microscopy - Physics of Image Formation and Microanalysis, Second Ed.*; Springer-Verlag: Berlin Heidelberg, **1998**.

[Reller-1984] A. Reller, J. M. Thomas, F. R. S., D. A. Jefferson, and M. K. Uppal, *Proc. R. Soc. Lond. A* **1984**, 394, 223-241.

[Rietveld-1967] H. M. Rietveld, *J. Appl. Cryst.* **1967**, 22, 151-152.

[Rietveld-1969] H. M. Rietveld, *J. Appl. Cryst.* **1969**, 2, 65-71.

[RPS-2005] NASA Science Mission, *Expanding Frontiers with Standard Radioisotope Power Systems*; Standard RPS Report, **2005**.

[Robert-2006] R. Robert, L. Bocher, M. Trottmann, A. Reller, A. Weidenkaff, *J. Solid State Chem.* **2006**, 179, 38933899.

[Robert-2007a] R. Robert, L. Bocher, B. Sipos, M. Döbeli, A. Weidenkaff, *Prog. Solid State Chem.* **2007**, 35, 447-455.

[Robert-2007b] R. Robert, M. H. Aguirre, P. Hug, A. Reller, A. Weidenkaff, *Acta Mater.* **2007**, 55, 4965-4972.

[Robert-2007c] *Synthesis, structure, and thermoelectric properties of cobaltate phases*; Augsburg University Dissertation - Verlag: Berlin, **2007**.

[Robert-2008] R. Robert, L. Bocher, M. H. Aguirre, and A. Weidenkaff, accepter in *J. Applied Energy* **2008**.

[RodriguezCarvajal-1993] J. Rodriguez-Carvajal, *Physica B: Condensed Matter.* **1993**, 192, 55-69.

[Rørmark-2002] L. Rørmark, K. Wiik, S. Stølen, and T. Grande *J. Mater. Chem.* **2002**, 12, 1058-1067.

[Rose-1990] H. Rose *Optik* **1990**, 85, 19-24.

[Rowe-1995] D.M. Rowe, *CRC Handbook of Thermoelectrics*; CRC Press/Taylor & Francis Group: Boca Raton, **1995**.

[Rowe-2006] D.M. Rowe, *Thermoelectrics Handbook - Macro to Nano*; CRC Press/Taylor & Francis Group: Boca Raton, **2006**.

[Ruddlesden-1958] S. N. Ruddlesden, and P. Popper *Acta Cryst.* **1958**, 11, 54-55.

- S -

[Scherzer-1936] O. Schwerzer, *Z Physik* **1936**, 101, 593-603.

[Scherzer-1947] O. Schwerzer, *Optik* **1947**, 2, 114-132.

[Schlapbach-2001] L. Schlapbach, and A. Züttel, *Nature*, **2001**, 414, 353-358.

[Schmalzried-1995] H. Schmalzried, *Chemical Kinetic of Solids* VCH Verlaggsgesellschaft: Weinheim, **1995**.

[Schwarzenbach-1970] G. Schwarzenbach, J. Muehlebach, and K. Mueller, *Inorg. Chem.* **1970**, 9, 2381-2390.

[Seebeck-1822] T. J. Seebeck, *Abhand. Deut. Akad. Wiss.* **1822**, 265-373.

[Schliting-2001] K. W. Schliting, N. P. Padture, and P. G. Klemens, *J. Mater. Sci.* **2001**, 36, 3003-3010.

[Shannon-1976] R. D. Shannon, *Acta Cryst. A* **1976**, 32, 751-767.

[Shikano-2003] M. Shikano, and R. Funahashi, *Appl. Phys. Lett.* **2003**, 82, 1851-1853.

[Shriver-1999] D. F. Shriver, and P. W. Atkins, *Inorganic Chemistry, Third Ed.*; University Press : Oxford, **1999**.

[Singh-2000] D. J. Singh, *Phys. Rev. B* **2000**, 61, 13397-13402.

[Snyder-2008] G. F. Snyder, and E. S. Toberer *Nat. Mat.*, **2008**, 7, 105-114.

[Sorell-2005] C. C. Sorell, S. Sugihara, and J. Nowotny, *Materials for energy conversion devices*; CRC Press : Cambridge, **2005**.

[Stadelmann-1987] P. A. Stadelmann, **Ultramicroscopy** **1987**, 21, 131-145.

[Steele-2001] B. C. H. Steele, and A. Heinzel, *Nature*, **2001**, 414, 345-352.

[Strobel-2007] R. Strobel, and S. E. Pratsinis, *J. Mater. Chem.* **2007**, 17, 4743-4756.

[SuperSTEM2] http://www.superstem.dl.ac.uk/facilities.html

- T -

[Taguchi-1985] H. Taguchi, *Phys. Stat- Sol. (a)* **1985**, 88, K79-K82.

[Taguchi-1989] H. Taguchi, M. Nagao, T. Sato, and M. Shimada, *J. Solid State Chem.* **1989**, 78, 312-315.

[Takada-2003] K. Takada, H. Sakurai, E. Takayama-Muromachi, F. Izumi, R. A. Dilanian and T. Sasaki *Nature* **2003**, 422, 53-55.

[Takahata-2000] K. Takahata, Y. Iguchi, D. Tanaka, T. Itoh, and I. Terasaki *Phys. Rev. B* **2000**, 19, 12551-12555.

[Terasaki-1997] I. Terasaki, Y. Sasago, and K. Uchinokura, *Phys. Rev. B* **1997**, 56, R12685-R12687.

[Terasaki-2004] I. Terasaki, H. Tanaka, A. Satake, S. Okada, and T. Fujii, *Phys. Rev. B* **2004**, 70, 214106 1-5.

[Thao-2003] P. X. Thao, T. Tsuji, M. Hashida, and Y. Yamamura, *J. Ceram. Soc. Jap.* **2003**, 111, 544-547.

[Thompson-1987] P. Thompson, D. E. Cox, J. B. Hastings, *J. Appl. Crystallogr.* **1987**, 20, 79-83.

[Tomes-2008] P. Tome, R. Robert, M. Trottmann, L. Bocher, M. H. Aguirre, J. Hejtmnek and A. Weidenkaff, *submitted to* **2008**

[Töpfer-1997] J. Töpfer and J. B. Goodenough, *J. Sol. St. Chem.* **1997**, 130, 117-128.

[Tritt-2004] T.M. Tritt, Theory, *Thermal Conductivity - Theory, Properties and Applications*; Kluwer Academic / Plenum Publishers: New York, **2004**.

[Tsubota-1997] T. Tsubota, M. Ohtaki, K. Egushi, and H. Arai, *J. Mater. Chem.* **1997**, 7, 85-.

[Tsuda-2000] N. Tsuda, K. Nasu, A. Fujimori, and K. Siratori, *Electronic Conduction in Oxides, Second Ed.*; Springer-Verlag: Berlin Heidelberg, **2000**.

- V -

[vanLaar-1984] B. van Laar, and W. B. Yelon, *J. Appl. Crystallogr.* **1984**, 17, 47-54.

[Varela-2005] M. Varela, A. R. Lupini, K. van Benthen, A. Y. Borisevich, M. F. Chrisholm, N. Shibata, E. Abe, and S. J. Pennycook, *Annu. Rev. Mater. Res. 2005*, 35, 539-569

[Vegas-1986] A. Vegas, M. Vallet-Regi, J. M. Gonzalez-Calbet, and M. A. Alario-Franco, *Acta Cryst- B* **1986**, 42, 167-172.

[Venkatasubramanian-2001] R. Venkatasubramanian, E. Siivola, Th. Colpitts, and B. O'Quinn, *Nature 2001*, 413, 597-602

[vonHelmot-1993] R. von Helmolt, J. Wecker, B. Holzapfel, L. Schultz, and K. Samwer, *Phys. Rev. Lett.* **1993**, 71, 2331-2333.

- W -

[Wang-1993] Y. Wang, and R. C. Liebermann, *Phys. Chem. Minerals* **1993**, 20, 147-158.

[Wang-2006] W. L. Wang, and H. Y. Lu, *J. Am. Ceram. Soc.* **2006**, 89, 281-291.

[Weidenkaff-2004] A. Weidenkaff, *Adv. Eng. Mater.* **2004**, 9, 709-714.

[White-2008] B. D. White, C. A. M. Dos Santos, J. A. Souza, K. J. McClellan, and J. J. Neumeier, *J. Cryst. Growth* **2008**, 310, 3325-3330.

[Williams-1996a] D. B. Williams, and C. B. Carter, *Transmission Electron Microscopy - Basics I*; Springer Science: New York, **1996**

[Williams-1996b] D. B. Williams, and C. B. Carter, *Transmission Electron Microscopy - Diffraction II*; Springer Science: New York, **1996**

[Williams-1996c] D. B. Williams, and C. B. Carter, *Transmission Electron Microscopy - Imaging III*; Springer Science: New York, **1996**

[Williams-1996d] D. B. Williams, and C. B. Carter, *Transmission Electron Microscopy - Spectrometry IV*; Springer Science: New York, **1996**

[Winter-2007] M. R. Winter, and D. R.Clarke, *J. Am. Ceram. Soc.* **2007**, 90, 533-540.

[Wollan-1955] E. O. Wollan, and W. C. Koehler, *Phys. Rev.*, **1955**, 100, 545-563.

- X -

[Xu-2002] G. Xu, R. Funahashi, M. Shikano, I. Matsubara, and Y. Zhou, *Appl. Phys. Lett.* **2002**, 80, 3760-3762.

[Xu-2004] G. Xu, R. Funahashi, Q. Pu, B. Liu, R. Tao, G. Wang, Z. Ding, *Sol. State Ionics* **2004**, 171, 147-151.

- Y -

[Yan-2004] YJ. Q. Yan, J. S. Zhou, and J. B. Goodenough, *Phys. Rev. B* **2004**, 69, 134409 1-6.

[Yang-1998] P. Yang, D. Zhao, D. I. Margolese, B. F. Chmelka, and G. D. Stucky, *Nature* **1998**, 396, 152-155.

[Yang-1999] P. Yang, D. Zhao, D. I. Margolese, B. F. Chmelka, and G. D. Stucky, *Chem. Mater* **1999**, 11, 2813-2826.

[Yang-2005] R. Yang, G. Chen, and M. Dresselhaus, *Phys. Rev. B* **2005**, 72, 125418 1-7.

[Yamaguchi-1996] S. Yamaguchi, Y. Okimoto, H. Taniguchi, and Y. Tokura, *Phys. Rev. B* **1996**, 53, R2926-2929.

[Young-1982] R. A. Young and D. B. Wiles, *J. Appl. Cryst.* **1982**, 15, 430-438.

[Young-1993] R. A. Young, *The Rietveld Method, Chapt. 1*; Oxford University Press: Oxford, **1993**

- Z -

[Zampieri-2002] G. Zampieri, *Solid State Communications* **2002**, 123, 81-85.

[Zandbergen-1987] H. W. Zandbergen, G. van Tendeloo, T. Okabe, and S. Amelinckk *Phys. Stat. Sol. (a)* **1987**, 103, 45-72.

[Zener-1951] C. Zener, *Phys. Rev.* **1951**, 82, 403-405.

[Zhou-2003] Y. Zhou, I. Matsubara, R. Funahashi, G. Xu, and M. Shikano, *Mater. Res. Bull.* **2003**, 38, 341-346.

Nomenclature

Acronyms

AFM	Antiferromagnetic
BET	Brunauer Emmet Teller *method*
BF	Bright Field
BJH	Barrett Joyner Halenda *method*
BSE	Back-Scattered Electrons
CA	Citric Acid
CMR	Colossal Magneto-Resistance
DE	Double Exchange *mechanism*
DF	Dark Field
DOS	Density Of States
DSC	Differential Scanning Calorimetry
DTA	Differential Thermal Analysis
DTG	Derivative Thermogravimetric *signal*
ED	Electron Diffraction
EDS	Energy Dispersive X-ray Spectroscopy
EELS	Electron Energy-Loss Spectroscopy
EGA	Evolved-Gas Analysis
ELNES	Energy-Loss Near-Edge Structure
ESCA	Electron Spectroscopy for Chemical Analysis
EXELFS	Extended Energy-Loss Fine Structure
fc	Field Cooled
FFT	Fast Fourier Transform
FM	Ferromagnetic
HAADF	High Angular Annular Dark Field
HRTEM	High Resolution Transmission Electron Microscopy
IR	Infrared *spectroscopy*
LFA	Laser Flash Analysis

MS	Mass Spectrometer
NPD	Neutron Powder Diffraction
PF	Power Factor
PGEC	Phonon-Glass Electron-Crystal *concept*
PM	Paramagnetic
PPMS	Physical Property Measurement System
RS	Rocksalt *layers*
S.G.	Space Group
SAD	Selected-Area Diffraction
SC	Soft Chemistry *synthesis method*
SE	Secondary Electrons
SEM	Scanning Electron Microscopy
SQUID	Superconducting Quantum Interferences Device
SSA	Specific Surface Area
SSR	Solid State Reaction *method*
STEM	Scanning Transmission Electron Microscopy
TCO	Transparent Conducting Oxides
TEM	Transmission Electron Microscopy
TGA	Thermogravimetric Analysis
TTO	Thermal Transport Option
USC	Ultrasonic Spray Combustion *process*
VSM	Vibrating Sample Magnetometer
XPS	X-ray Photoemission Spectroscopy
XRPD	X-ray Powder Diffraction
zfc	Zero-Field Cooled

Greek symbols

α	Thermal diffusivity
β	Parameter vector
β_e	Degeneracy factor considering electrons as charge carriers
β_h	Degeneracy factor considering holes as charge carriers
β_m	Degeneracy factor for mixed valence systems
β_S	Spin degeneracy
β_{th}	Thomson coefficient
χ	Magnetic susceptibility

χ^2	Least-square function
ΔT	Temperature gradient
ϵ	Energy flux per unite of applied electric field
η	Conversion efficiency
η_c	Carnot efficiency
γ	Surface tension
κ	Thermal conductivity
κ_{el}	Electronic thermal conductivity
$\kappa_{lattice}$	Lattice thermal conductivity
λ	Wavelength
μ	Carrier mobility
μ_B	Bohr's magneton
μ_c	Chemical potential
μ_{eff}	Effective magnetic moment
ν	IR frequency
ν_s	Velocity of sound
Ω	Number of configurations
ω_i	Weight assigned to the step intensity
ϕ	Heat flow rate
ϕ_R	Reflection function
ϕ_V	Volume porosity
Π	Peltier coefficient
ρ	Electrical resistivity
σ_{SB}	Stephan-Boltzmannn constant
σ	Electrical conductivity
θ	Diffraction angle
θ_D	Debye temperature
θ_W	Weiss temperature
ε	Emissivity
ς	Variance assigned to the intensity value

Roman symbols

$\mathscr{S}$	Entropy
i	Increment
$d_{particle}$	Average diameter of primary particles
T_C	Curie temperature
T_M	Magnetic ordering temperature
T_N	Néel temperature
y_{bi}	Background intensity at the ith step
y_{ci}	Calculated intensity at the ith step
y_i	Observed intensity at the ith step
ß	Heating rate
A	Absorption factor
A_{cs}	Cross sectional area
A_{total}	Total surface
c_e	Electron concentration
c_h	Hole concentration
C_p	Specific heat capacity *(with constant pressure)*
C_v	Specific heat capacity *(with constant volume)*
C	Curie constant
c	Charge carrier concentration
d_{hkl}	Interplanar spacing
$d_{particle}$	Density of the precursor solution
d	Density
E_a	Activation energy of thermally-activated conduction regime
E_f	Fermi level
E_H	Hopping energy of small polaron conduction model
e	Elementary charge
f_u	Ultrasonic frequency
f	Distance from the lens to the focal plane
F_K	Structure factor
hkl	Miller indices
H	Enthalpy
I	Current
J	Transfer integral
k_B	Boltzmann constant
K_R	Thermal resistance

K	Miller indices, *hkl*, for a Bragg reflection
L_o	Lorenz number
l_{ph}	Phonon mean free path
L	Lorenz factor
l	Distance
L_K	Lorentz polarization and Multiplicity factors
M	Metal cation
m	Mass
N_A	Avogadro's number
N_p	Number of particles
n_{RS}	Integer number of rock-salt layers
N	Number of available sites
n	Number of electrons
P	Electric power
p	Number of holes
P_K	Preferred orientation function
$Q*$	Carried heat per particle
Q	Heat energy
R_p	Residual factor of the pattern
R_{wp}	Residual factor of the weighted pattern
R	Resistance
r	Ionic radius
S_c	Scale factor
S_{eff}	Effective thermopower
S	Seebeck coefficient or Thermopower
T_{HT}	Onset temperature related to the thermal reduction
t_i	Transfer integrals
T_S	Structural transition temperature
T_t	Transition temperature from semiconducting to metallic-like regime
th	Thickness
T	Absolute temperature
t	Tolerance factor
$t^{1/2}$	Half-time
U	Internal energy
u	Distance from the object plane to the lens
V	Voltage

v	Distance from the lens to the image plane
W_J	Dissipative energy *induced by Joule effect*
W_p	Activation energy of small polaron conduction model
W	Bandwidth
ZT	Dimensionless figure of merit
Z	Figure of merit
z	Coordination number
$\mathtt{S}$	Spin
$\mathtt{V}$	Internal volume

Acknowledgements

I would like to express my gratitude to all those who supported me during my PhD thesis.

First of all, I would like to thank Prof. Dr. Armin Reller for accepting the academic supervision of my PhD thesis. I would like to express my profound gratitude to my supervisor Prof. Dr. Anke Weidenkaff for her encouragements, invaluable advices, and fruitful scientific discussions throughout my PhD thesis. I especially thank her for her continuous enthusiasm regarding my work, for giving me the opportunity to further develop my scientific skills, and for creating a stimulating working atmosphere in the Solid State Chemistry and Catalysis group. I would like also to thank Prof. Dr. Jochen Mannhart and Prof. Dr. Ulrich Eckern for accepting to evaluate my PhD thesis. I would like to acknowledge the Swiss Federal Office of the Energy (BfE) and Empa for financial support.

Many thanks to the whole Solid State Chemistry and Catalysis group for all the help, support, good advices, and cheerful atmosphere. I first would like to acknowledge all the people who help me partially or completely with the proof-reading of the manuscript. To Myriam Aguirre, for your precious advices, your inestimable encouragements, and your valuables knowledges that you transmitted me, especially in electron microscopy; you gave me the ”virus”. Myriam, you showed me the path that I now enjoyed being on! To Rosa Robert, for your inestimable help and great advices during all these years, as well as the fun we had together while working in the lab, running etc... To Myriam and Rosa, for all the fruitfull disucssions on so many exotic subjects! To Dmitry Logvinovich and its crystallographic skills, for your patience and precious help, especially with Rietveld refinements. To Dmitry and Nadya, for their continuous friendship. To Paul Hug, for your invaluable help, encouragements, advices, and knowledges with thermal analysis instruments, especially with the laser flash (no comment!), and in general with Science, I learnt more than you could imagine besides you! To Matthias Trottman and all his crazy ideas in the lab, for his eternal Swiss good mood and all the trips he organized through Switzerland, ice-climbing was my favorite one! To Andrey Shkabko and Petr Tomes for their kind helps, especially with the ppms measurements and with physics in general. Thanks also to Andrey for the XPS measurements. To my two successive office mates, Myriam and Petr, for the good atmosphere we shared and all the ”philosophical” discussions we had from time to time. To the Catalysis group, Davide Ferri for his enthusiastic italian mood, Oksana Korsak for her advices with jogging training, Armin Eyssler and its german skills, Santosh Kumar Matam, and Aglaé Auclaire, j'étais contente de retrouver une compatriote dans l'équipe, bonne chance à toi! To all the students who spent a bit of time in the group, Benjamin Savreux, Alexandros Hämmerli for his motivation and enthusiasm with the experiments in the lab, Sophie Wenger for all the good moments we had together, Gregor Klopfer, Patrick Hinz, Sven Toggweiler and his American dream, and Nina Schaüble. I wish good luck to my PhD colleagues from others departments, Aude Pélisson, Quang Thai, and Romain Fardel, with whom I discovered the joyce of writing the thesis. A special thank to Romain, as a friend, merci pour ton soutien, ta fidélité, tes conseils durant la rédaction et en général pour la découverte de la culture suisse romande! Et vive LaTex! Thanks also to all my jogging partners who will recognize themselves, I often got inspiration and motivation while running/suffering in the Swiss nature.

I would like also to acknowledge all the scientists who contribute to my research work. I especially thank Dr. Antoine Maignan who gave me the opportunity to work two months in the CRISMAT laboratory at Caen, in France, Dr. Sylvie Hébert for introducing me to the magnetism and the low temperature measurements, and Dr. Sylvie Malo for the electron microscopy studies. I express my gratitude to Dr. A. Maignan and Dr. S. Hébert for the valuables advices and the fruitful discussions about my work. In general, to all CRISMAT team which make my stay in Caen a good memory, and especially to the PhD students: Natalia, Clara, Carlos, Eva, Marlène and Sébastien. Thanks as well to the aquagym team: Sylvie M., Eva, Clara, and Natalia, I suffered a lot but it was fun! To Dr. Myriam Aguirre for the electron microscopy studies. To Dr. Jiri Hejtmánek for the low-temperature electrical measurements and constructive discussions about solid state physics. I would like also to acknowledge Dr. Ursel Bangert, who make possible the collaboration at the SuperSTEM. I thank her for her valuable knowledges with STEM/EELS studies and her help with the SuperSTEM data evaluations. To Dr. Andrew Bleloch, Dr. Peng Wang, and Dr. Mhairi Gass for their collaborations at the SuperSTEM, Daresbury, UK and the EPRSC grant for financial support. To Dr. Snejana Bakardjieva for her collaboration with the high-temperature TEM studies and the ministry of education of the Czech Republic for financial support (project LC 523). To Dr. Lorenzo Castaldi and Prof. Christian Baelocher for the precious help and the use of the high-temperature diffractometer, at ETHZ, Switzerland.

I would like also to acknowledge Thomas Lippert and his group at PSI for the cheerful atmosphere during every "Empa-PSI PhD student day", it was always a good training for oral presentations. I thank also Stephan Ebbinghaus and Denis Sheptyakov for their support during the neutron measurement campaigns at PSI.

Finally, I would like to thank my family who make everything possible. Je voudrais tout particulièrement remercier ma famille sans qui tout cela n'aurait jamais été possible. À mes parents, pour m'avoir donné l'éducation, la force et le courage de toujours y arriver. Vous m'avez toujours soutenu dans mes choix, vous avez toujours été à mes côtés dans les bons comme les mauvais moments. Ici ou ailleurs, ça a été souvent difficile d'être loin de vous mais votre constant soutien m'a toujours porté. C'est difficile de dire en quelques mots combien vous me manquez, mais je suis sûre que la vie nous rapprochera à nouveau. A mon frère, si loin et pourtant si proche! Romuald, un grand merci pour tout tes encouragements, ton soutien et tous ces bons moments passés à chaque fois que je rentre en Bretagne. À mes grands-parents, pour leurs immuables soutiens et toutes leurs pensées qui me vont droit au cœur. Je voudrais en particulier dédier cette thèse à la mémoire de mon grand-père. À toute ma famille en général, pour le bon temps passé ensemble durant ces dernières années. Une pensée particulière pour Fred et Nath, vive les énergies renouvables!!! À Cédric, pour son inestimable soutien durant ces quatre années et plus particulièrement durant ces derniers mois de rédaction. Merci pour ta patience, tes encouragements, tes précieux conseils, et pour avoir toujours crû en moi. Même si nos chemins sont à présent différents, tu m'as donné la force d'y croire! Merci également à ta famille et particulièrement à Dominique pour les agréables week-ends passés tous ensemble. Enfin, à mes ami(e)s de longues dates qui savent toujours être là quand il faut. À Gaëlle, Audrey, Guillaume, Lionel, Nico et Maïwenn, Sébastien et Cédric, pour tous les fous rires partagés et les soirées passées ensemble à la Falaise, et ce malgré des retrouvailles toujours difficiles à organiser!

Merci à tous!

Curriculum Vitae

Name: Laura Bocher

Date of birth: 15. November 1982

Nationality: French

Education

Sept. 1988 - June 1993	Elementary school Ecole Ste Élisabeth 4 rue Henri Dunant - 22500 Paimpol - France
Sept. 1993 - June 1997	Secondary school Collège de Lanvignec 17 rue de Lanvignec - 22500 Paimpol - France
Sept. 1997 - June 2000	High school Lycée Kerraoul Avenue Gabriel Le Bras - 22500 Paimpol - France French equivalent for GCSE A-levels
Sept. 2000 - June 2002	Technological University I.U.T de Lannion Rue Édouard Branly - 22303 Lannion - France Degree specialized in physical measurements
Sept. 2002 - June 2005	University of Rennes I 263 Avenue du Général Leclerc - 35042 Rennes - France BSc Honours Degree and MSc Degree in Materials Science Master degree in Solid State Chemistry and ”Magistère Matériaux”
Oct. 2005 - Jan. 2009	Empa, Materials Science and Technology Solid State Chemistry and Catalysis Ueberlandstrasse 129 - CH-8600 Duebendorf - Switzerland PhD thesis
Feb. 2007 - March 2007	Laboratoire CRISMAT - UMR6508 et ENSICAEN 6 Boulevard du Maréchal Juin - 14050 Caen - France Guest student in relation with the PhD thesis
from Apr. 2009	Laboratoire de Physique des Solides - UMR8502 Universit Paris-Sud - 91405 Orsay - France Postdoctoral researcher position